

Strain-Based Design and Assessment in Critical Areas of Pipeline Systems with Realistic Anomalies

Contract No. DTPH56-14-H-00003

Final Report

Prepared for

US Department of Transportation
Pipeline and Hazardous Materials Safety Administration
Office of Pipeline Safety

Prepared by

Ming Liu, Honggang Zhou, Bo Wang, and Yong-Yi Wang



Center for Reliable Energy Systems

Jason Bergman, Brent Ayton, and Mark Stephens



Timothy Weeks



Jim Gianetto



Natural Resources
Canada

Ressources naturelles
Canada

August 31, 2017

Notice

This project was funded by the Department of Transportation, Pipeline and Hazardous Materials Safety Administration under the Pipeline Safety Research and Development Program. The views and conclusions contained in this document are those of the authors and should not be interpreted as representing the official policies, either expressed or implied, of the Pipeline and Hazardous Materials Safety Administration, or the U.S. Government.

This work is the contribution of an agency of the U.S. government, and is not subject to copyright.



Natural Resources
Canada

Ressources naturelles
Canada

Acknowledgement

This report was prepared for the U.S. Department of Transportation Pipeline and Hazardous Materials Safety Administration (US DOT PHMSA). Many individuals have provided valuable contributions throughout this multi-year effort. The project team is particularly grateful for the guidance and encouragement of Mr. Steve Nanney and Mr. James Merritt of DOT PHMSA for their support and guidance. Mr. Nanney served as the technical manager on behalf of US DOT PHMSA.

An industry advisory committee was formed to assist the refinement of the project scope, the execution of the research work plan, and the review of technical deliverables and outputs. Their insightful and constructive inputs to the project are gratefully acknowledged. The members of the advisory committee are given in the following.

- Keith Meyer (ASAP, Alaska Gas Development Corporation)
- Frank Richards (ASAP, Alaska Gas Development Corporation)
- Greg Swank (ASAP, Alaska Gas Development Corporation)
- Rick Noecker (Alaska LNG)
- Michele Panico (Alaska LNG)
- Joe Kemp (Alaska State Pipeline Coordinator's Office)
- Louis Kozisek (Alaska State Pipeline Coordinator's Office)
- Mamdouh Salama (ConocoPhillips)
- Wes Watkins (ConocoPhillips)
- Kevin Bjella (Cold Regions Research and Engineering Lab – CRREL)
- Quentin Gehring (Cold Regions Research and Engineering Lab – CRREL)
- Peter Song (Enbridge)
- Robin Gordon (Microalloying)
- Da-Ming Duan (TransCanada)
- Dave Horsley (TransCanada)
- Phil Kormann (TransCanada)

Credits

The lead organization(s) for each section of the report is given below.

- Section 1 CRES
- Section 2 CANMET and NIST
- Section 3.1 – 3.5 C-FER
- Section 3.6 NIST
- Section 4 CRES
- Section 5 CRES
- Section 6 CRES
- Section 7 CRES
- Section 8 CRES
- Appendix A CANMET
- Appendix B NIST and CANMET
- Appendix C NIST
- Appendix D C-FER
- Appendix E C-FER
- Appendix F C-FER
- Appendix G C-FER

Strain-Based Design and Assessment in Critical Areas of Pipeline Systems with Realistic Anomalies

Executive Summary

Overview, Scope, and Deliverables

Ground settlement/movement or other unusual upsetting events may expose the gas and oil pipelines to high longitudinal strain. For such loading conditions, the traditional stress-based design and assessment methods are usually not suitable.

The strain-based design and assessment (SBDA) refer to the pipeline design and assessment methods with a focus on maintaining the pipeline integrity under high longitudinal strain (typically for strain $\geq 0.5\%$). For static loadings, at least three limit states (i.e., failure modes) should be considered for the SBDA: tensile rupture, compressive buckling, and burst.

For all the three limit states, the SBDA consist of two key components: load and resistance. The pipeline integrity can be determined by comparing the load with the resistance. The load corresponding to the tensile rupture, compressive buckling, and burst, is tensile strain demand, compressive strain demand, and operating pressure, respectively. The resistance to the tensile rupture, compressive buckling, and burst, is tensile strain capacity (TSC), compressive strain capacity (CSC), and burst pressure, respectively. This report is focused on the resistance, i.e., TSC, CSC, and burst pressure.

Over the past 15 years, extensive studies focused on the TSC and CSC have been conducted. Those studies were mainly targeted at the design and construction of new pipelines. The studies on the TSC were focused on regular girth welds (jointing two pipes of nominally equal wall thicknesses), for which planar flaws were of principal concerns. The studies on the CSC were focused on plain pipes (i.e., pipes free of girth welds and anomalies) and to some extent, pipes with regular girth welds. The resistance to burst (i.e., burst pressure) under high longitudinal strain has not been investigated.

Pipelines also contain transition girth welds (jointing two pipes of un-equal wall thicknesses). In pipeline construction and service, anomalies, such as corrosion anomalies, dents, and wrinkles can be formed. The transition welds and anomalies can affect the three limit states of the SBDA and should be included in the SBDA, but had not been addressed till the start of this project.

The key objective of this project was to develop practical guidelines and tools for the SBDA of pipeline segments containing transition welds or anomalies. In this project, the SBDA methods were extended to include pipes with transition girth welds, corrosion anomalies, dents, or wrinkles. Two types of transition welds, i.e., back-beveled and counterbore-tapered welds, were studied. For corrosion anomalies, the metal-loss type corrosion anomalies were studied. For dents and wrinkles, the studies were limited to plain dents and wrinkles (i.e., no gouges or cracks). No interactions between the anomalies and/or welds were considered.

The resistance to the most critical or relevant limit states associated with the transition welds and the anomalies were investigated. For the transition welds, the TSC and CSC were studied.

For corrosion anomalies, the TSC, CSC, and burst pressure were studied. For dents, the CSC was studied. For wrinkles, the burst pressure was studied.

The technical work conducted in this project included finite element analyses (FEA), small-scale material tests, and large-scale tests. The FEA results were used to assist the specimen and instrumentation design for the large-scale tests and to develop the SBDA guidelines. The large-scale tests generated resistance data for the studied limit states, which were used to evaluate the SBDA guidelines. The small-scale tests provided necessary inputs to assist the large-scale test design/confirmation and evaluate the SBDA guidelines.

The deliverables of the project are in two parts: (1) a SBDA guideline document and (2) a technical report. The guideline document covers the high-level SBDA methods and procedures for end users and does not contain the details for the development of the guidelines. The technical report provides detailed supporting information on the development of the guidelines. The guideline document and the report cover the following major output.

- TSC and CSC of pipes with girth welds including transition welds
- TSC and CSC of pipes containing metal-loss corrosion anomalies
- Burst pressure of pipes containing metal-loss corrosion anomalies under longitudinal compressive strain
- CSC of pipes containing plain dents
- Burst pressure of pipes containing wrinkles under longitudinal compressive strain

Summary of Key Findings

Transition Girth Welds

The TSC of the transition welds were found to be greatly affected by the strength difference between the thick and thin pipes jointed by the welds. The existing pipe strength and thickness specifications for the transition welds focusing on pressure containment (e.g., ASME B31.8) are not adequate for the pipes subjected to high longitudinal strain (i.e., for the SBDA).

Enhanced pipe strength and wall thickness specifications for back-beveled and counterbore-tapered transition welds were developed to address both pressure containment and longitudinal strain. The enhanced specifications prevent strain localization in the wall thickness transition area and increase the TSC.

Assessment equations were developed to calculate the TSC of the transition girth welds. The assessment equations were derived from the PRCI-CRES TSC equations for regular girth welds by considering the strength difference between the thick and the thin pipes.

The CSC were found to be greatly reduced by/at the transition welds. The back-beveled welds usually show higher reduction in the CSC than the counterbore-tapered welds. The reduction of the CSC is largely independent of the wall thickness ratio of the two pipes jointed by the welds as long as the wall thickness ratio is greater than 1.10.

Assessment equations were developed to calculate the CSC of the girth welds (regular and transition) based on the CRES CSC equations for plain pipes. In the assessment equations, the girth welds are simplified as equivalent geometry imperfections. The equivalent geometry

imperfections of the girth welds increase with the increase of the pipe manufacturing geometry imperfections. For the pipes with negligible manufacturing geometry imperfections, the equivalent geometry imperfections of the regular and transition girth welds are $4\%t$ and $13\%t$ (t being the pipe wall thickness), respectively.

When conducting full-scale tests to examine the effects of the transition girth welds on CSC, proper loading conditions must be used. The loading should be applied in such a way that the highest moment along the length of the pipe (at least on the thin pipe) is reached at the transition weld.

Corrosion Anomalies

The TSC of a pipe was found to be greatly reduced by corrosion anomalies. The reduction in the TSC is greatly affected by the size and shape of the anomaly. The TSC decreases with the increase of the anomaly depth or circumferential width. If the longitudinal length of the anomaly is greater than a critical value ($\sim\sqrt{Dt}$), the TSC is largely independent of the longitudinal length. If the longitudinal length is less than the critical value, the TSC decreases with the decrease of the longitudinal length. As a result, the circumferential groove often shows a higher reduction in the TSC than the general corrosion or longitudinal groove of similar dimensions.

Guidelines were developed to calculate the TSC of the pipes with corrosion anomalies. The guidelines include two key components: a TSC diagram for determining the reference TSC for a given corrosion size and an equation to convert the reference TSC to the TSC by incorporating the effect of pipe properties and internal pressure.

The CSC of a pipe was found to be greatly reduced by corrosion anomalies. The reduction in the CSC is greatly affected by the size and shape of the anomaly. The CSC decreases with the increase of the anomaly depth, circumferential width, and/or longitudinal length. However, if the longitudinal length of the anomaly is greater than a critical value ($\sim 2\sqrt{Dt}$), the CSC becomes largely independent of the longitudinal length, i.e., further increasing the longitudinal length can only decrease the CSC slightly. As a result, the general corrosion often shows a higher reduction in the CSC than the circumferential and longitudinal grooves of similar dimensions.

Guidelines were developed to calculate the CSC of the pipes with corrosion anomalies. The guidelines include two key components: a CSC diagram for determining the reference CSC for a given corrosion size and an equation to convert the reference CSC to the CSC by incorporating the effect of pipe properties, pipe D/t ratios, and internal pressure.

The burst pressure of a corroded pipe was found to be reduced by longitudinal compressive strain. Increasing the longitudinal compressive strain can decrease the burst pressure. However, the burst pressure reduction due to the longitudinal compressive strain is relatively small. For example, for the corrosion anomalies, up to 40% of pipe wall thickness, compared with the burst pressure at no longitudinal compressive strain, the longitudinal compressive strain up to 2% can reduce the burst pressure for about 12%.

A burst pressure reduction equation was developed to calculate the burst pressure of corroded pipes subjected to longitudinal compressive strain. The pressure reduction equation is a function

of the longitudinal compressive strain and can be applied to the existing burst pressure equations for corroded pipes, which do not consider the effect of the longitudinal strain.

Dents

The CSC of a pipe was found to be reduced by all types of dents (i.e., formed in construction vs. formed in service, restrained vs. unrestrained). For dents of the same depth, the unrestrained dents formed in construction show the highest reduction to the CSC. The CSC reduction under zero internal pressure is much larger than that under high internal pressure. In addition, the CSC decreases as the dent depth increases.

Assessment equations were developed to calculate the CSC for pipes containing dents under high internal pressure. The equations were based on the CRES CSC equations for plain pipes and the dents were simplified as equivalent geometry imperfections. An equation was developed to determine the equivalent geometry imperfections for given dents.

Wrinkles

Under static loading, the wrinkles (if free of cracks or other types of defects) of reasonably large sizes and longitudinal compressive strain (e.g., height of 4% of pipe diameter and average compressive strain of 2%) were found to have negligible effects on the burst pressure of the pipe. Even severe wrinkles of extremely large sizes (e.g., a wrinkle folded onto itself) showed very limited effects on the burst pressure (i.e., < 15% reduction) as long as the wrinkles did not form any cracks or other types of defects in the pipe wall. In addition, the reduction of the burst pressure was found to be caused by the increase of the pipe longitudinal compliance due to the severe wrinkles, not the strain and stress concentration near the wrinkles.

Therefore, it was concluded that the wrinkles, that are free of cracks or other types of defects, experiencing longitudinal compressive strain may not negatively affect the pipe burst pressure in the absence of cycle loads in the form of lateral bending or pressure fluctuation. Cycle loads can initiate or cause growth of flaws, which in turn may change the stiffness of the pipeline segment, potentially leading to high-cycle or low-cycle fatigue failures. The effects of fatigue loads were not in the scope of the project and not examined in this project.

Table of Contents

Notice	i
Acknowledgement	ii
Executive Summary	iii
 Nomenclature	 1
Abbreviations	1
Symbols	2
Organizations	5
1 Introduction	6
1.1 Overview of Strain-Based Design and Assessment (SBDA)	6
1.1.1 Application of SBDA	6
1.1.2 Framework of SBDA	6
1.1.3 Key Components of SBDA	7
1.2 Assessment of Anomalies in Pipelines	9
1.2.1 Assessment of Corrosion	9
1.2.2 Assessment of Mechanical Damage	10
1.3 Gaps in SBDA and Incentives for this Project	10
1.3.1 Gaps in SBDA with respect to Pipeline Fittings	10
1.3.2 Gaps in SBDA with respect to Anomalies in Pipelines	10
1.4 Project Overview	10
1.4.1 Overall Objective	10
1.4.2 Project Scope	11
1.4.3 Deliverables	11
1.5 Overview of the Program	12
1.5.1 Project Team Structure	12
1.5.2 Overall Flow of the Work	13
1.6 Structure of the Report	13
2 Material Property Characterizations	15
2.1 Overview of Materials Used for Tests	15
2.2 Properties of Pipe Materials Used in Full-Scale Pipe Tests	16
2.2.1 Overview of Small-Scale Material Tests	16
2.2.2 Tensile Testing of Selected Pipes	16
2.2.3 Tensile Property Data for Selected Steel Pipes	17
2.2.4 Compression Testing of Selected Pipes	24
2.2.5 Compression and Tension Properties of Selected Pipes	24
2.3 Properties of Materials Used in Curved Wide Plate Tests	28
2.3.1 Overview of the Small-Scale Tests	28
2.3.2 Pipe Properties	28
2.3.3 Girth Weld Properties	36
3 Large-Scale Tests and Testing Results	48

3.1 Overview of Large-Scale Testing Program	48
3.2 Full-Scale Bending Tests of Pipes with Transition Welds and Anomalies (Task 9)	48
3.2.1 Specimen Configuration	48
3.2.2 Specimen Anomalies	50
3.2.3 Specimen Grid Layout and Measurements	53
3.2.4 Test Setup	54
3.2.5 Calculation of Critical Compressive Strain Capacity for Bend Tests	57
3.2.6 Test Procedure	61
3.2.7 Test Results	61
3.3 Full-Scale Bending-Burst Tests of Pipes with Corrosion Anomalies (Task 10)	65
3.3.1 Specimen Configuration	65
3.3.2 Specimen Anomalies	65
3.3.3 Specimen Grid Layout and Measurements	66
3.3.4 Test Setup	66
3.3.5 Test Procedure	66
3.3.6 Test Results	67
3.4 Full-Scale Compression-Burst Tests of Pipes with Wrinkles (Task 11)	69
3.4.1 Specimen Configuration	69
3.4.2 Specimen Grid Layout and Measurements	69
3.4.3 Test Setup	70
3.4.4 Instrumentation	70
3.4.5 Test Procedure	72
3.4.6 Test Results	73
3.5 Full-Scale Tension Tests of Pipes with Corrosion Anomalies (Task 12)	75
3.5.1 Specimen Configuration	75
3.5.2 Specimen Anomalies	75
3.5.3 Specimen Grid Layout and Measurements	76
3.5.4 Test Setup	77
3.5.5 Instrumentation	78
3.5.6 Test Procedure	80
3.5.7 Test Results	80
3.6 Curved Wide Plate Tension Tests of Transition Welds (Task 13)	82
3.6.1 Overview of Testing Setup	82
3.6.2 Testing Matrix	82
3.6.3 Testing Results	83
4 Girth Welds Subjected to Longitudinal Strain	89
4.1 Overview of the Studies on Girth Welds	89
4.1.1 Limit States Associated with Girth Welds Subjected to Longitudinal Strain	89
4.1.2 Types of Girth Welds	89
4.1.3 Section Structure and General Approach	90
4.2 Tensile Strain Capacity of Girth Welds	91
4.2.1 Application and Definition of Tensile Strain Capacity	91

4.2.2 Basis of Studies	91
4.2.3 Assessment of Counterbore-Tapered Transition Welds	93
4.2.4 Assessment of Back-Beveled Transition Welds	97
4.3 Compressive Strain Capacity of Girth Welds	107
4.3.1 Application and Definition of Compressive Strain Capacity	107
4.3.2 Basis of Studies	108
4.3.3 Basic Methods for CSC of Girth Welds	109
4.3.4 Analysis of Full-Scale Tests and Loading Conditions for Transition Welds	110
4.3.5 Parametric Studies	124
4.3.6 Establishment of Equivalent Geometry Imperfections of Girth Welds	131
4.3.7 Compressive Strain Capacity Equations	133
4.3.8 Evaluation of the CSC Equations of Transition Welds	134
5 Pipes with Corrosion Anomalies Subjected to Longitudinal Strain	136
5.1 Overview of the Studies on Corrosion	136
5.1.1 Limit States Associated with Corrosion Subjected to Longitudinal Strain	136
5.1.2 Section Structure and General Approach	137
5.2 Tensile Strain Capacity of Corroded Pipes	138
5.2.1 Application and Definition of Tensile Strain Capacity	138
5.2.2 Analysis of Full-Scale Tests	138
5.2.3 Parametric Analyses	145
5.2.4 Procedures for Assessing Tensile Strain Capacity of Corroded Pipes	152
5.3 Compressive Strain Capacity of Corroded Pipes	154
5.3.1 Application and Definition of Compressive Strain Capacity	154
5.3.2 Simulation of Experimental Tests	155
5.3.3 Parametric Studies	159
5.3.4 Procedures for Assessing Compressive Strain Capacity of Corroded Pipes	164
5.4 Burst Pressure of Corroded Pipes Subjected to Longitudinal Strain	167
5.4.1 Background and Application of Burst Pressure	167
5.4.2 Analysis of Burst Pressure of Corroded Pipes under Longitudinal Strain	168
5.4.3 Comparison of the FEA and Experimental Results	171
5.4.4 Burst Pressure Equation for Corroded Pipes Subjected to Longitudinal Strain	174
6 Pipes with Dents Subjected to Longitudinal Strain	175
6.1 Overview of the Studies on Dents	175
6.1.1 Limit States Associated with Dents Subjected to Longitudinal Strain	175
6.1.2 Section Structure and General Approach	176
6.2 Effects of Dent Forming and Restraint Conditions on Compressive Strain Capacity	176
6.2.1 Rationale of Analysis	176
6.2.2 Finite Element Analysis Models	177
6.2.3 Material Properties	178
6.2.4 Analysis Process	178
6.2.5 Typical Analysis Results and Calculation of Compressive Strain Capacity	180
6.2.6 CSC Calculated at Different Dent Forming and Restraint Conditions	182

6.2.7 Effect of Indenter Sizes on CSC	182
6.3 Comparison of Full-Scale Testing with FEA Results	185
6.3.1 Predicted vs. Measured Dent Depths	185
6.3.2 Predicted vs. Measured CSC of Dented Pipes	185
6.4 Parametric Studies of CSC of Dented Pipes	187
6.4.1 Overview of the Parametric Studies	187
6.4.2 Effect of Pipe Dt Ratio on CSC	187
6.4.3 Effect of Pipe YT Ratio on CSC	189
6.4.4 Effect of Internal Pressure on CSC	191
6.5 Establishment of Equivalent Geometry Imperfections of Dented Pipes	193
6.6 Compressive Strain Capacity Equations of Dented Pipes	193
6.6.1 Equations for 2D CSC	193
6.6.2 Equations for CSC by Extrapolation	194
6.6.3 Evaluation of the CSC Equations of Dented Pipes	194
7 Pipes with Wrinkles Subjected to Longitudinal Strain	197
7.1 Overview of the Studies on Wrinkles	197
7.1.1 Limit States Associated with Wrinkles Subjected to Longitudinal Strain	197
7.1.2 Section Structure and General Approach	197
7.2 Finite Element Analyses	198
7.2.1 Finite Element Analysis Models	198
7.2.2 Loading Conditions and Material Properties	199
7.2.3 Typical Results and Failure Criteria	200
7.3 Comparison of Full-Scale Testing Data with Finite Element Analyses	200
7.4 Burst Pressure of Wrinkled Pipes under Compressive Strain	203
8 Concluding Remarks	204
8.1 General	204
8.2 Girth Welds	205
8.2.1 Tensile Strain Capacity	205
8.2.2 Compressive Strain Capacity	206
8.3 Pipes with Corrosion Anomalies	207
8.3.1 Tensile Strain Capacity	207
8.3.2 Compressive Strain Capacity	208
8.3.3 Burst Pressure	208
8.4 Pipes with Dents	209
8.5 Pipes with Wrinkles	209
8.6 Gaps and Future Work	210
9 Reference	212

Nomenclature

Abbreviations

3-D	Three dimensional
BM	Pipe base metal
CS	Compressive strain
CSC	Compressive strain capacity
CMOD	Crack mouth opening displacement
CTOD	Crack tip opening displacement
CTOD _A	Apparent CTOD toughness
CTOD _F	CTOD driving force
CTOD _{pipe}	Crack tip opening displacement measured on pipe side
CTOD _R	CTOD resistance
CTOD _{weld}	Crack tip opening displacement measured on weld side
CWP	Curved wide plate
DF	Design factor
DIC	Digital image correlation
ERW	Electric resistance welding
FEA	Finite element analysis
FCAW	Flux-cored arc welding
GMAW	Gas metal arc welding
HAZ	Heat affected zone
ID	Inside diameter
ILI	Inline inspection
IMU	Inertial measurement unit
LVDT	Linear variable displacement transducer
MAOP	Maximum allowable operating pressure
OD	Outside diameter
OM	Weld strength overmatching ratio
OV	Cross section ovality
SBD	Strain based design
SBDA	Strain based design and assessment
SEN(B)	Single edge notch bending
SEN(T)	Single edge notch tension
SE(T)	Single edge notch tension

SMAW	Shielded metal arc welding
SMYS	Specified minimum yield strength
SMTS	Specified minimum tensile strength
SSC	Stress-strain curves
TS	Tensile strain
TSC	Tensile strain capacity
uEL	Uniform strain (uniform elongation)
UOE	'U', 'O', and expansion
UTS	Ultimate tensile strength
WCL	Weld center line
WT	Wall thickness
YS	Yield strength
Y/T	Yield to tensile strength ratio

Symbols

a	Flaw height
c	Half flaw length
d_c	Depth of corrosion anomaly
d_{de}	Dent depth after elastic re-rounding
d_{di}	Indentation depth
d_{dp}	Dent depth of pressurized pipe
d_{d0}	Dent depth of unpressurized pipe
D	Pipe outside diameter (OD)
D_f	Design factor
D_{\max}	Maximum pipe outside diameter
D_{\min}	Minimum pipe outside diameter
E	Young's modulus
f_p	Pressure factor
f_n	Net-section stress factor
h or h_m	Height of girth weld high-low misalignment
h_g	Height of pipe geometry imperfection
h_g^e	Height of equivalent pipe geometry imperfection for dent and transition weld
h_w	Height of pipe wrinkle
L	Gauge length, length of pipe specimen, or counterbore length
L_c	Length of a corrosion anomaly in pipe longitudinal direction
L_g	Wavelength of pipe geometry imperfection in pipe longitudinal direction

L_w	Wavelength of wrinkle in pipe axial (longitudinal) direction
l_0	Gauge length for CSC measurement
n	Strain hardening exponent
O_v	Cross section ovality (OV), $O_v = (D_{\max} - D_{\min}) / (D_{\max} + D_{\min})$
P_b	Burst pressure of pipes without longitudinal strain
$P_b^{\varepsilon_c}$	Burst pressure of pipes under longitudinal compressive strain
p_i	Internal pressure
p_e	External pressure
R_a or η	Normalized depth of crack-like planar anomalies, i.e., a/t
R_b	Pipe bending radius
R_c or β	Normalized length of crack-like planar anomalies, i.e., $2c/t$
R_G	Pipe SMYS ratio between the thin-wall pipe and the thick-wall pipe jointed by a transition weld, i.e., $\sigma_{SMYS}^{thin} / \sigma_{SMYS}^{thick}$
R_h or ψ	Normalized weld high-low misalignment, i.e., h/t
R_M or ϕ	Weld metal strength mismatch ratio, i.e., σ_u^w / σ_u
R_t	Wall thickness ratio between the thick-wall pipe and the thin-wall pipe jointed by a transition weld, i.e., t_{thick} / t_{thin}
R_u	Pipe ultimate tensile strength ratio between the thin-wall pipe and the thick-wall pipe jointed by a transition weld, i.e., $\sigma_u^{thin} / \sigma_u^{thick}$
R_y	Pipe yield strength ratio between the thin-wall pipe and the thick-wall pipe jointed by a transition weld, i.e., $\sigma_y^{thin} / \sigma_y^{thick}$
R_{YT} or ξ	Pipe yield to tensile strength ratio, or Y/T ratio, i.e., σ_y / σ_u
t	Pipe wall thickness
t_{thick}	Wall thickness of the thick-wall pipe jointed by a transition weld
t_{thin}	Wall thickness of the thin-wall pipe jointed by a transition weld
W_c	Length of a corrosion anomaly in pipe circumferential direction
α	Angle of geometry imperfection in pipe circumferential direction
β or R_c	Normalized length of crack-like planar anomalies, i.e., $2c/t$
η or R_a	Normalized depth of crack-like planar anomalies, i.e., a/t
ψ or R_h	Normalized weld high-low misalignment, i.e., h/t
ρ	Normalized geometry imperfection: h_g/t
ρ^e	Normalized equivalent geometry imperfection: h_g^e/t
δ_A	Apparent CTOD toughness (CTOD _A)
δ_F	Crack tip opening displacement

θ	Taper angle of transition girth weld
θ_1, θ_2	Pipe cross section rotation angles
ν	Poisson's ratio
ε	Strain
ε_c	Compressive strain
ε_c^{crit}	Compressive strain capacity (CSC) under bending-dominant loading
$\varepsilon_c^{crit,2D}$	2D compressive strain capacity
ε_c^{dem}	Compressive strain demand
$\varepsilon_{c,corr}^{crit}$	Compressive strain capacity of pipes with corrosion anomalies
$\varepsilon_{c,corr}^{ref}$	Reference compressive strain capacity of a pipe with corrosion
$\varepsilon_{c,dent}^{crit,2D}$	2D compressive strain capacity of dented pipes
$\varepsilon_{c,dent}^{crit,ex}$	Compressive strain capacity by extrapolation of dented pipes
$\varepsilon_{c,gw}^{crit,2D}$	2D compressive strain capacity of regular girth welds
$\varepsilon_{c,gw}^{crit,ex}$	Compressive strain capacity by extrapolation of regular girth welds
$\varepsilon_{c,tw}^{crit,1DS}$	1DS compressive strain capacity of transition girth welds
$\varepsilon_{c,tw}^{crit,ex}$	Compressive strain capacity by extrapolation of transition girth welds
ε_e	Strain where the Lüders extension ends
ε_t	Tensile strain
ε_t^{crit}	Tensile strain capacity
$\varepsilon_t^{crit} _{cb}$	Reference tensile strain capacity in the counterbore
$\varepsilon_{t,corr}^{crit}$	Tensile strain capacity of pipes with corrosion anomalies
$\varepsilon_{t,tw}^{crit}$	Tensile strain capacity of transition girth welds
ε_t^{ref}	Reference tensile strain capacity of a regular girth weld with $\delta_A = 0.8$ mm
$\varepsilon_{t,corr}^{ref}$	Reference tensile strain capacity of a pipe with corrosion
ε_u	Pipe uniform strain or uniform elongation (uEL)
σ	Stress
σ_a	Applied axial (longitudinal) stress
σ_h	Applied hoop (circumferential) stress
σ_{mises}	von Mises stress

σ_{SMYS}	Pipe SMYS
σ_u	Ultimate tensile strength or tensile strength
σ_u^w	Weld metal ultimate tensile strength
σ_y	Yield strength
σ_y^w	Weld metal yield strength
ξ or R_{YT}	Pipe yield to tensile strength ratio, or Y/T ratio, i.e., σ_y / σ_u
ϕ or R_M	Weld metal strength mismatch ratio, i.e., σ_u^w / σ_u

Organizations

API	American Petroleum Institute
ASME	The American Society of Mechanical Engineers
CRES	Center for Reliable Energy Systems
CSA	Canadian Standards Association
DNV	Det Norske Veritas
DOT	Department of Transportation
NIST	Nation Institute of Standards and Technology
PHMSA	Pipeline and Hazardous Materials Safety Administration
PRCI	Pipeline Research Council International
UOA	University of Alberta

1 Introduction

1.1 Overview of Strain-Based Design and Assessment (SBDA)

1.1.1 Application of SBDA

Strain-based design and assessment (SBDA) of pipelines focuses on potential failures driven by or in presence of high longitudinal strain. In most cases, failures driven by longitudinal stress or strain are associated with ground settlement/movement or other unusual upsetting events, which can have serious life safety and environmental consequences.

Although the development of the SBDA has been primarily targeted for the applications in the design and construction of new pipelines [1,2,3], the principles of the SBDA can be applied to the assessment of in-service pipelines as well. For instance, the fitness-for-service principles embedded in the SBDA can be applied to guide the maintenance of vintage pipelines [4].

1.1.2 Framework of SBDA

The two predominant limit states (or failure modes) associated with high longitudinal stress and strain are tensile rupture (or leak) and compressive buckling (see Figure 1-1). The tensile rupture is considered as an ultimate limit state due to the breach of the pipe wall. On the other hand, the compressive buckling is usually considered as a service limit state, since the buckling typically results in distortion of pipe cross sections without the breach of pipe walls. However, excessive distortion of the pipe cross section can interfere with the operation of ILI tools and even cause the breach of the pipe wall.

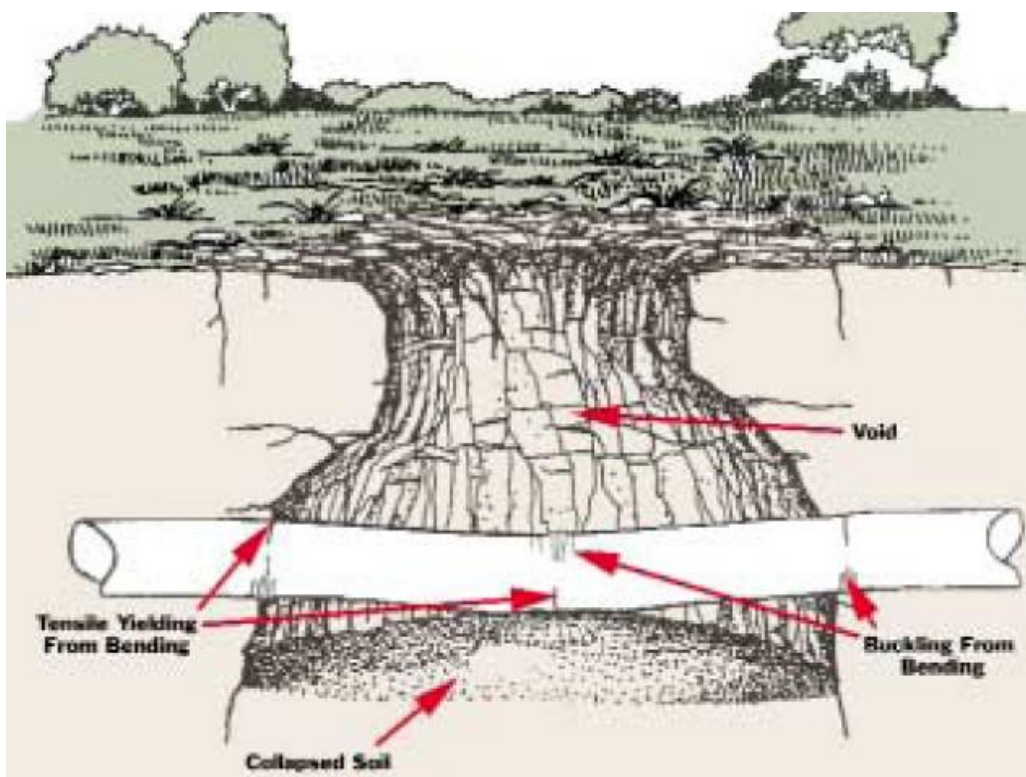


Figure 1-1 Possible failure models of a pipeline due to mine subsidence

The SBDA consists of two key components: strain demand and strain capacity. The strain demand measures the load applied to the pipeline and the strain capacity measures the resistance of the pipeline to failures. For each failure mode (or limit state), there exist corresponding strain demand and strain capacity. For example, for tensile rupture, tensile strain demand and tensile strain capacity are used. Additional discussions about the strain demand and strain capacity can be found in Section 1.1.3.

The fitness of the pipeline subjected to high longitudinal strain can be assessed by comparing the strain demand with the strain capacity, as shown Figure 1-2. If the capacity is determined to be greater than the demand by a sufficient margin of safety, the pipeline is deemed safe. The comparison of the demand and capacity needs to be conducted for all possible failure modes.

In addition to the tensile and compressive failure modes, under certain circumstances, e.g., pipes with corrosion anomalies, burst is another limit state which needs to be considered for the SBDA. The burst pressure can be compared with the maximum allowable operating pressure (MAOP) of the pipeline to check if adequate safety margin can be maintained.

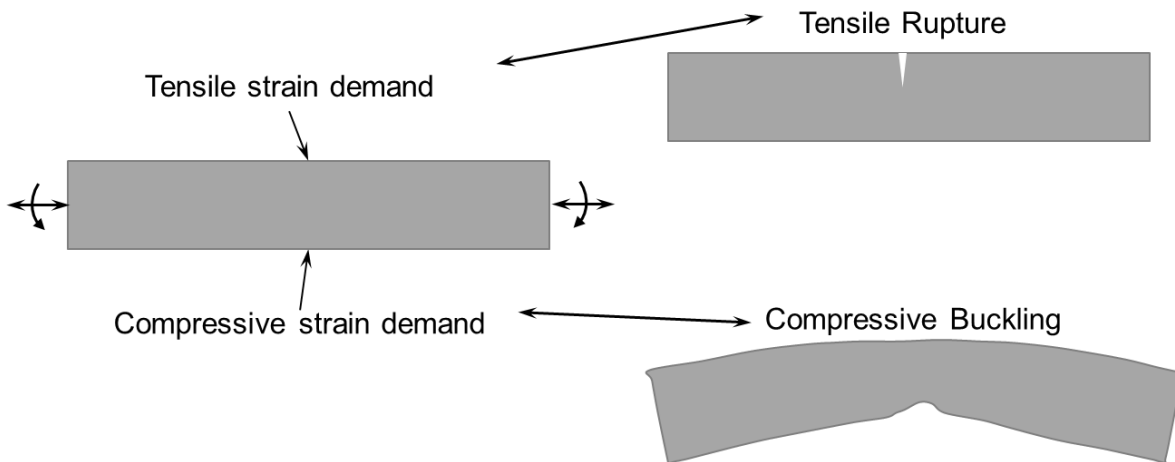


Figure 1-2 Schematic illustration of the relationship between strain demand and strain capacity in SBDA

1.1.3 Key Components of SBDA

1.1.3.1 Strain Demand

1.1.3.1.1 *Nature and Characteristics of Strain Demand*

The loadings applied to a pipeline can be broadly categorized as displacement-controlled and load-controlled. A loading is considered load-controlled if the magnitude of the loading is not affected by the displacement of the pipe. Some examples of such loadings are internal pressure, free span loading, and dead weight loading. One important characteristic of the load-controlled loading is that if the load is beyond the maximum load carrying capacity of a pipe, instantaneous failures (collapse or rupture) will take place.

Under a strict definition, a loading is considered displacement-controlled if the magnitude of the pipe displacement is not affected by the stiffness of the pipe. Some good examples of such a displacement-controlled loading are pipe bending by a mandrel and reeling-on a pipe string in spool-based installation.

On the other hand, for onshore buried pipelines, the displacement-controlled loading is often loosely defined as the condition, in which the loading is applied through soil movement of given magnitude. Although the soil displacement is set, the pipe displacement does vary with the pipe stiffness. An important characteristic of this type of displacement-controlled loading is that the actual load applied to the pipe decreases with the pipe displacement. Therefore, instantaneous failures (collapse or rupture), in general, do not take place even if the applied load is beyond the maximum load carrying capacity of the pipe.

It should be noted that for buried pipelines, under certain circumstances, the displacement-controlled loading can change to a load-controlled loading. For example, the load due to slow-moving and small-magnitude ground movement is primarily displacement-controlled. However, under large-magnitude soil movement, especially for loose sandy conditions, the soil can flow around the pipe. Under this circumstance, the load becomes load-controlled. As a result, for most buried pipes, strictly speaking, the soil loading is a combination of displacement- and load-controlled.

1.1.3.1.2 *Determination/Estimation of Strain Demand*

A number of methods are available for estimating strain demand. The most frequently used methods are inertial measurement units (IMU), strain gauges, fiber optical cables, and numerical simulations (e.g., using pipe-soil interaction models). Other measurement techniques are being developed. Various techniques for the estimation and monitoring of strain demand can be found in a JIP report [5].

Each strain estimation method offers certain advantages and disadvantages. For instance, the strain measured by strain gauges is considered highly reliable. However, the strain gauges can only monitor very small localized areas. On the other hand, pipe and soil interaction models can be used for long or short segments of pipelines. However, the strain computed from such models highly depends on the accuracy of the parameters representing soil properties. Site-specific soil properties are generally not available and can change over time or even from season to season because the water content and its state in the soil can affect soil properties.

1.1.3.2 Strain Capacity

1.1.3.2.1 *Tensile Strain Capacity Models*

The tensile strain capacity (TSC) refers to the highest tensile strain a pipe or weld can sustain without leaking or rupturing. A number of tensile strain models are available for estimating the TSC, including the models from PRCI-CRES [6,7,8,9], ExxonMobil [10,11,12], and many other organizations [13,14,15,16,17,18,19].

Almost all models developed in the last decade were targeted at new pipeline constructions, in which the concept of strain-based design was used at the start of the pipeline projects. Some of these models, such as the PRCI-CRES models, can be adapted to assessing in-service pipelines (including vintage pipelines), since they can use Charpy impact energy as a measure of toughness. The models using CTOD or J -resistance curves exclusively as the toughness measure are less adaptive.

1.1.3.2.2 *Compressive Strain Capacity*

There are many compressive strain models/equations for calculating the compressive strain capacity (CSC) of pipes in codes and standards, such as DNV OS F101 [20], CSA Z662 [21], and API RP 1111 [22]. Newer models include those by University of Alberta (UOA) [23,24,25] and CRES for US DOT PHMSA [26,27]. The CRES models incorporate key parameters for the CSC, including D/t ratio, internal pressure, geometry imperfection, pipe Y/T ratio, uniform strain, and Lüders strain. These models also provide improved assessment for the effects of girth welds and have a greater range of applicability than most existing models [26,27].

1.1.3.3 Strain Demand Limit and Safety Factor

There are uncertainties in both strain demand and strain capacity. The accuracy of the strain demand estimation depends strongly on the techniques used for estimating the strain demand and the knowledge of the local geotechnical conditions. It is not feasible to suggest a unique safety factor for the strain demand with the current state of knowledge.

The *strain demand limit* may be set by considering the uncertainty in the procedures/models used to estimate the strain capacity and the consequence of exceeding the limit. As described in prior sections, reaching CSC has limited consequences under displacement-controlled loading. Consequently, the safety factor can be set rather high. For example, CSA Z662 Annex C has a safety factor of 0.8 on compressive strain capacity.

Curved wide plate and full-scale pipe tests have shown that the measured TSC can vary by a factor of two under “identical” material, geometric, and flaw conditions [28]. Assuming the predicted TSC by the tensile strain models is in the middle of the low- and high-end capacity from the experimental measurement, the low-end strain capacity would be 0.67 of the predicted value. In order to have the predicted TSC equal to the measured lower-end strain capacity, the safety factor of 0.67 should be applied to the predicted value. So, an appropriate safety factor for the TSC models can be 0.67. The PHMSA’s SBD Special Permit conditions specify a safety factor of 0.60 [29]. The 2007 version of CSA Z662 Annex C [30] on limit state design specifies a resistance factor (equivalent to a safety factor) of 0.70.

1.2 Assessment of Anomalies in Pipelines

1.2.1 Assessment of Corrosion

The burst pressure for pipelines with corrosion anomalies, alternatively termed remaining strength, may be estimated using a number of widely used methods, including ASME B31G [31], modified ASME B31G [31], RSTRENG [31], API 579/ASME FFS-1 [32], PCORRC [33], and DNV RP F101 (LPC-1/ BS7910) [34]. Most of these models consider only longitudinal (axial) corrosion anomalies. The DNV models also address circumferential corrosion anomalies where failures due to both internal pressure and longitudinal stress are recognized.

A joint industry project completed in early 2000 developed a guidance document (PDAM - pipeline defect assessment manual) for the selection of the best methods for assessing corrosion defects [35]. In a series of recently completed projects [36,37,38,39] supported by PRCI and PHMSA, a guidance document on assessing the integrity of corroded pipes was developed [40].

However, the focus of those efforts was on longitudinal corrosion defects under predominantly hoop stress. Although an assessment method was given for the situation where the pipe experiences both hoop and longitudinal stresses [41], the method is stress-based and the maximum allowable longitudinal stress is limited to the yield strength of the pipe.

1.2.2 Assessment of Mechanical Damage

Dents and gouges (often associated with dents) are some of the most frequently found anomalies. The existing assessment models for dents and gouges mainly focus on the potential failures induced by internal pressure, i.e., burst under static pressure and fatigue under cyclic pressure (e.g., CSA Z662 [21], ASME B31.8 [42], Q-factor [43], and British Gas [44]).

Some of the most recent research activities include a joint industry project which produced the PDAM [45] and a number of projects sponsored by PHMSA and PRCI [46,47,48,49,50,51]. Most of the existing work does not address the effect of the longitudinal stress/strain on the burst pressure and fatigue life. In addition, under high longitudinal stress/strain, the failures due to tensile rupture and compressive buckling have not been studied.

For plain dents, it is believed that the burst is not a critical concern for the SBDA, while the critical concerns are fatigue failures and compressive buckling.

1.3 Gaps in SBDA and Incentives for this Project

1.3.1 Gaps in SBDA with respect to Pipeline Fittings

While the PRCI-CRES tensile strain and CRES compressive strain models are technically advanced and supported by a substantial body of large-scale experimental test data [6,7,8,26,28,52,53,54,55,56], these models, similar to almost all other models, were developed for and are applicable to regular girth welds (welds joining pipes of equal wall thicknesses). Most pipelines contain fittings such as hot bends, elbows, tees, and valves. The manual welds connecting those fittings to the adjacent linepipes usually have lower strength and toughness than mechanized GMAW welds. Some of these fittings, such as hot bends and elbows, may be located in the areas of high strain demand due to the topography of the right-of-way. The geometry of the fitting welds introduces strain concentrations due to wall thickness transitions and/or high-low misalignment. In summary, fitting welds are potentially subjected to higher longitudinal strains and have less desirable properties than mainline welds. The strain capacity of these welds is largely unknown and a corresponding assessment methodology has not yet been developed.

1.3.2 Gaps in SBDA with respect to Anomalies in Pipelines

Most pipelines have anomalies, such as corrosion and mechanical damage, in their lifetime. The current methodologies for assessing and mitigating those anomalies were developed for pipelines for which hoop stress is the primary driver for potential failures. The validity of these current methods has not been established for pipelines under conditions of high longitudinal strain.

1.4 Project Overview

1.4.1 Overall Objective

The primary objective of the project is to develop practical and easy-to-use guidelines and

tools for the strain-based design and assessment (SBDA) of pipeline segments, which contain transition girth welds or anomalies (including corrosion anomalies, dents, and wrinkles). The work in this project involves collaborative development, generation, and promotion of new technologies for the strengthening of industry consensus standards.

1.4.2 Project Scope

The project covers transition welds (typically associated with fittings), metal loss corrosion anomalies, plain dents, and wrinkles. For each feature listed above, various limit states relevant to the SBDA are investigated. The technical work includes finite element analysis, small-scale material characterization tests, and large-scale tests.

The focus of this project is to fill the critical technology gaps in the existing SBDA methods, specifically (shown in Figure 1-3):

- (1) Tensile strain capacity (TSC) and compressive strain capacity (CSC) of transition welds,
- (2) Tensile strain capacity (TSC), compressive strain capacity (CSC), and burst pressure of pipes containing metal loss corrosion anomalies,
- (3) Compressive strain capacity (CSC) of pipes containing plain dents, and
- (4) Burst pressure of pipes containing wrinkles.

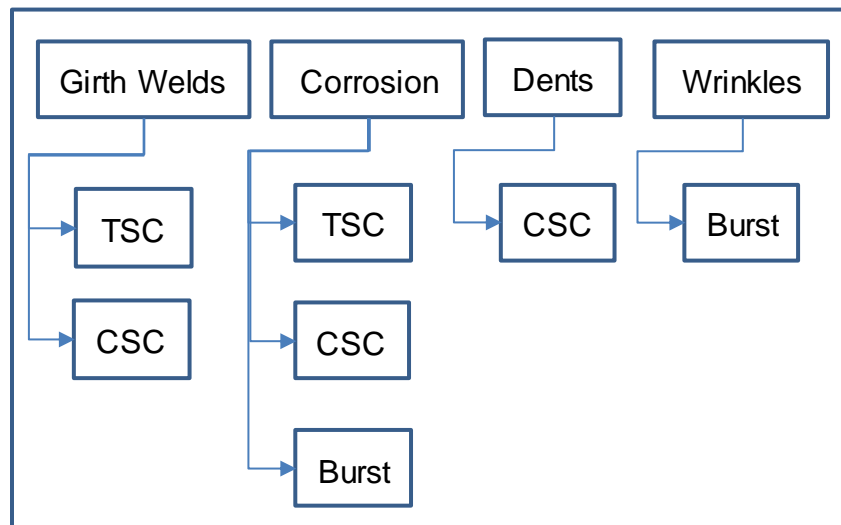


Figure 1-3 Project scope

As shown above, the scope of the project includes the limit states for static loadings only. The limit states for cyclic loadings are not in the project scope. However, it should be noted that for the pipeline segments subjected to longitudinal strain, the fatigue behaviors of the pipes under cyclic loadings need to be further investigated, especially for pipes containing dents.

1.4.3 Deliverables

The major deliverables for the project are provided in two main documents:

- (1) a guideline reference document for the SBDA and
- (2) a comprehensive technical report.

The guideline reference document is a separate standalone report [57], while this document serves as the comprehensive technical report. The guideline reference document targets end users for project applications and does not contain the technical details for the development of the guidelines. The technical report covers the work completed and provides detailed technical information, which supports the development of the guideline reference document.

Some notable deliverables from the technical work include:

- Material properties of the pipes and welds used in the tests,
- Large-scale test results
 - Tensile and compressive strain capacities of girth welds including transition welds,
 - Tensile and compressive strain capacities of pipes containing metal loss corrosion anomalies,
 - Burst pressure of pipes containing metal loss corrosion anomalies under longitudinal compressive strain,
 - Compressive strain capacities of pipes containing plain dents, and
 - Burst pressure of pipes containing wrinkles under longitudinal compressive strain.
- Assessment guidelines for
 - Tensile and compressive strain capacities of girth welds including transition welds,
 - Tensile and compressive strain capacities of pipes containing metal loss corrosion anomalies,
 - Burst pressure of pipes containing metal loss corrosion anomalies under longitudinal compressive strain,
 - Compressive strain capacities of pipes containing plain dents, and
 - Burst pressure of pipes containing wrinkles under longitudinal compressive strain.

1.5 Overview of the Program

1.5.1 Project Team Structure

The project team members include CRES, C-FER, NIST, CanmetMATERIALS (CANMET), and an industry advisory committee. CRES, C-FER, NIST, and CANMET are collectively called the research team.

- CRES served as the project lead. CRES was primarily responsible for developing large-scale test protocols with C-FER and NIST, developing assessment models, and drafting SBDA guidelines.
- C-FER was primarily responsible for procuring materials, fabricating of test assemblies, and conducting full-scale tests.
- NIST was primarily responsible for conducting curved-wide-plate tests and some small-scale material characterization tests.
- CANMET was primarily responsible for conducting small-scale material characterization tests.

- The industry advisory committee members advised the research team during the project execution. They also reviewed and provided critical feedbacks regarding the final documents to ensure accuracy and relevance to practical applications.

1.5.2 Overall Flow of the Work

The main components of the technical work included finite element analyses (FEA), small-scale material characterization tests, and large-scale tests. The workflow or the correlation of the different components of the technical work is schematically shown in Figure 1-4. This workflow was used for the assessment of all the limit states.

In summary, the FEA provided critical inputs, such as specimen and instrumentation design, to the large-scale tests. At the same time, the FEA also provided the data for the development of the assessment models and guidelines. The large-scale test data provided direct resistance data for the different limit states. More importantly, the large-scale test data were used to evaluate the assessment models and guidelines. The small-scale tests provided necessary inputs to assist with the large-scale test design/confirmation and evaluation of the assessment models and guidelines.

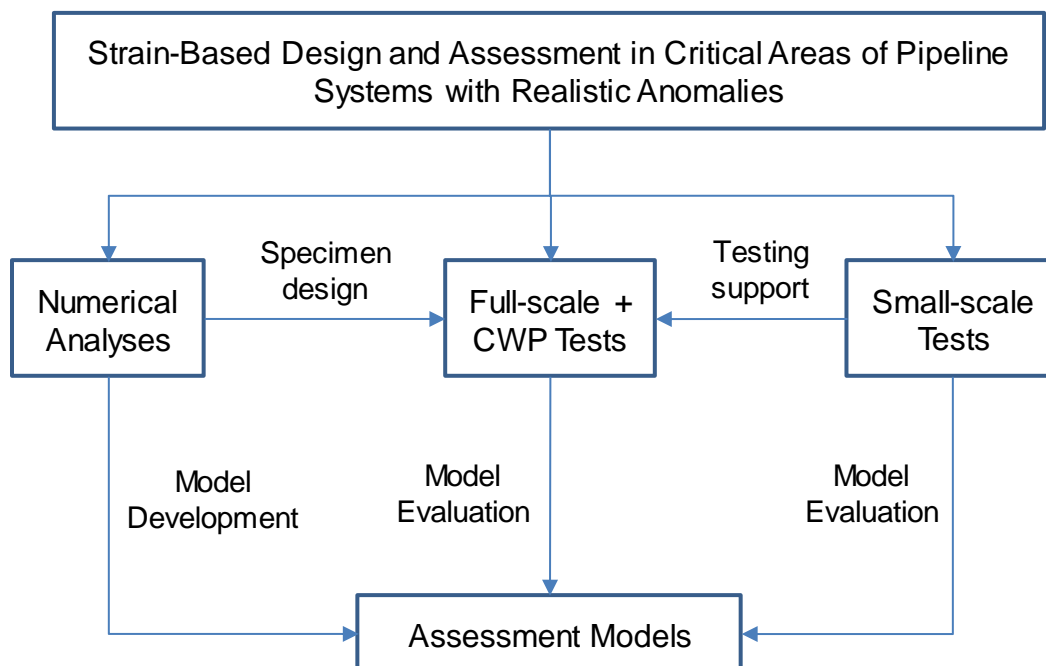


Figure 1-4 Overall work flow

1.6 Structure of the Report

Section 2 provides the details of the small-scale tests and summarizes the testing results. The focus was on the evaluation of the mechanical properties (i.e., strength and toughness) of the pipe and weld materials tested in this project.

Section 3 provides the details of all the large-scale tests (full-scale pipe tests and curve-wide-plate tests) and summarizes the testing results. The full-scale tests for the determination of the compressive strain capacity of pipes containing transition welds, corrosion anomalies, and dents are presented in Section 3.2. The full-scale tests for the determination of the burst pressure of pipes containing corrosion anomalies are presented in Section 3.3. The full-scale tests for the

determination of the burst pressure of pipes containing wrinkles are presented in Section 3.4. The full-scale tests for the determination of the tensile strain capacity of pipes containing corrosion anomalies are presented in Section 3.5. The curved-wide-plate tests for the determination of the tensile strain capacity of pipes containing transition welds are presented in Section 3.6.

Section 4 provides the details of the studies for the assessment of transition welds and summarizes the assessment guidelines and models for transition welds. The studies for the tensile strain capacity and compressive strain capacity are given in Section 4.2 and Section 4.3, respectively.

Section 5 provides the details of the studies for the assessment of corrosion anomalies and summarizes the assessment guidelines and models for corrosion anomalies. The studies for the tensile strain capacity, compressive strain capacity, and burst pressure are given in Sections 5.2, 5.3, and 5.4, respectively.

Section 6 provides the details of the studies for the assessment of dents and summarizes the assessment guidelines and models for dents. The focus of the studies is given to the compressive strain capacity.

Section 7 provides the details of the studies for the assessment of wrinkles and summarizes the assessment guidelines for wrinkles. The focus is given to the burst pressure.

Section 8 summarizes the main conclusions and discusses future work.

Appendices A and B present the details of the small-scale tests and test results. Appendix C presents the details of the CWP tests and results. Appendix D-F present the details of the full-scale pipe tests and results.

2 Material Property Characterizations

2.1 Overview of Materials Used for Tests

A series of full-scale pipe and curved wide plate (CWP) tests were conducted in this project. In this section, the basic material properties are presented. The details of the full-scale and CWP tests are given in Section 3.

The full-scale pipe tests consist of three sets of 324-mm (12.75") OD ERW pipes and one 610-mm (24") OD DSAW pipe. The characteristics of these pipes are summarized below.

- (1) X65 ERW-1: 324 mm OD x 6.35 mm W.T. (12.75" x 0.250"),
- (2) X65 ERW-2: 324 mm OD x 9.52 mm W.T. (12.75" x 0.375"),
- (3) X70 ERW-3: 324 mm OD x 7.14 mm W.T. (12.75" x 0.281"), and
- (4) X80 DSAW: 610 mm OD x 12.7 mm W.T. (24.0" x 0.500").

The X65 ERW-1 and X65 ERW-2 pipes were manufactured and marketed as X52/X60 per mill certificates. Their actual strength was higher than the specified minimums of API 5L. The strength or grade designation within this project had an impact on the pressure level applied during the full-scale test. In order to test the materials to their fullest strength level, these pipes were treated as X65 as their actual strength met the specified minimums of X65. More details of the pipes used in the full-scale tests are given in Table 2-1.

Table 2-1 Pipes used in full-scale pipe tests

Pipe Material ID	Pipe Grade and Type	Pipe OD	Pipe Wall Thickness	Large-Scale Tests (Corresponding features)
		mm (inch)	mm (inch)	
X65-ERW-1	X65 ¹ ERW	324 (12.75)	6.35 (0.250)	Full-scale bending tests (Corrosions, dents, and regular/transition welds)
X65-ERW-2	X65 ² ERW	324 (12.75)	9.53 (0.375)	Full-scale bending tests (Transition welds)
X70-ERW-3	X70 ERW	324 (12.75)	7.14 (0.281)	Full-scale bending-burst and tension tests (Corrosions)
X80-DSAW	X80 UOE	610 (24.0)	12.7 (0.500)	Full-scale compression-burst tests (Wrinkles)

¹ The pipe was specified as API 5L X52/X60 PSL2 pipe per Mill Certificates. The pipe was referred to as X65 in this project for two reasons: (1) the actual pipe yield strength is close to 65 ksi and (2) the actual hoop stress due to the pressure of a given design factor is higher than that using the original grade.

² The pipe was specified as API 5L X52 PSL2 pipe per Mill Certificates. The pipe was referred to as X65 in this project for similar reasons mentioned above.

The pipes and girth welds for the CWP tests were donated to the project by a team member. Two X70 DSAW pipes, X70-DSAW-1 and X70-DSAW -2, had wall thickness of 16 mm and 19 mm, respectively. Two pups of the X70-DSAW-1 were welded together to form a girth weld, with either side of the girth weld having the same wall thickness. One pup of the X70-DSAW-1 and one pup of the X70-DSAW-2 were welded together to form the "transition" girth weld, with one side of the girth weld having greater wall thickness than the other side. The welding

procedure and consumables were selected by the team member as a part of its welding procedure qualification process with a major goal of achieving highly overmatching weld strength. More details of the pipe and girth welds are summarized in Table 2-2 and Table 2-3, respectively.

Table 2-2 Pipes used in curved wide plate tests

Pipe Material ID	Pipe Grade and Type	Pipe OD	Pipe Wall Thickness	Large-Scale Tests (Corresponding features)
		mm (inch)	mm (inch)	
X70-DSAW-1	X70 UOE	914 (36.0)	16.0 (0.625)	Curved wide plate tension tests (Regular and transition welds)
X70-DSAW-2	X70 UOE	914 (36.0)	19.0 (0.750)	Curved wide plate tension tests (Transition welds)

Table 2-3 Girth welds used in curved wide plate tests

Weld Material ID	Pipe Material ID		Large-Scale Tests (Corresponding features)
	Pipe 1	Pipe 2	
Weld-1	X70-DSAW-1		Curved wide plate tension tests (Regular welds)
Weld-2	X70-DSAW-1	X70-DSAW-2	Curved wide plate tension tests (Transition welds)

2.2 Properties of Pipe Materials Used in Full-Scale Pipe Tests

2.2.1 Overview of Small-Scale Material Tests

A series of small-scale tests were conducted in this project to measure and verify the actual material properties for the pipes used in the full-scale pipe tests (see Table 2-1). The small-scale tests included uni-axial tension and compression tests as well as limited optical microscopy and microhardness tests. Duplicate tests were used to help with understanding of the consistency and/or variations in measured properties.

The following sections summarize the mechanical properties of the pipe materials obtained from those uni-axial tension and compression tests. The results from the microhardness testing and optical microscopy are included in Appendix A, along with the details for the small-scale tests.

2.2.2 Tensile Testing of Selected Pipes

The full-scale tests involved the use of four small diameter pipe materials, i.e., X65 ERW-1, X65 ERW-2, X70 ERW-3, and X80 DSAW (as shown in Table 2-1).

For X65 ERW-1, three pipe joints were used in all the full-scale tests. It was originally not known if the three pipe joints were from the same heat. Therefore, the small-scale un-axial tensile tests were conducted for all three joints, i.e., X65 ERW-1 (a), (b), and (c). The test results showed that the properties of the three pipe joints are very similar (see Section 2.2.3).

For X70 ERW-3, two pipe joints were used in all the full-scale tests. The two joints were from the same heat and their properties were expected to be similar. Therefore, the un-axial tensile tests were conducted for one pipe joint.

For X65 ERW-2 and X80 DSAW, only one pipe joint of each material was used in the full-scale tests. Therefore, for each pipe material, the un-axial tensile tests were conducted for one pipe joint.

All the materials used for the small-scale tests were taken near the end of the corresponding pipe joint. Duplicate sub-size strip tensile and full-thickness strap tensile specimens were cut and machined from the selected pipe joints. Both transverse and longitudinal specimens were cut from close to the 3:00 (or 9:00) and 6:00 clock positions, where the seam weld is at 12:00 clock position. The details of the specimens are shown in Appendix A.

The small-strip specimens were machined in the transverse-to-pipe-axis (TPA) direction with the maximum possible thickness used for the small diameter pipes and their respective wall thicknesses. The full-thickness strap tensile specimens were waterjet profiled with a longitudinal-to-pipe-axis (LPA) orientation from the same clock positions. Table 2-4 provides the details of the gauge dimensions for the TPA and LPA tensile specimens. The details of individual TPA tensile specimens and the LPA specimens are provided in Figures A2 and A3 in Appendix A.

All testing was preformed using a hydraulic universal testing machine with the required capacity and appropriate sized wedge grips for the TPA and LPA specimens. All tensile testing was performed at room temperature following general guidelines provided in ASTM E8M [58]. The reported tensile property data includes 0.2% offset and 0.5% underload yield strengths, ultimate tensile strengths (UTS), Y/T ratios, uniform strains, and total elongations (measured by the extensometer and by gauge marks after testing). Stress vs strain curves were created to allow comparisons of selected tests for the different orientations (TPA and LPA) and clock positions.

2.2.3 Tensile Property Data for Selected Steel Pipes

Since the data from the duplicate tests were generally very consistent, the average tensile properties are reported in Table 2-5 and Table 2-6 to show the trends with respect to the different specimen orientations (TPA and LPA) and their corresponding clock positions. Further specific examples of the tensile properties obtained for the selected pipe steels are presented in Table 2-7 to Table 2-10 and graphically in corresponding stress-strain curves in Figure 2-1 to Figure 2-4.

For the three X65 ERW-1 steel pipe sections (a, b, and c), the results were very consistent and repeatable and followed the same overall trends. The results showed an unexpectedly large difference in yield strengths and post yielding behavior (discontinuous and continuous) as a function of clock position (3:00 versus 6:00) for both TPA and LPA specimen orientations (Table 2-7 and Figure 2-1). Along with the higher yield strengths and Y/T ratios for the 6:00 position, the UTS values were marginally higher, while the uniform strains and total elongations were considerably lower than those for the specimens from the 3:00 position.

The X65 ERW-2 pipe steel exhibited tensile properties that were very similar as a function clock position (3:00 and 6:00) for a given specimen orientation, i.e., TPA or LPA (Table 2-8 and Figure 2-2). The specimens from the TPA orientation exhibited a more roundhouse type stress-

strain curve compared to the LPA orientation. This resulted in the later exhibiting higher yield strengths and Y/T ratios in conjunction with lower uniform strain and total elongation values.

The tensile property results for the X70 ERW-3 pipe steel in Table 2-9 and Figure 2-3, show relatively consistent trends with respect to specimen orientation and clock position. In this case, the yield strengths were higher for the LPA specimens, while the UTS values were lower compared with the TPA specimens. This resulted in higher Y/T ratios, but similar uniform strains and total elongation values.

Table 2-10 lists the tensile properties obtained for the X80-DSAW pipe steel, while Figure 2-4 shows the corresponding stress-strain curves as a function of specimen orientation and clock position. In contrast to the ERW pipes, the X80 DSAW pipe revealed a trend of higher tensile properties for the TPA orientation, i.e., yield and ultimate strengths, Y/T, uniform strain and total elongation. Again, the results for the 6:00 specimens revealed higher yield strengths, UTS, and Y/T values, with lower values for uniform strain and total elongation compared to the corresponding specimens from the 3:00 position.

Table 2-4 Detail of Pipes and Corresponding Tensile Specimens

Pipe ID	Pipe Diameter and Wall Thickness	Specimens Gauge Section Dimensions Width x Thickness mm	
		TPA	LPA
ERW-1(a), 1(b), and 1(c)	324 mm OD x 6.35 mm W.T. (12.75 in OD x 0.250 in W.T.)	6 x 4.0	25.4 x 6.4
ERW-2	324 mm OD x 9.52 mm W.T. (12.75 OD in x 0.375 in W.T.)	10 x 6.7	25.4 x 9.5
ERW-3	324 mm OD x 7.14 mm W.T. (12.75 in O.D. x 0.281 in W.T.)	7.25 x 5.0	25.4 x 7.25
X80-DSAW	610 mm OD x 12.7 mm W.T. (24 in OD x 0.5 in W.T.)	14.1 x 9.5	25.4 x 12.7

Table 2-5 List of Average Tensile properties for X65 Pipes

Pipe ID	Specimen Orientation	Specimen ID	Yield 0.2% MPa (ksi)	Yield 0.5% MPa (ksi)	UTS MPa (ksi)	0.2% Y/T	0.5% Y/T	uEL %	EL- 1 %	EL- 2 %
X65 ERW-1	TPA	03:00	453 (66)	457 (66)	556 (81)	0.82	0.82	13.9	30	31
		06:00	499 (72)	512 (74)	578 (84)	0.86	0.89	7.5	24	25
	LPA	03:00	464 (67)	468 (68)	527 (76)	0.88	0.89	14.7	34	35
		06:00	542 (79)	545 (79)	557 (81)	0.97	0.98	5.0	29	29
X65 ERW-2	TPA	03:00	428 (62)	439 (64)	535 (77)	0.80	0.82	11.6	39	41
		06:00	447 (65)	456 (66)	531 (77)	0.85	0.86	10.8	39	40
	LPA	03:00	469 (68)	477 (69)	528 (76)	0.89	0.91	9.1	35	36
		06:00	491 (71)	496 (72)	526 (76)	0.94	0.94	7.7	34	34

Table 2-6 List of Average Tensile properties for X70 and X80 Pipes

Pipe ID	Specimen Orientation	Specimen ID	Yield 0.2% MPa (ksi)	Yield 0.5% MPa (ksi)	UTS MPa (ksi)	0.2% Y/T	0.5% Y/T	uEL %	EL- 1 %	EL- 2 %
X70 ERW-3	TPA	03:00	548 (79)	556 (81)	675 (98)	0.82	0.83	10.1	29	31
		06:00	546 (79)	556 (81)	677 (98)	0.81	0.82	9.3	26	29
	LPA	03:00	565 (82)	568 (82)	635 (92)	0.89	0.90	9.9	28	30
		06:00	577 (84)	580 (84)	645 (93)	0.90	0.90	9.4	28	29
X80 DSAW	TPA	03:00	648 (94)	647 (94)	695 (101)	0.93	0.93	6.0	34	39
		06:00	702 (102)	701 (102)	715 (104)	0.98	0.98	4.2	32	38
	LPA	03:00	616 (89)	614 (89)	683 (99)	0.90	0.90	4.0	25	29
		06:00	642 (93)	637 (92)	693 (100)	0.93	0.92	3.1	16	28

Table 2-7 Typical Tensile Properties of X65 ERW-1(c) Pipe Body

Specimen Orientation/ Clock Position	Yield 0.2% MPa (ksi)	Yield 0.5 % MPa (ksi)	UTS MPa (ksi)	0.2%Y/T	Uniform Strain %	Elongation %
TPA-3:00	430 (62)	448 (65)	554 (80)	0.78	13.2	29
TPA-6:00	498 (72)	512 (74)	577 (84)	0.86	8.7	23
LPA-3:00	458 (66)	461 (67)	525 (76)	0.87	13.9	34
LPA-6:00	543 (78)	545 (79)	559 (81)	0.97	3.4	26

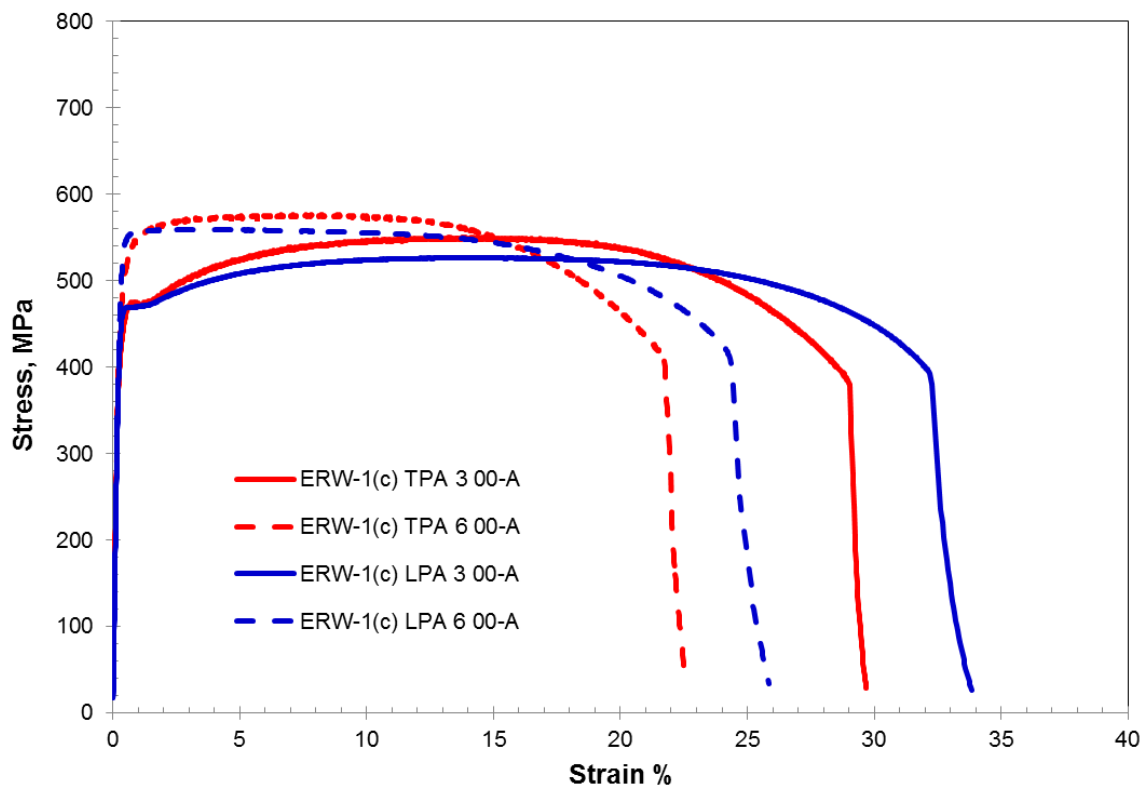


Figure 2-1 Representative stress-strain curves for X65 ERW-1(c) pipe body as a function of orientation (TPA and LPA) and clock position (3:00 and 6:00)

Table 2-8 Typical Tensile Properties of X65 ERW-2 Pipe Body

Specimen Orientation/ Clock Position	Yield 0.2% MPa (ksi)	Yield 0.5 % MPa (ksi)	UTS MPa (ksi)	0.2%Y/T	Uniform Strain %	Elongation %
TPA-3:00	432 (63)	442 (64)	539 (78)	0.80	11.2	38
TPA-6:00	440 (64)	450 (65)	526 (76)	0.84	11.3	39
LPA-3:00	473 (68)	480 (69)	529 (77)	0.89	9.3	33
LPA-6:00	490 (71)	495 (72)	524 (76)	0.94	7.1	33

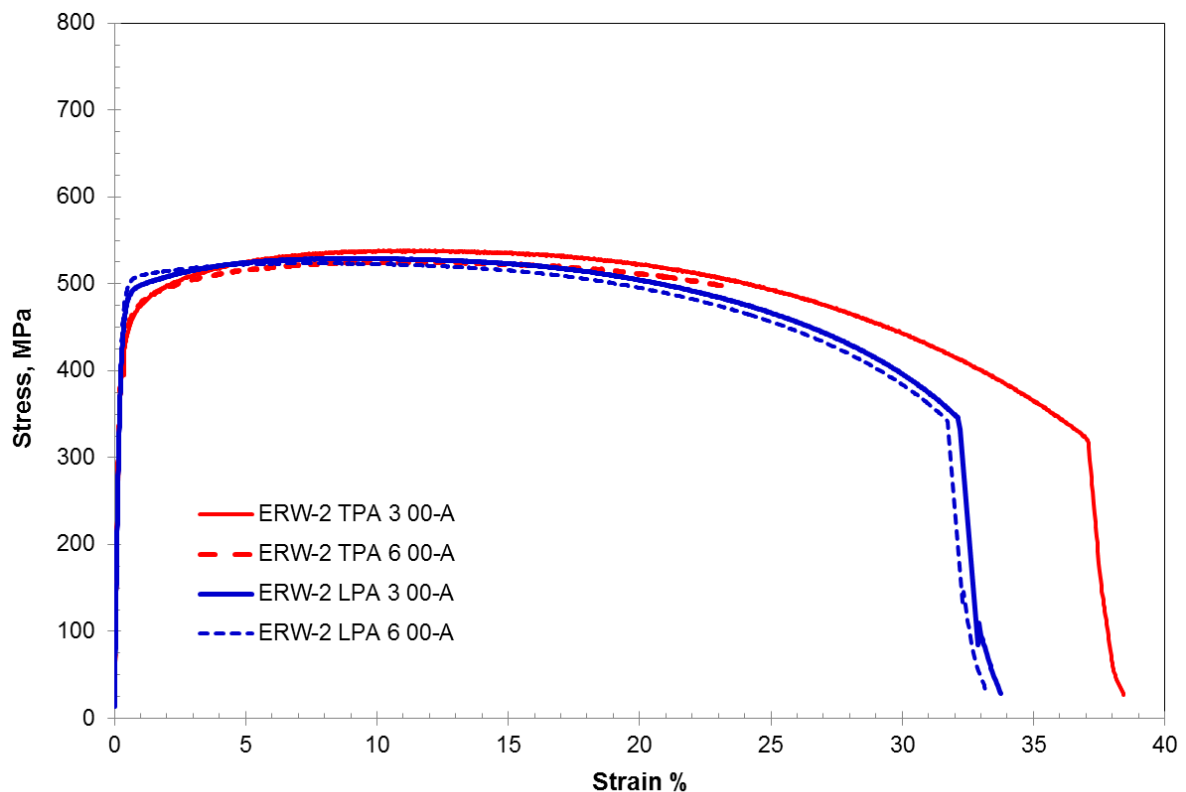


Figure 2-2 Representative stress-strain curves for X65 ERW-2 pipe body as a function of orientation (TPA and LPA) and clock position (3:00 and 6:00)

Table 2-9 Typical Tensile Properties of X70 ERW-3 Pipe Body

Specimen Orientation/ Clock Position	Yield 0.2% MPa (ksi)	Yield 0.5 % MPa (ksi)	UTS MPa (ksi)	0.2%Y/T	Uniform Strain %	Elongation %
TPA-3:00	551 (80)	558 (81)	672 (97)	0.82	10.2	30
TPA-6:00	543 (79)	553 (80)	674 (98)	0.81	9.1	28
LPA-3:00	564 (82)	568 (82)	632 (92)	0.89	9.2	27
LPA-6:00	575 (83)	578 (84)	644 (93)	0.89	9.3	28

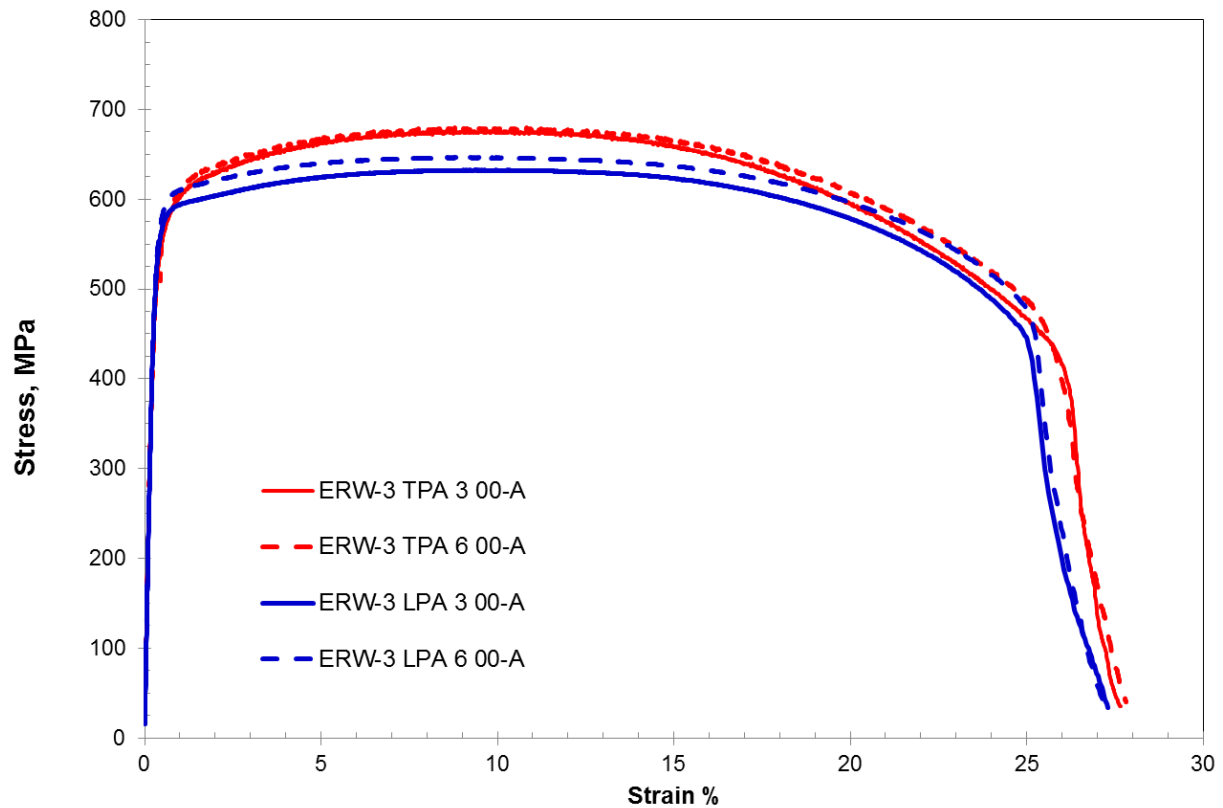


Figure 2-3 Representative stress-strain curves for X70 ERW-3 pipe body as a function of orientation (TPA and LPA) and clock position (3:00 and 6:00)

Table 2-10 Typical Tensile Properties of X80 DSAW Pipe Body

Specimen Orientation/ Clock Position	Yield 0.2% MPa (ksi)	Yield 0.5 % MPa (ksi)	UTS MPa (ksi)	0.2%Y/T	Uniform Strain %	Elongation %
TPA-3:00	645 (94)	645 (94)	699 (101)	0.92	6.0	35
TPA-6:00	699 (101)	698 (101)	714 (104)	0.98	3.7	30
LPA-3:00	615 (89)	614 (89)	680 (99)	0.90	4.1	26
LPA-6:00	641 (93)	635 (92)	693 (100)	0.92	2.8	24

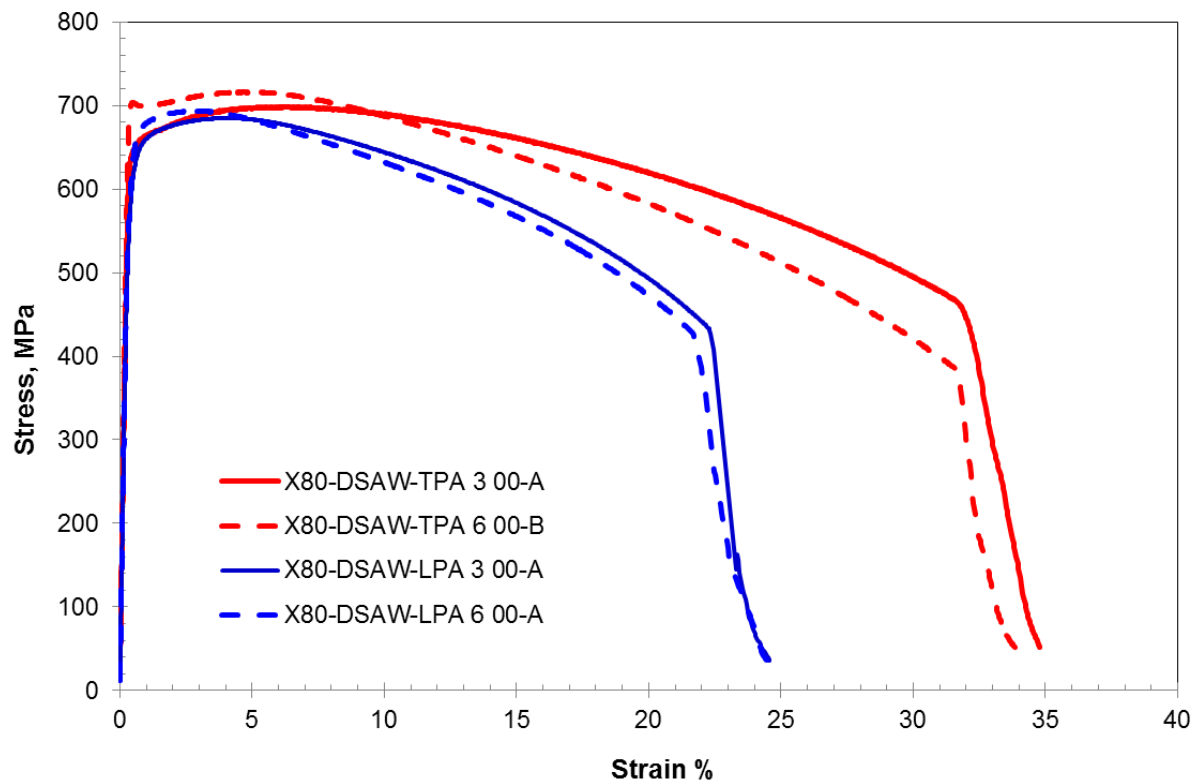


Figure 2-4 Representative stress-strain curves for ERW-3 pipe body as a function of orientation (TPA and LPA) and clock position (3:00 and 6:00)

2.2.4 Compression Testing of Selected Pipes

The uni-axial compression tests were conducted for three pipe joints: X65 ERW-1 (c), X70 ERW-3, and X80 DSAW. The X65 ERW-2 pipe was not tested. The X65 ERW-2 pipe was only used as the thick pipe of the transition weld in the full-scale bending tests, the strain in the X65 ERW-2 pipe was elastic and the compressive stress-strain curve was not needed.

For the X65 ERW-1 pipes, all three pipe joints, i.e., X65 ERW-1 (a), (b), and (c), showed similar tensile properties. Because it was expected that the compressive properties of the three joints would also be similar, only X65 ERW-1 (c) was tested.

Cylindrical specimens with diameters as close to the pipe wall thicknesses as possible were machined from longitudinal to pipe axis (LPA) strips cut from the 3:00 and 6:00 positions of selected ERW and DSAW pipes. The specimens were machined to their respective diameters with a constant length to diameter ratio of 3:1 (see Figure A8 in Appendix A). All testing was performed at room temperature ~ 25 °C. Further details regarding the compression testing are provided in Appendix A.

2.2.5 Compression and Tension Properties of Selected Pipes

The yield strength results obtained for the pipe steels are listed in Table 2-11 to Table 2-13, while corresponding true stress versus true strain curves are shown in Figure 2-5 to Figure 2-7. In general, the compression yield strengths and true stress strain curves were very consistent for a given pipe steel and the respective 3:00 or 6:00 clock positions.

For the X65 ERW-1(c) pipe steel (Table 2-11), near identical yield strengths were obtained for both compression and tension tests from the 3:00 position. The trend for higher yield strengths obtained for the tension specimens from 6:00 position was also observed for the corresponding compression tests. In this case, the results were slightly lower than for the corresponding tension tests. Figure 2-5 clearly shows that the compression and tension curves were very close at or just beyond yield, but that the compression curves tended to be marginally higher for larger strains.

The results (Table 2-12) for the X70 ERW-3 pipe steel were very consistent for both compression and tension tests. The trend of marginally higher yield strength results for the tests from the 6:00 position is evident in the true stress-true strain curves shown in Figure 2-6.

Very consistent and similar trends for both tension and compression tests were observed for the X80 DSAW pipe steel, as shown in Table 2-13 and Figure 2-7. The trend of slightly higher yield strengths for the test specimens from the 6:00 position is also clearly evident.

From the comparison of tension and compression tests conducted on the selected pipe steels the following trends were observed. In all cases the tension and compression data matched very well, including the marked difference in behavior observed for the ERW-1 pipe, where the specimens from 6:00 exhibited much higher strengths. For the X70 ERW and X80 DSAW the results were extremely close between tension and compression revealing consistent trends of slightly higher strengths for the specimens from the 6:00 position.

Table 2-11 LPA Tensile and Compression Yield Strengths for X65 ERW-1(c) Pipe Body

Pipe Steel	Orientation – Clock Position	Yield Strength, MPa (ksi)
ERW-1(c)	Tension-3:00	466, 458 (68, 66)
	Compression-3:00	460, 460, 464 (67, 67, 67)
	Tension-6:00	543, 547 (79, 79)
	Compression-6:00	518, 529, 532 (75, 77, 77)

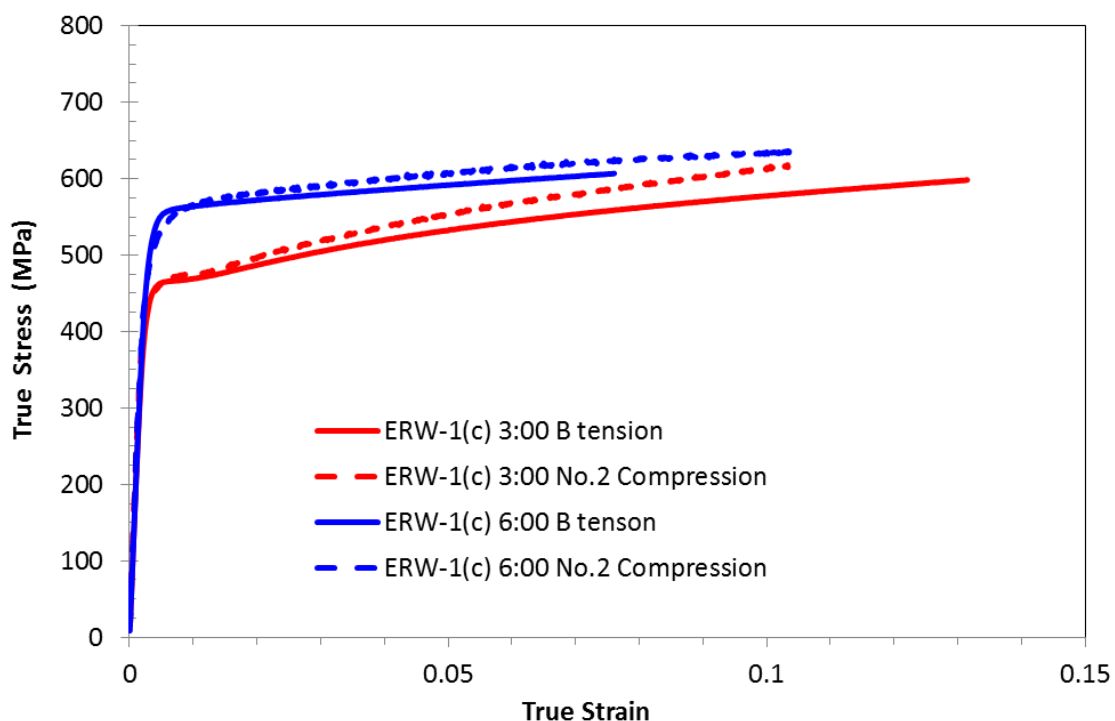


Figure 2-5 Representative true stress-true strain curves for LPA tension and compression tests for the 3:00 and 6:00 positions of X65 ERW-1(c) pipe steel

Table 2-12 LPA Tensile and Compression Yield Strengths for X70 ERW Pipe Body

Pipe Steel	Orientation – Clock Position	Yield Strength, MPa (ksi)
ERW-3	Tension-3:00	564, 565 (82, 82)
	Compression-3:00	548, 551 (79, 80)
	Tension-6:00	579, 575 (84, 83)
	Compression-6:00	564, 558, 576 (82, 81, 83)

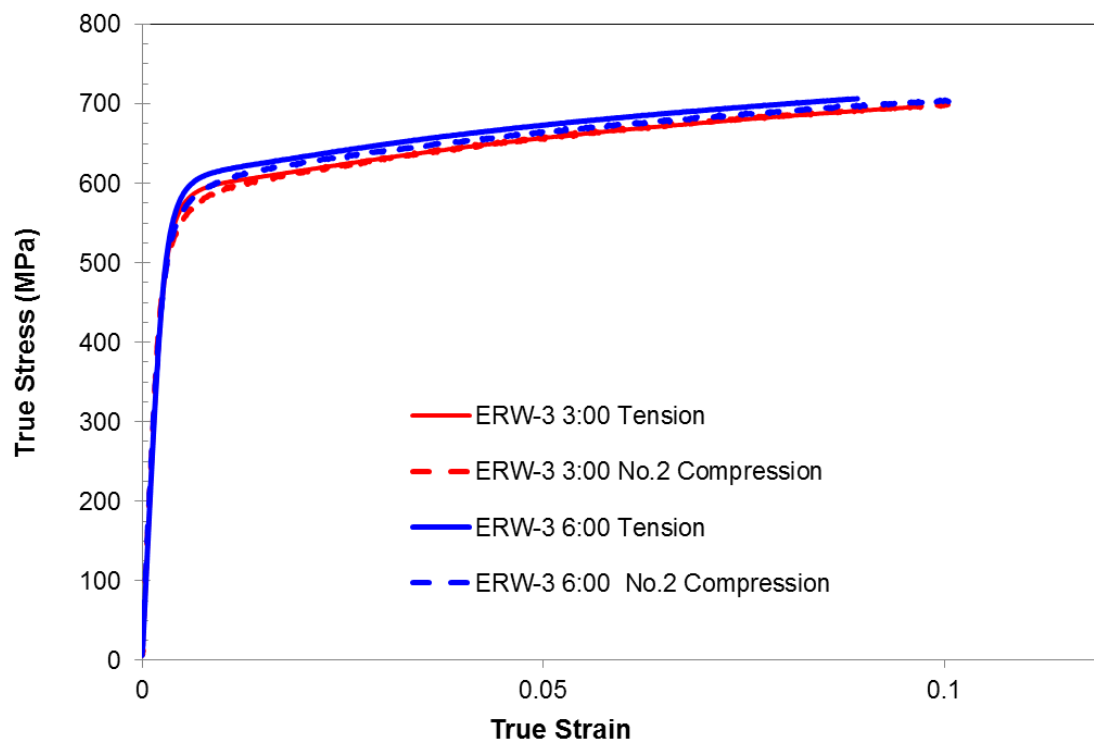


Figure 2-6 Representative true stress-true strain curves for LPA tension and compression tests for the 3:00 and 6:00 positions of X70 ERW-3 pipe steel

Table 2-13 LPA Tensile and Compression Yield Strengths for X80-DSAW Pipe Body

Pipe Steel	Orientation – Clock Position	Yield Strength, MPa (ksi)
X80-DSAW	Tension-3:00	617, 615 (89, 89)
	Compression-3:00	615, 605 (89, 88)
	Tension-6:00	643, 641 (93, 93)
	Compression-6:00	632, 642 (92, 93)

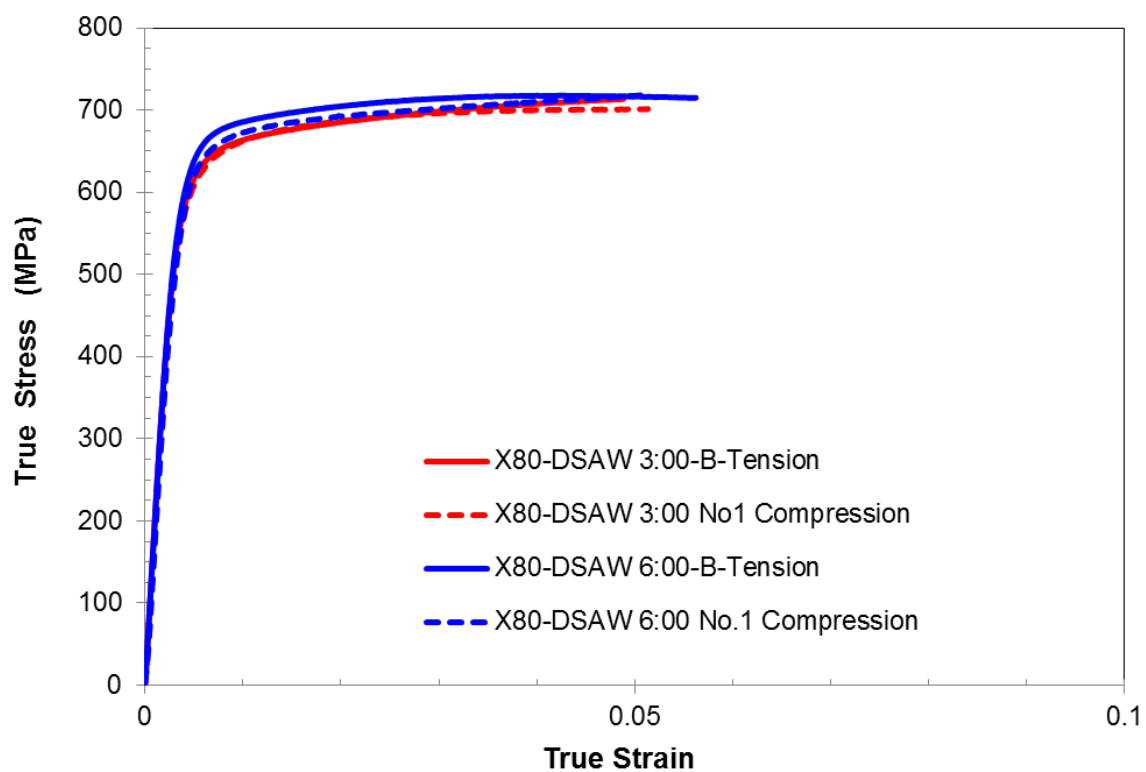


Figure 2-7 Representative true stress-true strain curves for LPA tension and compression tests for the 3:00 and 6:00 positions of X80-DSAW pipe steel

2.3 Properties of Materials Used in Curved Wide Plate Tests

2.3.1 Overview of the Small-Scale Tests

A series of small-scale tests were conducted in this project to measure and verify the actual material properties of the pipe steels and girth welds used in the curved-wide plate (CWP) tests (see Table 2-2 and Table 2-3). For the pipe steels, the small-scale tests included uni-axial tension tests for both the longitudinal and circumferential specimens. For the weld materials, the small-scale tests included all weld metal uni-axial tension tests, microhardness tests, various toughness tests (Charpy, CTOD, and SENT or SE(T)), and optical microscopy. Duplicate tests were used to help with understanding the consistency and/or variations in measured properties. The materials for the small-scale tests were cut from the same pipe used for the CWP tests. The details of the small-scale specimen locations can be found in Appendix B.

The following sections summarize the mechanical properties of the pipe and weld materials obtained from those uni-axial tension and toughness tests. The details of all the small-scale tests are given in Appendix B, in addition to the results of the microhardness testing and optical microscopy tests.

2.3.2 Pipe Properties

As shown in Table 2-2, two pipes (*i.e.*, X70-DSAW-1 and X70-DSAW -2) were used in the CWP tests. The wall thickness of the X70-DSAW-1 and X70-DSAW -2 pipes are 16 mm and 19 mm, respectively. Base metal tensile properties of the two different steel pipe sections were determined by the following test matrix shown in Table 2-14.

Table 2-14 Base Metal Tensile Test Matrix
914 mm (36 in) Outside Diameter – X70 DSAW-1 and X70 DSAW -2

Pipe Wall Thickness	Specimen Geometry	No. of Circumferential Locations	Specimen Orientation	Replicates (Total # of Tests)
16 mm (0.625 in)	Strap	Two	Longitudinal	4 (8)
19 mm (0.750 in)	Strap	Two	Longitudinal	4 (8)
16 mm (0.625 in)	Round	Two	Longitudinal	3 (6)
19 mm (0.750 in)	Round	Two	Longitudinal	3 (6)
16 mm (0.625 in)	Round	Two	Transverse	3 (6)
19 mm (0.750 in)	Round	Two	Transverse	3 (6)

Each specimen section was taken from a panel coaxial to two of the CWP specimens in each pipe shown schematically in Figure 2-8. Specimen geometries and testing protocol were in accordance with ASTM E8/E8M: *Standard Test Methods for Tension Testing of Metallic*

Materials [58] and met the requirements also found in ASTM A370: *Standard Test Methods and Definitions for Mechanical Testing of Steel Products* [59]. Detailed machine drawings for sectioning and specimen machining are found in Appendix B.



Figure 2-8 Schematic view of small scale base metal specimen sectioning (relative to the CWP specimen)

The engineering stress-strain curves for the strap tensile tests are shown in Figure 2-9. Each plot shows the resultant data for the four specimens associated with each pipe and each circumferential location within the pipe. The reduced data for each of the 16 mm wall thickness specimens are given in tabular form in Table 2-15. The reduced data for each of the 19 mm wall thickness specimens are given in tabular form in Table 2-16.

Table 2-15 Base metal strap tensile test results from 16 mm wall thickness pipe
914 mm (36 in) Outside Diameter – X70 DSAW-1

Pipe Wall Thickness	Specimen ID	0.5 % EUL Yield Strength MPa (ksi)	Tensile Strength MPa (ksi)	Uniform Elongation (%)
16 mm (0.625 in)	236-ST-1	503 (73)	668 (97)	10.2
	236-ST-2	506 (73)	642 (93)	10.3
	236-ST-3	496 (72)	603 (87)	6.7
	236-ST-4	501 (73)	602 (87)	7.0
	Average	502 (73)	629 (91)	8.5
	St. Dev.	4 (0.5)	32.2 (4.7)	1.9
16 mm (0.625 in)	236-ST-5	513 (74)	610 (88)	7.5
	236-ST-6	520 (75)	626 (91)	7.5
	236-ST-7	513 (74)	630 (91)	7.0
	236-ST-8	524 (76)	605 (88)	7.3
	Average	517 (75)	618 (90)	7.3
	St. Dev.	5.5 (0.8)	12.0 (1.7)	0.2

Table 2-16 Base metal strap tensile test results from 19 mm wall thickness pipe

914 mm (36 in) Outside Diameter – X70 DSAW-2

Pipe Wall Thickness	Specimen ID	0.5 % EUL Yield Strength MPa (ksi)	Tensile Strength MPa (ksi)	Uniform Elongation (%)
19 mm (0.750 in)	233-ST-1	505 (73)	592 (86)	6.9
	233-ST-2	498 (72)	616 (89)	9.8
	233-ST-3	517 (75)	628 (91)	8.9
	233-ST-4	506 (73)	632 (92)	9.3
	Average	507 (74)	617 (89)	8.7
	St. Dev.	7.6 (1.1)	18.3 (2.6)	1.3
19 mm (0.750 in)	233-ST-5	515 (75)	639 (93)	9.0
	233-ST-6	499 (72)	634 (92)	10.0
	233-ST-7	507 (74)	634 (92)	9.0
	233-ST-8	513 (74)	637 (92)	8.2
	Average	508 (74)	636 (92)	9.1
	St. Dev.	6.8 (0.9)	2.9 (0.4)	0.8

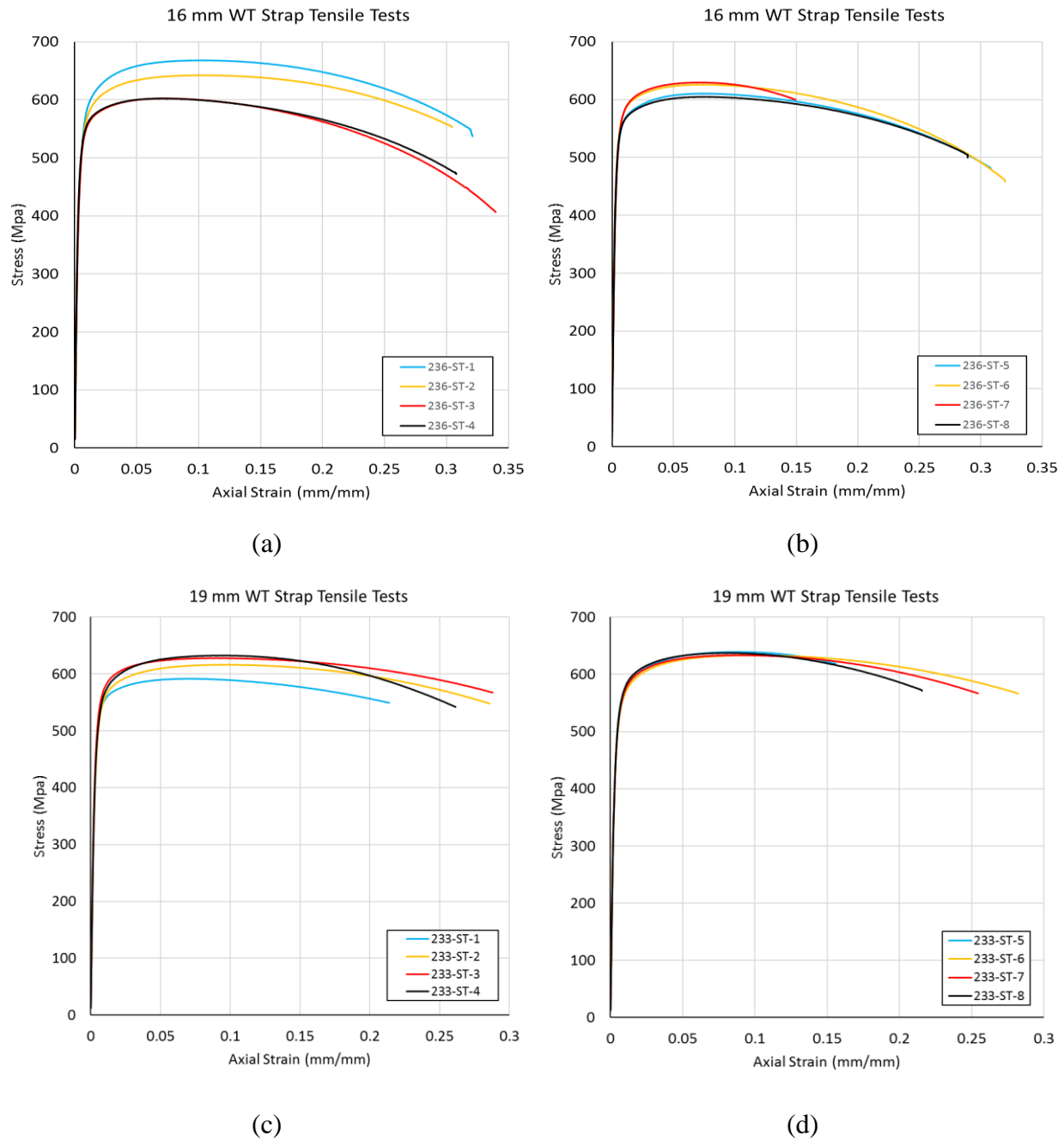


Figure 2-9 Engineering stress-strain plots for strap tensile specimens. Plot (a) is for the 16-mm WT pipe specimens (X70-DSAW-1) sectioned coaxially with 236-CWP-1, plot (b) is for the 16-mm WT pipe specimens (X70-DSAW-1) sectioned coaxially with 236-CWP-3, plot (c) is for the 19-mm WT pipe specimens (X70-DSAW-2) sectioned coaxially with 233-CWP-4 and plot (d) for the same (X70-DSAW-2) but coaxial with 233-CWP-2.

The engineering stress-strain curves for the round tensile tests are shown in Figure 2-10. Each plot shows the resultant data for the six specimens (longitudinal or transverse orientations) associated with each pipe and each circumferential location within the pipe. The reduced data for each of the 16 mm wall thickness specimens are given in tabular form in Table 2-17. The reduced data for each of the 19-mm wall thickness specimens are given in tabular form in Table 2-18. The tensile results do not show a statistically significant correlation between the results and the circumferential location within the pipe.

Table 2-17 Base metal round tensile test results from 16 mm wall thickness pipe.

914 mm (36 in) Outside Diameter – X70 DSAW-1

Pipe Wall Thickness (Orientation)	Specimen ID	0.5 % EUL Yield Strength MPa (ksi)	Tensile Strength MPa (ksi)	Uniform Elongation (%)
16 mm (0.625 in) (Transverse)	236-RT-1	560 (81)	613 (89)	8.8
	236-RT-2	555 (80)	613 (89)	8.3
	236-RT-3	585 (85)	678 (98)	10.1
	236-RT-4	562 (81)	624 (90)	9.6
	236-RT-5	561 (81)	624 (90)	8.5
	236-RT-6	560 (81)	627 (91)	8.7
	Average	564 (82)	630 (91)	9.0
	St. Dev.	11 (1.6)	25 (3.6)	0.7
16 mm (0.625 in) (Longitudinal)	236-RL-1	491 (71)	625 (91)	7.6
	236-RL-2	486 (70)	587 (85)	7.0
	236-RL-3	484 (70)	586 (85)	7.6
	236-RL-4	501 (73)	631 (91)	6.0*
	236-RL-5	500 (70)	615 (89)	7.8
	236-RL-6	489 (71)	595 (86)	8.1
	Average	492 (71)	607 (88)	7.6
	St. Dev.	7.1 (1.0)	19.6 (2.8)	0.4

* The specimen necked and failed near the extensometer knife edge – UEL for this specimen is not included in the average.

Table 2-18 Base metal round tensile test results from 19 mm wall thickness pipe.

914 mm (36 in) Outside Diameter – X70 DSAW-2

Pipe Wall Thickness (Orientation)	Specimen ID	0.5 % EUL Yield Strength MPa (ksi)	Tensile Strength MPa (ksi)	Uniform Elongation (%)
19 mm (0.750 in) (Transverse)	233-RT-1	544 (79)	633 (92)	10.6
	233-RT-2	556 (81)	635 (92)	11.3
	233-RT-3	567 (82)	642 (93)	9.1
	233-RT-4	573 (83)	659 (95)	10.5
	233-RT-5	572 (83)	655 (95)	10.4
	233-RT-6	563 (82)	628 (91)	7.8
	Average	562 (81)	642 (93)	10.0
	St. Dev.	11.0 (1.6)	12.4 (1.8)	1.3
19 mm (0.750 in) (Longitudinal)	233-RL-1	497 (72)	571 (83)	7.4
	233-RL-2	490 (71)	580 (84)	4.8*
	233-RL-3	501 (73)	601 (87)	4.9*
	233-RL-4	497 (72)	612 (89)	7.5
	233-RL-5	496 (72)	613 (89)	8.6
	233-RL-6	495 (72)	585 (85)	7.0
	Average	496 (72)	594 (86)	7.6
	St. Dev.	3.3 (0.4)	17.6 (2.5)	0.7

* The specimen necked and failed near the extensometer knife edge – UEL for this specimen is not included in the average.

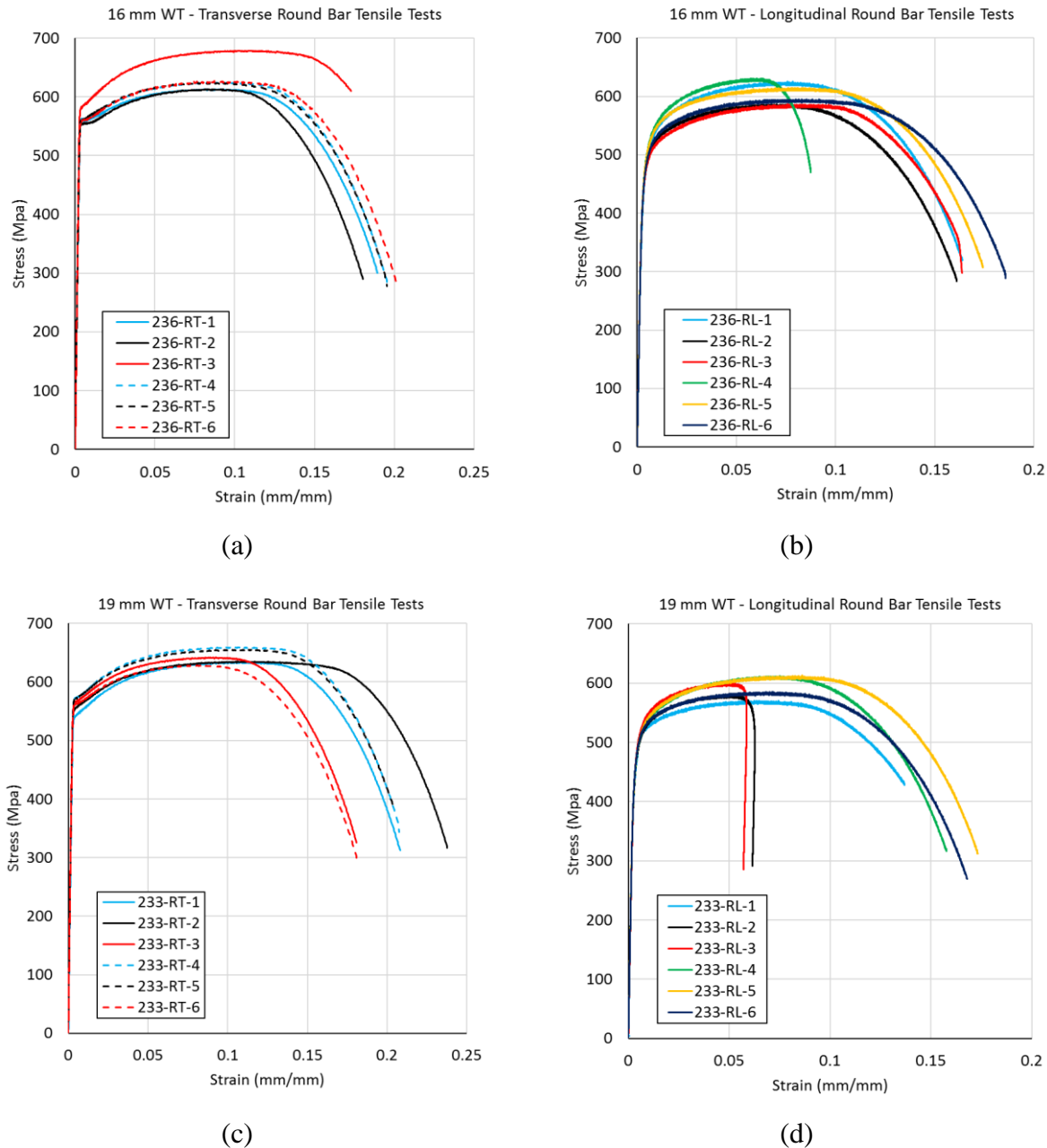


Figure 2-10 Engineering stress-strain plots for round tensile specimens. Plot (a) is for the 16 mm WT pipe (X70-DSAW-1) transversely oriented specimens sectioned from panels coaxially with 236-CWP-1 (solid lines) and 236-CWP-3 (dashed lines), plot (b) is for the 16 mm WT pipe (X70-DSAW-1) longitudinally oriented specimens sectioned from panels coaxially with 236-CWP-1 (RL-1 thru RL-3) and 236-CWP-3 (RL-4 thru RL-6), plot (c) is for the 19 mm WT pipe (X70-DSAW-2) transversely oriented specimens sectioned from panels coaxially with 233-CWP-4 (solid lines) and 233-CWP-2 (dashed lines) and plot (d) for the same as (b) but are for 19 mm WT specimens (X70-DSAW-2).

2.3.3 Girth Weld Properties

2.3.3.1 Girth Weld Strength – Uniaxial Tensile Tests

All weld metal tensile properties of the two different steel pipe sections were determined by the following test matrix in Table 2-19.

Table 2-19 All Weld Metal Tensile Test Matrix
914 mm (36 in) Outside Diameter – API-5L X70

Weld Material ID	Specimen Geometry	No. of Circumferential Locations	Specimen Orientation	Replicates (Total # of Tests)
Weld-1	Round	Four	Transverse	1 (4)
Weld-2	Round	Five	Transverse	1 (5)

Each specimen was taken from a section adjacent to or as close as achievable to each of the CWP specimens. Specimen geometries and testing protocol were per ASTM E8/E8M [58] and met the requirements also found in ASTM A370 [59]. Detailed machine drawings for sectioning and specimen machining are found in Appendix B.

Engineering stress-strain curves for the round tensile tests are shown in Figure 2-11. Each plot shows the resultant data for the specimens associated with each welded pipe. While not statistically correlated, there are differences in the tensile response based on the circumferential location. In general, the tensile response of the transition weld for the 16 mm-19 mm pipes, i.e., Weld-2 (233), can be characterized as having a more distinct yield point, lower yield and tensile strengths and higher uniform elongation than that of the 16 mm-16 mm pipes, i.e., Weld-1 (236).

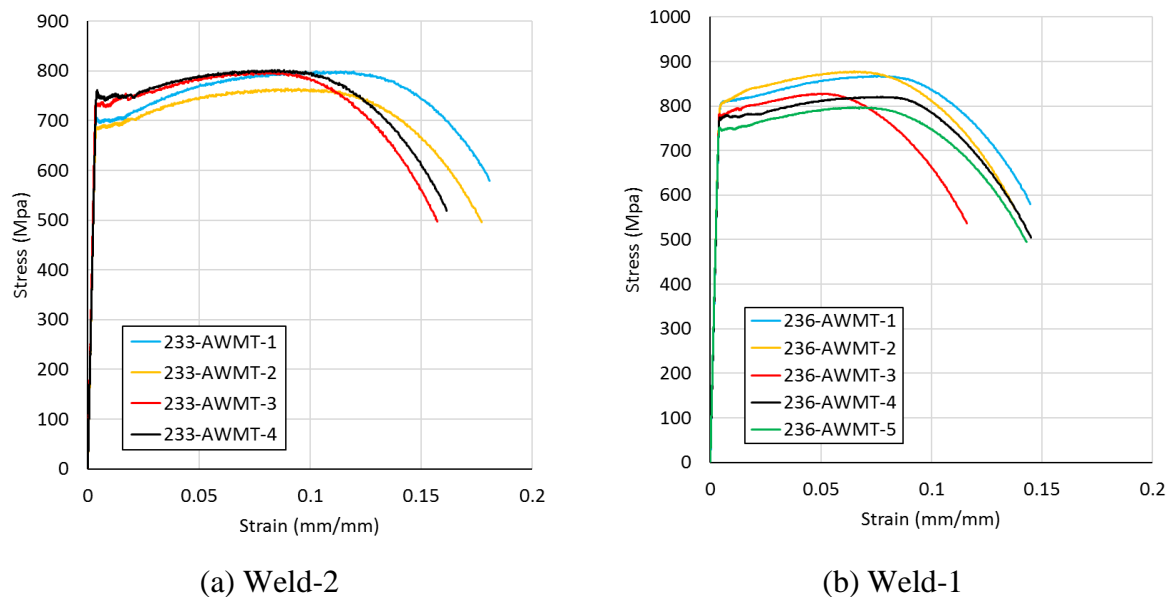


Figure 2-11 Engineering stress-strain plots for all weld metal round tensile specimens. Plot (a) is for the 16 mm-19 mm wall thickness transition weld (Weld-2) and plot (b) is for the 16 mm-16 mm wall thickness weld (Weld-1).

The reduced data for each of the weld metal tensile specimens are given in tabular form in Table 2-20.

Table 2-20 Weld metal round tensile test results from Weld-1 and Weld-2

Weld	Specimen ID	0.5 % EUL Yield Strength MPa (ksi)	Tensile Strength MPa (ksi)	Uniform Elongation (%)
16 mm – 19 mm (0.625 in – 0.750 in) (Weld-2)	233-AWMT-1	700 (101)	799 (116)	11.4
	233-AWMT-2	685 (99)	764 (111)	9.5
	233-AWMT-3	732 (106)	798 (116)	8.4
	233-AWMT-4	749 (109)	802 (116)	8.5
	Average	716 (104)	791 (115)	9.4
	St. Dev.	29 (4.2)	18 (2.6)	1.4
16 mm – 16 mm (0.625 in – 0.625 in) (Weld-1)	236-AWMT-1	806 (117)	867 (126)	8.1
	236-AWMT-2	804 (117)	878 (127)	6.5
	236-AWMT-3	778 (113)	827 (120)	5.2
	236-AWMT-4	772 (112)	820 (119)	7.8
	236-AWMT-5	747 (108)	797 (115)	6.6
	Average	782 (113)	838 (121)	6.8
	St. Dev.	24 (3.5)	34 (5)	1.2

2.3.3.2 Girth Weld Charpy Toughness - Charpy Impact Tests

The Charpy impact transition behaviors of the two pipe girth welds were determined for both the weld metal center and HAZ regions with the aim of establishing the overall performance and consistency of the respective welds.

Briefly, multiple pipe girth weld sections cut from the regions between the CWP specimens were used to prepare a large number of Charpy-V-notch (CVN) test specimens from each girth weld. A total of 33 and 36 CVN test specimens were machined from the two pipe girth welds: Weld-1 and Weld-2, respectively. Since the specimens were cut from different circumferential positions around the pipe girth weld, the totals were divided so that the even numbered specimens were allocated to test the weld metal and the odd numbered specimens were used for HAZ tests. The specimens were cut transverse to the girth weld according to the guidelines in API 1104 and as shown in the macrograph in Figure 2-12. Further details of the preparation of the test specimens and testing conditions are provided in Appendix B.

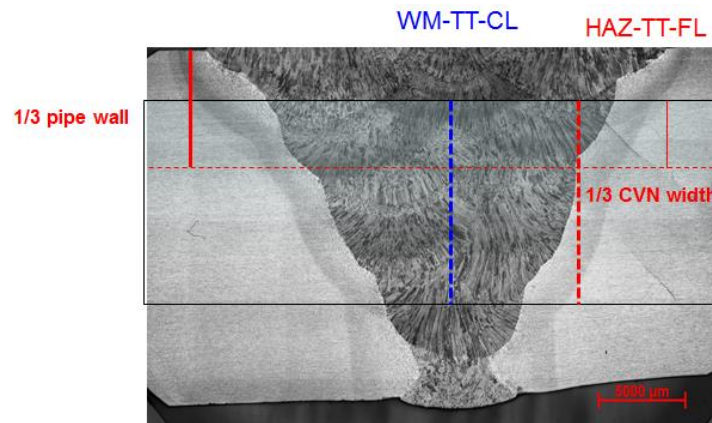


Figure 2-12 CVN test specimen location and notch positions for the for WMC (WCL) and HAZ tests are superimposed on a typical macrograph of the pipe girth weld

The Charpy impact energies obtained for the two weld metals are listed in Table 2-21 and in Figure 2-13, where the impact energy versus temperature transition curves are plotted. From the results in Table 2-21, it is clear that there was some variation in the impact toughness as a function of test temperature for the respective welds. In both cases, near fully ductile upper shelf energies were recorded at the 24°C test temperature. A marked decrease in impact energies (68 and 55 J) can be found for tests conducted at 0°C and -18°C for Weld 1, whereas the average impact energies for Weld 2 only decreased by 8 to 10 J for the same test conditions. The trend of higher impact energies for Weld 2 compared to Weld 1 was evident for the remaining tests, shown in Figure 2-13. The relatively low upper shelf energies obtained for the pipe girth weld metals can be explained in part by the very high strengths achieved in combination with the very high oxygen contents (non-metallic inclusion volume fraction). The differences in the Charpy impact behaviors for the two pipe girth welds are attributable to the lower strength and hardness observed for Weld 2, which may be related to differences in welding procedures including the pass sequences used.

The results listed in Table 2-22 and shown in Figure 2-14, clearly indicate that the HAZ performance is characterized by high upper shelf energies and a low ductile-to-brittle transition temperature (between -45 to -50°C). However, this was accompanied by some considerable scattering of test results, where high and low impact energy values lead to some calculated averages being higher than expected for some low-test temperatures, e.g., Weld 1 tests at -75°C and those for Weld 2 at the -50 and -60°C.

Despite this and the considerable difference in upper shelf energies between the two welds, the transition curves are very similar through the transition and lower shelf regions. It is generally recognized that the degree of scatter observed for HAZ CVN testing can be very large due to the fraction of HAZ being sampled and inconsistency in fusion line profile that leads to notches being offset from the intended targets, i.e., towards the WM or BM, resulting in higher toughness values being recorded.

Table 2-21 CVN impact energies for WMC (WCL) testing of Weld 1 and Weld 2

Test Temperature	Weld 1 (236)	Weld 2 (233)
	WMC Absorbed Energy	WMC Absorbed Energy
°C	J	J
24	117 (114, 110, 128)	104 (107, 107, 97)
0	68 (64, 73, 67)	96 (101, 98, 89)
-18	55 (56, 50, 59)	94 (81, 96, 104)
-45	31 (43, 19, 32)	45 (47, 43, 44)
-60	24 (24, 19, 29)	33 (31, 32, 35)

Note: **avg. (individual values)**

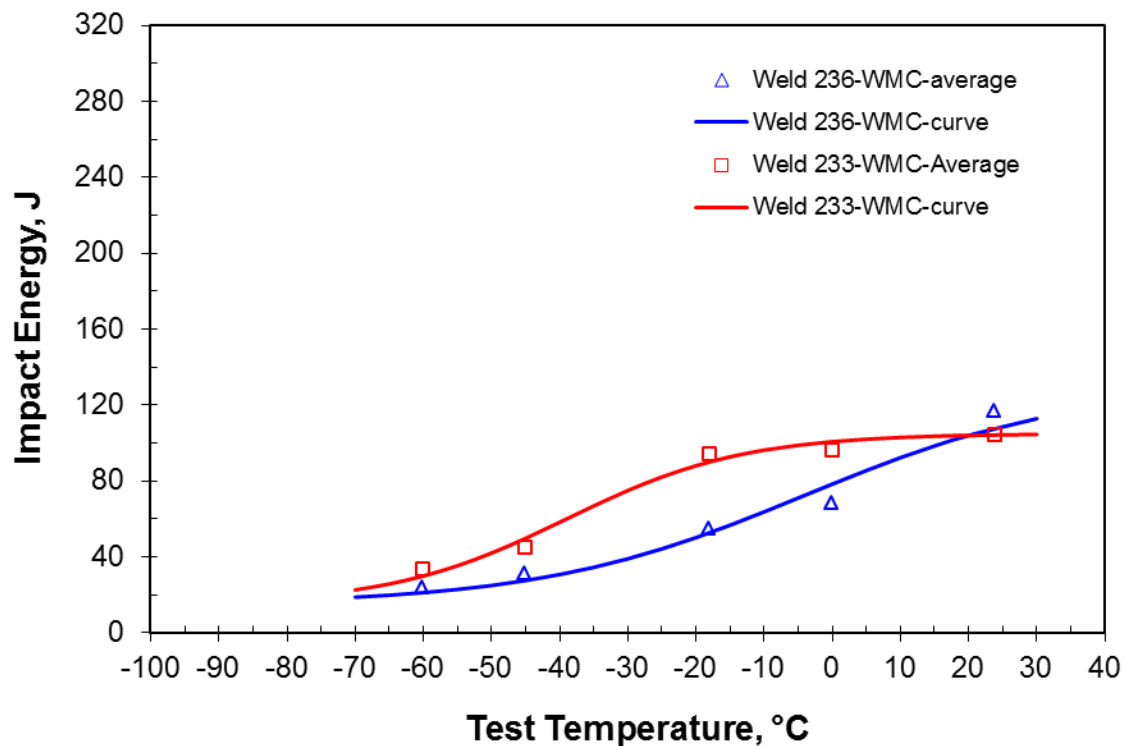


Figure 2-13 Charpy impact transition curves for the WMC (WCL) of Weld-1 (236) and Weld-2 (233)

Table 2-22 CVN impact energies for HAZ testing of Weld 1 and Weld 2

Test Temperature	Weld 1 (236)	Weld 2 (233)
	HAZ Absorbed Energy	HAZ Absorbed Energy
°C	J	J
-18	259 (261, 267, 249)	317 (348, 304, 300)
-30	-	198 (129, 258, 207)
-45	258 (261, 255, 258)	193 (66, 284, 228)
-50	113 (49, 231, 60)	79 (58, 58, 121)
-60	55 (48, 55, 61)	92 (91, 36, 149)
-75	28 (28, 216*, 29)	41 (40, 30, 54)
-75	44 (272*, 51, 38)	-

Note: avg. (individual values) and *High values recorded at -75 °C were excluded from average due to possible inconsistent notch positioning.

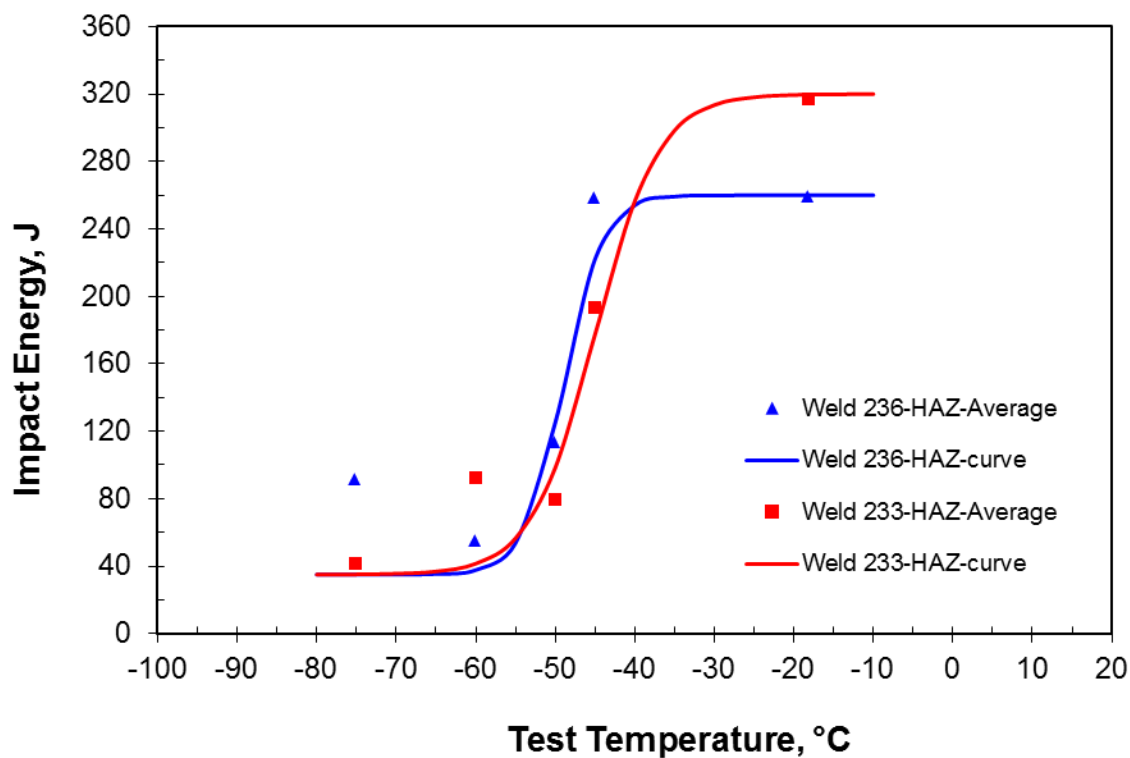


Figure 2-14 Charpy impact transition curves for the HAZ of Weld 1 (236) and Weld 2 (233)

2.3.3.3 Girth Weld CTOD Toughness – SENB Tests

A total of six preferred geometry Bx2B single edge notch bend (SENB) test specimens were cut from the small sections of girth weld (Weld 1 and Weld 2) that were saved from between the CWP specimens. As a result, the specimen blanks came from different clock positions to evaluate both weld metal and HAZ fracture toughness. Through-thickness notches were placed at the WMC and in the HAZ as shown in Figure 2-15, below.

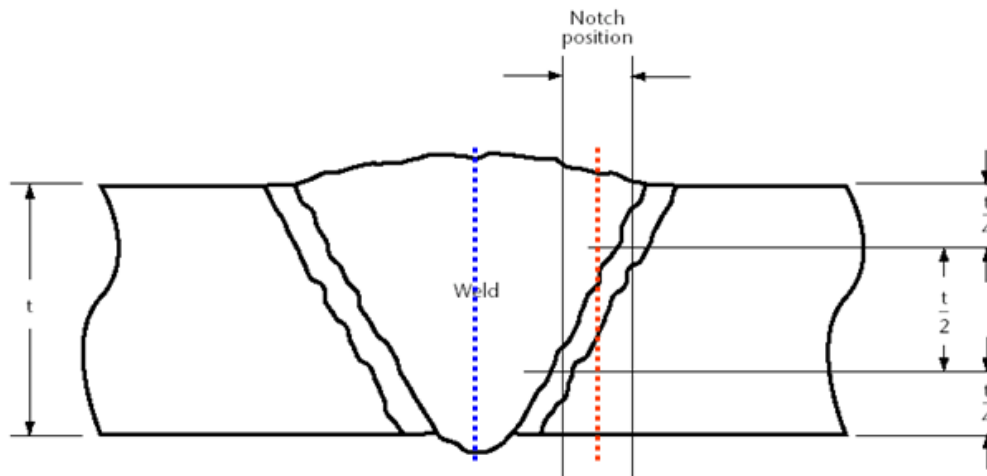


Figure 2-15 Schematic diagram showing the notch position for WMC (dashed blue vertical line) and HAZ (dashed red vertical line) for CTOD fracture specimens

All specimens were tested at $-10\text{ }^{\circ}\text{C}$ in a universal testing machine after stabilizing the temperature for approximately 15 mins prior to testing. Yield and ultimate tensile strengths for precracking and for calculation of CTOD were obtained using the room temperature all weld metal and longitudinal pipe base metal test data obtained by NIST. The values for the sub-zero test temperature were derived from the test data from NIST according to the methods outlined in ISO 15653 Section 12.1 [60]. Load-CMOD displacement curves were recorded for each test and used to determine the significance of any pop-ins as well as in the calculations of crack-tip opening displacement as outlined in the standard.

A summary of the CTOD test results is presented in Table 2-23. From the data listed in the table, it is clear that the WMC tests exhibited reasonably consistent fracture toughness with a similar range of δ_c , δ_u , and δ_m values obtained, e.g., lower bound δ_c values of 0.012 mm and 0.010 mm, while the δ_m values of 0.21 mm and 0.15 mm for Welds 1 (236) and Weld 2 (233), respectively. These results are consistent with a large pop-in fracture for the former and smaller thumb nail shaped fracture for the latter, as shown in individual photographs in Appendix B.

In contrast, there were considerable differences in fracture toughness observed for the HAZ test conducted on Weld 1 (236). In this case, two very low δ_c values = 0.02 mm and one very high δ_m value = 0.77 mm were obtained. In the former case, isolated pop-ins (see photographs in Appendix B) resulted in the low values, while the much high value may have resulted from inconsistent notch placement and/or the fracture deviating towards the base metal, although this would require more detailed investigations to confirm that this was the case. For the Weld 2

(233), the HAZ CTOD results were generally more consistent with two δm values of 0.36 mm and 0.48 mm and one δc value of 0.18 mm.

Some factors that should be considered to have potentially influenced the HAZ fracture toughness were the differences in the fusion line profile, which ultimately could affect the fraction of coarse grain HAZ sampled in a given test specimen. The very low toughness values obtained for Weld 1 (236), require some further investigation in order to fully explain the cause of the fracture initiations.

Table 2-23 CTOD results for WMC and HAZ testing of Weld 1 (236)

Weld ID	Notch Location	Specimen ID	Notch Position	CTOD mm	CTOD In.	Fracture Mode
Weld 1 (236)	WMC	236-WMC-2	centered	0.12	0.005	c
		236-WMC-4	off center	0.20	0.008	u/c
		236-WMC-6	centered	0.21	0.008	m
	HAZ	236-HAZ-1	HAZ targeted	0.02	0.0006	c
		236-HAZ-3	HAZ targeted	0.02	0.0007	c
		236-HAZ-5	away from FL	0.77	0.0302	m
Weld 2 (233)	WMC	233-WMC-1	off center	0.14	0.005	u
		233-WMC-3	centered	0.15	0.006	m
		233-WMC-5	centered	0.10	0.004	c
	HAZ	233-HAZ-2	biased to WM	0.36	0.014	m
		233-HAZ-4	HAZ targeted	0.18	0.007	c
		233-HAZ-6	biased to WM	0.48	0.019	m

2.3.3.4 Girth Weld CTOD Resistance Curve - SENT Tests

Single edge notched tensile (SENT) tests were performed on representative specimens sectioned adjacent to or as close as achievable to CWP specimens. The sectioning plan and detailed machine drawings are available in Appendix B. Specimens were sectioned and ground to maximize available material using the OD surface of the section as a reference. The ground blanks were polished to determine the location of the welds and to provide reference lines for proper placement of the notches. Notches in the heat affected zone (HAZ) targeted the fusion line from the ID (root) side of the pipe and were normal to the specimen surface. Notches in the

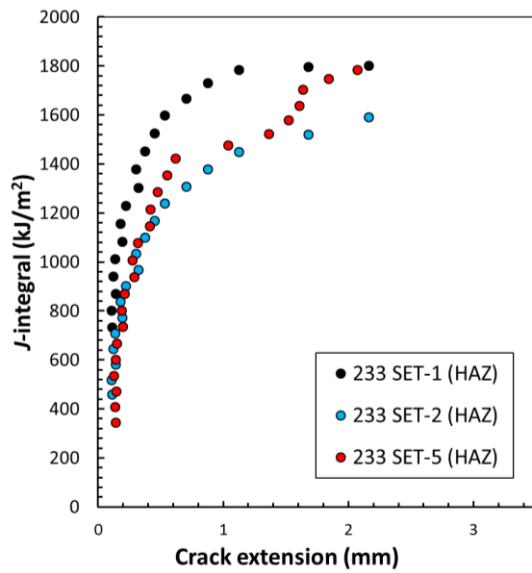
weld centerline (WCL) were normal to the specimen surface and located to bisect the root gap. Locations of the notches (HAZ or WCL) were defined by the adjacent CWP specimen. Notches and integral knife edges were cut by use of wire electrical discharge machining (EDM). Side grooves were also cut by wire EDM, and to simplify the machining, a constant side groove geometry was used for each specimen. Holes were then drilled and tapped into the front face (OD side of specimen) to install a double clip gage fixture.

The specimens were tested per the test matrix defined in Table 2-24. The specimens were tested and analyzed per the CanmetMATERIALS recommended practice [61]. Procedure details are provided in Appendix B.

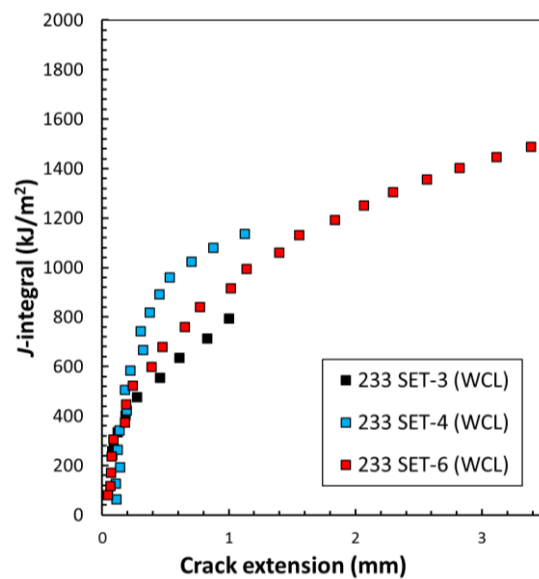
Table 2-24 Single Edge Notched Tension (SENT) Test Matrix

Weld	Specimen ID	Notch Location	Notch Depth (mm)	a_0/W	W X B (mm)	Adjacent to CWP
16 mm – 19 mm (0.625 in – 0.750 in) (Weld-2)	233-SET-1	HAZ	4.51	0.35	13.03 X 13.03	N/A
	233-SET-2	HAZ	4.50	0.33	13.54 X 13.54	233-CWP-1
	233-SET-3	WCL	4.52	0.33	13.54 X 13.54	233 CWP-2
	233-SET-4	WCL	4.71	0.34	13.89 X 13.89	233-CWP-2
	233-SET-5	HAZ	4.54	0.34	13.45 X 13.45	233-CWP-3
	233-SET-6	WCL	4.52	0.33	13.65 X 13.65	233-CWP-4
16 mm – 16 mm (0.625 in – 0.625 in) (Weld-1)	236-SET-1	HAZ	4.72	0.34	14.09 X 14.10	236-CWP-1
	236-SET-2	HAZ	4.72	0.34	14.09 X 14.09	236-CWP-1
	236-SET-3	HAZ	4.76	0.34	14.08 X 14.10	236-CWP-2
	236-SET-4	WCL	4.52	0.33	13.54 X 13.54	236-CWP-3
	236-SET-5	WCL	4.74	0.34	14.10 X 14.10	236-CWP-3
	236-SET-6	WCL	4.75	0.34	14.10 X 14.10	236-CWP-4

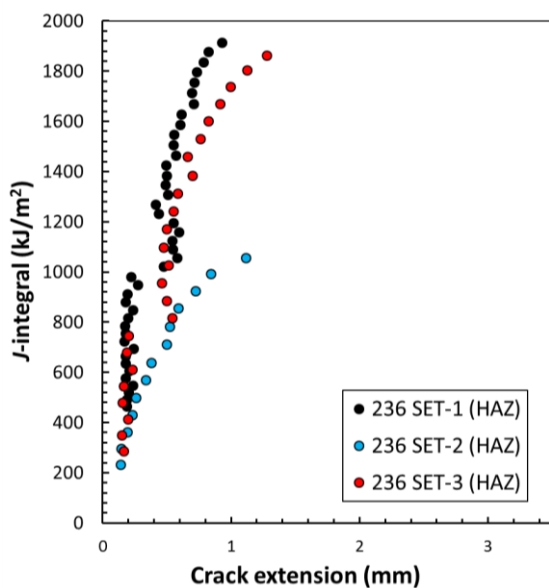
J-R curves for the SE(T) tests are shown in Figure 2-16. CTOD-R curves for the SE(T) tests are shown in Figure 2-17. Each plot shows the resultant data for the three specimens associated with each notch location and each weld. Note that specimen 236-SET-5 had no crack growth, supporting details of this specimen can be found in Appendix B.



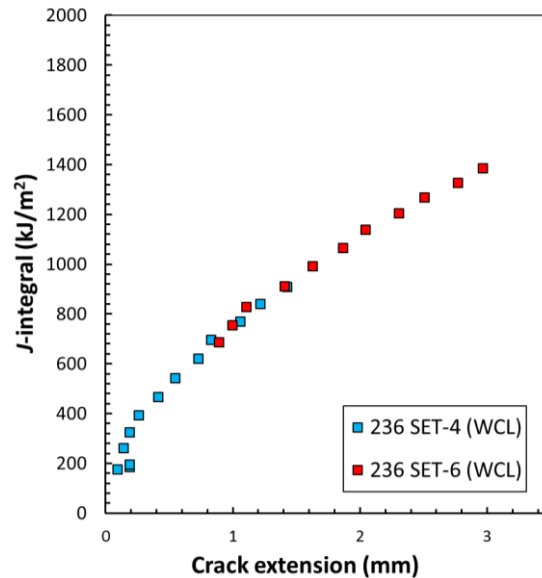
(a) Weld-2 HAZ



(b) Weld-2 WCL

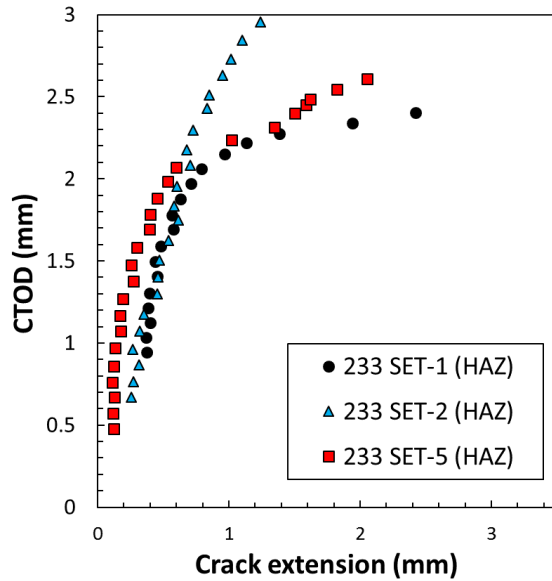


(c) Weld-1 HAZ

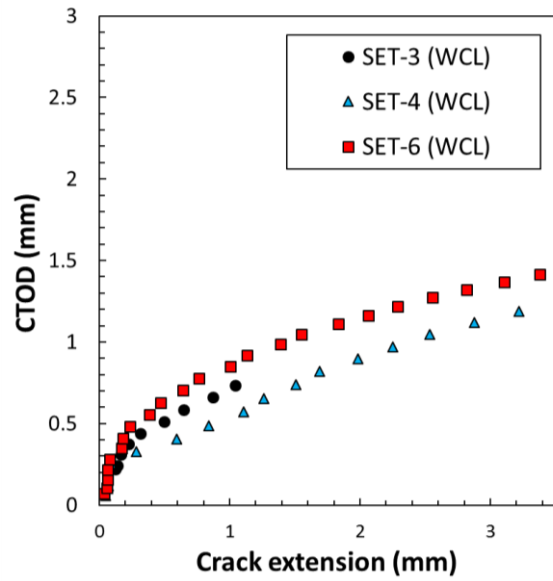


(d) Weld-1 WCL

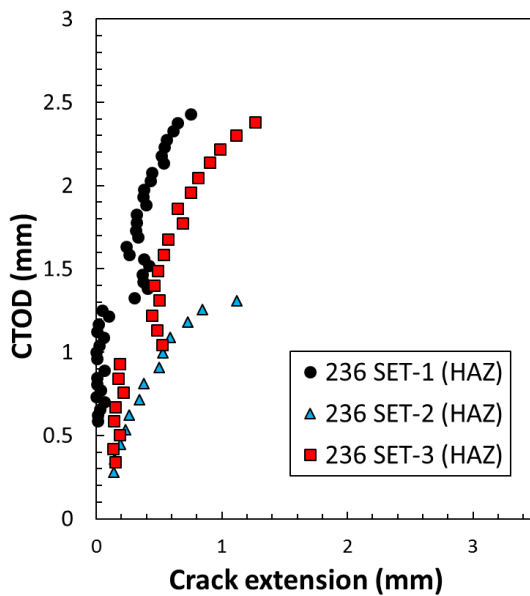
Figure 2-16 J-R curve plots for SE(T) specimens. Plot (a) is for the 16 mm – 19 mm (Weld-2) transition weld with notches in the HAZ, plot (b) is for the 16 mm – 19 mm (Weld-2) transition weld with notches in the WCL, plot (c) is for the 16 mm – 16 mm (Weld-1) with notches in the HAZ and plot (d) for the same but with notches in the WCL (Weld-1).



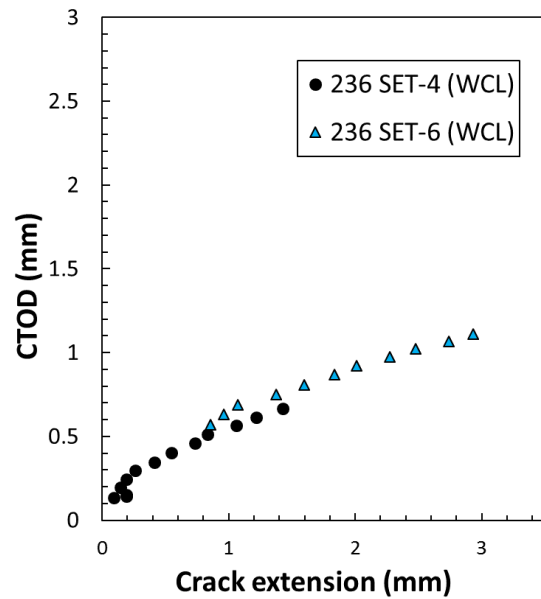
(a) Weld-2 HAZ



(b) Weld-2 WCL



(c) Weld-1 HAZ



(d) Weld-1 WCL

Figure 2-17 CTOD-R curve plots for SE(T) specimens. Plot (a) is for the 16 mm – 19 mm (Weld-2) transition weld with notches in the HAZ, plot (b) is for the 16 mm – 19 mm (Weld-2) transition weld with notches in the WCL, plot (c) is for the 16 mm – 16 mm (Weld-1) with notches in the HAZ and plot (d) for the same but with notches in the WCL (Weld-1).

The scatter in the J -R and CTOD-R curves is primarily attributed to the weld overmatch. Considering the 16 mm – 16 mm WT welds (Weld-1), there are obvious discontinuous J -R curves and the discontinuity is attributed to the apparent crack extension due to large scale shear plasticity in the specimen. The CMOD measurements after the discontinuity are therefore associated with this shear plasticity and crack extension. The relative strain distributions in the specimen before and after the discontinuity are shown in Figure 2-18. These photos illustrate the shear strain in the specimen. The shear strain does not follow the fusion line and is a geometric mechanical response rather than a material response. The last photo (c) in Figure 2-18 is for specimen 236 SET-2 which did not result in a discontinuous J -R curve, this shows a shear angle that followed more closely to the fusion line. This test was terminated when the specimen failed from the OD side of the weld. Post-test fractographs of all the specimens tested are available in Appendix B.

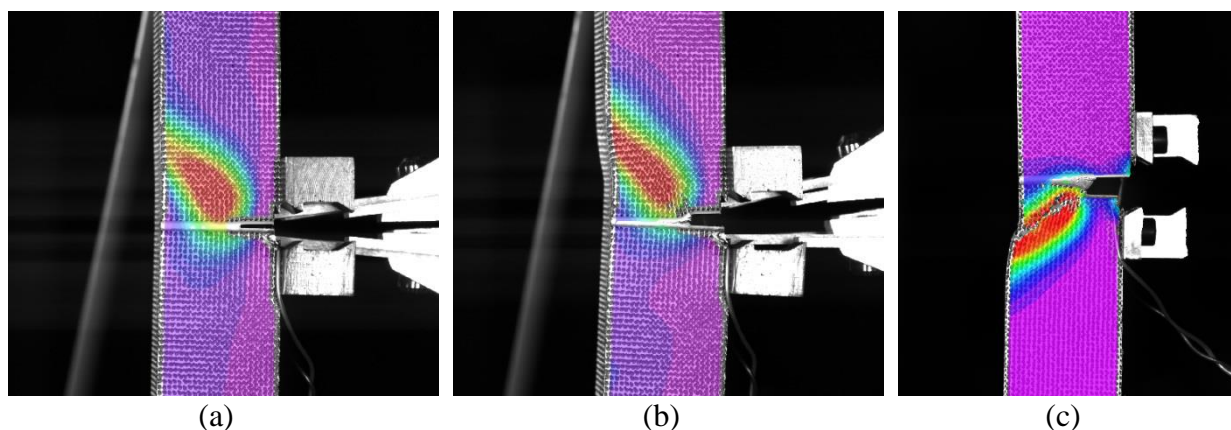


Figure 2-18 DIC images showing relative strain gradients during SE(T) testing. Photo (a) is of 236 SET-1 prior to the discontinuity in the resultant J -R curve while (b) is of the same specimen after the discontinuity. Photo (c) is of 236 SET-2 at the end of the test showing significant shear strain in the specimen.

Specimens 236 SET-1, 236 SET-2 and 236 SET-3 (for Weld-1) were examined more closely with respect to notch placement and subsequent crack growth. These specimens were sectioned along the axial centerline and prepared for metallography. The metallographic cross-sections are shown in Figure 2-19. In the case of 236 SET-1 and 236 SET-3, the notch tips were placed very near the fusion lines and crack extension was initially impeded by weld material in both specimens. This impediment and subsequent shear deformation is the best explanation for the discontinuity in the J -R (and CTOD-R) curves. In the case of 236 SET-2, the notch was placed further away from the fusion line and it's clear that crack extension remained in the HAZ at an angle commensurate with specimens 236 SET-1 and 236 SET-3. The shear strain, however, followed more closely with the fusion line angle. Again, the test was terminated earlier in 236 SET-2 than either of 236 SET-1 and 236 SET-3 because a lack-of-fusion flaw on the OD side of the weld caused a large stress concentration and failure from that side of the weld. See Appendix B for more details.

Comparisons between SE(T) specimen results and adjacent curved wide plate (CWP) results will be discussed in Section 3.2.3.3.

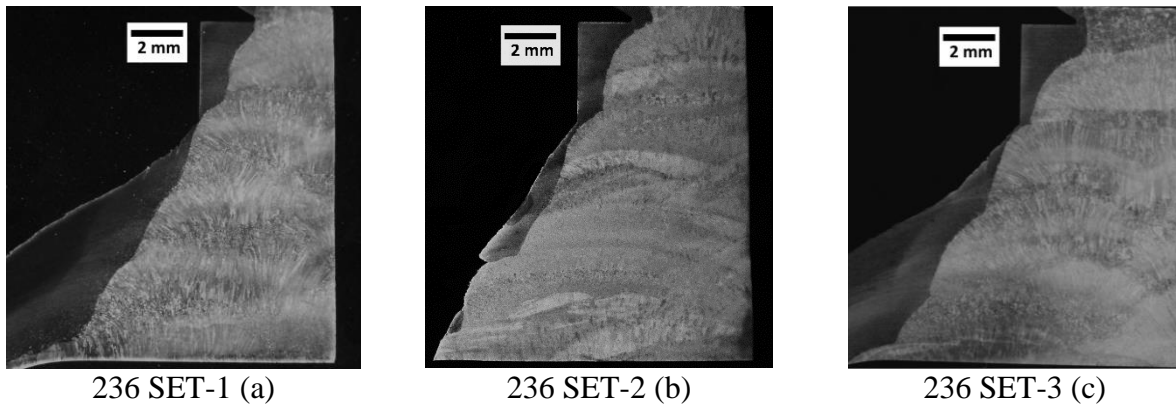


Figure 2-19 Metallographic cross-sections from specimen 236 SET-1 (a), 236 SET-2 (b) and 236 SET-3 (c)

3 Large-Scale Tests and Testing Results

3.1 Overview of Large-Scale Testing Program

This section describes the large-scale tests performed to support the model development and calibration process. The large-scale tests consisted of four full-scale pipe testing programs and one curve-wide-plate testing program. Each testing program was intended to address a different aspect of pipe performance in response to high longitudinal strain. The specific testing programs are shown in Table 3-1.

The line pipes used for the large-scale tests and the corresponding girth welds associated with each test can be found in Table 2-1, Table 2-2, and Table 2-3.

Table 3-1 List of large-scale testing programs

Testing Program ID	Type of Tests	Features or Anomalies Tested	Limit States Tested
Task 9	Full-scale bending tests	Transition welds, metal loss corrosions, and dents	Compressive strain capacity
Task 10	Full-scale bending-burst tests	Metal loss corrosions	Burst pressure
Task 11	Full-scale compression-burst tests	Wrinkles	Burst pressure
Task 12	Full-scale tension tests	Metal loss corrosions	Tensile strain capacity
Task 13	Curved-wide-plate tension tests	Transition welds	Tensile strain capacity

3.2 Full-Scale Bending Tests of Pipes with Transition Welds and Anomalies (Task 9)

The purpose of the Task 9 tests was to evaluate how the compressive strain capacity of line pipes is affected by geometric and material property discontinuities associated with transition welds, metal loss from corrosion and mechanical damage in the form of plain dents.

3.2.1 Specimen Configuration

NPS 12 pipe joints (see Figure 3-1) were cold-cut at C-FER to obtain ten test specimens approximately 2,855 mm (112 inches) in length. All specimens were fabricated from 324 mm OD x 6.35 mm WT (12.75 x 0.25 inch), Grade X65, ERW line pipe, except for the Task 9.a specimens involving thickness transitions, for which 324 mm OD x 9.5 mm WT (12.75 x 0.375 inch) Grade X65 line pipe was also used for the thicker sections (see Table 2-1).

Specimens were numbered and measured, after which they were sent for fabrication (i.e. girth welding and end fixture installation). All specimens were welded to short, thick-walled end sections, which in turn were welded to flat-plate end caps. (The thick pipe end sections were incorporated to minimize the potential for premature specimen buckling near the ends and to facilitate a heavier and thereby more robust weld between the specimen and the end caps.)

Nine of the ten specimens in this test series were subject to additional fabrication or treatment to simulate the presence of geometric and/or material property discontinuities associated with either pipe fittings, metal loss corrosion, or plain dents. A baseline specimen, without anomalies or discontinuities, was also included in the series to provide a basis for quantifying the relative change in compressive strain capacity attributable to the anomalies or discontinuities introduced in the other specimens.



Figure 3-1 Pipes Received at C-FER for Specimen Fabrication

Table 3-2 summarizes the ten specimens fabricated for testing in this series. Figure 3-2 depicts two specimens, one with and one without welded end caps.

Table 3-2 Specimens for Task 9 Tests

Specimen Identification	C-FER Specimen Number	Anomaly	Loading Type*
9 (baseline)	X65-ERW-1-3-9BL	None	Bend
9.a.i	X65-ERW-1-3-9AI to X65-ERW-1-3-9ASP	Weld Transition	Bend
9.a.ii	X65-ERW-1-3-9AII to X65-ERW-2-9AII	Weld & Thickness Transition	Bend
9.a.iii	X65-ERW-1-3-9AII to X65-ERW-2-9AIII	Weld & Thickness Transition	Bend
9.b.i	X65-ERW-1-2-9BI	Corrosion Feature	Bend
9.b.ii	X65-ERW-1-2-9BII	Corrosion Feature	Bend
9.b.iii	X65-ERW-1-2-9BIII	Corrosion Feature	Bend
9.c.i	X65-ERW-1-1-9CI	Plain Dent	Pressure Cycle and Bend
9.c.ii	X65-ERW-1-1-9CII	Plain Dent	Pressure Cycle and Bend
9.c.iii	X65-ERW-1-1-9CIII	Plain Dent	Pressure Cycle and Bend



Figure 3-2 Specimens Before and After End Cap Installation

3.2.2 Specimen Anomalies

Geometric and material property discontinuities associated with fittings were simulated in the three Task 9.a specimens by girth welding pipe sections of differing wall thickness and yield strength (i.e. pipe grade). Specimen 9.a.i was fabricated by welding together two joints of the same 6.35 mm (0.25 inch) wall thickness. The girth weld joint geometry is shown in Figure 3-3. Two additional specimens were fabricated by welding together two joints of dissimilar thickness to create a wall thickness transition from 6.35 mm to 9.53 mm (0.25 inch to 0.375 inch). One specimen (9.a.ii) was fabricated with a bevel as shown in Figure 3-4. The other specimen (9.a.iii), shown in Figure 3-5, was prepared with a counterbore and bevel. The transition welds were made using a gas metal arc welding (GMAW) procedure.

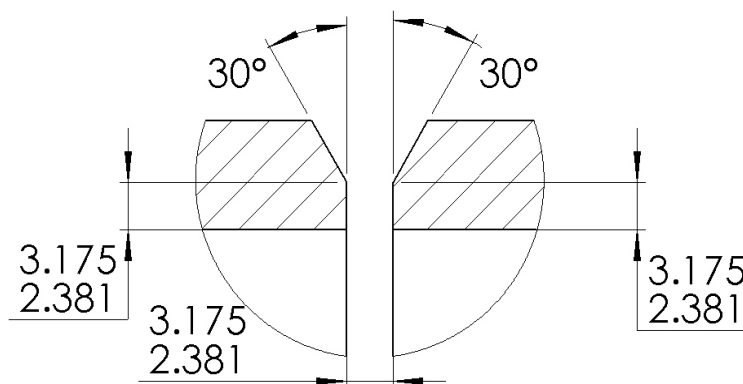


Figure 3-3 6.35 mm-to-6.35 mm (0.25 inch-to-0.25 inch) Wall Thickness Match (Dimensions in mm)

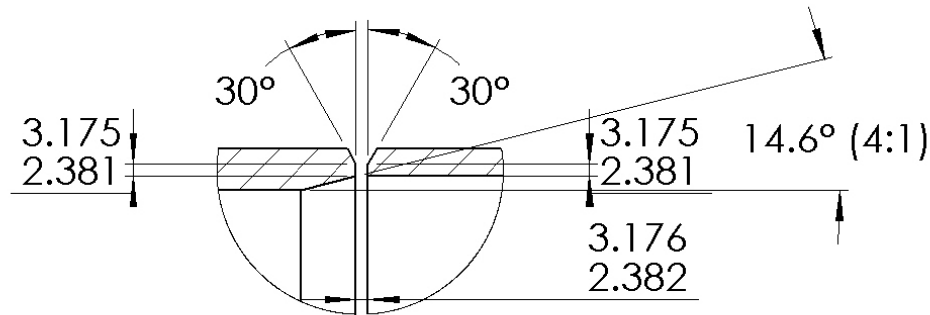


Figure 3-4 6.35 mm-to-9.53 mm (0.25 inch-to-0.375 inch) Wall Thickness Step with Bevel (Dimensions in mm)

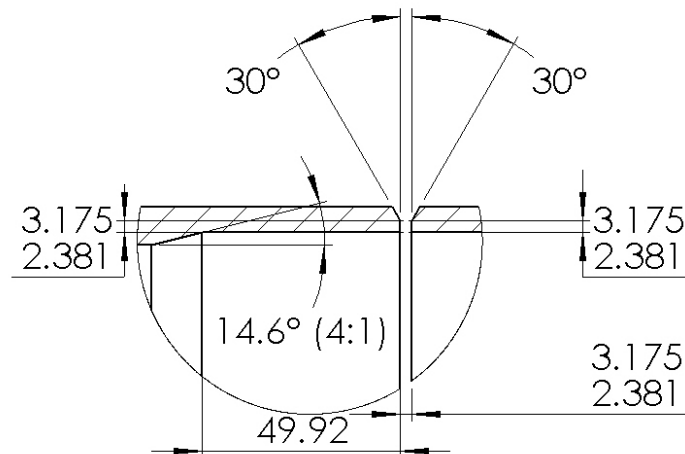


Figure 3-5 6.35 mm-to-9.53 mm (0.25 inch-to-0.375 inch) Wall Thickness Step with Counterbore (Dimensions in mm)

Metal loss associated with corrosion was simulated in three of the Task 9.b specimens by machining material from the outer pipe surface at specimen mid-length at a circumferential position on the pipe that would later correspond to the location of the extreme compression fiber under bending load. Feature dimensions are detailed in Table 3-3 and an example of a machined metal loss feature is shown in Figure 3-6.

Table 3-3 As Installed Metal Loss Feature Dimensions

Specimen Identification	Anomaly Description	Feature Dimensions (mm)		
		Length	Width	Depth
9.b.i	Shallow General Metal Loss	64.0	65.0	1.45
9.b.ii	Shallow Circumferential Groove	16.0	65.0	1.55
9.b.iii	Deep General Metal Loss	65.0	65.0	2.49

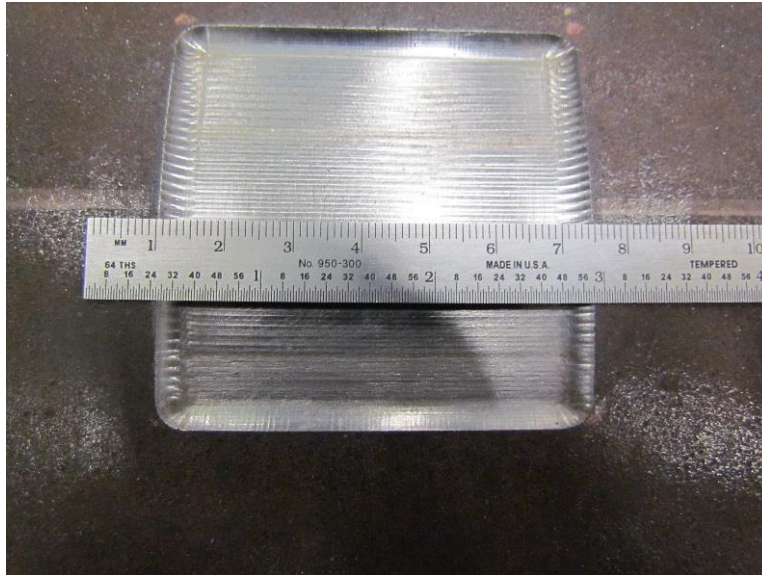


Figure 3-6 Metal Loss Feature Installed in Specimen Test 9.b.iii

Mechanical damage was simulated in the three Task 9.c specimens by indenting each pipe from the outside at mid-length at a circumferential position that would later correspond to the extreme compression fiber under bending load. The specimens were dented using C-FER's Universal Testing System (UTS), a servo-hydraulic load frame capable of generating 15 MN of tensile or compressive force. Specimens were positioned horizontally, secured to the floor and slowly indented using a 63.5-mm (2.5 inch) steel ball as the indenter (see Figure 3-7 and Figure 3-8). The installed dent dimensions are summarized in Table 3-4.



Figure 3-7 Pipe Indentation Setup in the UTS



Figure 3-8 Example of Specimen after Denting Showing the Steel Ball Indenter

Table 3-4 As Installed Plain Dent Dimensions

Specimen Identification	Anomaly Description	Dent Depth (mm)	Dent Depth (% OD)
9.c.i	Shallow Dent	5.2	1.6%
9.c.ii	Moderate Dent	13.6	4.2%
9.c.iii	Deep Dent	43.1	13.3%

3.2.3 Specimen Grid Layout and Measurements

Prior to end fixture attachment and testing, specimens were grid marked and measured in accordance with the marking layout shown in Figure 3-9. These measurements were taken to quantify the geometric characteristics of the specimens prior to testing. Measurements taken included specimen length and diameter measurements at each of the axial stations located 324 mm (12.75 inches) apart along the length of each specimen. The radial grid involved measurement stations spaced circumferentially at 45-degree increments. Estimates of ovality were obtained from the diameter measurements, as were the maximum diameter, minimum diameter, and the mean and standard deviation of the diameter. Ovality as reported herein is defined by:

$$Ovality = \frac{(D_{max} - D_{min})}{D_{nom}} * 100\% \quad (3-1)$$

In addition, wall thickness measurements were taken at the grid intersection points using an ultrasonic hand-held instrument.

Selected specimen measurements are summarized in Table 3-5. The full set of specimen measurements for Task 9 can be found in Appendix D.

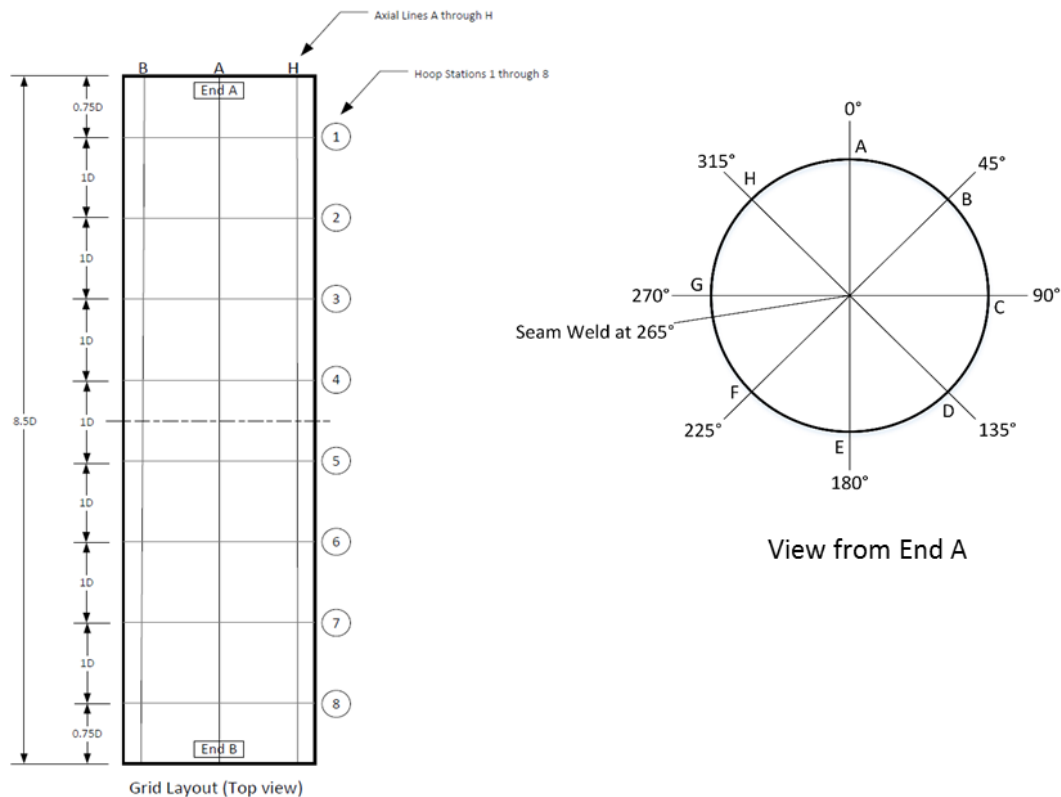


Figure 3-9 Task 9 Specimen Marking Scheme

Table 3-5 Selected Task 9 Specimen Geometry Measurements

Specimen Identification	Average OD mm (in)	Average Wall Thickness mm (in)	Ovality (%)		
			Station Positions		
			4	5	6
9 (baseline)	324.02 (12.75)	6.46 (0.254)	0.74	0.68	0.72
9.a.i	323.98/323.94* (12.75/12.75)	6.55/6.60* (0.257/0.259)	0.67	0.52 /0.27*	0.43
9.a.ii	324.06/323.73* (12.75/12.74)	6.49/9.49* (0.255/0.373)	0.60	0.64/0.08*	0.03
9.a.iii	324.03/323.76* (12.75/12.74)	6.43/9.57* (0.253/0.376)	0.58	0.46/0.09*	0.07
9.b.i	323.87 (12.75)	6.38 (0.251)	0.67	0.71	1.0
9.b.ii	324.07 (12.75)	6.38 (0.251)	0.56	0.65	0.74
9.b.iii	324.08 (12.75)	6.35 (0.25)	0.58	0.51	0.75
9.c.i	324.06** (12.75)	6.32 (0.248)	0.68	0.76	0.85
9.c.ii	324.04** (12.75)	6.34 (0.249)	0.52	0.71	0.77
9.c.iii	324.11** (12.76)	6.39 (0.251)	0.61	0.60	0.71

* End A/End B measurements for wall thickness transition pipes

** Measurements taken post dent installation

3.2.4 Test Setup

The Task 9 tests were performed in CFER's custom-designed bend frame. The apparatus, shown in Figure 3-10, is a servo-hydraulically controlled load system incorporating three hydraulic rams, each with a capacity of 1.34 MN (302 kip). The system allows for independent

control of the applied bending moment and axial force and the ability to automatically compensate for the axial force generated on the specimen end caps by internal pressure. For these tests, the system was configured to fully compensate for the pressure-induced end cap forces; thereby enabling the specimens to be subjected to a pure bending load.

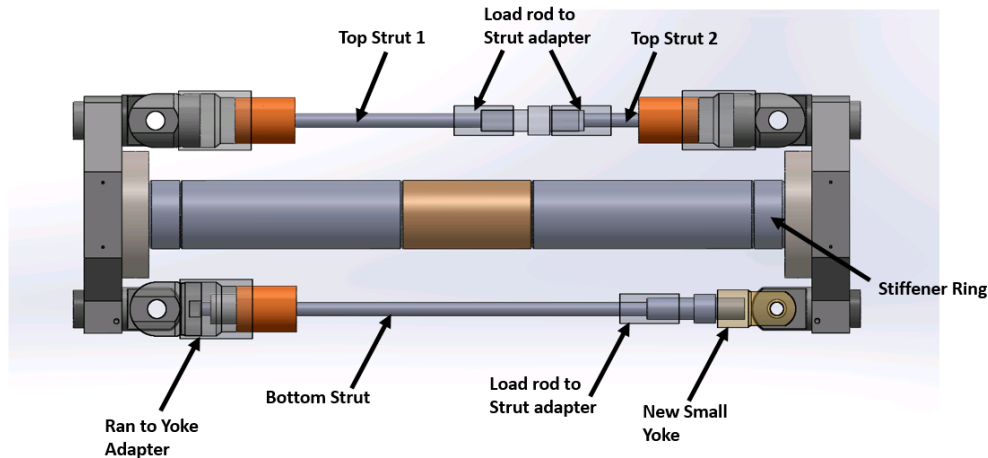


Figure 3-10 Bend Test Apparatus

3.2.4.1 Instrumentation

The instrumentation employed for testing is summarized below (see also Figure 3-11).

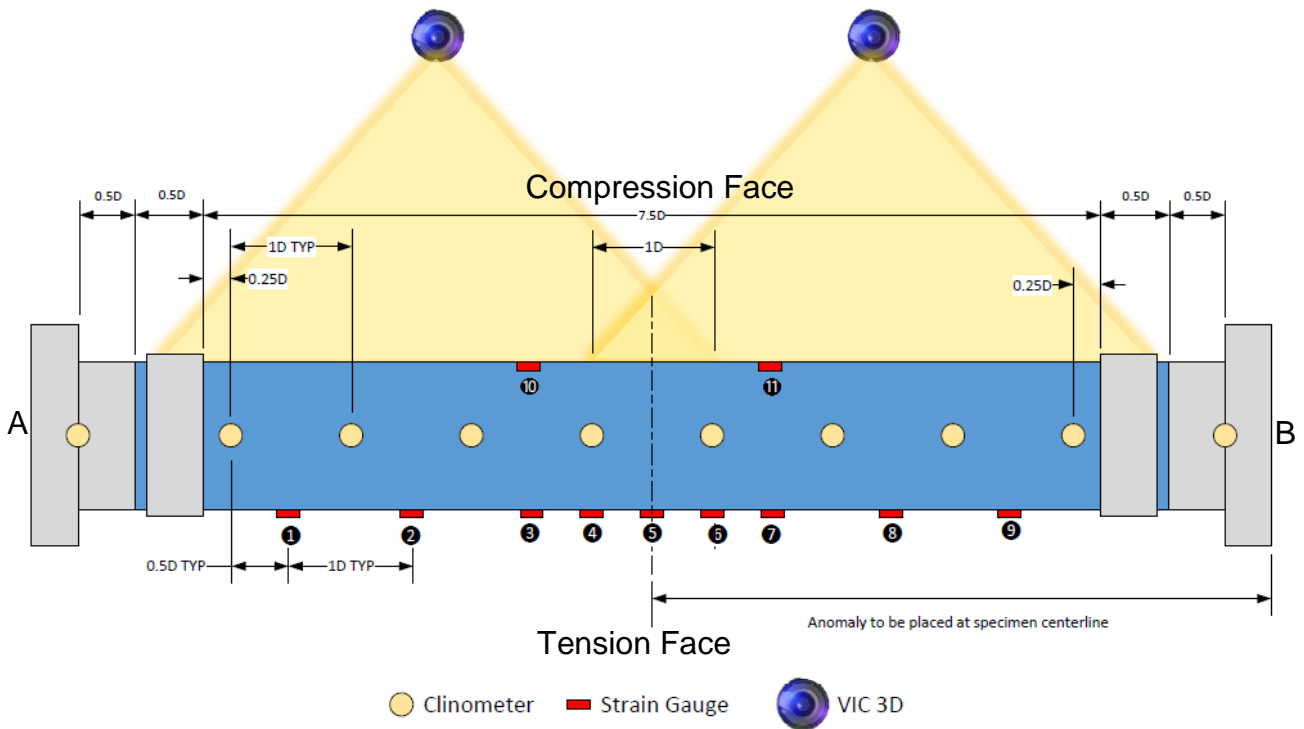


Figure 3-11 Instrumentation Diagram for Task 9 and Task 10 Tests

- For local strain measurement:
 - eight uniaxial gauges and one biaxial gauge (gauge 3) were used to measure strain on the tension side of the specimen; and
 - two uniaxial gauges were used to measure strain on the compression side of the specimen. (Task 9.a added two uniaxial gauges 50 mm (2 inch) on either side of the center of the transition weld).
- For pressure measurement:
 - one calibrated pressure transducer was plumbed to a port on the A side flange to measure specimen internal pressure; and
 - six calibrated pressure transducers were used to measure the hydraulic pressure in the rams (two on each ram) on the extension and contraction sides of the test apparatus.
- For displacement measurement:
 - three calibrated displacement transducers were used, one to measure the stroke of each ram on the test apparatus;
 - one cable potentiometer was suspended from the roof of the containment system and attached at the mid span of the specimen to measure lateral deflection; and
 - two Visual Image Correlation (VIC) 3D camera systems (four cameras total) were used to map the strain on the compressive side of the pipe. (Camera pairs were separated sufficiently to provide full coverage of the mid-length region of the specimen.)
- For rotational displacement:
 - eight calibrated clinometers were placed along the length of the specimen, to measure rotation at their attachment points; and
 - two calibrated clinometers were installed, one on each end plate to measure specimen end rotation.
- For load measurement, two calibrated load cells were used, one to measure the applied axial force on each strut.

Instrument readings were recorded at a sampling rate of 4 Hz using a computer-based digital data acquisition system (DAS) programmed in LabVIEW™. Data was acquired continuously throughout each test from all instruments, except for the strain mapping camera system and digital cameras. Digital images of the specimens were taken at predetermined intervals during each test using both sets of cameras. A photo of the test setup with instrumentation in place is shown in Figure 3-12.

3.2.4.2 Visual Image Correlation System

The VIC system is a non-contact optical technology used in these tests primarily to determine strains on the compression face of the specimens. A stereo camera system (Figure 3-13a) captures images of the target area, which is painted with a speckled pattern (Figure 3-13b) to facilitate subsequent interpretation of pipe surface movement. The paired digital images captured periodically during testing can be processed using the principle of stereo-triangulation

to provide 3D measurements of changes in the position of elements of the speckled pattern on the pipe surface. This information can be further processed to develop strain field contour maps or uniaxial strain profiles in orthogonal directions (e.g. in the longitudinal and hoop directions on a pipe specimen).

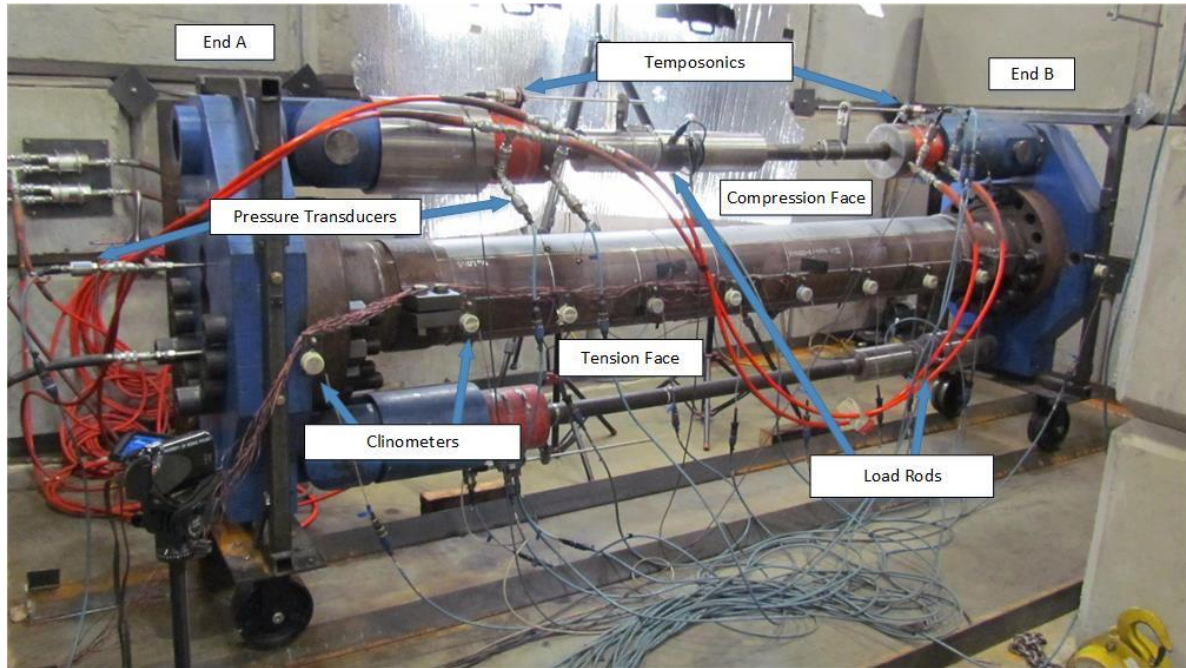


Figure 3-12 Side View of Bend Test Setup

3.2.5 Calculation of Critical Compressive Strain Capacity for Bend Tests

The objective of the Task 9 tests was to evaluate the effect of anomalies and discontinuities on the critical compressive strain capacity (CSC) of line pipe, defined here as the average axial membrane compressive strain over a finite gauge length at the attainment of the peak bending moment. This was determined two ways: 1) using the readings obtained from discrete on-specimen instrumentation, specifically clinometers and strain gauges, and 2) using the results of post-processed images taken using the VIC 3D system.

For axial compressive strain estimation from discrete instrument (DI) readings, specimen curvature was first calculated from clinometer readings using Eq. (3-2):

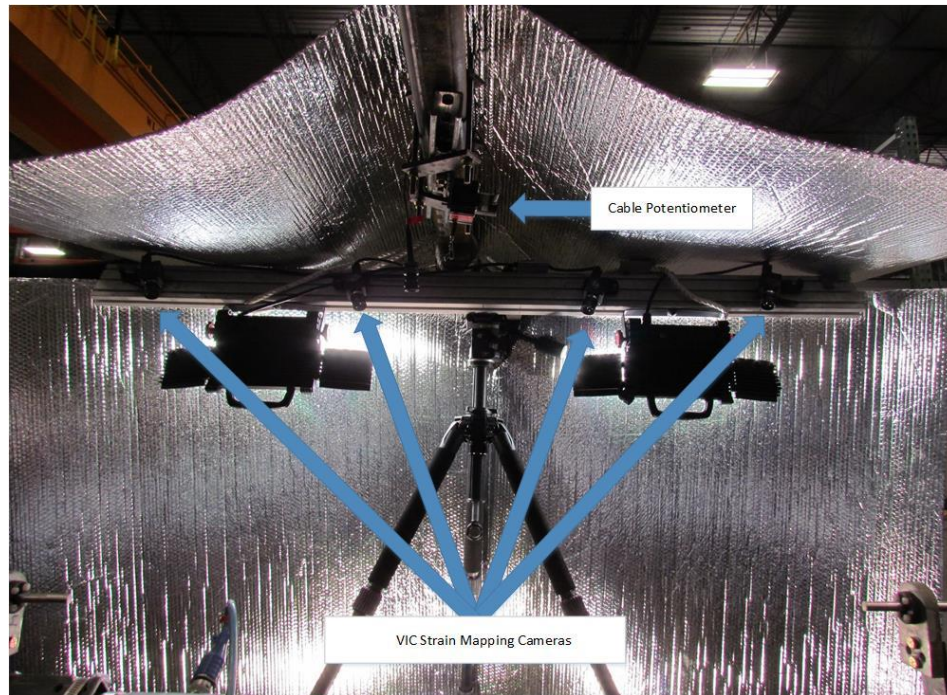
$$K = \frac{\Delta\theta}{L} \quad (3-2)$$

where:

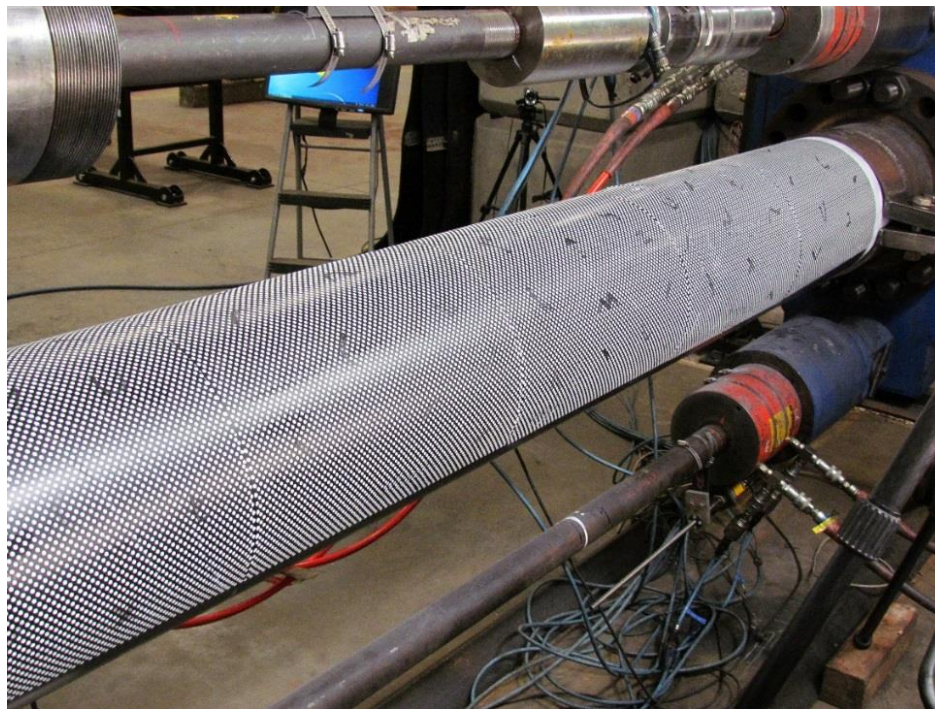
K = curvature over a given gauge length;

$\Delta\theta$ = change in angle between sections at the gauge length ends (i.e. difference between the clinometer measurements bounding the selected gauge length); and

L = gauge length (i.e. distance between clinometers prior to deformation).



(a)



(b)

Figure 3-13 VIC System Used for Displacement and Strain Measurements: (a) VIC Strain mapping cameras and cable potentiometer above specimen; (b) Speckle pattern painted on compression face of test specimen.

A 1D spacing of clinometers (i.e. a gauge length of $L = 1D$) was selected as it is commonly assumed to be the shortest gauge length over which meaningful average compressive membrane strain levels can be experimentally determined, in large part because it is generally sufficiently long to capture the entire buckle region.

The curvature over a 1D gauge length, calculated as described above, together with the local tensile strain obtained from an axial strain gauge located on the extreme tension fiber of the specimen, was then used to calculate the average compressive strain using Eq. (3-3) (the concept of calculation is illustrated in Figure 3-14).

$$|\varepsilon_c| = |\varepsilon_t - KD| \quad (3-3)$$

where:

- ε_c = average compressive strain over a given gauge length;
- ε_t = tensile strain (measured by the tensile strain gauge closest to the center of the selected gauge length); and
- D = pipe diameter.

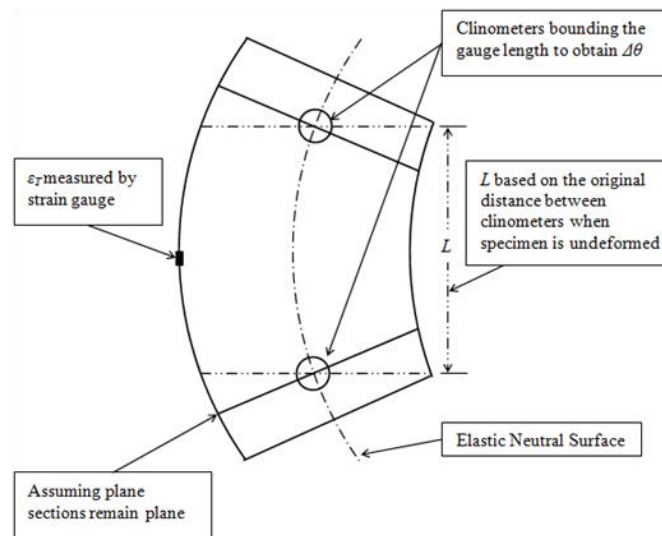


Figure 3-14 Schematic of Average Axial Compressive Strain Estimation

The average axial compressive membrane strain calculated using Eq. (3-3) is valid for thin-walled pipe in both the elastic and plastic deformation ranges, provided that: curvature is constant between the reference planes; plane sections remain plane; and specimen diameter remains constant. In fact, curvature is not constant between reference planes, particularly when a buckle begins to form; plane sections do not remain plane, especially in the plastic deformation range when local anomalies are present, and pipe diameter does not remain constant due to cross-section ovalization induced by bending. However, while these issues can and do affect the results obtained to some degree, this approach to compressive strain estimation is preferred over estimates obtained from strain gauges placed directly on the compression face of the test specimen. This is because local axial compressive strains on the pipe surface in the buckle region vary significantly in close proximity to the buckle and surface strains measured by the

gauges do not provide a good representation of the membrane strain (i.e. the average through-thickness axial strain) in the pipe wall because the surface strains include significant levels of through-thickness, bending-induced strain associated with the developing buckle.

Given the above limitations inherent in compressive axial strain estimation using discrete instruments, complimentary estimates of the average compressive membrane strain were obtained using the VIC 3D system. The approach taken was to process digital images obtained at discrete points in time to first determine the axial separation distance between two prescribed reference points on the pipe surface. The average compressive strain between those two points at each point in time was then obtained by dividing the change in separation distance, relative to that at the start of testing, by the initial separation distance.

Average compressive strains based on discrete instrument readings are necessarily associated with the 1D gauge length defined by the chosen clinometer spacing, whereas average compressive strains obtained from the VIC system can be determined for any desired gauge length. For these tests, VIC strains based on 1D and 2D gauge lengths centered on the buckle location were chosen¹. Figure 3-15 shows the relationship between the various gauge lengths typically employed for compressive strain estimation in the bending tests. Note that the axial start and end points of the gauge lengths used for 1D strain estimation based on discrete instruments and 1D strain estimation using the VIC system do not necessarily align. This, combined with the other issues associated with strain estimation based on discrete instruments described above, suggests that 1D gauge length strain estimates obtained using discrete instrument and the VIC system are not likely to agree.

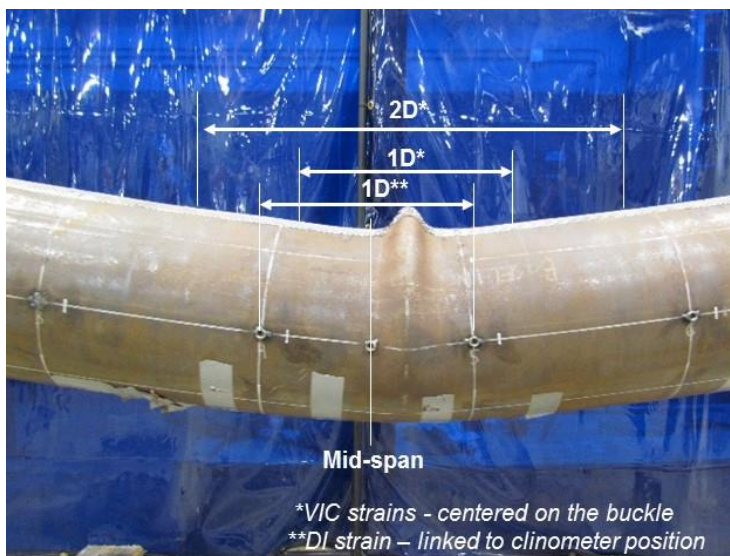


Figure 3-15 Gauge Lengths for Average Compressive Strain Estimation

¹ For specimens with girth welds and thickness transitions (i.e. 9.a.i, 9.a.ii and 9.a.iii), one-sided VIC strains were also determined over gauge lengths positioned such that one end was centered on the buckle location and the other end was located 1D away on the side of the specimen containing the thinner-walled pipe.

In general, the average compressive strain estimates obtained using the VIC system are preferred, however, verified VIC strain data was not typically available in real-time during testing and test control actions that relied on strain readings were, therefore, necessarily based on strain estimates obtained from discrete instrument readings.

3.2.6 Test Procedure

Specimens were installed in the test frame and split-ring assemblies were clamped to each end of the test section (inboard of the thickened end sections) to prevent buckle formation at the specimen ends (see Figure 3-2). Instrumentation was attached and specimens were filled with water at ambient temperature. All specimens were pressurized to a prescribed internal pressure of 12.7 MPa (1,835 psi) prior to the application of bending load (The target pressure was chosen to produce a nominal hoop stress level equal to 72% of SMYS.). Prior to pressurizing the Task 9.c pipes to their prescribed level they were pressurized to a nominal hoop stress level equal to 90% of SMYS, to induce the plastic re-rounding of indentations expected to result from a pre-service hydrotest, and then to an additional five pressure cycles to a hoop stress level of 72% of SMYS to stabilize the dents.

The specimen loading sequence was as follows:

1. Specimens were pressurized at approximately 1.4 MPa/min (200 psi/min) until the prescribed pressure level was achieved while counteracting the end cap forces by applying a net compressive axial force with the bending control system. During the pressurization step (and the pressure cycling stage where applicable), the total bending moment on the specimen was kept near zero.
2. Bending moment was then progressively applied by stroking the top strut at a fixed rate of 5.1 mm/min (0.2 in/min), while simultaneously adjusting the load on the bottom strut using a LabVIEW™ based control program to compensated for end cap forces and increment the bending load.
3. Bending continued until the deformation limitations of the test apparatus were reached or specimen failure occurred due to loss of pressure containment, after which the system was unloaded.

3.2.7 Test Results

The key results for the Task 9 tests include the peak local bending moment and the average compressive membrane strain at peak moment over prescribed gauge lengths bridging the buckle location. As discussed in Section 3.2.5, the reported average compressive strains were calculated two ways: first using tension-side strain gauges and clinometers, referred to here as 1D Strain (DI), and second, using the VIC data from images of the compression face, referred to here as 1D and 2D Strain (VIC).

Selected results for the Task 9 tests are summarized in Table 3-6 together with a description of the specimen condition at the end of each test. Complete results for each test are included in Appendix D.

The test end points for the Task 9.a specimens containing wall thickness transitions intended to represent the presence of fittings are shown in Figure 3-16. The test end points for the Task

9.c specimens containing plain dents are shown in Figure 3-17. The test end points for the Task 9.b specimens containing metal loss features and the leak locations relative to the metal loss features, where applicable, are shown in Figure 3-18. The detailed analyses and discussions of the Task 9.a, Task 9.b, and Task 9.c tests are given in Sections 4.3.4, 5.3.2, and 6.3, respectively.

Table 3-6 Summary of Results for Task 9 Tests

Specimen Identification	Anomaly or Discontinuity	Peak Local Moment (kN·m)	1D Strain (DI) (%ε)	1D Strain (VIC) (%ε)	One-sided 1D Strain** (VIC) (%ε)	2D Strain (VIC) (%ε)	Test End Condition
9 (baseline)	None	281	-3.5	-3.6	N/A	-3.3	Outward buckle near specimen midpoint
9.a.i	Girth weld (6.35 to 6.35 mm)	254	-2.2	-2.8	-2.8	-2.2	Outward buckle near specimen midpoint
9.a.ii	Girth weld & thickness step (6.35 to 9.53 mm with bevel)	247	-3.0	-2.8	-2.8	-2.0	Outward buckle near specimen midpoint
9.a.iii	Girth weld & thickness step (6.35 to 9.53 mm with counterbore & bevel)	265	-1.8	-3.0	-3.2	-2.4	Outward buckle near specimen midpoint
9.b.i	Shallow General Metal Loss (0.20D x 0.20D x 0.23t)	229	-1.7	-2.3	N/A	-1.5	Outward buckle near specimen midpoint followed by leak at corrosion feature at 14.1% 1D strain
9.b.ii	Shallow Circumferential Groove (0.05D x 0.20D x 0.24t)	255	-2.5	-2.8	N/A	-2.5	Outward buckle near specimen midpoint
9.b.iii	Deep General Metal Loss (0.20D x 0.20D x 0.39t)	208	-2.5	-2.6	N/A	-1.5	Outward buckle near specimen midpoint followed by leak at corrosion feature at 11.3% 1D strain
9.c.i	Shallow Dent (Re-rounded depth 1.2%D*)	255	-3.7	-3.3	N/A	-3.0	Outward buckle near specimen midpoint
9.c.ii	Moderate Dent (Re-rounded depth 2.7%D*)	249	-2.9	-2.5	N/A	-2.3	Outward buckle near specimen midpoint
9.c.iii	Deep Dent (Re-rounded depth 5.5%D*)	249	-2.1	-2.3	N/A	-2.1	Outward buckle near specimen midpoint

* Re-rounded dent depth after pressure cycling with no internal pressure.

** Gauge lengths had one end centered on buckle and the other 1D away on the specimen side containing thinner-walled pipe.

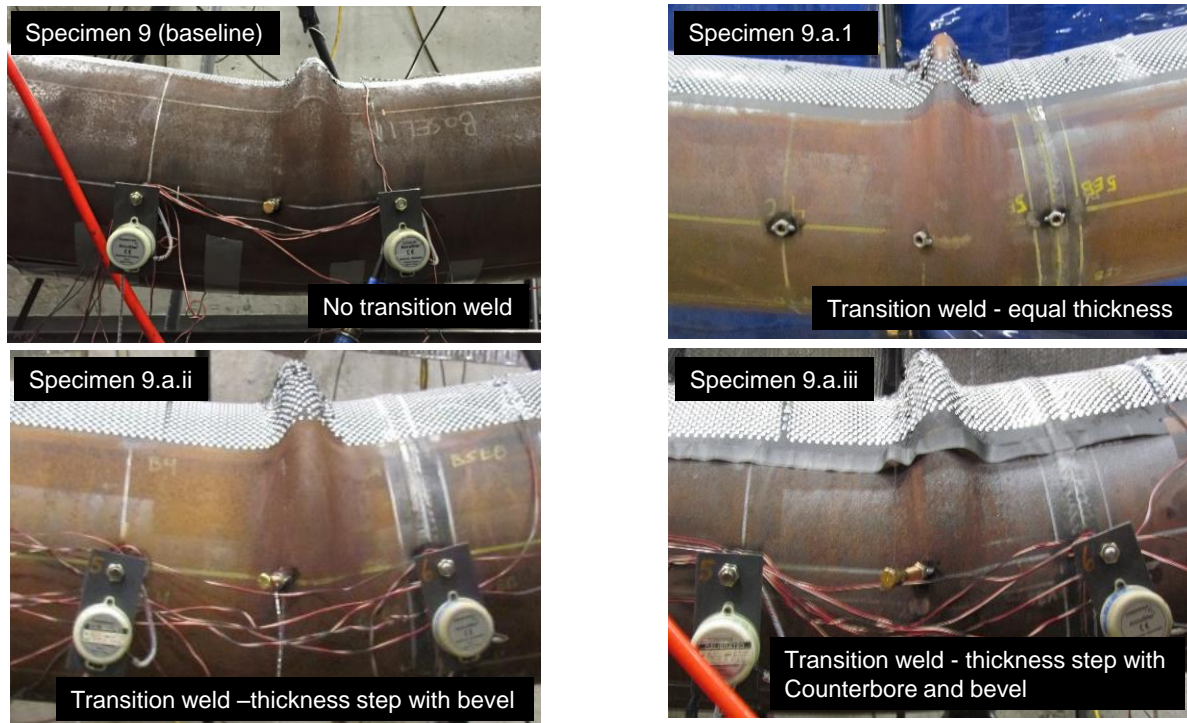


Figure 3-16 Test End Points for Task 9.a Specimens Containing Girth-welded Thickness Transitions in Comparison to the Baseline Specimen without Transitions

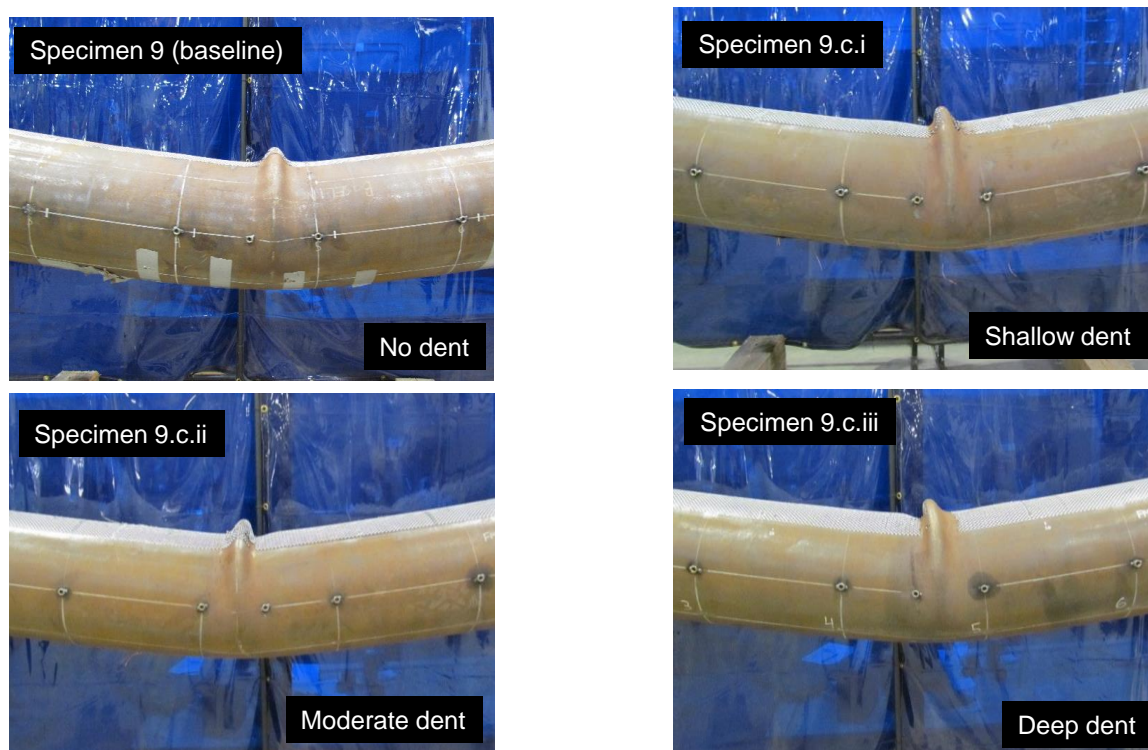


Figure 3-17 Test End Points for Task 9.c Specimens Containing Dents in Comparison to the Baseline Specimen without a Dent

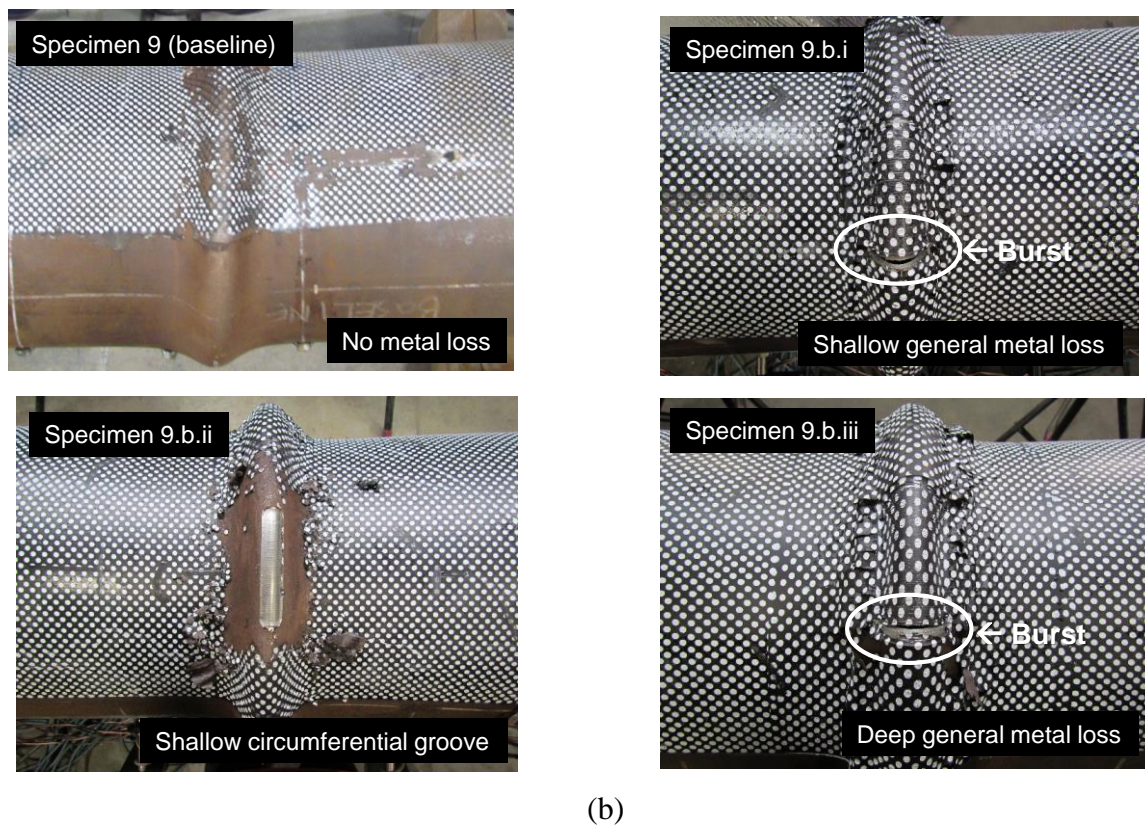
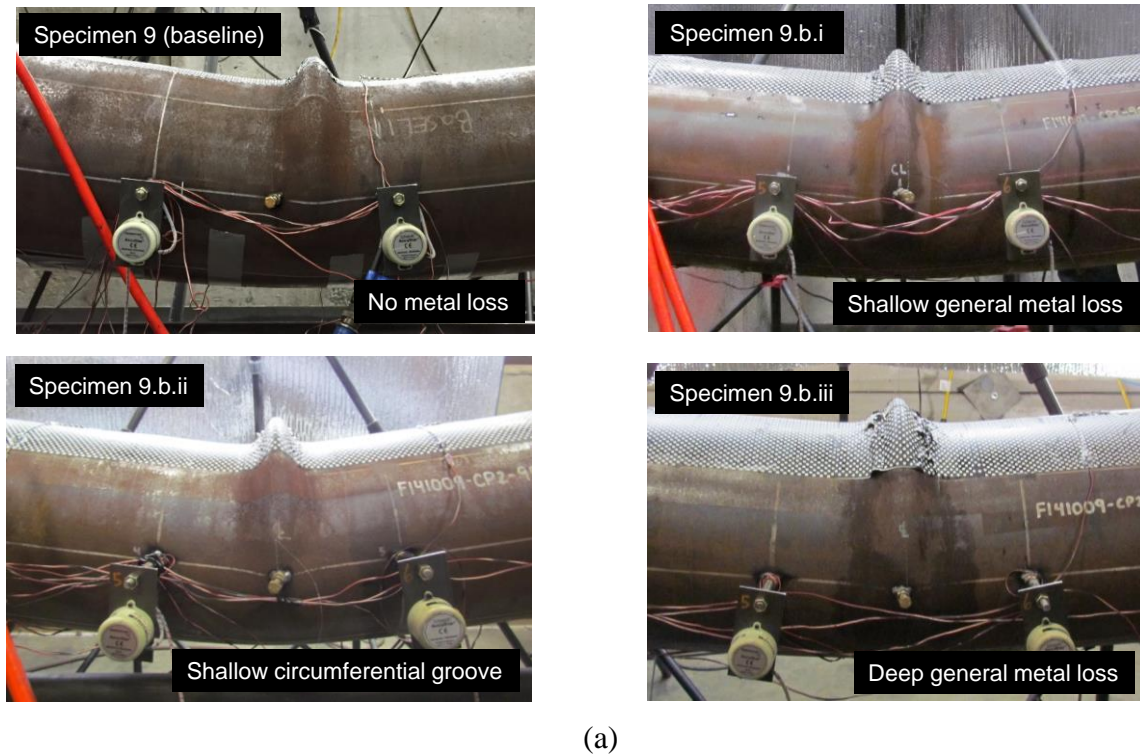


Figure 3-18 Test End Points for Task 9.b Specimens Containing Metal Loss in Comparison to the Baseline Specimen without Metal Loss (a) Side view and (b) Top view

3.3 Full-Scale Bending-Burst Tests of Pipes with Corrosion Anomalies (Task 10)

The objective of the Task 10 tests was to evaluate the effect of high longitudinal compressive strain on the burst capacity of line pipe containing metal loss corrosion.

3.3.1 Specimen Configuration

Four test specimens were cold-cut at C-FER from a single joint of NPS 12 pipe into sections approximately 2,855 mm (112 inches) in length (see Figure 3-1). The source pipe was 324 mm OD x 7.14 mm WT (12.75 x 0.281 inch), Grade X70, ERW line pipe (see Table 2-1).

Specimens were numbered and measured, after which they were sent for fabrication (i.e., end fixture installation). The Task 10 specimens were welded to short, thick-walled end sections, which in turn were welded to flat-plate end caps (see Figure 3-2 for general configuration).

Three of the four specimens in this test series were subject to additional fabrication to simulate the presence of metal loss corrosion. A baseline specimen, without metal loss, was also prepared to provide a basis for quantifying the relative change in burst capacity attributable to the anomalies and pre-strain introduced in the other specimens. Table 3-7 summarizes the four specimens fabricated for testing.

Table 3-7 Specimens for Task 10 Tests

Specimen Identification	C-FER Specimen Number	Anomaly	Loading Type
10 (baseline)	X70-ERW-3-10bl	None	Pressure
10.a	X70-ERW-3-10a	Corrosion Feature	Pressure
10.b	X70-ERW-3-10b	Corrosion Feature	Bend & Pressure
10.c	X70-ERW-3-10c	Corrosion Feature	Bend & Pressure

3.3.2 Specimen Anomalies

The metal loss associated with corrosion was simulated by machining material from the outer pipe surface at specimen mid-length at a circumferential position on the pipe that would later correspond to the location of the extreme compression fiber under bending load. Feature dimensions are detailed in Table 3-8 and an example of a metal loss feature is shown in Figure 3-6.

Table 3-8 As Installed Metal Loss Feature Dimensions

Specimen Identification	Anomaly Description	Feature Dimensions (mm)		
		Length	Width	Depth
10.a	Axial Groove	65.0	16.0	2.74
10.b	Axial Groove	66.0	16.0	2.72
10.c	General Metal Loss	65.0	65.0	2.62

3.3.3 Specimen Grid Layout and Measurements

Prior to end fixture attachment and testing, specimens were grid marked and measured according to the same marking layout used for the Task 9 specimens (see Figure 3-9). As for the Task 9 specimens, the specimen measurements recorded included: length, diameter, ovality and wall thickness (see Section 3.2.3 for details). Selected measurements are summarized in Table 3-9. The full set of measurements can be found in Appendix E.

Table 3-9 Selected Task 10 Specimen Geometry Measurements

Specimen Identification	Average OD mm (in)	Average Wall Thickness mm (in)	Ovality (%)		
			Station Positions		
			4	5	6
10 (baseline)	324.91 (13)	7.14 (0.281)	0.10	0.06	0.13
10.a	324.95 (13)	7.15 (0.281)	0.09	0.13	0.13
10.b	324.97 (13)	7.12 (0.280)	0.13	0.14	0.12
10.c	324.94 (13)	7.11 (0.279)	0.12	0.18	0.21

3.3.4 Test Setup

The Task 10 tests were performed in the same custom-designed bend frame used for the Task 9 tests (see Figure 3-10). The instrumentation employed for the Task 10 tests was identical to that used for testing in Task 9 (see Section 3.2.4.1). The deployment of the VIC system for the Task 10 tests was identical to that used for testing in Task 9 (see Section 3.2.4.2).

3.3.5 Test Procedure

Specimens were installed in the test frame and split-ring assemblies were clamped to each end of the test section (inboard of the thickened end sections) to prevent buckle formation near the specimen ends (see Figure 3-2). Instrumentation was attached and specimens were filled with water at ambient temperature. The two specimens subjected to internal pressure with no axial pre-strain (Specimens 10 and 10.a) were pressurized at approximately 1.4 MPa/min (200 psi/min) until loss of containment by burst failure occurred. The two specimens subjected to internal pressure and axial pre-strain (Specimens 10.b and 10.c) were similarly pressurized to burst, but prior to that, they were first pressurized to a prescribed pressure of 15.3 MPa (2,222 psi) and then bent until the target axial pre-strain level was obtained. (The 15.3 MPa pressure was chosen to produce a nominal hoop stress level equal to 72% of SMYS).

A more detailed description of the loading sequence for Specimens 10.b and 10.c is as follows:

1. Specimens were pressurized at approximately 1.4 MPa/min (200 psi/min) until the prescribed pressure level was achieved while counteracting the end cap forces by applying a net compressive axial force with the bending control system. During the initial pressurization step, the total bending moment on the specimen was kept near zero.
2. Bending moment was then progressively applied by stroking the top strut at a fixed rate of 5.1 mm/min (0.2 in/min), while simultaneously adjusting the load on the

- bottom strut using a LabVIEW™ based control program to compensated for end cap forces and increment the bending load.
3. Bending was continued until a target axial compressive bending strain level of approximately 2.3% (over a 2D gauge length centered on the buckle region) was achieved.
 4. Displacement on all three rams on the bend frame was then held constant and the specimen was further pressurized at a rate of 1.4 MPa/min (200 psi/min) until burst failure occurred.

3.3.6 Test Results

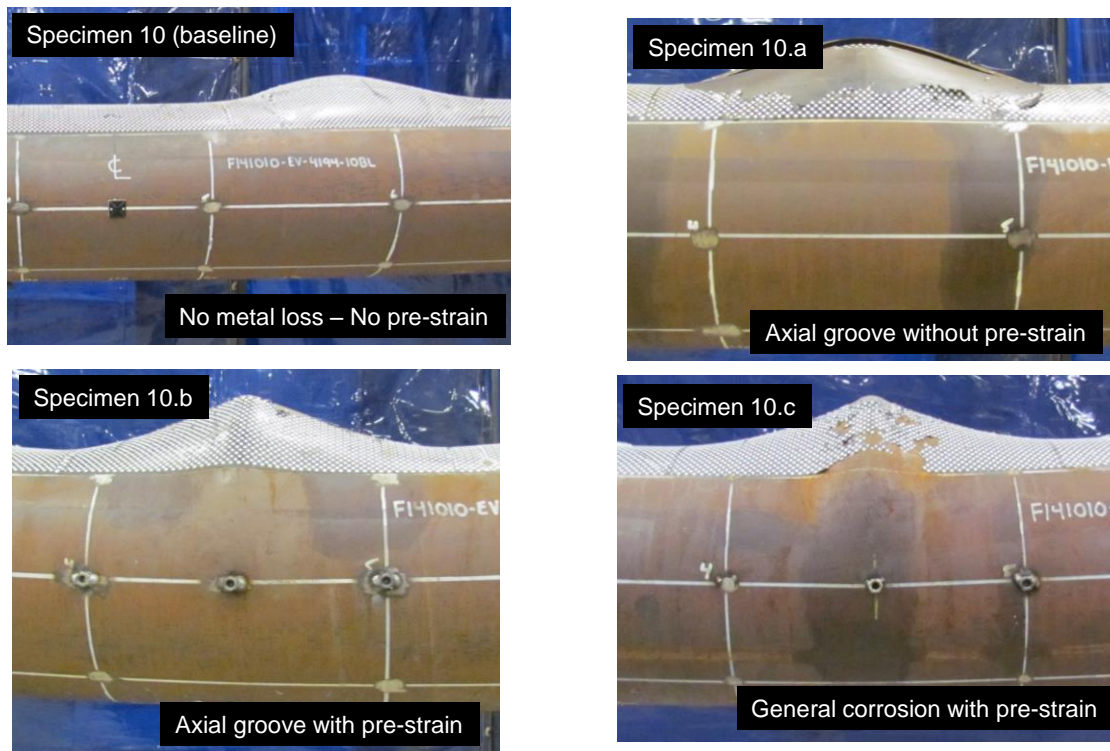
The key results for the Task 10 tests include the average compressive pre-strain prior to final pressurization to burst and the burst pressure. As for the Task 9 tests, the reported average compressive strains were calculated two ways: first using tension-side strain gauges and clinometers, referred to 1D Strain (DI), and second, using the visual image correlation data from images of the compression face, referred as 1D and 2D Strain (VIC).

Selected results for the Task 10 tests are summarized in Table 3-10 together with a description of the specimen condition at the end of each test. Complete results for each test are included in Appendix E.

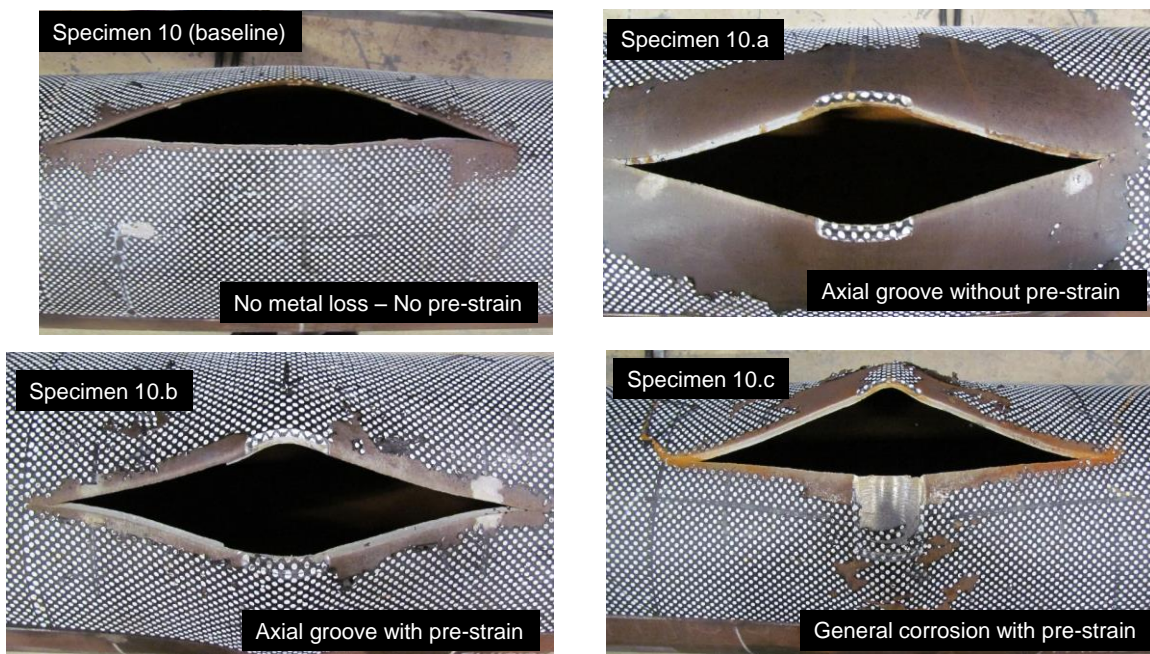
The test end points for each Task 10 specimen and the leak locations relative to the metal loss features, where applicable, are shown in Figure 3-19. The detailed analyses and discussions of the Task 10 tests are given in Sections 5.4.2 and 5.4.3.

Table 3-10 Summary of Results for Task 10 Tests

Specimen Identification	Anomaly	1D Pre-strain (DI) (%ε)	1D Pre-strain (VIC) (%ε)	2D Pre-strain (VIC) (%ε)	Burst Pressure (MPa)	Test End Condition
10 (baseline)	None	NA	NA	NA	30.2	Pipe body burst with longitudinal fracture
10.a	Axial Groove (0.20D x 0.05D x 0.38t)	NA	NA	NA	27.3	Pipe body burst with longitudinal fracture intersecting corrosion feature
10.b	Axial Groove (0.20D x 0.05D x 0.38t)	-3.2	-3.8	-2.4	25.9	Pipe burst with longitudinal fracture intersecting corrosion feature
10.c	General Metal Loss (0.20D x 0.20 D x 0.37t)	-3.7	-4.4	-2.4	27.4	Pipe burst with longitudinal fracture intersecting corrosion feature



(a)



(b)

Figure 3-19 Test End Points for Task 10 Specimens Containing Metal Loss in Comparison to the Baseline Specimen without Metal Loss: (a) Side view and (b) Top view

3.4 Full-Scale Compression-Burst Tests of Pipes with Wrinkles (Task 11)

The purpose of the Task-11 tests was to experimentally evaluate the burst pressure of the line pipes with compression-induced wrinkles/buckles and the impact of high axial compressive pre-strain on burst pressure.

3.4.1 Specimen Configuration

Specimens were obtained from girth welded sections of NPS 24 pipe; more specifically, 610 mm OD x 12.7 mm WT (24 x 0.5 inch), Grade X80, DSAW line pipe (see Table 2-1).

Pipe preparation involved cutting specimens to a length of approximately 1,830 mm (72 inch) and welding flat-plate end caps to each end to provide contain pressure containment and facilitate the application of concentric axial load to the specimen. Specimens were cut from the girth welded source pipe such that a weld was located at specimen mid-length. Table 3-11 summarizes the three specimens fabricated for testing.

Table 3-11 Test Specimens for Task 10

Specimen Identification	C-FER Specimen Number	Anomaly	Loading Type
11.a	X80-DSAW-M5a	None	Pressure without axial pre-strain
11.b	X80-DSAW -M5b	None	Pressure with moderate axial pre-strain
11.c	X80-DSAW -M5c	None	Pressure with high axial pre-strain

3.4.2 Specimen Grid Layout and Measurements

Pre-test geometry measurements were taken of each test specimen in accordance with the marking layout shown in Figure 3-20. Measurements included specimen length, circumference at each end, diameter at each axial station along the length of the specimen, and wall thickness at each grid intersection point.

Selected parameters are summarized in Table 3-12. The full set of measurements can be found in Appendix F.

Table 3-12 Selected Task 11 Specimen Geometry Measurements

Specimen Identification	Average Diameter mm (in)	Average Wall Thickness mm (in)
11.a	610.4 (24)	12.94 (0.509)
11.b	610.4 (24)	13.07 (0.514)
11.c	610.4 (24)	12.97 (0.510)

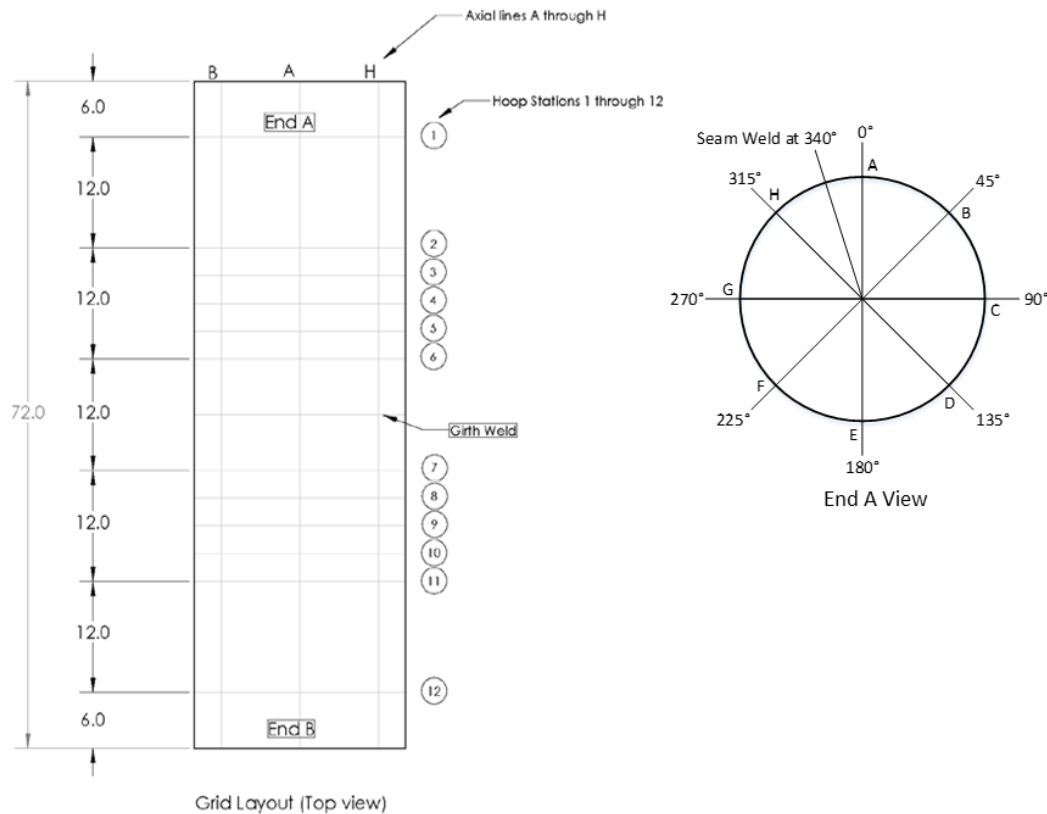


Figure 3-20 Pipe Marking Scheme for Task 11 Tests

3.4.3 Test Setup

The tests were performed in C-FER's Universal Testing System (UTS), a servo-hydraulically controlled load frame capable of generating 15 MN (3.4 million lb) of tensile and compressive load. The test configuration, shown in Figure 3-21, enabled control of the axial separation of the specimen end caps prior to and during pressurization. This test configuration, in combination with specimen axial loading via the UTS in displacement-controlled mode, facilitated progressive compensation for the specimen end cap forces induced by internal pressure and the ability to induce a prescribed level of axial compressive pre-strain prior to final specimen loading to failure under increasing internal pressure.

3.4.4 Instrumentation

The instrumentation employed for testing is summarized below (see also Figure 3-22).

- For local strain measurement:
 - six uniaxial strain gauges (2, 3, 4, 6, 7, 8) were used to monitor longitudinal (axial) pipe strain; and
 - two biaxial strain gauges (1, 5) were used to monitor longitudinal strain and confirm prescribed circumferential (hoop) strains.
- For internal pressure measurement one calibrated pressure transducer was plumbed to a port on the top end-cap of the specimen.

- For displacement measurement:
 - six displacement transducers were used to measure specimen length change, two over the full 2D gauge length of the specimen and four in pairs over the upper and lower specimen 1D half-lengths²; and
 - two VIC 3D camera systems (four cameras total) were used to map the strain on opposing sides of the specimen.
- For measurement of the axial load applied to the test specimen, the calibrated UTS load cell was used.

Instrument readings were recorded at a sampling rate of 4 Hz using a computer-based digital data acquisition system (DAS) programmed in LabVIEWTM. Data was acquired continuously throughout each test from all instruments, with the exception of the strain mapping camera system and digital cameras. Digital images of the specimens were taken at predetermined intervals during each test using both sets of cameras. The speckle pattern painted onto the specimen surface to facilitate strain field mapping using the VIC system is clearly visible in Figure 3-21.

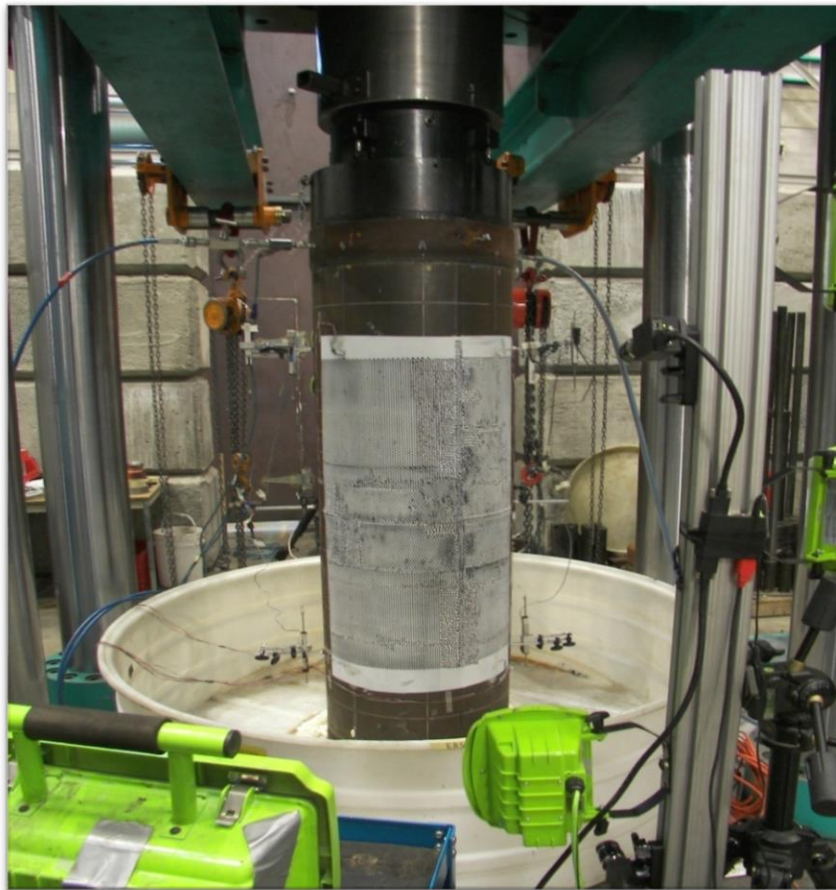


Figure 3-21 Test Setup for Task 11 Tests

² Average axial strains over 2D and 1D gauge lengths were obtained by averaging the strains calculated from pairs of displacement transducer spaced 180 degrees apart with nominal gauge lengths of 2D and 1D, respectively.

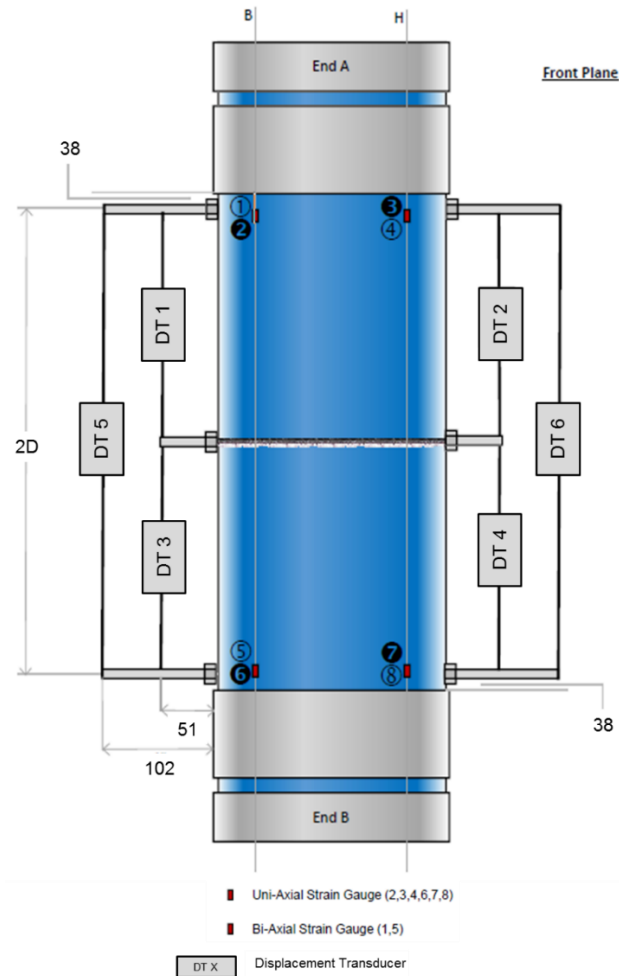


Figure 3-22 Instrumentation Layout for Task 11 Tests

3.4.5 Test Procedure

Specimens were installed in the UTS and split-ring collars were clamped to each end to prevent buckle formation in those areas (see Figure 3-23). Specimens were then instrumented and filled with water at ambient temperature. Prior to testing specimens were also subject to low levels of axial compressive load to verify specimen positioning (i.e., to ensure the line of action of the external axial load was concentric with specimen centroidal axis).

The loading sequence for each specimen in this test series was as follows:

- **Specimen 11.a** – Internal pressure was applied at a rate of between 1.4 and 2.8 MPa/min (200 to 400 psi/min). As pressure was increased, the total axial deformation of the specimen was monitored and the external applied axial load was adjusted to effectively maintain zero axial deformation. Pressure increase was continued until loss of containment occurred.
- **Specimen 11.b** – Internal pressure was applied at the same rate as for Specimen 11.a with the specimen ends being fully restrained from axial movement. The pressure was increased until a pressure level of 16.5 MPa (2,400 psi) was reached, which is consistent with a nominal hoop stress level in the pipe wall of 72% of SMYS. With pressure

maintained at the reference level, the specimen was then subjected to progressive axial shortening until the total shortening was approximately 26 mm (1 inch), which corresponded to an axial compressive strain over a 1D gauge length containing the buckled region of approximately 2.3%. At this stage, further axial deformation was restrained and the internal pressure was gradually increased until loss of containment occurred.

- **Specimen 11.c** – The loading sequence for this specimen was identical to that of Specimen 11.b, except the imposed axial displacement, following the attainment of the reference pressure but prior to final pressurization to burst, was approximately 220 mm (8.5 inches), which corresponded to an average axial compressive strain over a 1D gauge length containing the buckled region of approximately 34%.

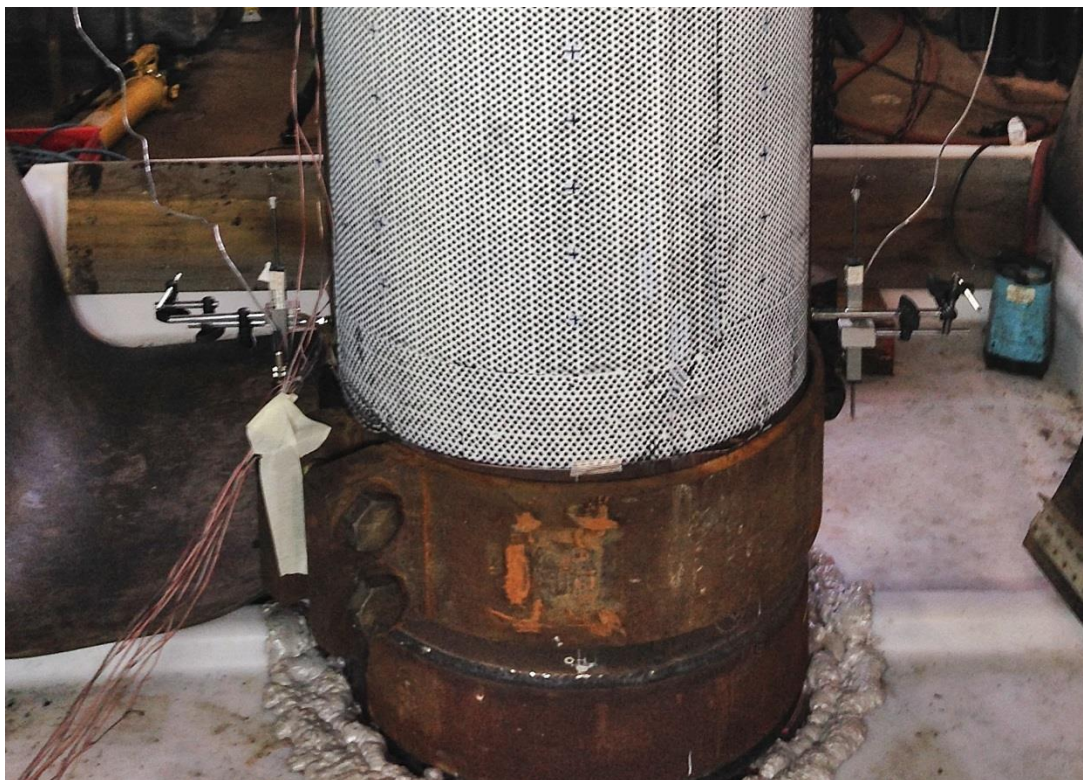


Figure 3-23 Collars to Prevent Buckling Near the End Caps

3.4.6 Test Results

The key results for the Task 11 tests include the average compressive pre-strain prior to final pressurization to burst, the burst pressure, the net axial load at burst and the maximum hoop strain at burst. Selected test results are summarized in Table 3-13 together with a description of the specimen condition at the end of each test. Complete results for each test are included in Appendix F. The test end points for each Task 11 specimen, indicating the burst location relative to the buckle induced by axial pre-strain (where applicable), are shown in Figure 3-24. The detailed analyses and discussions of the Task 11 tests are given in Sections 7.2 to 7.4.

Table 3-13 Summary of Test Results for Task 11

Specimen Identification	1D Axial Pre-strain (DI) *	2D Axial Pre-strain (DI)	Burst Pressure	Net Axial Load at Burst	Maximum Hoop Strain at Burst	Test End Condition
	Top/Bottom (% ϵ)	(% ϵ)	(MPa)	(kN)	Top/Bottom (% ϵ)	
11.a	0	0	31.2	4379	1.4 / 6.4	Pipe body burst with longitudinal fracture in bottom pup
11.b	-2.26 / -0.50	-1.11	31.9	3743	7.7 / 1.4	Pipe body burst with longitudinal fracture in top pup containing pre-strain buckle
11.c	-0.27/-34.4	-17.2	28.2	-2096	3.3 / 31.4 (19.3 at burst location)	Pipe body burst with longitudinal fracture in bottom pup containing primary pre-strain buckle (fracture occurred in pipe body below pre-strain buckle)

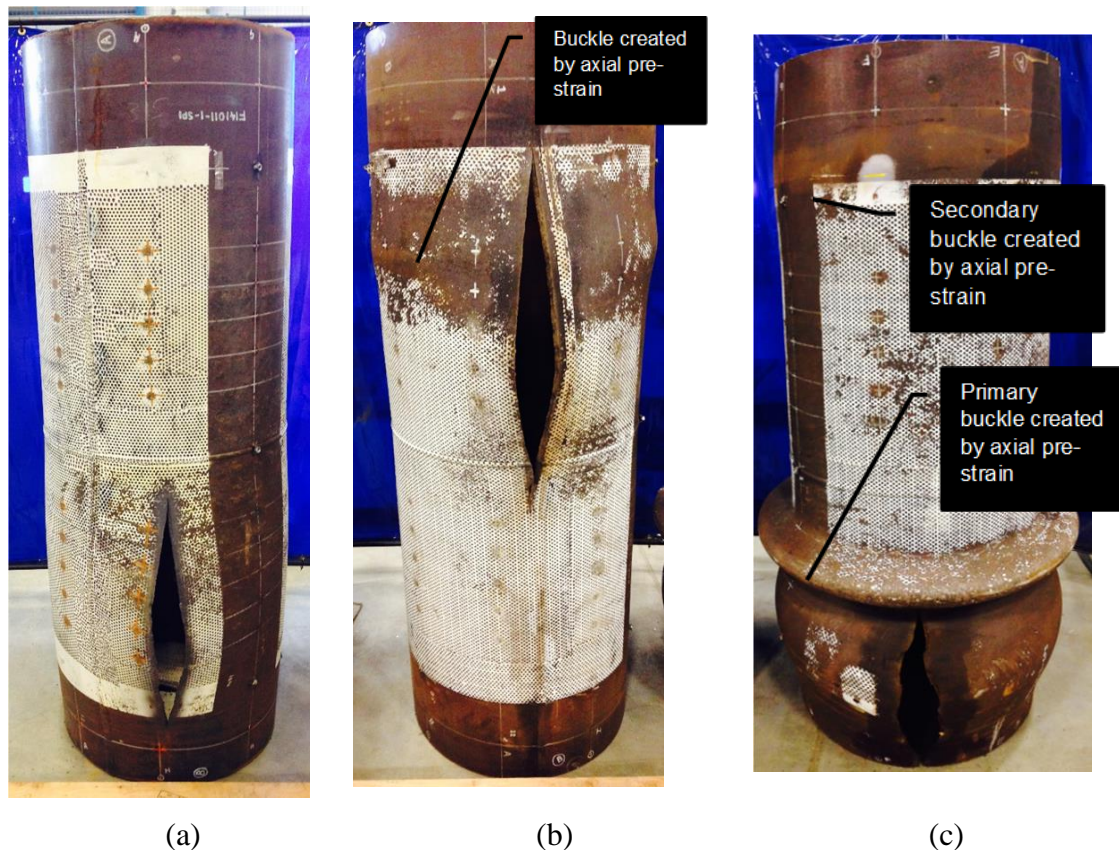


Figure 3-24 Test End Condition for Task 10 Specimens with Axial Pre-strain Compared to Reference Specimen without Pre-strain: (a) Specimen 11a, no axial pre-strain; (b) Specimen 11b, moderate axial pre-strain; (c) Specimen 11c, high axial pre-strain

3.5 Full-Scale Tension Tests of Pipes with Corrosion Anomalies (Task 12)

The purpose of the Task 12 tests was to evaluate how the tensile strain capacity of the line pipes is affected by geometric discontinuities associated with metal loss from corrosion.

3.5.1 Specimen Configuration

Four test specimens were cold-cut at C-FER from a single joint of NPS 12 pipe into test sections approximately 1,780 mm (70 inches) in length. The source pipe was 324 mm OD x 7.14 mm WT (12.75 x 0.281inch), Grade X70, ERW line pipe material (see Table 2-1).

Specimen fabrication involved welding flat-plate end caps to each end to provide pressure containment and facilitate the application of concentric axial tensile load to the specimen. Three of the four specimens in this test series were subjected to additional fabrication to simulate the presence of metal loss corrosion. A baseline specimen, without metal loss, was also prepared to provide a basis for quantifying the relative change in strain capacity attributable to the anomalies introduced in the other specimens. Table 3-14 summarizes the four specimens fabricated for testing.

Table 3-14 Test Specimens for Task 12

Specimen Identification	C-FER Specimen Number	Anomaly	Loading Type*
12 (baseline)	X70-ERW-3-12bl	None	Axial Tension
12.a	X70-ERW-3-12a	Corrosion Feature	Axial Tension
12.b	X70-ERW-3-12b	Corrosion Feature	Axial Tension
12.c	X70-ERW-3-12c	Corrosion Feature	Axial Tension

* Loading in addition to internal pressure maintained during axial extension.

3.5.2 Specimen Anomalies

The metal loss associated with corrosion was simulated by machining material from the outer pipe surface at specimen mid-length. Feature dimensions are detailed in Table 3-15 and photos of each feature prior to testing, after application of the speckle pattern required for optical strain measurement, are shown in Figure 3-25.

Table 3-15 As Installed Metal Loss Feature Dimensions

Specimen Identification	Anomaly Description	Feature Dimensions (mm)		
		Length	Width	Depth
12 (baseline)	None	n/a	n/a	n/a
12.a	Shallow General Metal Loss	64.8	62.7	1.70
12.b	Shallow Circumferential Groove	15.7	63.0	1.55
12.c	Deep General Metal Loss	63.5	64.5	2.67

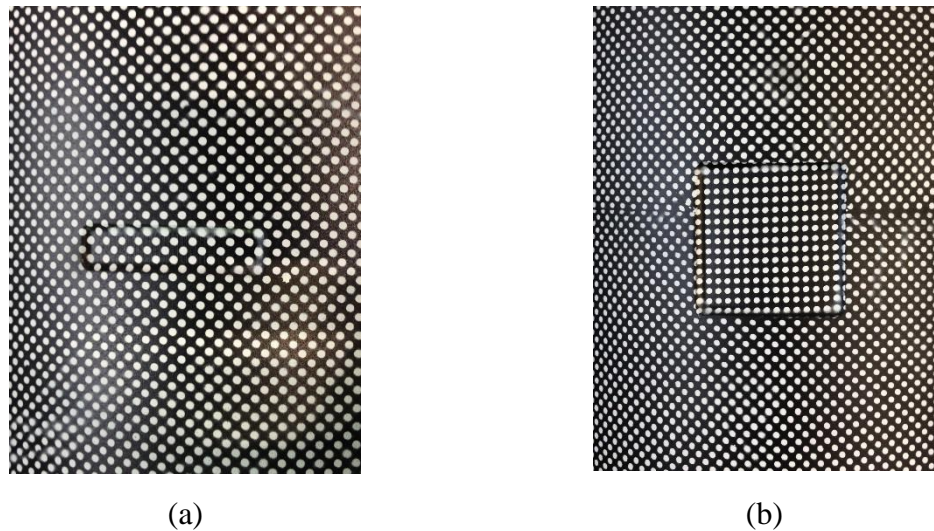


Figure 3-25 Metal Loss Features for Selected Task 12 Tests: (a) Circumferential groove – Specimen 12.b and (b) General Metal Loss – Specimen 12.c

3.5.3 Specimen Grid Layout and Measurements

Prior to end fixture attachment and testing, specimens were grid marked and measured in accordance with the marking layout shown in Figure 3-26. Measurements included specimen length, pipe diameter and circumference at each of the axial stations spaced 324 mm (12.75 inches) apart along the length of each specimen, and wall thickness at each grid intersection point.

Selected specimen measurements are summarized in Table 3-16. The full set of measurements can be found in Appendix G.

Table 3-16 Selected Task 12 Specimen Geometry Measurements

Specimen Identification	Average Diameter mm (in)	Average Wall Thickness mm (in)
12 (baseline)	324.96 (12.79)	7.11 (0.279)
12.a	324.99 (12.79)	7.20 (0.283)
12.b	325.05 (12.80)	7.16 (0.281)
12.c	325.02 (12.80)	7.13 (0.280)

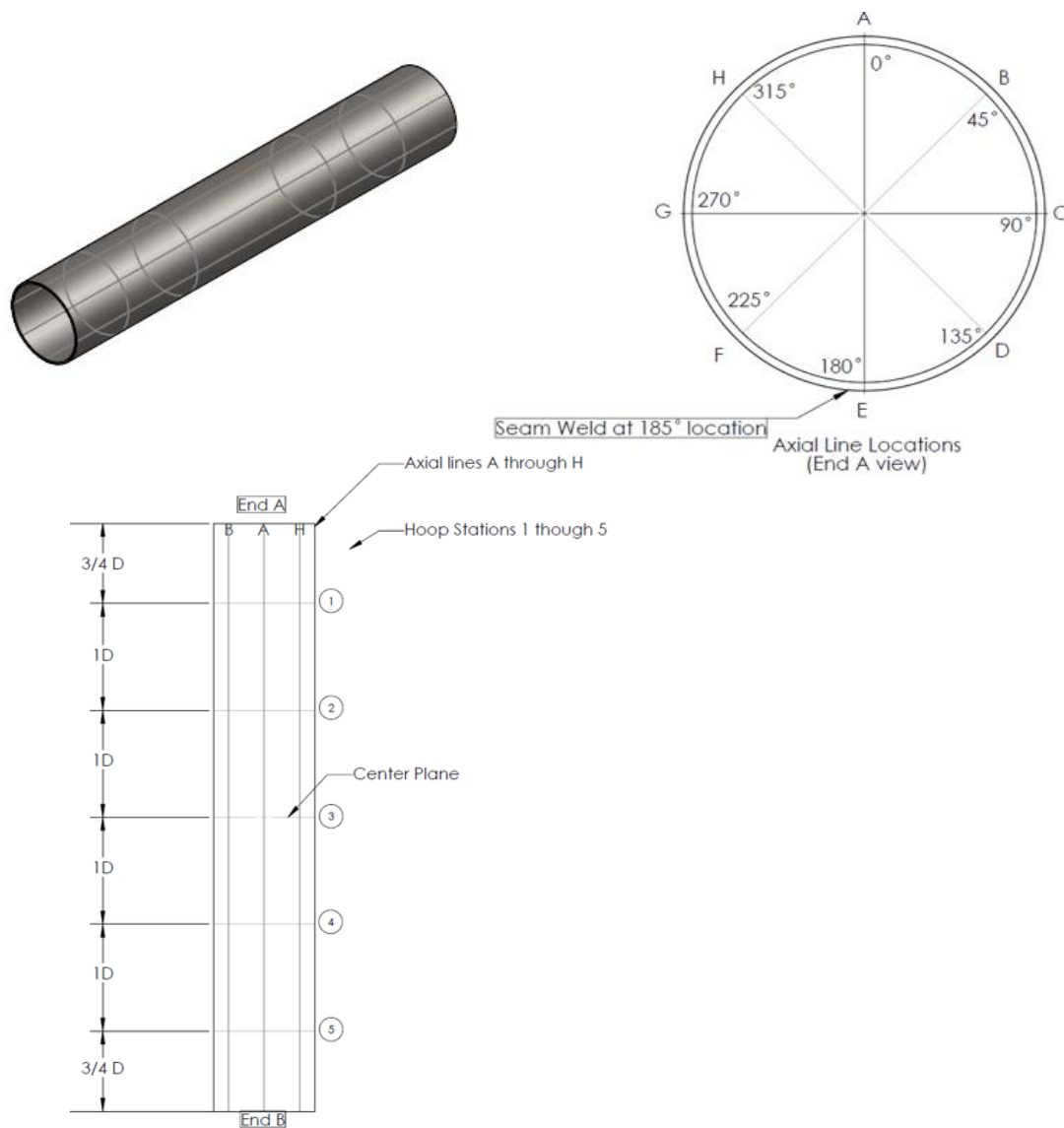


Figure 3-26 Task 12 Specimen Marking Scheme

3.5.4 Test Setup

The tests were performed in C-FER's Universal Testing System (UTS), a servo-hydraulically controlled load frame capable of generating 15 MN (3.4 million lb) of tensile and compressive load. The test configuration, shown in Figure 3-27, enabled control of the axial separation of the specimen end caps prior to and during pressurization. This test configuration, in combination with specimen axial loading via the UTS in displacement-controlled mode and continuous internal pressure monitoring and control, facilitated the inducement of a prescribed rate of axial tensile elongation while maintaining a prescribed internal pressure.



Figure 3-27 Setup of Task 12 Tests in C-FER's TTS Load Frame

3.5.5 Instrumentation

The instrumentation employed for testing is summarized below (see also Figure 3-28).

- For local strain measurement:
 - four uniaxial strain gauges (in pairs at two locations along the specimen length) were used to monitor longitudinal (axial) pipe strain; and
 - one biaxial strain gauge (at mid-length) was used to provide supplemental longitudinal strain data and monitor circumferential (hoop) strain.
- For displacement measurement:
 - six displacement transducers (in pairs at three locations along the specimen length) were used to measure specimen length change over prescribed 1D and 2D gauges

- length³, and
- one VIC 3D camera system (two cameras) was used to map the strain on the side of the specimen containing metal loss.
 - For measurement of internal pressure in the test specimen one calibrated pressure transducer was plumbed to a port on the bottom end-cap of the specimen.
 - For measurement of the axial load applied to the test specimen, the calibrated UTS load cell was used.

Instrument readings were recorded at a sampling rate of 4 Hz using a computer-based digital data acquisition system (DAS) programmed in LabVIEW™. Data was acquired continuously throughout each test from all instruments, except for the strain mapping camera system and digital cameras. Digital images of the specimens were taken at predetermined intervals during each test. The speckle pattern painted onto the specimen surface to facilitate strain field mapping using the VID system is clearly visible in Figure 3-27.

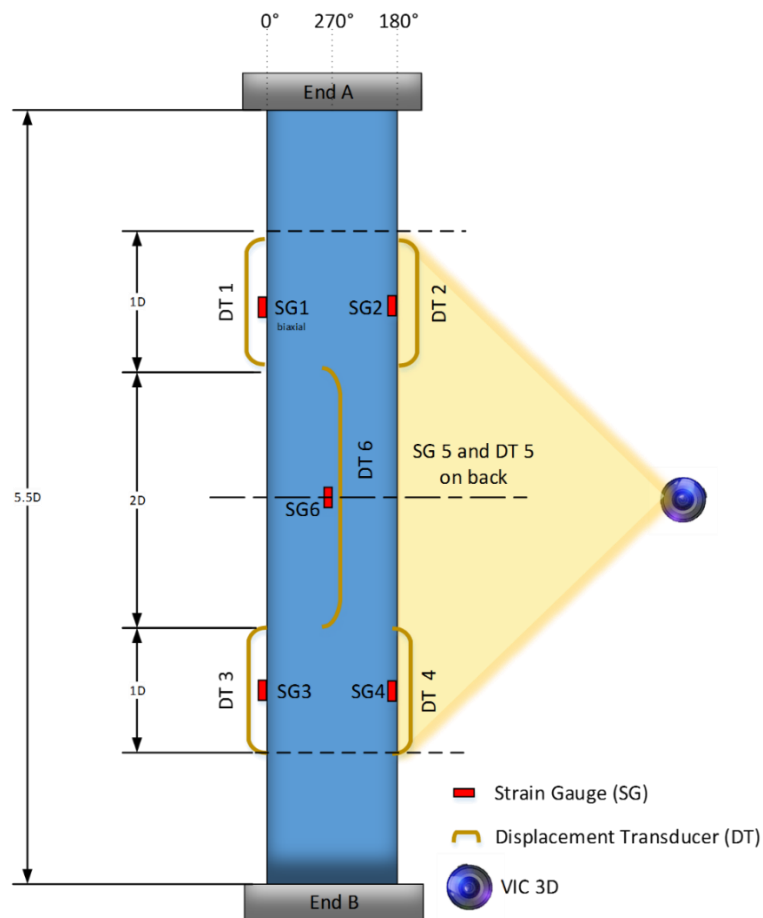


Figure 3-28 Instrumentation Layout for Task 12 Tests

³ Average axial strains over 2D and 1D gauge lengths were obtained by averaging the strains calculated from pairs of displacement transducer spaced 180 degrees apart with nominal gauge lengths of 2D and 1D, respectively.

3.5.6 Test Procedure

Specimens were positioned in the UTS and split-ring collars were used to connect the specimen end plates to the UTS loading fixtures. Specimens were then instrumented and filled with water at ambient temperature (see Figure 3-23). Prior to testing, specimens were also subject to low levels of axial tensile load to verify specimen positioning (i.e., to ensure the line of action of the external axial load was concentric with specimen centroidal axis).

The loading sequence for each specimen in this test series was as follow:

- Internal pressure was applied at a rate of approximately 2.8 MPa/min (400 psi/min) until an internal pressure of 15.3 MPa (2,220 psi) was achieved, which is consistent with a nominal hoop stress level in the pipe wall of 72% of SMYS.
- With pressure maintained at this reference level, the specimen was elongated by separating the end fixtures at a rate of 1.6 mm/min, which corresponds to an axial strain rate of approximately 1.5×10^{-5} per second.
- Axial extension was continued until specimen rupture occurred.

3.5.7 Test Results

The key results for the Task 12 tests are the average axial tensile strain levels at specimen rupture and the maximum net tensile load. For these tests, the reported strains include the average axial strains in the pipe body well removed from the metal loss locations (i.e. the remote axial strain) and the average axial strain in the pipe body in the region containing the metal loss (i.e., the bridging strain). Remotes strains over a 1D gauge length and bridging strains over a 2D length centered on the metal loss feature were determined using discrete instruments and the VIC system.

Selected test results are summarized in Table 3-17 together with a description of the specimen condition at the end of each test. Complete results for each test are included in Appendix G. The test end points for each Task 12 specimen, indicating the rupture location relative to the metal loss feature (where applicable), are shown in Figure 3-29. The detailed analyses and discussions of the Task 12 tests are given in Section 5.2.2.

Table 3-17 Summary of Test Results for Task 12

Specimen Identification	Maximum Net Tensile Load	Remote 1D Axial Strain (DI)	Remote 1D Axial Strain (VIC)	Bridging 2D Axial Strain (DI)	Bridging 2D Axial Strain (VIC)	Test End Condition
	(kN)	Top/Bottom (% ϵ)	Top/Bottom (% ϵ)	(% ϵ)	(% ϵ)	
12 (baseline)	4,769	6.08 / 7.18	6.68 / 7.30	7.56	7.66	Tensile rupture of pipe body
12.a	4,671	2.49 / 2.83	2.39 / 2.67	2.96	2.93	Tensile rupture of pipe body intersecting metal loss feature
12.b	4,613	1.36 / 1.05	1.26 / 1.04	1.37	1.40	
12.c	4,564	1.02 / 1.05	0.86 / 0.85	1.68	1.62	

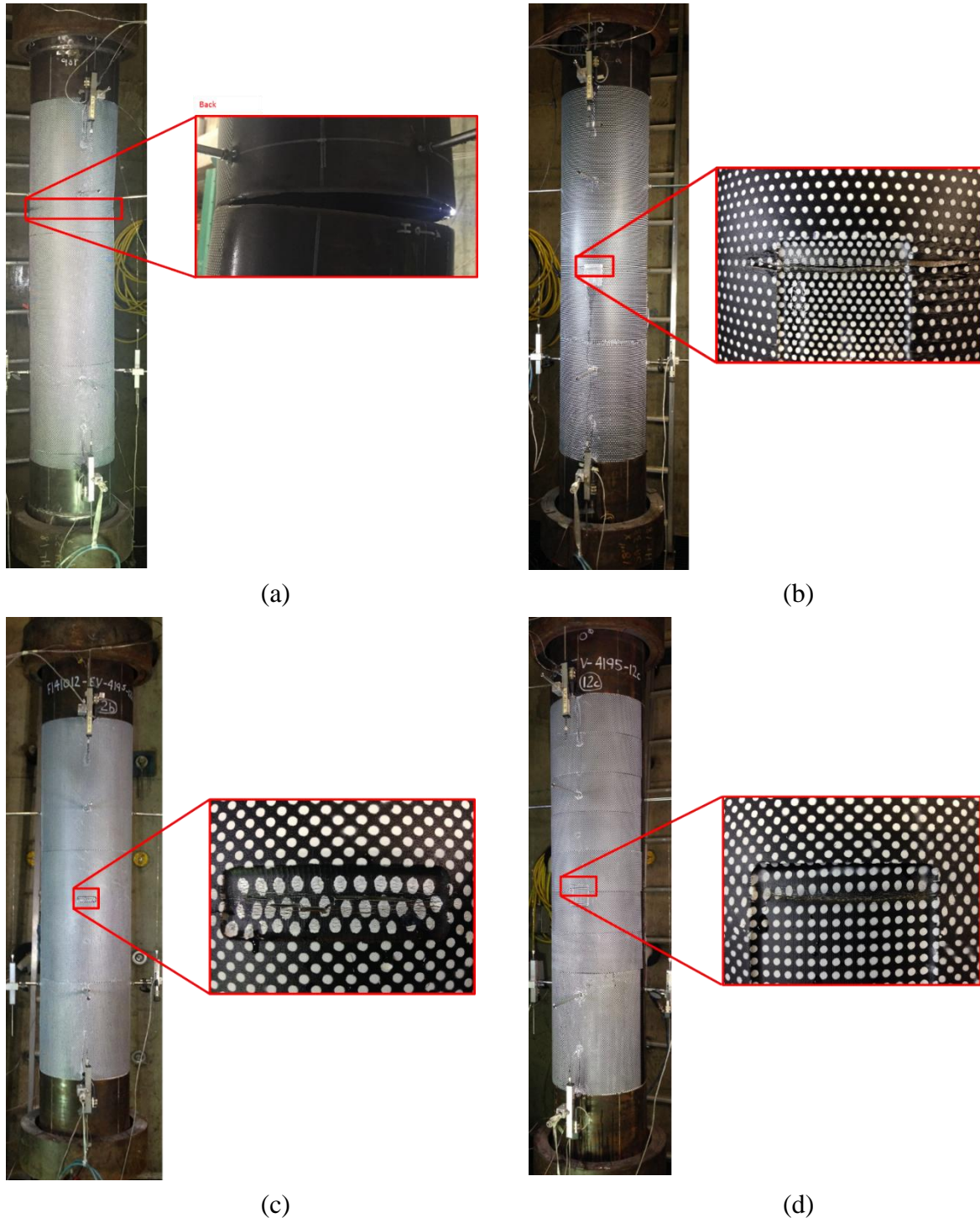


Figure 3-29 Test End Condition for Task 12 Specimens with and without Metal Loss: (a) Specimen 12 Baseline; (b) Specimen 12.a; (c) Specimen 12.b; (d) Specimen 12.c

3.6 Curved Wide Plate Tension Tests of Transition Welds (Task 13)

3.6.1 Overview of Testing Setup

The curved wide plate (CWP) tests were conducted on two welds; the first on a 16-mm wall thickness (WT) API-5L X70 PSL2 pipe joint (Weld-1) and the second on a transition weld between 16 mm and 19 mm wall thickness API-5L X70 PSL2 pipes. The 19 mm WT pipe was internally counterbored for 100 mm (~ 4 in), to an ID closely matching the 16 mm WT pipe. The bevel angle at the end of the counterbore was 15 degrees. The counterbore resulted in a slightly thinner wall thickness than the mating 16 mm WT pipe, where the average wall thickness remaining in the counterbore was 15.69 mm and the average wall thickness of the 16 mm WT pipe was 16.89 mm.

Four specimens were taken from each welded section, the details of the pipe sectioning, specimen machining and testing procedures are provided in detail in Appendix C. Each of the specimens was notched in either the weld along the weld center-line (WCL) or the adjacent heat affected zone (HAZ). The prepared specimens were tension tested in a 4.45 MN (1 Mlbf) capacity servo-hydraulic test frame while measuring the applied force, remote strain, cross-weld strain and the crack mouth opening displacement. Each specimen was tested at ambient room temperature.

The test matrix presented in the next section was used to determine the tensile strain capacity of the flawed welds under tensile loading. The data were used to validate the tensile strain capacity models developed in Section 4.2.

3.6.2 Testing Matrix

The CWP test matrix presented in Table 3-18 includes two welds, four specimens per weld, notch location and geometry as well as the coincident specimen from the other pipe. The matrix had only three variables, the weld, the clock position of the specimen (See Appendix B) and the notch location. The matrix was designed to have a mixture of duplicate and unique data sets. For example, 233 CWP-1 and 236 CWP-4 are close in clock position but not exact so they represent unique data sets, whereas 233 CWP-4 and 236 CWP-1 have the same clock position with different notch locations and represent unique data sets. Specimens 233 CWP-2, 233 CWP-3 and 236 CWP-3, 236 CWP-2 are respectively coincident and with the same notch locations allowing a duplication or direct comparison of data sets.

Table 3-18 Curved Wide Plate (CWP) Test Matrix
914 mm (36 in) Outside Diameter – API-5L X70

Weld	Specimen ID	Notch Location	Notch Depth (mm)	Notch Width (mm)	a_0/W	Coincident with CWP
16 mm – 19 mm (0.625 in – 0.750 in) (Weld-2)	233-CWP-1	HAZ	5	30	0.32	None
	233-CWP-2	WCL	5	30	0.32	236 CWP-3
	233-CWP-3	HAZ	5	30	0.32	236 CWP-2
	233-CWP-4	WCL	5	30	0.32	236 CWP-1
16 mm – 16 mm (0.625 in – 0.625 in) (Weld-1)	236-CWP-1	HAZ	5	30	0.30	233 CWP-4
	236-CWP-2	HAZ	5	30	0.30	233 CWP-3
	236-CWP-3	WCL	5	30	0.30	233 CWP-2
	236-CWP-4	WCL	5	30	0.30	None

3.6.3 Testing Results

The results of the tests included force, stress, average remote strain (upper and lower pipe), average cross-weld strain, and crack mouth opening displacement (CMOD). The stress was calculated differently for the three different sections of the transition weld (Weld-2), where the stress in the upper pipe used the 16 mm WT pipe thickness, the stress in the lower pipe used the 19 mm WT pipe thickness and the cross-weld stress used the thickness of the counter-bore. Plots of stress and strain for Weld-2 are shown in Figure 3-30. Plots of stress and strain for Weld-1 are shown in Figure 3-31.

Trends and correlations from each of these plots are not evident. Specimens 233 CWP-1 and 233 CWP-2 resulted in a great deal of strain and subsequent necking in the upper pipe (16 mm WT side) which dominated the response and stunted the strain that the lower pipe (19 mm WT side) exhibited. Specimens 233 CWP-3 and 233 CWP-4 had similar strain responses in the upper pipe (16 mm WT) and the cross-weld, where most of the strain was concentrated within the counter-bored region of the specimen. The locations of the notches in the specimens did not seem to influence the strain response. Similarly, neither the location of the notch nor the clock position of the specimens for Weld-1 appeared to have an influence on the strain response. The most likely influence on strain response was the variability in base metal properties of those specimens.

All specimens from Weld-2 demonstrated a stunted cross-weld strain response compared to the upper and lower base metal pipes which are nominally equivalent but also subject to variability in the base metal properties.

All specimens from Weld-2 demonstrated some crack extension as evident from post-test fractographs shown in Appendix C and from the force vs. CMOD data records. In all specimens, the base metal strains dominated the results. This is even more prominent in the force vs. CMOD data plots from Weld-1 where there was very little CMOD opening. The small CMOD was also evident in the post-test fractographs for those specimens. The force vs. CMOD data for Weld-2 and Weld-1 are shown in Figure 3-32.

Comparing the CWP results to the SE(T) results and especially the SE(T) specimens adjacent to specific CWP specimens there is little directly correlated behavior. Only 233 SET-6 shows the largest crack extension (see Figure 2-16 (b)) which is correlative with the largest CMOD data from its adjacent CWP specimen (see Figure 3-32 (a) 233 CWP-4) and the exact opposite is true for 236 SET-6 (see Figure 2-16 (d)) showing the largest crack extension where the lowest CMOD data results from its adjacent CWP specimen (see Figure 3-32 (b) 236 CWP-4). The disparity in the results, resulting from variability in the base metal properties is exacerbated by the weld over-match.

Furthermore, there is little evidence for general trends based on notch location or clock position. For Weld-2, the HAZ notched specimens indicated the lowest CMOD, whereas the HAZ notched specimens indicated the highest CMOD for Weld-1. Additionally, clock position correlations aren't supported by the data.

The tensile strain capacity for each of the CWP tests was defined as the strain experienced in the specimen at the maximum load. In all cases, this strain capacity value was taken as the strain measured in either the upper pipe, lower pipe, or across the weld.

Table 3-19 contains the strains at the maximum load for each of the sections with the limiting section identified for the strain capacity. For the case of Weld-2, the upper pipe section in each of the specimens was the 16 mm WT pipe. Additionally, for Weld-2 specimens 233-CWP-3 and 233-CWP-4, the Cross-Weld limiting sections were the counter bores (thinnest material) in the 19 mm WT pipe (lower pipe). DIC images that show the relative strains in each of the specimen sections for each of the specimens at the maximum load can be found in Appendix C. The detailed analyses and discussions of the test results are given in Section 4.2.3.

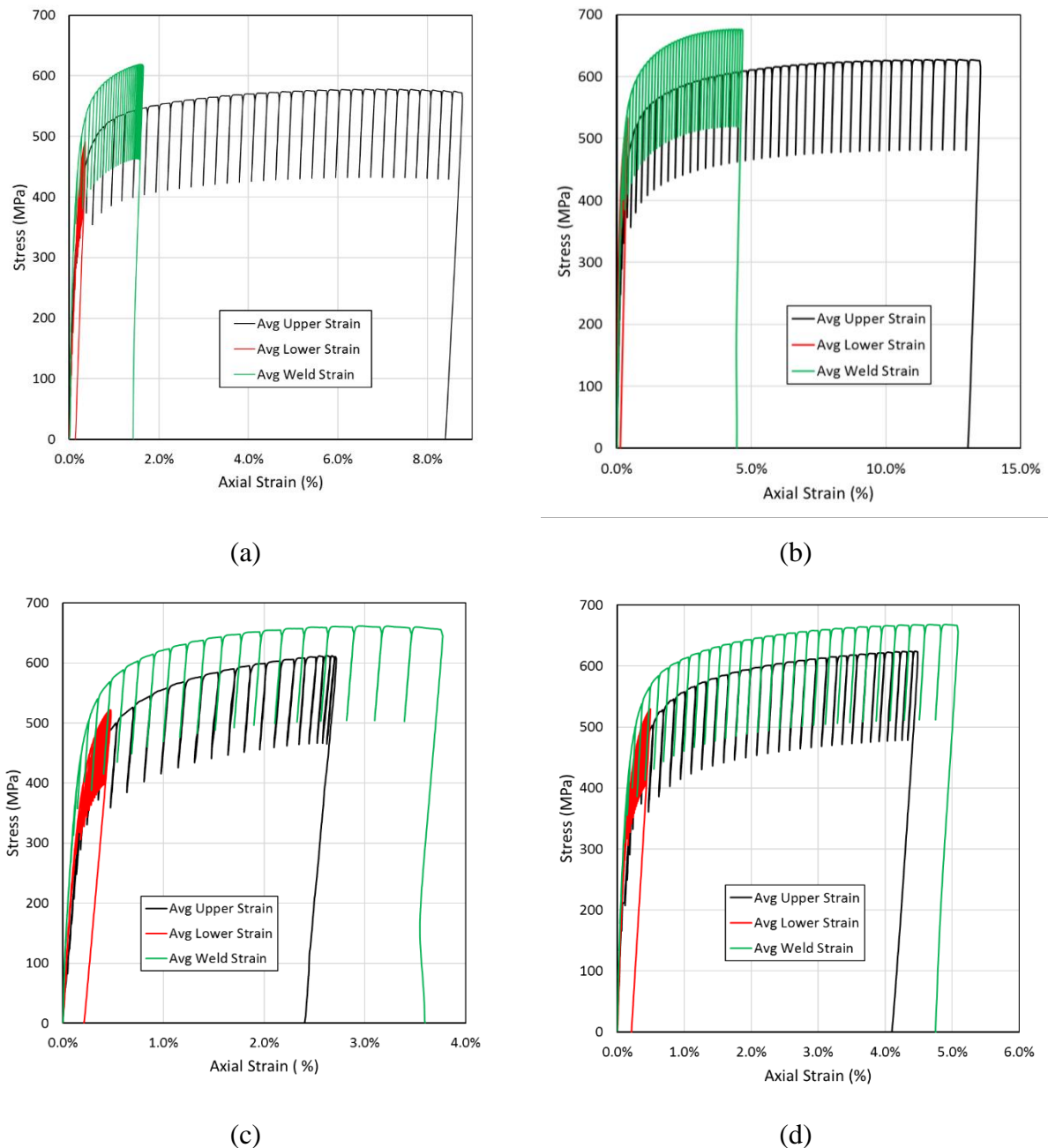


Figure 3-30 Stress-strain curves for Weld-2; showing upper and lower remote strains and the cross-weld strain for specimen 233 CWP-1 (a), 233 CWP-2 (b), 233 CWP-3 (c) and 233 CWP-4 (d).

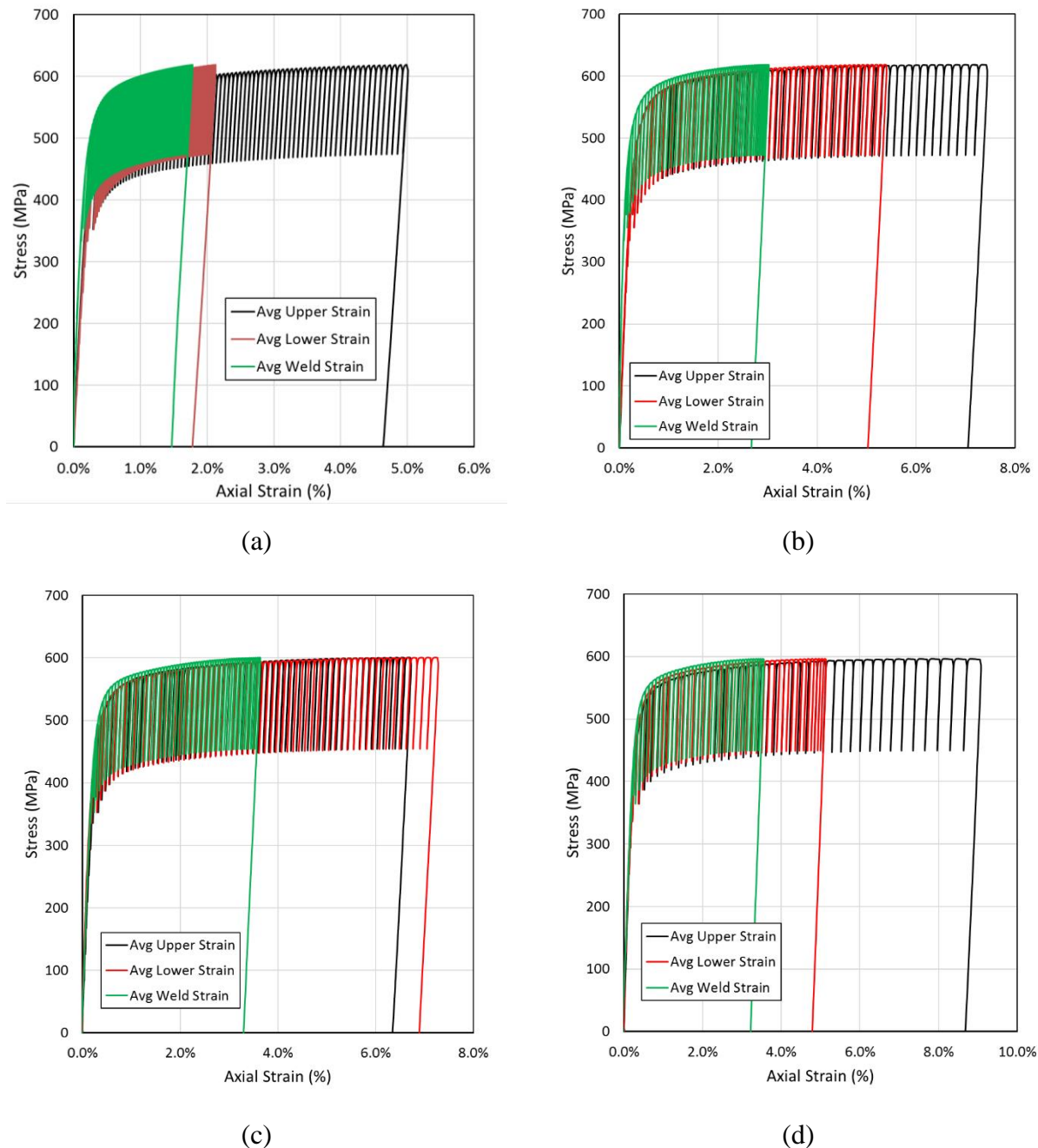


Figure 3-31 Stress-strain curves for Weld-1; showing upper and lower remote strains and the cross-weld strain for specimen 236 CWP-1 (a), 236 CWP-2 (b), 236 CWP-3 (c) and 236 CWP-4 (d).

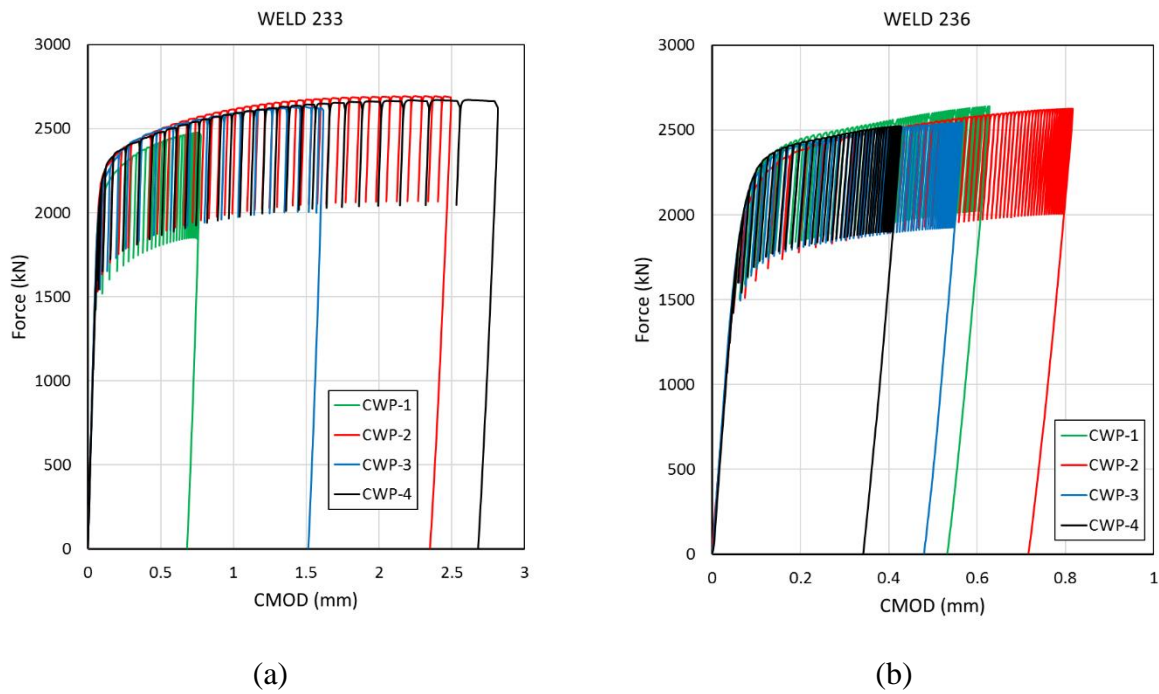


Figure 3-32. Force vs. CMOD plots for Weld-2 (a) and Weld-1 (b).

Table 3-19 Curved Wide Plate (CWP) Tensile Strain Capacity
914 mm (36 in) Outside Diameter – API-5L X70

Weld	Specimen ID	Notch Location	Average Upper Pipe Strain (%)	Average Lower Pipe Strain (%)	Average Cross-Weld Strain (%)	Limiting Section
16 mm – 19 mm (0.625 in – 0.750 in) (Weld-2)	233-CWP-1	HAZ	6.9%	0.4%	1.6%	Upper
	233-CWP-2	WCL	11.9%	0.4%	4.3%	Upper
	233-CWP-3	HAZ	2.6%	0.5%	2.9%	Cross-Weld
	233-CWP-4	WCL	4.4%	0.5%	4.9%	Cross-Weld
16 mm – 16 mm (0.625 in – 0.625 in) (Weld-1)	236-CWP-1	HAZ	5.0%	2.1%	1.8%	Upper
	236-CWP-2	HAZ	7.0%	5.2%	2.9%	Upper
	236-CWP-3	WCL	6.7%	7.2%	3.6%	Lower
	236-CWP-4	WCL	8.5%	5.0%	3.5%	Upper

4 Girth Welds Subjected to Longitudinal Strain

4.1 Overview of the Studies on Girth Welds

4.1.1 Limit States Associated with Girth Welds Subjected to Longitudinal Strain

When subjected to longitudinal load, girth welds (including weld metal, fusion boundary, and heat-affected zone, i.e., HAZ) are often the weakest link of a pipeline due to the existence of weld defects and deteriorative metallurgical and/or mechanical property changes resulting from welding thermal cycles [28,52].

Transition welds (joining pipes of unequal wall thicknesses) are more prone to failure than regular girth welds (joining pipes of equal wall thicknesses), when subjected to longitudinal load, due to the factors given below:

- (1) Transition welds are often used to connect fittings such as elbows, induction bends, tees, etc. These types of connections may be subjected to high stress and strain demands.
- (2) Transition welds may have weld defects due to their complicated weld geometries.
- (3) The geometrical discontinuity in the vicinity of the transition welds may induce additional stress and strain concentrations.

The longitudinal load can induce tensile and compressive strains to a pipe. Excessive tensile strain can result in tensile rupture (or leak). The tensile rupture is considered as an ultimate limit state. Excessive compressive strain can cause buckling or wrinkling of the pipe wall. Since wrinkles or buckles usually don't cause immediate leaking or rupturing, buckling or wrinkling is, in general, considered as a service limit state.

The resistance to the tensile rupture and compressive buckling is called tensile strain capacity (TSC) and compressive strain capacity (CSC), respectively. In this project, the TSC and CSC of the girth welds were both studied.

4.1.2 Types of Girth Welds

The transition welds were the focus of this project. Two types of transition welds, i.e., back-beveled and counterbore-tapered welds were studied. The studies for the transition welds were based on those for regular girth welds. The studies conducted in this project did not consider the interaction of a girth weld with other anomalies (e.g., corrosion, gouge, dent, etc.).

Figure 4-1 shows the joint design of a regular girth weld. Figure 4-2 and Figure 4-3 show the joint designs of two types of transition welds, i.e., back-beveled design and counterbore-tapered design.

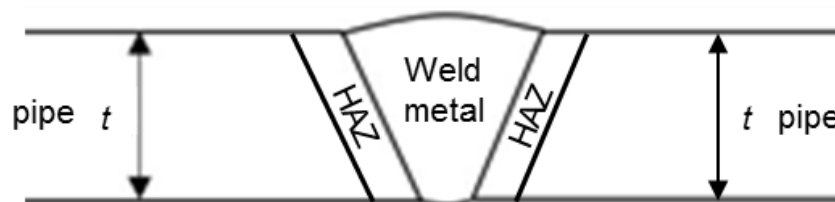


Figure 4-1 Joint design of regular girth welds

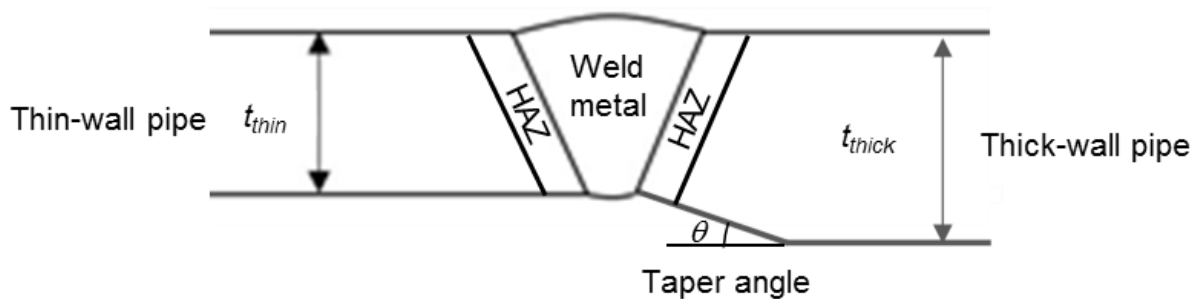


Figure 4-2 Joint design of transition welds - back-beveled design

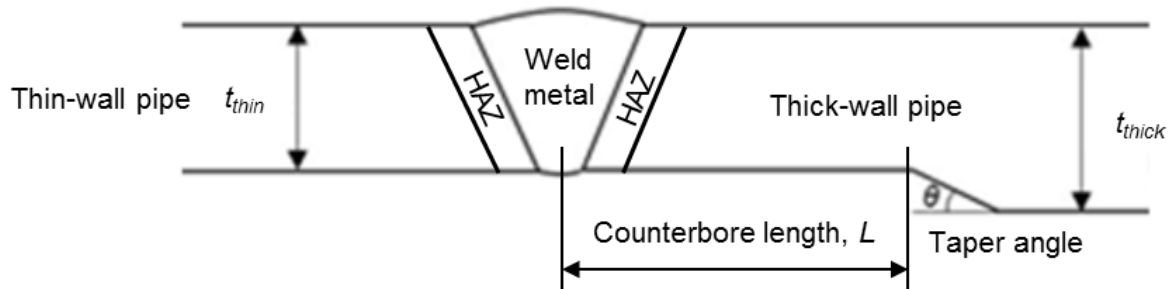


Figure 4-3 Joint design of transition welds - counterbore-tapered design

4.1.3 Section Structure and General Approach

In this project, both the TSC and CSC of the girth welds were studied. The studies on the TSC are shown in Section 4.2 and the studies on the CSC are shown in Section 4.3.

The general approach used for the girth weld TSC studies and the structure of Section 4.2 are summarized below:

- The application and general definition of the TSC were introduced in Section 4.2.1. The target application of the TSC, i.e., how the TSC is to be used, was discussed. The general concept or definition of the TSC was introduced based on the target application.
- The basis of the studies conducted in this project for the girth weld TSC was introduced in Section 4.2.2. The work was based on a prior PHMSA-PRCI co-sponsored project [28] aimed at the TSC of the regular girth welds.
- The studies related to the counterbore-tapered welds were shown in Section 4.2.3. The studies used simple analytical derivations based on basic engineering principles such as load equilibrium. The pipe strength and wall thickness specifications for the counterbore-tapered welds were developed. Procedures for calculating the TSC of the counterbore-tapered welds were developed based on the TSC models for the regular girth weld. The procedures were evaluated with the CWP tests conducted in this project.
- The studies on the back-beveled welds were shown in Section 4.2.4. Those studies were based on systematic finite element analyses (FEA). Selected FEA were conducted first to study the sensitivity of the TSC to key pipe strength parameters, based on which, the pipe strength and wall thickness specifications for the back-beveled welds were developed. Parametric FEA studying the TSC of the back-beveled welds were then conducted, based on which, the TSC models for the back-beveled welds were developed.

The general approach used for the girth weld CSC studies and the structure of Section 4.3 are summarized below:

- The application and general definition of the CSC were introduced in Section 4.3.1. The target application of the CSC, i.e., how the CSC is to be used, was discussed. The general concept or definition of the CSC was introduced based on the target application.
- The basis of the studies conducted in this project for the girth weld CSC was introduced in Section 4.3.2. The studies were based on a prior PHMSA sponsored project [26].
- The methods used to address the effect of the girth welds on the CSC were introduced in Section 4.3.3. All girth welds (including regular girth welds and counterbore-tapered and back-beveled transition welds) were treated as equivalent geometry imperfections, which were determined through systematic FEA.
- The effect of the loading conditions on the CSC was discussed in Section 4.3.4. Proper loading conditions for the full-scale tests and numerical analyses were developed. The results were evaluated and confirmed with the full-scale test results.
- Parametric FEA aimed at studying the effects of various parameters on the CSC were shown 4.3.5. Through the parametric FEA, equivalent geometry imperfections for the girth welds were established in Section 4.3.6 and the CSC equations for the girth welds were established in Section 4.3.7.

4.2 Tensile Strain Capacity of Girth Welds

4.2.1 Application and Definition of Tensile Strain Capacity

The tensile strain capacity (TSC) of a girth weld is the maximum tensile strain that the girth weld can withstand before any leaking or rupturing. The TSC is designated to capture the overall capacity of the girth weld to accommodate global/nominal longitudinal deformation.

The tensile strain (and tensile strain capacity) is measured at a location which is sufficiently far away from the girth weld, so that the reported tensile strain capacity is not affected by the strain concentration in the local girth weld area.

For a regular girth weld, the material properties and wall thicknesses of the two pipes joined by the girth weld are often considered to be nominally the same. In this case, the tensile strain capacity can be obtained from either pipe. For a transition weld, the material properties and wall thicknesses of the two pipes joined by the girth weld are usually different and the tensile strain capacities obtained from the two pipes are different. In this report, the tensile strain capacity is obtained from the thinner pipe.

The pipe integrity is usually determined by comparing strain capacity with strain demand. To properly use the strain capacity determined by this guideline, the strain demand should be defined consistently with the strain capacity in this guideline. Otherwise, the assessment results may become either overly conservative or non-conservative.

4.2.2 Basis of Studies

In the past two decades, many research investigations related to the tensile strain capacity (TSC) of regular girth welds have been published. A thorough review of the studies on TSC can

be found in [7,26,28]. The studies conducted in this project were based on the prior studies sponsored by PHMSA and PRCI [6,7,8,28,52]. The key outcome of the prior PHMSA/PRCI studies is introduced in this section.

In the prior PHMSA/PRCI research project, a set of equations were developed to calculate the tensile strain capacity (TSC) of regular girth welds. Separate equations were developed for GMAW and FCAW/SMAW welds. For both types of girth welds, the TSC equations adopted the same form, i.e.,

$$\varepsilon_t^{crit} = \min \left(\varepsilon_u, P(f_p) G(t) \varepsilon_{t,f_p}^{crit} \right). \quad (4-1)$$

where the functions $G(t)$ and $P(f_p)$ characterize the effect of wall thickness and internal pressure, respectively. The unit of the TSC (ε_t^{crit}) is mm/mm (in/in). The function $G(t)$ is given as

$$G(t) = \left(\frac{15.9}{t} \right)^{0.8096} \left[1 + 1.503 \left(\frac{h}{t} \right)^{1.229} \right], \quad (4-2)$$

where, the unit of t is mm. The function $P(f_p)$ is in the form of

$$P(f_p) = \begin{cases} P_{max} - \frac{5f_p}{3} (P_{max} - 1) & \text{if } 0 < f_p < 0.6 \\ 1 & \text{if } 0.6 \leq f_p < 0.8 \end{cases} \quad (4-3)$$

A conservative fixed value of 1.5 was initially selected for P_{max} [28]. A more refined relation was developed later [7] as:

$$P_{max} = 2.25 - 2 \frac{a}{t}. \quad (4-4)$$

The term $\varepsilon_{t,f_p}^{crit}$ in Eq. (4-1) is the tensile strain capacity when the pressure factor (f_p) equals 0.72. $\varepsilon_{t,f_p}^{crit}$ is in the form of

$$\varepsilon_{t,f_p}^{crit} = A \frac{f(\delta_A)}{1 + f(\delta_A)}. \quad (4-5)$$

The $\varepsilon_{t,f_p}^{crit}$ obtained from Eq. (4-5) is in the unit of mm/mm. The function f is given as

$$f(\delta_A) = (C \delta_A)^{B(\delta_A)^D}. \quad (4-6)$$

In Eqs. (4-5) and (4-6), the symbols A , B , C , and D are fitted functions of normalized geometry and material parameters. The function form of A , B , C , and D are given in [7,28].

The input parameters and their applicable ranges in the TSC Equations are listed below:

a/t	0.05 – 0.50,
$2c/t$	1.0 – 20.0,
h/t	0.0 – 0.2,
σ_y/σ_u	0.75 – 0.94,
R_M	1.0 – 1.3,
f_p	0.0 – 0.8,
δ_A	0.2 mm – 2.5 mm (0.0079 in – 0.10 in), and

$$t \quad 12.7 \text{ mm} - 25.4 \text{ mm} (0.50 \text{ in} - 1.0 \text{ in}).$$

The pipe OD (D) and yield strength (σ_y) are not directly used as input parameters. But, the equations are recommended for the following ranges:

$$D \quad 304 \text{ mm} - 1,219 \text{ mm} (12 \text{ in} - 48 \text{ in}) \text{ and}$$

$$\sigma_y \quad 386 \text{ MPa} - 690 \text{ MPa} (56 \text{ ksi} - 100 \text{ ksi}).$$

In this project, the TSC Eq. (4-1) was extended to cover transition girth welds. The work on the counterbore-tapered welds is shown in Section 4.2.3 and the work on the back-beveled welds is shown in Section 4.2.4.

4.2.3 Assessment of Counterbore-Tapered Transition Welds

4.2.3.1 Pipe Strength and Thickness Specifications for Counterbore-Tapered Welds

In existing design specifications, the pipe strength specifications for the counterbore-tapered welds vary. In most specifications, the SMYS of the thick-wall pipe is required to be equal to or higher than the SMYS of the thin-wall pipe. However, some specifications allow the specified minimum yield strength (SMYS) of the thick-wall pipe to be lower than the SMYS of the thin-wall pipe, similar to the specifications for the back-beveled welds. It should be noted that the SMYS of a pipe is usually for the strength of the circumferential direction.

The main purpose of these pipe strength specifications is to limit the design factor (i.e., ratio between internal-pressure induced hoop stress and pipe SMYS) in the thick-wall pipe (or the counterbore region) to be below or equal to the design factor in the thin-wall pipe.

Another key specification for the counterbore-tapered weld is the minimum counterbore length. The pipe wall thickness change at the transition weld can create additional through-wall local bending stress in the area near the wall thickness transition [62]. The minimum counterbore length is specified to ensure the local bending stress is satisfactorily attenuated at the weld.

The existing pipe strength and thickness specifications of the counterbore-tapered welds are aimed at pressure containment and not adequate for strain-based design and assessment (SBDA), especially when the expected longitudinal strain is beyond yield limit. For example, the SMYS represents the minimum yield strength in the pipe circumferential direction. Under longitudinal loading, however, the pipe longitudinal strength determines the strain in the pipe. If the actual longitudinal strength of the thick-wall pipe is lower than that of the thin-wall pipe (even if the two pipes have the same SMYS), plastic strains in the longitudinal direction can take place and concentrate in the counterbore zone. As a result, the strain in the rest of the pipe, i.e., the tensile strain capacity, can be very low. To get adequate strain capacity, the strain concentration in the counterbore zone should be prevented through proper pipe strength and thickness specifications.

For the SBDA, the pipe strength and thickness specifications should address both pressure containment and longitudinal strain. Enhanced pipe strength and thickness specifications for counterbore-tapered welds were developed in this project and are presented below:

- (1) The longitudinal yield and ultimate tensile strengths of the thick-wall pipe should be no less than those of the thin-wall pipe, respectively.

- (2) The SMYS (circumferential) of the thick-wall pipe should be no less than the SMYS of the thin-wall pipe.
- (3) If the wall thickness ratio is greater than 1.50, the wall thickness ratio should be treated as 1.50 for design and assessment.

4.2.3.2 Procedures for Assessing TSC of Counterbore-Tapered Welds

4.2.3.2.1 *General Procedures*

When the enhanced pipe strength and thickness specifications and the minimum counterbore length are satisfied, the TSC of the counterbore-tapered transition welds is no worse than that of the regular welds. Therefore, the TSC of the counterbore-tapered welds can be assessed with the TSC equations for regular welds shown in Eq. (4-1). Depending on the welding procedures of the actual girth welds, proper equations for GMAW or FCAW/SMAW should be selected.

All input parameters related to the pipe body, e.g., pipe strength, Y/T ratio, and thickness, should be determined from the thin-wall pipe. The apparent CTOD toughness (i.e., $CTOD_A$) should be determined based on the flaw location. It should be noted that the $CTOD_A$ of the two HAZ may be different. If the flaw location is not known, the lowest $CTOD_A$ of the weld metal and the two HAZ should be used.

4.2.3.2.2 *Procedures for Cases of Unsatisfied Pipe Strength Specifications*

The counterbore of the thick-wall pipe has the same thickness as that of the thin-wall pipe. If the enhanced pipe strength specifications for counterbore-tapered welds are not satisfied, i.e., the longitudinal yield and/or ultimate tensile strengths of the thick-wall pipe are lower than those of the thin-wall pipe, the transition weld would fail at the counterbore of the thick-wall pipe since the longitudinal tensile strain concentrates in the counterbore of the thick-wall pipe. Thus, the tensile strain capacity (i.e., the maximum tensile strain achieved in the thin pipe) depends on the strain in the counterbore of the thick-wall pipe. The TSC can be determined with the following procedures:

- (1) Determine a reference tensile strain capacity ($\epsilon_t^{crit}|_{cb}$) in the counterbore with Eq. (4-1) using the material properties of the thick-wall pipe and thickness of the counterbore;
- (2) Determine the longitudinal stress capacity ($\sigma_t^{crit}|_{cb}$) in the thin-wall pipe and counterbore from the full stress-strain curve of the thick-wall pipe at the reference tensile strain capacity ($\epsilon_t^{crit}|_{cb}$) (as shown in Figure 4-4); and
- (3) Determine the tensile strain capacity (ϵ_t^{crit}) in the thin-wall pipe from the full stress-strain curve of the thin-wall pipe at the longitudinal stress ($\sigma_t^{crit}|_{cb}$) (as shown in Figure 4-4).

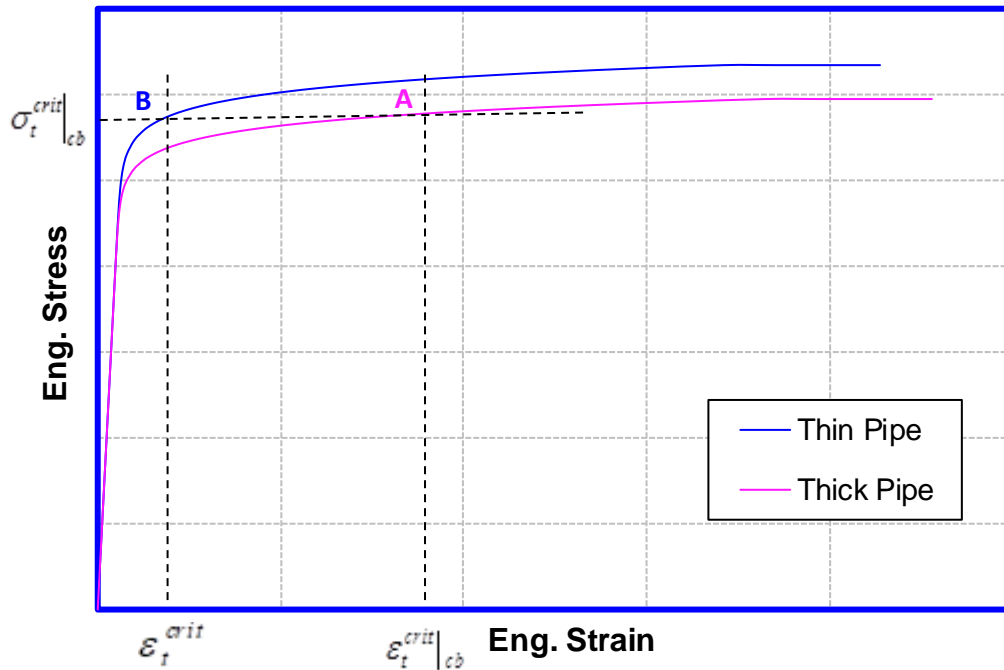


Figure 4-4 Determination of reference tensile strain capacity

4.2.3.3 Evaluation of Assessment Procedures with Experimental Tests

Eight curved wide plate (CWP) tensile tests were conducted in this project. Four tests were for a regular girth weld (Weld-1) and the other four tests were for a counterbore-tapered transition weld (Weld-2). Flaws in both HAZ and weld metal center line (WMC or WCL) were tested. The same flaw size was used in all the tests. Two tests (duplicate) were conducted for each girth weld and each flaw location. The details of the CWP tests are given in Section 3.6.

The regular girth weld (Weld-1) jointed two sections of the X70-DSAW-1 pipe (16-mm wall thickness). The counterbore-tapered transition weld (Weld-2) jointed a section of the X70-DSAW-1 pipe with a section of the X70-DSAW-2 pipe (19-mm wall thickness). The average longitudinal tensile properties of the pipes used in the CWP tests are shown in Table 4-1, in which the properties were from strap specimens. The details of the small-scale test results are given in Section 2.3.

Table 4-1 shows that the two pipes have very similar strength properties. The enhanced pipe strength and thickness specifications for the counterbore-tapered welds are satisfied. Therefore, as discussed in the previous section, Eq. (4-1) can be used to calculate the TSC for both welds. Table 4-2 shows all the input parameters used in the assessment. The average strength and Y/T ratio of the thin pipe and the average weld tensile strength were used. It is seen that both welds show extremely high weld strength overmatching (regular weld 35% and transition weld 27%).

The apparent toughness ($CTOD_A$) was determined from multiple small-scale toughness tests, i.e., CVN (Charpy impact tests), CTOD (SENB tests), and CTOD resistance curve (SENT tests), following the procedures given in [28]. The CVN- $CTOD_A$ equation of X70-X80 pipes was applied to convert CVN to $CTOD_A$. A multiplying factor of 1.75 was applied to convert CTOD (SENB tests) to $CTOD_A$. The CTOD resistance (SENT tests) at 0.6-mm (based on the pipe wall

thickness) flaw growth was used to determine the $CTOD_A$ from the CTOD resistance curve. The $CTOD_A$ obtained from different tests showed reasonable variations. For simplicity, the median $CTOD_A$ were used to calculate the TSC.

In addition to the strength and toughness properties, in the calculations, the flaw depth was 5.0 mm, the flaw length was 30.0 mm, the weld high-low misalignment was zero, the pipe wall thickness (thin pipe) was 16 mm, and the internal pressure was zero.

The calculated TSC for the CWP tests are shown in Table 4-3. Due to duplicated tests, only four TSC values were calculated. For both the regular and counterbore-tapered welds, the TSC for the HAZ flaw is about 7% and the TSC for the weld center line (WCL) flaw is about 3%. It should be noted that the TSC equations, i.e., Eq. (4-1), were developed based on HAZ flaws. For WCL flaws, the equations can significantly under-estimate the TSC if there is significant weld strength overmatching. Therefore, due to the high weld overmatching for those two welds, it is believed that the TSC of the WCL flaws were under-estimated.

It should be noted that the calculated TSC is beyond the recommended applicable range of the TSC equations, i.e., half pipe uniform strain. When the strain is greater than half of the pipe uniform strain, the pipe stress-strain curve usually becomes very flat, i.e., a small change in the stress can lead to a large change in the strain. Due to the flat stress-strain curve, the TSC can be very sensitive to the pipe strength variation [8,52]. As a result, for experimental tests, the TSC often show very large scatters and for equation calculations, the large scatter in the TSC cannot be reproduced since the pipe strength variation is not captured by the equations.

Based on the discussions, it can be expected that the TSC of all the tests (regular or transition welds and HAZ or WCL flaws) are similar and greater than half pipe uniform strain. However, the precise prediction of the TSC of each individual test can be very difficult.

The TSC measured from the tests are shown in Section 3.6. The measured TSC appeared not depend on the weld (regular vs. transition) or flaw location (HAZ or WCL) and all tests failed in the pipe materials. For the regular girth weld (Weld-1), the TSC varied from 3.5% to 7.0%. For the transition girth weld (Weld-2), two tests failed in the thin pipe, of which the measured TSC varied from 6.9% - 11.9%. The other two tests failed in the counterbore area of the thick pipe, of which the measured TSC varied from 2.6% - 4.4%. The measured TSC showed large scatters and showed good agreement with the discussions given above.

Table 4-1 Average pipe properties for CWP tests

Pipe Material ID	Pipe Wall Thickness	Average Pipe Longitudinal Properties (Strap)		
		Yield	Tensile	Y/T
	(mm)	(MPa)	(MPa)	
X70-DSAW-1	15.88	510	623	0.82
X70-DSAW-2	19.05	508	627	0.81

Table 4-2 Strength and toughness properties for TSC calculation

Weld Material ID	Weld Type	Average Pipe Longitudinal Properties (Strap Specimen)			Average Weld Properties	Weld Strength Mismatch Ratio	Flaw Location	Upper-Shelf CVN	CTOD (δ_m)	CTOD _A			
		Yield Strength	Tensile Strength	Y/T	Tensile Strength					From CVN	From CTOD	From SENT R-Curve ($\Delta a = 0.6$ mm)	Median
		(MPa)	(MPa)		(MPa)			(J)	(mm)	(mm)	(mm)	(mm)	(mm)
Weld-1	Regular	510	623	0.82	838	1.35	HAZ	259	0.77	1.08	1.35	1.10	1.10
							WCL	117	0.21	0.51	0.37	0.45	0.45
Weld-2	Counterbore-Tapered	510	623	0.82	791	1.27	HAZ	317	0.42	1.28	0.74	1.80	1.28
							WCL	104	0.15	0.44	0.26	0.60	0.44

Table 4-3 Calculated TSC for the CWP tests

Weld Material ID	Weld Type	Flaw Location	TSC from Assessment Equation (%)
Weld-1	Regular	HAZ	6.95
		WCL	2.88
Weld-2	Counterbore-Tapered	HAZ	7.80
		WCL	2.84

4.2.4 Assessment of Back-Beveled Transition Welds

4.2.4.1 Overview of the Analysis Approach

Finite element analyses (FEA) were conducted to determine the crack driving force (CTOD_F) curves of the back-beveled transition welds. The CTOD_F curve shows the relationship between the crack tip opening displacement (CTOD_F) and the nominal/remote strain applied to the pipe [28]. The details on the CTOD_F curve can be found in Section 4.2.4.2.

The CTOD_F of the back-beveled transition welds was compared with that of the regular girth welds. A TSC reduction factor was developed by comparing the CTOD_F of the back-beveled transition welds and regular girth welds. The TSC of the back-beveled transition welds can be determined by applying the TSC reduction factor to the TSC equations of regular girth welds in Eq. (4-1).

4.2.4.2 Overview of Finite Element Analyses

4.2.4.2.1 Weld Profiles and Finite Element Analysis Models

Finite element analyses were conducted to determine the CTOD_F curves for various pipe and weld parameters. Commercial finite element software ABAQUS® was used in the analysis. The pipe was modeled with three-dimensional hybrid eight-node solid elements with reduced integration (C3D8RH). The effect of mesh sizes on the analysis results was thoroughly examined. Adequate mesh refinement was used to obtain converged (i.e., mesh independent) solutions.

Due to symmetry conditions in the circumferential direction, as shown in Figure 4-5, only a half of the pipe (half circumference) was modeled. The length of the pipe in the model was kept to six times the pipe OD to obtain a finite uniform strain zone, i.e., a finite pipe segment, in which the strain is uniform (not affected by the pipe ends or girth weld).

The FEA model contains a transition weld joining two pipes with different wall thicknesses, as shown in Figure 4-5. The typical groove weld profile for SMAW was used. The weld bevel angle was kept at 30° , the cap height was kept at 1.5 mm, the HAZ width was kept at 4.5 mm, and the taper angle was kept at 22° .

A surface breaking flaw of a semi-elliptical shape was modeled in the transition weld. The flaw was located on the ID surface of the thick pipe side along the fusion line (i.e., HAZ flaw), as shown in Figure 4-5. The flaw location was selected to obtain the upper bound crack driving force for all possible flaw locations. Since weld strength overmatching is generally required for strain-based design, the HAZ flaw often sees higher crack driving force than the weld metal flaw due to the HAZ softening. In addition, the HAZ flaw on the thick pipe side usually see higher crack driving force than the HAZ flaw on the thin pipe side since the thick pipe usually has lower strength than the thin pipe.

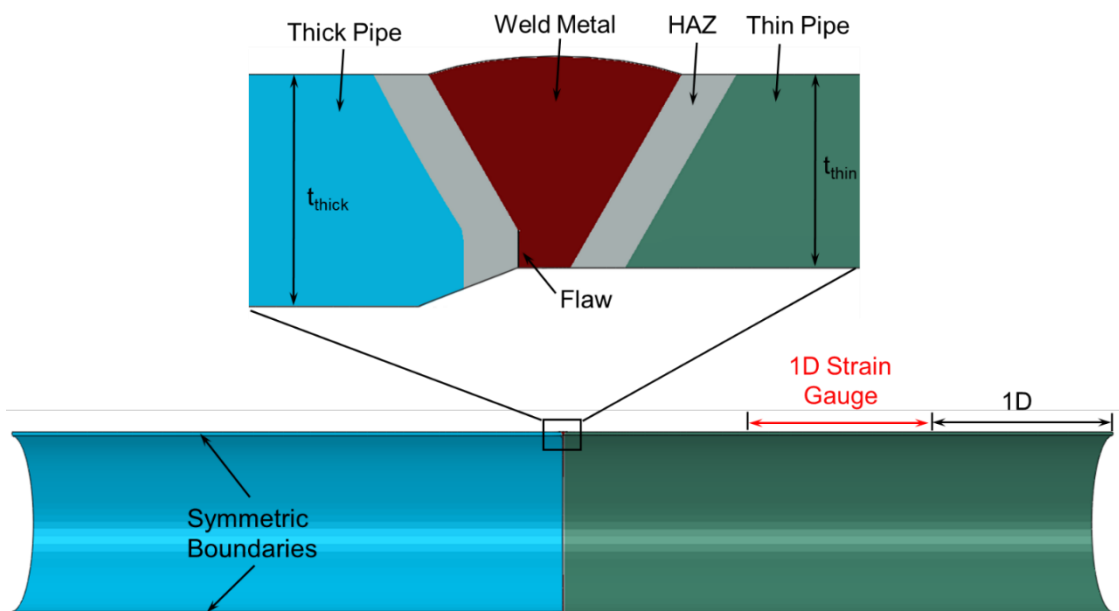


Figure 4-5 Finite element model of a pipe joint with a back-beveled transition weld

4.2.4.2.2 Loading Conditions

In the FEA, the loading was applied in two steps. In the first step, internal pressure was applied on the pipe ID surface. The hoop stress induced by the internal pressure was 72% of the SMYS of the thin pipe (i.e., Class 1 location). In the second step, a uniaxial tensile displacement was applied to the end of the thin-wall pipe, while the end of the thick-wall pipe was fixed. The internal pressure was kept constant during the second step.

4.2.4.2.3 Typical FEA Results and Calculation of Crack Driving Force Curves

Figure 4-6 shows the deformation of a flaw in a transition weld and the strain distribution near the crack tip. Under longitudinal straining, the flaw first opened and blunted with plastic strain concentrated at the crack tip. When longitudinal straining increases, the crack tip further opened and the zone of plastic strain concentration gradually grew through the wall thickness along a 30-40° shear band.

The key output of the FEA is the crack driving force curves, i.e., the relationship between the crack tip opening displacement ($CTOD_F$) and the remote strain. The $CTOD_F$ was calculated from the deformed crack surface profile following the traditional 90°-line method as shown in Figure 4-7.

The remote strain was measured from the thin-wall pipe as the average strain within a gauge length of $1D$ (D is the pipe OD). The gauge is $1D$ away from the end of the model, as shown in Figure 4-5. The longitudinal strain within the gauge is uniform. The strain was only measured on the thin-wall pipe.

Figure 4-8 shows a schematic illustration of the crack driving force curve. The vertical axis is the crack tip opening displacement ($CTOD_F$ or δ_F) and the horizontal axis is the remote strain. The $CTOD_F$ (or δ_F) increases as the remote strain increases. The TSC (ϵ_t^{crit}) is reached when the $CTOD_F$ (or δ_F) reached the apparent CTOD toughness: $CTOD_A$ (or δ_A).

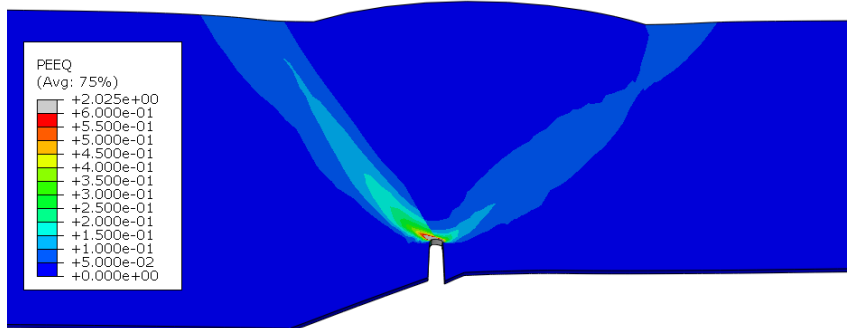


Figure 4-6 Strain distribution near the crack tip

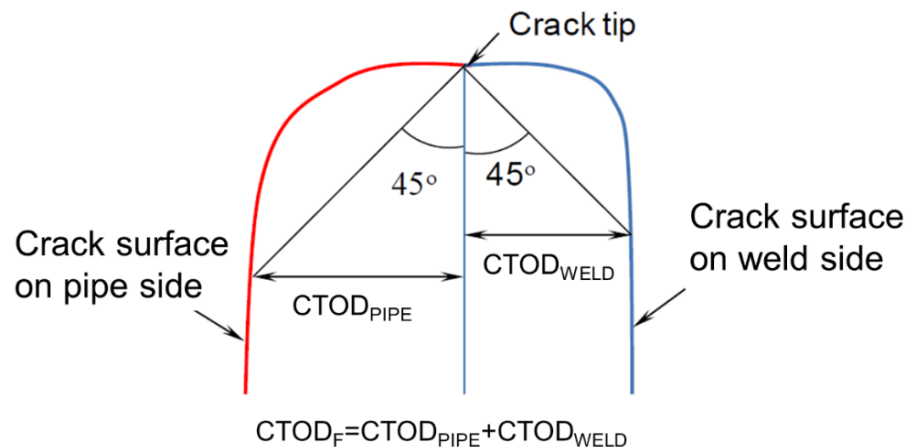


Figure 4-7 Schematic drawing of $CTOD_F$ calculation [28]

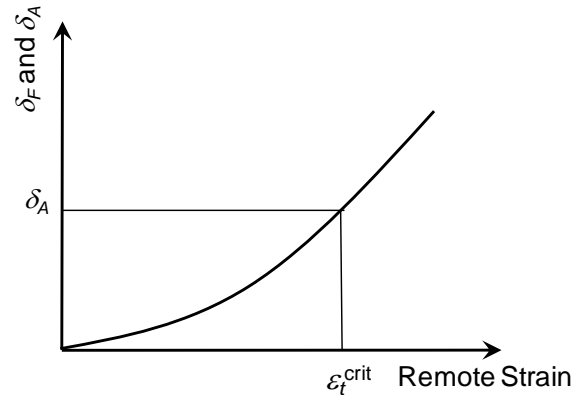


Figure 4-8 Schematic illustration of CTOD driving force curve (CTOD_F) and how to obtain TSC (ϵ_t^{crit}) using apparent CTOD toughness (δ_A)

4.2.4.3 Pipe Strength and Thickness Specifications for Back-Beveled Welds

The existing pipe strength and thickness specifications for the back-beveled welds are aimed at pressure containment. For example, in ASME B31.8 [42] and B31.4 [63], if the thick pipe has a lower grade than the thin pipe, the minimum required thickness ratio of the thick-to-thin pipe is the ratio between the SMYS of the thin-to-thick pipe, i.e., $t_{\text{thick}}/t_{\text{thin}} \geq \text{SMYS}_{\text{thin}}/\text{SMYS}_{\text{thick}}$. It is equivalent to limit the design factor of the thick pipe to equal or less than the design factor of the thin pipe. The maximum allowed wall thickness ratio for design in the ASME codes ($t_{\text{thick}}/t_{\text{thin}}$) is 1.5, which in fact limits the maximum allowed SMYS ratio ($\text{SMYS}_{\text{thin}}/\text{SMYS}_{\text{thick}}$) to be 1.5.

The existing pipe strength and thickness specifications for the back-beveled welds are not adequate for strain-based design and assessment (SBDA). Similar to the counterbore-tapered welds, the actual longitudinal strength of the pipe should be specified instead of the SMYS of the pipe.

Unlike the counter-bore tapered welds, the back-beveled welds do not have a counterbore zone. Due to the reinforcement effect of the thick pipe, the strength of the thick pipe can be lower than the strength of the thin pipe. To determine the proper strength difference, a set of FEA were conducted to study the effect of pipe strength and wall thickness ratios on the pipe strain capacity (see Table 4-4 and Figure 4-9).

The results indicate that if the ultimate tensile strength of the thick pipe is less than the flow stress of the thin wall pipe, the wall thickness transition zone in the thick pipe (i.e., the tapered area) can become the weakest link and significant strain concentration can be found in the transition zone. The strain capacity measured in the thin pipe is very small. Therefore, in order to achieve adequate tensile strain capacity, the existing pipe strength and thickness specifications for the back-beveled welds need to be tightened to avoid the strain concentration and failure in the transition zone.

For the SBDA, the pipe strength and thickness specifications should address both pressure containment and longitudinal strain. Enhanced pipe strength and thickness specifications for back-beveled welds were developed in this project and are shown below:

- The longitudinal ultimate tensile strength of the thick-wall pipe should be no less than the longitudinal flow stress of the thin-wall pipe, where the flow stress of the thin-wall pipe is the average of the yield strength and ultimate tensile strength of the thin-wall pipe.
- $R_t \geq \max(R_G, R_y, R_u)$, where R_t is the ratio between the thickness of thick-wall pipe and that of the thin-wall pipe; R_G is the ratio between the SMYS of thin-wall pipe and that of the thick-wall pipe; R_y is the ratio between the longitudinal yield strength of thin-wall pipe and that of the thick-wall pipe; R_u is the ratio between the longitudinal ultimate tensile strength of the thin-wall pipe and that of the thick-wall pipe.
- If the wall thickness ratio (R_t) is greater than 1.50, the wall thickness ratio should be treated as 1.50 for design and assessment.

Table 4-4 Parameters in studying the effect of pipe strength and wall thickness ratios on the pipe strain capacity

Case #	D	a	2c	h	Thin Pipe					Thick Pipe					Ratios				WM
					Grade	t _{thin}	YS	UTS	Y/T	Grade	t _{thick}	YS	UTS	Y/T	R _G	R _y	R _u	R _t	OM (to pipe UTS)
	in	mm	mm	mm		mm	MPa	MPa			mm	MPa	MPa						
1	36	3	50	0	X70	15.9	558	634	0.88	X65	16.99	524	596	0.88	1.08	1.07	1.06	1.07	1.1
2	36	3	50	0	X70	15.9	558	634	0.88	X65	18.10	492	558	0.88	1.08	1.14	1.14	1.14	
3	36	3	50	0	X70	15.9	558	634	0.88	X65	19.06	471	535	0.88	1.08	1.19	1.19	1.20	
4	36	3	50	0	X70	15.9	558	634	0.88	X65	23.8	471	535	0.88	1.08	1.19	1.19	1.50	

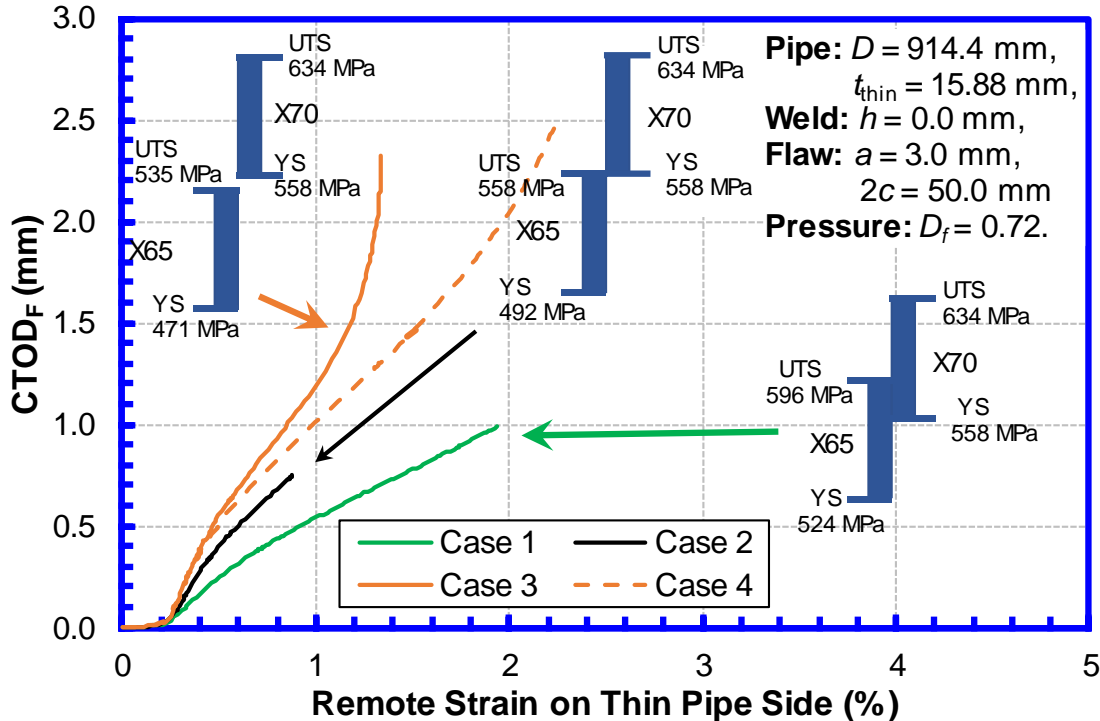


Figure 4-9 Effect of pipe strength and wall thickness ratios on the pipe strain driving force

4.2.4.4 Determination of Transition Weld TSC Reduction Factor

4.2.4.4.1 Definition of TSC Reduction Factor

As discussed in Section 4.2.4.1, a transition weld TSC reduction factor (F_{tw}) was introduced for calculating the TSC of the back-beveled transition welds. The definition of F_{tw} is shown in Figure 4-10.

Figure 4-10 shows the CTOD_F curves of a back-beveled weld and its corresponding regular girth weld. The pipes of the corresponding regular girth weld are identical to the thin pipe of the back-beveled weld (i.e., same dimension and material properties). All the other parameters, e.g., flaw location, flaw size, weld high-low misalignment, weld strength mismatching, and internal pressure, were kept the same for the two CTOD_F curves.

Figure 4-10 shows that the CTOD_F curve of the back-beveled transition weld can be estimated reasonably well by multiplying a factor, $(1 - F_{tw})$, to the remote strain of the CTOD_F curve of the corresponding regular girth weld. The F_{tw} shows the reduction in the TSC of the back-beveled transition weld from its corresponding regular girth weld.

In the following sections, the F_{tw} for the back-beveled transition welds of various parameters were established through parametric finite element analyses (FEA).

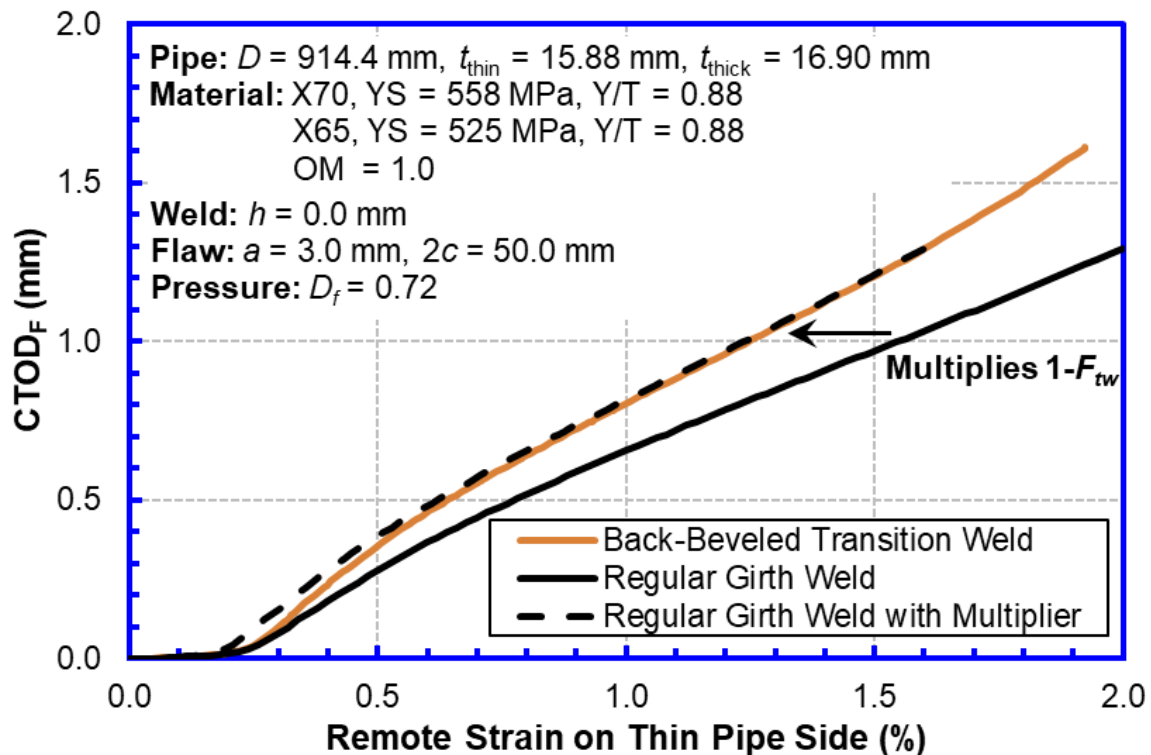


Figure 4-10 Definition of the transition weld reduction factor (F_{tw})

4.2.4.4.2 Parametric Studies

The TSC reduction factor (F_{tw}) can be affected by many factors. A key factor affecting F_{tw} is the yield strength ratio between the thin pipe and thick pipe (R_y). In this section, the relationship

between F_{tw} and R_y was established. The parametric FEA cases used to establish the relationship between F_{tw} and R_y are shown in Table 4-5.

The parametric FEA cases included five groups of studies. For each group, the yield strength ratio R_y was varied from 1.0 to 1.25. The analyses in each group determined the $F_{tw} - R_y$ relationship for a given set of parameters (i.e., flaw size, pipe Y/T ratio, girth weld high-low misalignment, and girth weld strength mismatching⁴ level). One of the parameters listed above was varied in each group to show the effect of that parameter on the $F_{tw} - R_y$ relationship. The parameters were selected since they can affect the TSC greatly based on the previous studies of the TSC of regular girth welds [28].

For all the cases analyzed in Table 4-5, the pipe strength and wall thickness were varied with R_y to meet the minimum requirement given in the enhanced strength and thickness specifications for the back-beveled welds (shown in Section 4.2.4.3). Therefore, for any given R_y , the upper bound F_{tw} (i.e., upper bound TSC reduction) can be obtained.

The detailed pipe material properties and wall thicknesses of the thin and thick pipes for each R_y ratio used in Table 4-5 are listed in Table 4-6 and Table 4-7. The cases with $R_y > 1.0$ were for the back-beveled welds and the cases with $R_y = 1.0$ were for the corresponding regular girth welds.

The full stress-strain curves of the pipe are plotted Figure 4-11. The full stress-strain curves of the weld metal are plotted in Figure 4-12. The UTS of the welds in Group 2 and Group 3 are even-matched to that of the thin-wall pipe, while the UTS of the welds in the rest of the groups are overmatched (1.15) to that of the thin-wall pipe. For reference, the full stress-strain curves of the X70 pipe are also plotted in Figure 4-12. All the stress-strain curves were created using the procedures in [28].

Table 4-5 FEA matrix for $F_{tw} - R_y$ relationship studies

Group ID	$a \times 2c$	h	R_{YT} of Thin Pipe	Mismatch	R_y
	mm \times mm	mm			
1	2.0 \times 25.0	0.0	0.88	1.15	1.00, 1.01, 1.06, 1.25
2	2.0 \times 25.0	0.0	0.88	1.00	
3	3.0 \times 50.0	0.0	0.88	1.00	
4	2.0 \times 25.0	1.6	0.88	1.15	
5	2.0 \times 25.0	0.0	0.92	1.15	

⁴ The weld strength mismatch was defined as the ratio between the UTS of the weld metal and the UTS of the thin-wall pipe.

Table 4-6 Pipe material properties and related ratios for Groups 1-4

Pipe Side		Thin Pipe	Thick Pipe			
			Reference Case	1	2	3
Grade		X70	X70	X65		
R_{YT}		0.88	0.88	0.75	0.88	0.93
YS	MPa	558	558	447	525	554
UTS	MPa	634	634	596	596	596
R_G		N/A	1.00	1.08		
R_y			1.00	1.25	1.06	1.01
R_u			1.00	1.06	1.06	1.06
D	mm	914.4				
t	mm	15.88	15.88	19.85	17.15	17.15
R_t		N/A	1.00	1.25	1.08	1.08

Table 4-7 Pipe material properties and related ratios for Group 5

Pipe Side		Thin Pipe	Thick Pipe			
			Reference Case	1	2	3
Grade		X70	X70	X65		
R_{YT}		0.92	0.92	0.75	0.88	0.93
YS	MPa	558	558	447	525	554
UTS	MPa	607	607	596	596	596
R_G		N/A	1.00	1.08		
R_y			1.00	1.25	1.06	1.01
R_u			1.00	1.02	1.02	1.02
D	mm	914.4				
t	mm	15.88	15.88	19.85	17.15	17.15
R_t		N/A	1.00	1.25	1.08	1.08

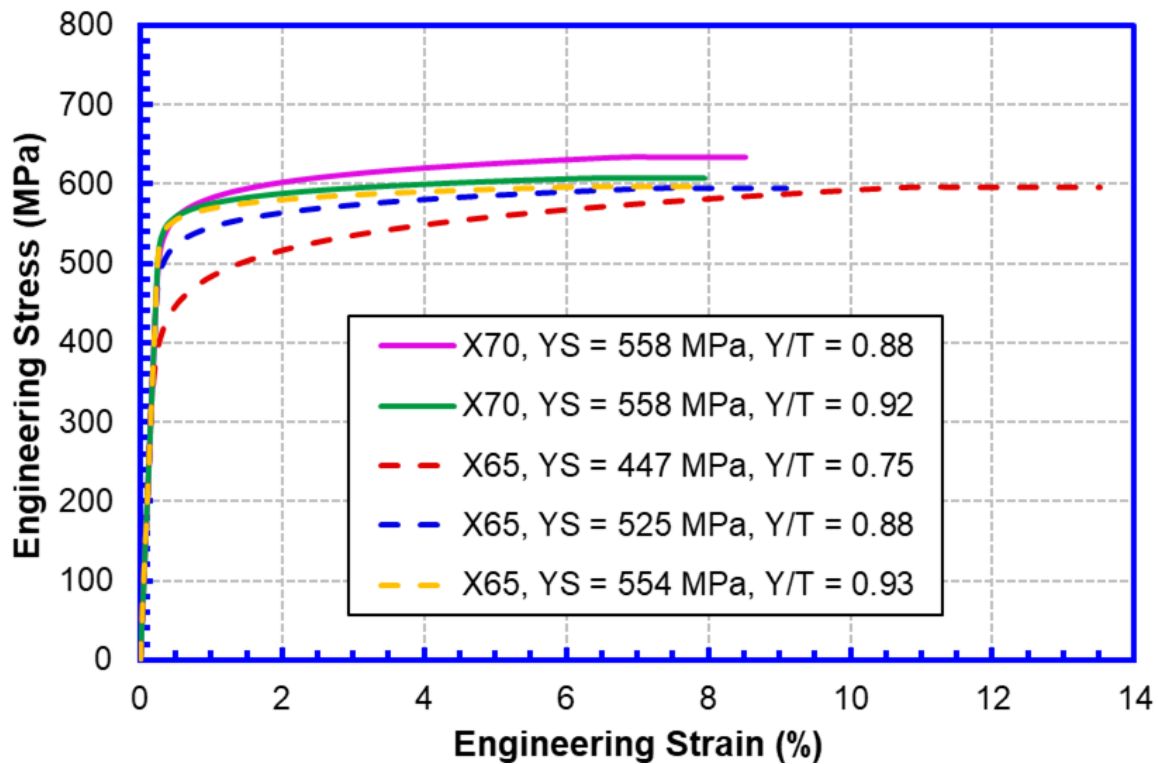


Figure 4-11 Stress-strain curves of pipes

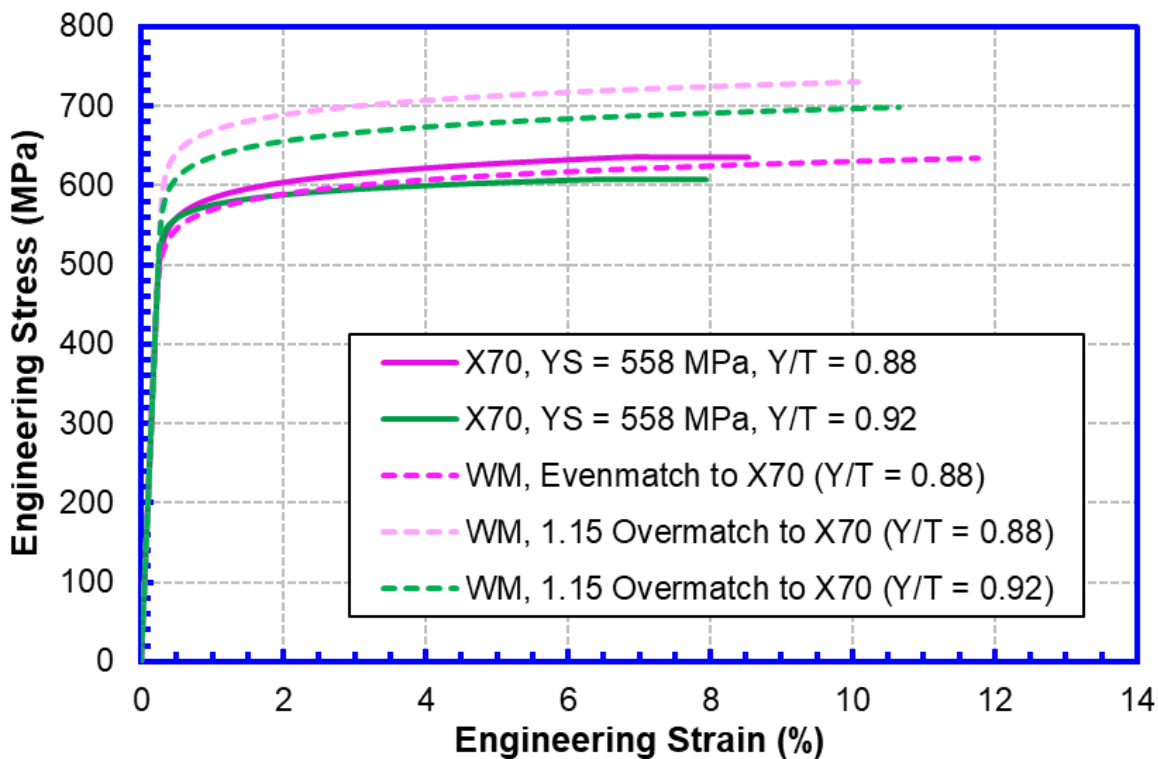


Figure 4-12 Stress-strain curves of thin wall pipes and corresponding weld metals

4.2.4.4.3 Analysis Results

The F_{tw} - R_y relationship obtained from the cases in Table 4-5 is plotted in Figure 4-13. The results show that F_{tw} (TSC reduction factor) increases with R_y (thin-to-thick pipe yield strength ratio), which implies that increasing R_y reduces the tensile strain capacity of back-beveled welds when all the other parameters were kept the same.

By examining the TSC of the reference case (i.e., corresponding regular girth weld) for each group in Table 4-5, it is found that F_{tw} tends to increase with the TSC for the reference case. A nonlinear equation was determined using the analysis data in Figure 4-13 for the transition weld reduction factor (F_{tw}), which is in the form of

$$F_{tw} = 0.1443 \cdot [\max(1.0, R_y) - 1]^{0.4241} (100\epsilon_t^{ref} + 3.053), \quad (4-7)$$

where, ϵ_t^{ref} is the TSC of the corresponding regular girth weld for $\delta_A = 0.8$ mm, i.e., $\epsilon_t^{ref} = \epsilon_t^{crit}|_{\delta_A=0.8 \text{ mm}}$. $\epsilon_t^{crit}|_{\delta_A=0.8 \text{ mm}}$ should be calculated from Eq.(4-1), in which all the input parameters should be determined from the thin-wall pipe.

The transition weld reduction factor (F_{tw}) calculated from the FEA and Eq. (4-7) are plotted in Figure 4-13. The results show that the F_{tw} calculated by Eq. (4-7) match those from the FEA reasonably well.

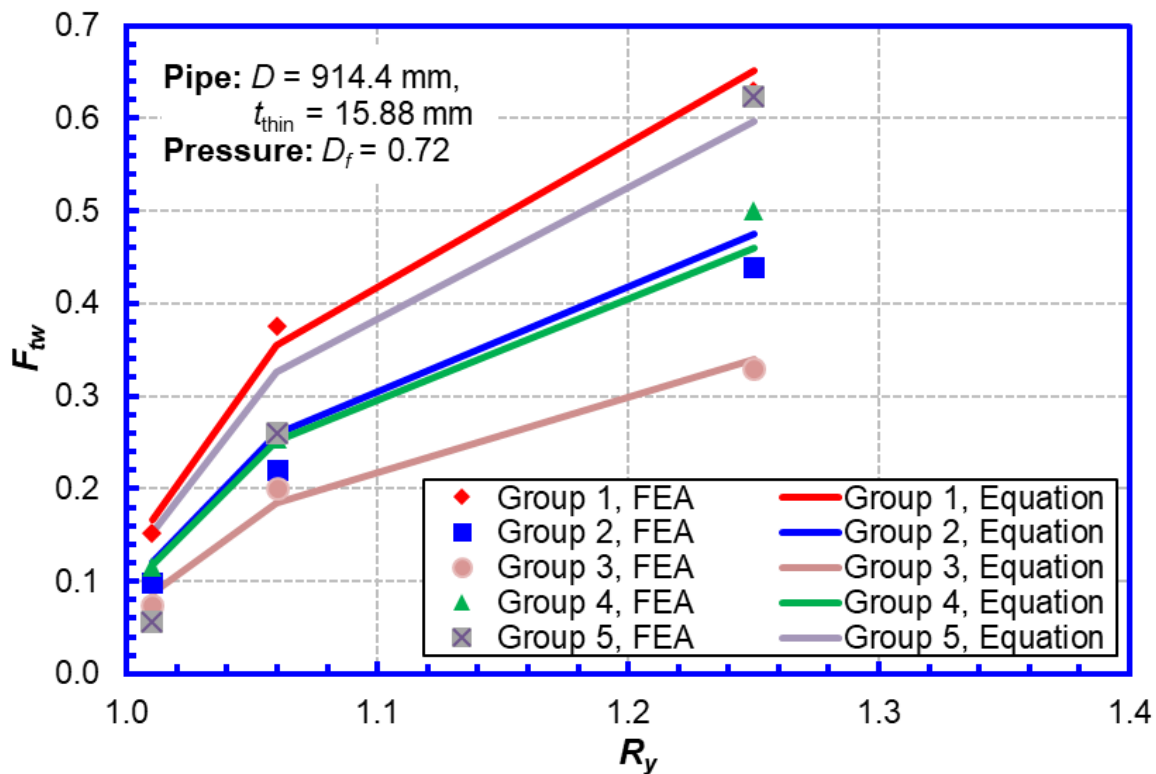


Figure 4-13 Comparison of transition weld reduction factor (F_{tw}) from FEA and Eq. (4-7)

4.2.4.5 Procedures for Assessing TSC of Back-Beveled Welds

For the back-beveled transition welds, the TSC can be evaluated by applying the transition weld reduction factor to the TSC of regular girth welds, i.e.,

$$\varepsilon_{t,tw}^{crit} = \varepsilon_t^{crit}(1 - F_{tw}). \quad (4-8)$$

where, ε_t^{crit} is the TSC of the corresponding regular girth welds given by Eq. (4-1) and F_{tw} is the TSC reduction factor given by Eq. (4-7). The pipe dimensions and properties required for Eq. (4-1) should be determined from the thin-wall pipe. The applicable range of the input parameters are given below:

a/t	0.05 – 0.50,
$2c/t$	1.0 – 20.0,
h/t	0.0 – 0.2,
σ_y/σ_u	0.75 – 0.92,
R_M	1.0 – 1.15,
f_p	0.0 – 0.8,
R_y	1.00 – 1.25,
δ_A	0.2 mm – 2.5 mm (0.0079 in – 0.10 in), and
t	12.7 mm – 25.4 mm (0.50 in – 1.0 in).

In addition to the above parameters, the enhanced pipe strength and thickness specifications for the back-beveled welds (Section 4.2.4.3) should be satisfied, i.e.,

$$\sigma_u^{thick} \geq \sigma_f^{thin}, \text{ and}$$

$$R_t \geq \max(R_G, R_u, R_y).$$

The pipe OD (D) and yield strength (σ_y) are not directly used as input parameters. But, the equations are recommended for the following ranges:

D	304 mm – 1,219 mm (12 in – 48 in) and
σ_y	386 MPa - 690 MPa (56 ksi – 100 ksi).

4.3 Compressive Strain Capacity of Girth Welds

4.3.1 Application and Definition of Compressive Strain Capacity

The compressive strain capacity (CSC) is designated to measure the capacity of a pipe to accommodate global/nominal longitudinal deformation. In the current practice, the CSC is usually defined as the compressive strain at the maximum bending moment the pipe can withstand. After the maximum bending moment is reached, the compressive strain can be highly localized in a small area of the pipe and the pipe capacity to accommodate global longitudinal deformation can become limited. In this project, the CSC was also defined as the compressive strain at the maximum bending moment.

At the maximum bending moment, small wrinkles are often formed in the pipe and therefore strain localization can be found near the wrinkle. In this project, two methods were selected to

measure the CSC. One measures the average strain near the wrinkle, i.e., local CSC. The other measures the strain away from the wrinkle and is extrapolated to the wrinkle location, i.e., global CSC. The local CSC is affected by the strain localization at the wrinkle. The global CSC is not affected by the strain localization at the wrinkle. Details of the definitions and calculations of the CSC can be found in Sections 4.3.4.7.

The pipe integrity is usually determined by comparing strain capacity with strain demand. To properly use the strain capacity determined by this project, the strain demand should be defined consistently with the strain capacity in this project. Otherwise, the assessment results may become either overly conservative or non-conservative.

The local CSC is recommended to be used with the strain demand, which captures the strain localization near a wrinkle, e.g., the strain measured from IMU tools using similar gauge length. The global CSC is recommended to be used with the strain demand, which does not capture the strain localization near a wrinkle, e.g., the strain determined from finite element analyses using beam-type models for the pipe.

4.3.2 Basis of Studies

Many research work related to the compressive strain capacity (CSC) of pipes was published. A thorough review of the work on CSC can be found in [26,27,64]. The work conducted in this project was based on the prior research work sponsored by PHMSA [26]. One of the major outcomes of this PHMSA project is the refined compressive strain models (i.e., CRES models). The refined compressive models are given in the following.

$$\varepsilon_c^{crit,2D} = \min(\varepsilon_u, F_{LD} * \varepsilon_r) \quad (4-9)$$

$$F_{LD} = \begin{cases} 1 - 0.50 * (1 - 0.75\varepsilon_r^{-0.23}) \left[1 + \tanh \left(8.0 \frac{\varepsilon_e}{\varepsilon_r} - 8.2 \right) \right] & \text{(With Lüders Strain)} \\ 1 & \text{(No Lüders Strain)} \end{cases} \quad (4-10)$$

$$\varepsilon_r = F_{DP} * F_{YT} * F_{GI} * F_{NF} \quad (4-11)$$

$$F_{DP} = \begin{cases} 980 * \left[0.5 \left(\frac{D}{t} \right)^{-1.6} + 1.9 * 10^{-4} \right] & \text{if } f_p < f_{pc} \\ 980 * (1.06f_p + 0.5) \left(\frac{D}{t} \right)^{-1.6} & \text{if } f_p \geq f_{pc} \end{cases} \quad (4-12)$$

$$f_{pc} = 1.8 * 10^{-4} * \left(\frac{D}{t} \right)^{-1.6} \quad (4-13)$$

$$F_{YT} = 2.7 - 2.0R_{YT} \quad (4-14)$$

$$F_{GI} = 1.84 - 1.6 \left(\frac{h_g}{t} \right)^{0.2} \quad (4-15)$$

$$F_{NF} = 1.2f_n^2 + 1 \quad (4-16)$$

In the above equations, $\varepsilon_c^{crit,2D}$ is the local CSC, which is the average compressive strain measured in a 2D gauge length centered at the wrinkle location. Details about the definition of

the CSC can be found in Section 4.3.4.7.2. In addition, ε_u is the pipe uniform strain, ε_e is the strain where the Lüders extension ends, and ε_r is a reference strain. The units of $\varepsilon_c^{crit,2D}$, ε_u , ε_e , and ε_r are all %.

In addition, f_p is the pressure factor (i.e., the ratio between the pressure induced hoop stress and the pipe yield strength), h_g is the height (peak to valley) of the pipe manufacturing geometry imperfection, f_n is the net-section stress factor (i.e., the ratio between the longitudinal stress induced by the net-section force and the pipe yield strength), D is the pipe OD, t is the pipe wall thickness, and R_{YT} is the pipe Y/T ratio.

The applicable range of the refined compressive strain models is determined by the range of the parameters used in the finite element analyses. The applicable range of the compressive strain models is given in the following:

- (1) $20 \leq D/t \leq 104$;
- (2) $0.0 \leq f_p \leq 0.80$;
- (3) $0.70 \leq R_{YT} \leq 0.96$;
- (4) $0.01 \leq h_g/t \leq 0.30$;
- (5) $0 \leq \varepsilon_e(\%) \leq 2.0$; and
- (6) $0 \leq f_n \leq 0.40$.

4.3.3 Basic Methods for CSC of Girth Welds

A key finding made in the development of the most recent CSC models is the recognition of the effect of the pipe geometry imperfection on the CSC [24,26,65,66,67,68,69,70]. The pipe geometry imperfection considered in those models is the imperfection generated during pipe manufacturing in the form of non-uniform diameter or wall thickness along the length of a pipe.

For example, the expansion procedure in the typical UOE pipe manufacturing process can generate a wave-like pipe diameter variation along the length of a pipe (referred to as surface undulations) as shown in Figure 4-14. The surface undulations are typically small in magnitude (e.g., $4\%t - 8\%t$ in height), but can be very detrimental to the pipe CSC. Both the height (h_g) and the wavelength (L_g) of the surface undulations were found to be critical to the CSC [26]. Only the surface undulations within a critical wavelength range were found to reduce the CSC greatly. The geometry imperfection of the pipes manufactured without the expansion procedure is usually small and may not have the wave-like shape. In this project, the pipe manufacturing geometry imperfection was modeled as surface undulations and the wavelength of the surface undulations was set within the critical wavelength range.

With proper weld strength overmatching and weld reinforcement (e.g., weld cap), the girth weld generally works as a ring of reinforcement to the pipe, which can prevent pipe cross section distortion. On the other hand, a girth weld is a type of geometry imperfections, which can often initiate wrinkle and buckle formation. Furthermore, the girth weld may interact with the pipe manufacturing geometry imperfection (as shown in Figure 4-15) and further reduce the CSC. Therefore, wrinkles and buckles can be often found very close to girth welds.

The previous studies [26] indicated that at pressurized conditions, the effect of a regular girth weld alone on the CSC was no worse than a $4\%t$ pipe manufacturing geometry imperfection for the weld high-low misalignment up to $50\%t$ and the interaction between the regular girth weld and the pipe manufacturing geometry imperfection was relatively low.

In this work, the transition girth weld was treated as a geometry imperfection. Finite element analyses (FEA) were conducted to examine the effect of the interaction between the transition girth weld and the pipe manufacturing geometry imperfection on the CSC. Equivalent geometry imperfections for transition welds were established.

For transition welds, the FEA were focused on the back-beveled welds. For the counterbore-tapered welds, due to the counterbore length and weld reinforcement effect, the wrinkle location can be pushed further away from the thickness transition, which therefore results in higher CSC than the back-beveled welds. Therefore, the CSC of the counterbore-tapered welds can be conservatively estimated as the CSC of the back-beveled welds.

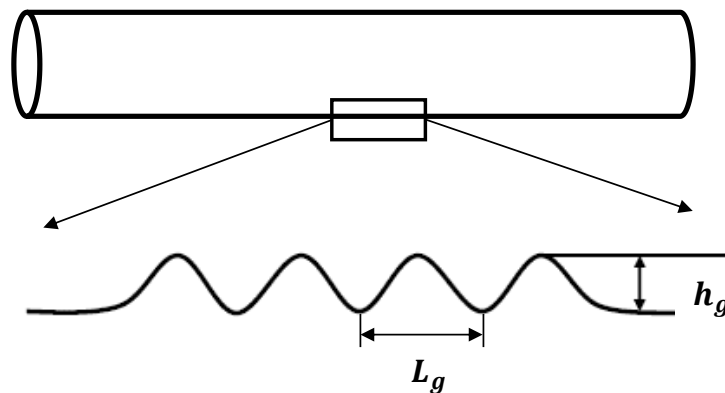


Figure 4-14 Schematic of pipe geometry imperfection

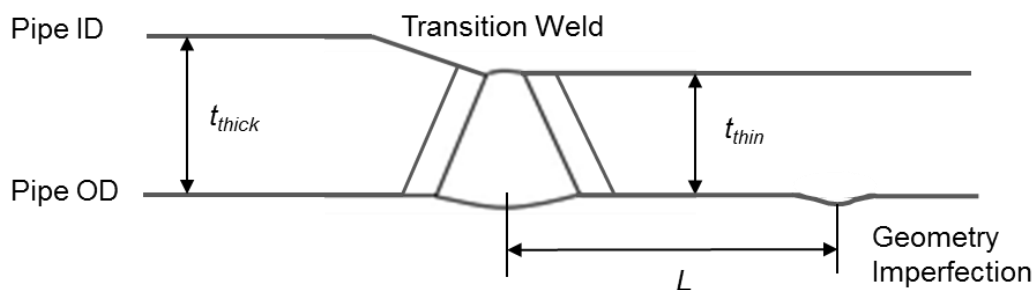


Figure 4-15 Schematic of interaction between transition weld and pipe geometry imperfection

4.3.4 Analysis of Full-Scale Tests and Loading Conditions for Transition Welds

4.3.4.1 Rationale for Proper Loading Conditions

In full-scale tests, when a pipe specimen is pressurized, net-section tensile force is generated by the internal pressure on the end cap. It is known that the net-section tensile force can increase the CSC. To minimize the increase of the CSC due to the net-section tensile force and obtain conservative CSC, external compressive force is often applied to the pipe in full-scale tests or numerical analyses to cancel the pressure induced tensile force.

As shown in Figure 4-16, when a pipe is loaded under the compressive force P (P is along the line connecting the two ends of the pipe) and bending moment M , the moment distribution along the length of the pipe is affected by the so-called P - δ (δ is pipe lateral deflection) effect. The pipe lateral deflection, δ , can induce additional bending moment $P\delta$ to the pipe. As a result, the moment is not uniform along the length of the pipe. The highest moment is reached at the point having the highest lateral deflection.

Since the wrinkle tends to form at the location with the highest bending moment, to test the effect of the girth weld on the CSC, it is ideal to keep the highest moment as close to the girth weld as possible. If the highest moment is far away from the weld, the effect of the weld on the CSC may not be exposed.

For plain pipes and pipes with a regular girth weld (when the girth weld is at the center of the pipe), the pipe lateral deflection is symmetric to the center of the pipe under the loading shown in Figure 4-16. So, the highest moment is reached at the center of the pipe and wrinkles are often found at or near the center of the pipe specimen (and therefore near the girth weld).

However, for pipes with a transition weld, since the deflection of the thick pipe is often much smaller than that of the thin pipe, the location of the highest bending moment is often not at the center of the pipe. In fact, the location of the highest moment depends on the lengths of the thick and thin pipe segments and the loading conditions. Proper specimen designs and loading conditions are needed to keep the highest bending moment close to the transition weld and to expose the effect of the transition weld on the CSC.

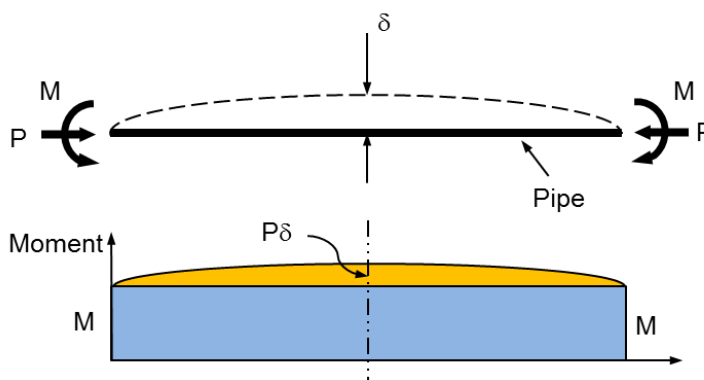


Figure 4-16 Schematics of P-delta effects

4.3.4.2 Loading Conditions for Full-Scale Tests and FEA Assessment Models

Two loading conditions were used in this project. The first condition was used in the full-scale pipe tests (testing load conditions). In the full-scale tests, the bending moment M and the external axial compressive force P were applied to both ends of the pipe specimen (as shown in Figure 4-16). The direction of the force P was along the line connecting the two pipe ends. The external force P was not perfectly aligned with the end cap tensile force once the pipe was deformed.

The other loading condition was used in the numerical analyses for developing assessment models (modeling load conditions). Under the modeling load conditions, the end of the thick pipe was clamped/fixed and a rotation angle (or the bending moment) was applied to the thin

pipe end (as shown in Figure 4-17). The external compressive force P was applied along the direction of the initial pipe axis (length direction). Like the testing load conditions, the external force P was not perfectly aligned with the end cap tensile force once the pipe was deformed. However, it should be noted that under the modeling load conditions, the external force P was not along the line connecting the two pipe ends once the pipe is deformed.

The key difference between the two loading conditions is the direction of the external force P . The direction of the force P affects the moment distribution along the pipe length. Under the testing load conditions, the highest moment is reached at the location with the largest lateral deflection. The location of the largest lateral deflection is affected by the length and the stiffness (depending on pipe diameter, thickness, and strength) of the thick and thin pipes. Therefore, the highest bending moment may not be applied to the girth weld and the effect of the girth weld on the CSC may not be exposed.

For the modeling load conditions, the bending moment gradually decreases from the thick-pipe end to the thin-pipe end. Although the thick pipe experiences high bending moment, the wrinkle is still formed in the thin pipe due to the wall thickness difference. For the thin pipe, the highest bending moment is always at the weld location. Therefore, the effect of the girth weld on the CSC can be exposed.

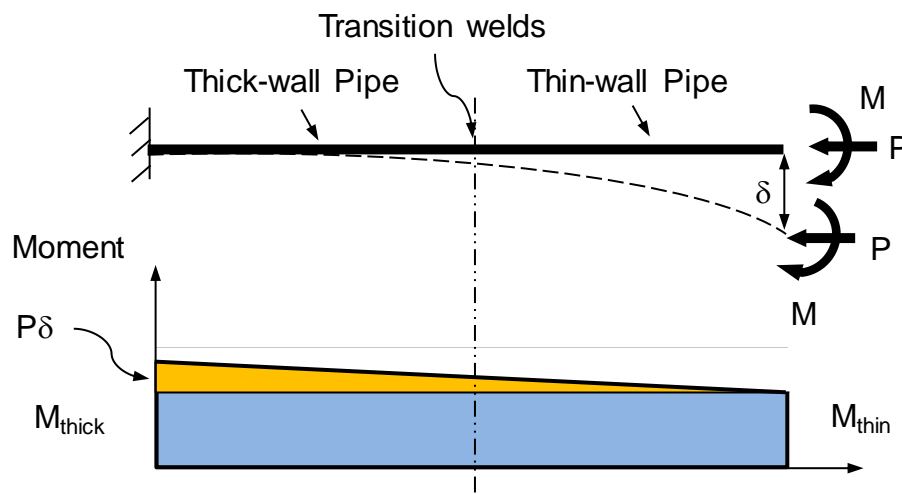


Figure 4-17 Schematics of modeling load conditions

4.3.4.3 Finite Element Analysis Models

Finite element analyses (FEA) were conducted to simulate the full-scale tests and to examine the effect of the loading conditions on the CSC. Two FEA models were created to simulate the two loading conditions discussed in Section 4.3.4.2.

The FEA model for the testing load conditions is shown in Figure 4-18. The pipe sizes and loading conditions were the same as those in the full-scale tests (Section 3.2). The length of the thin- and thick-wall pipe is $3.75D$ and $4.75D$, respectively. The compressive force was applied on the pipe end to compensate the pressure induced tensile force. Connector elements were used to apply the compressive force along the line connecting the two pipe ends.

The FEA model for the modeling load conditions is shown in Figure 4-19. The length of the thin- and thick-wall pipe is same and equal to $3D$. The total length of the pipe in the FEA model was $6D$. The pipe length was long enough to avoid the effect of boundary conditions at the pipe ends on the stress/strain near the transition weld. The compressive force was applied on the pipe end along the initial pipe axis (i.e., horizontal) direction.

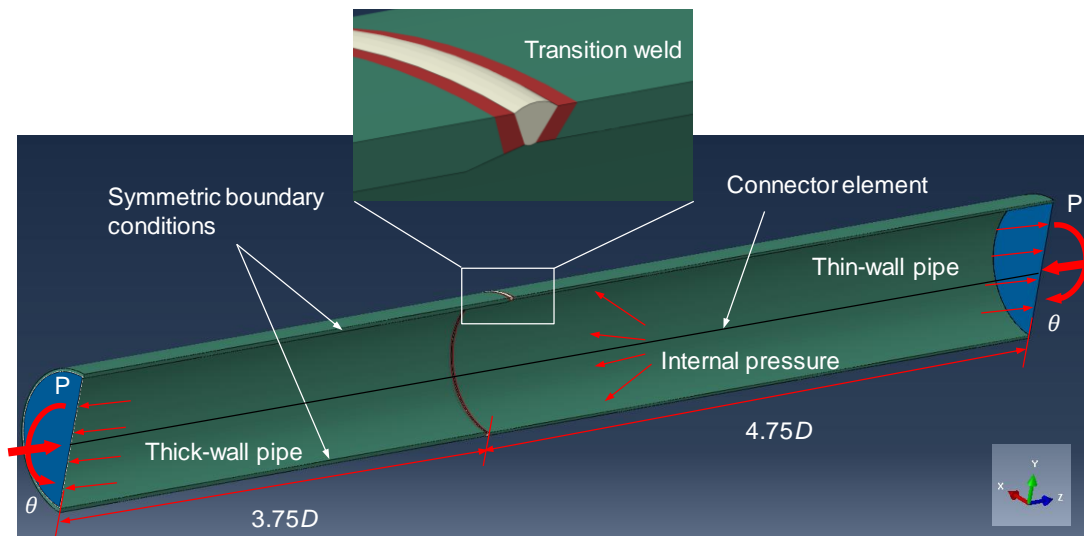


Figure 4-18 Example FEA model for transition welds under the testing load conditions

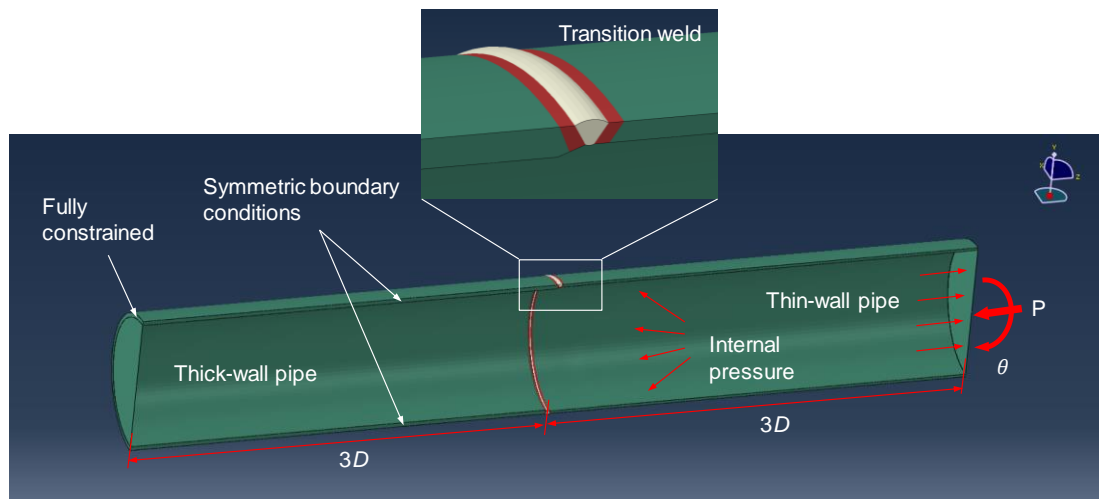


Figure 4-19 Example FEA model for transition welds under the modeling load conditions

The commercial FEA software ABAQUS® was used for the analyses. For both models (i.e., the testing and modeling load conditions), due to symmetry conditions, only one half of the pipe (i.e., full length, half circumference) was modeled. Both regular girth welds and back-beveled welds were analyzed. To capture the geometry of the weld, the pipe was modeled using 3D solid elements (C3D8RH) and large-strain formulation. The weld profiles are shown in Figure 4-20.

The pipe outer diameter (D) is 323.85 mm (12.75 in). For the regular girth welds, the pipe wall thickness is 6.35 mm (0.25 in). For the back-beveled welds, the wall thickness of the thick-

and thin-wall pipes is 9.525 mm (0.375 in) and 6.35 mm (0.25 in), respectively, which gives the wall thickness ratio of 1.5. The end caps were modeled on both pipe ends.

The effect of the mesh size on the analysis results was thoroughly examined. The element was refined adequately to obtain converged (mesh independent) solutions and the element size in the pipe longitudinal and circumferential direction was determined as about 2.16 mm ($D/150$) and 8.48 mm, respectively. Six layers of elements were used through the wall thickness.

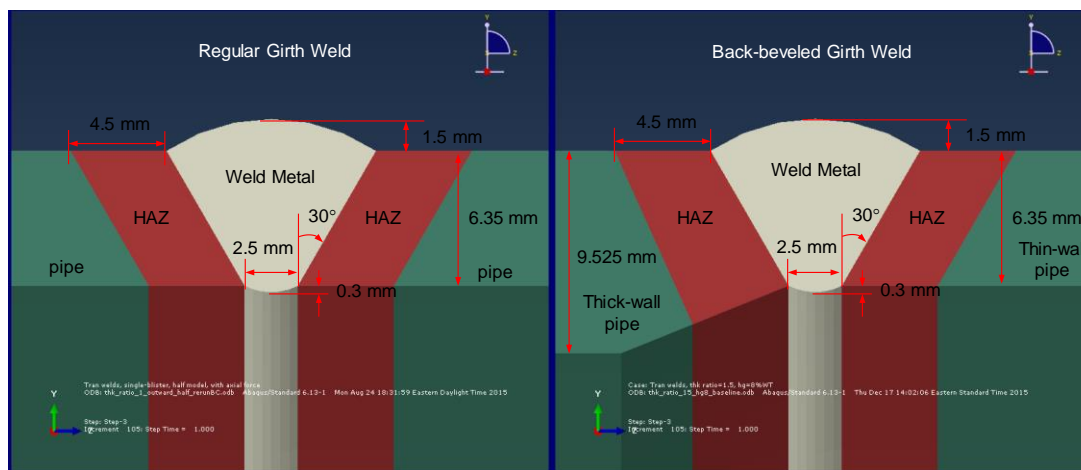


Figure 4-20 Weld profile of regular girth weld and back-beveled girth weld used in FEA

4.3.4.4 Material Properties

The grades of the thick- and thin-wall pipes are both X65. When the FEA were conducted, the small-scale test data of the pipe materials were not available. The material properties from the Mill certificates were used to create the full stress-strain curve for the FEA. The stress-strain curve was created using the pipe yield and ultimate tensile strengths following the procedures developed in [7,28]. The same material properties were used for the thick- and thin-wall pipes: yield strength of 471 MPa (68.3 ksi), ultimate tensile strength of 535 MPa (77.6 ksi). The Y/T ratio is equal to 0.88.

The created full stress-strain curve is shown in Figure 4-21. The comparison of the stress-strain curves obtained from the small-scale tests and those used in FEA is shown in Figure 4-32 in Section 4.3.4.8.

4.3.4.5 Analysis Steps

To simulate the loading sequence used in the full-scale tests, three loading steps were used in the FEA:

Step 1: pressurize the pipe to reach the hoop stress of 72% SMYS;

Step 2: apply a longitudinal compression force to cancel the pressure induced longitudinal tension force on the end cap; and

Step 3: bend the pipe by applying a rotation angle at the thin-wall pipe end.

For the testing load conditions, the longitudinal compression force in Step 2, was applied along the line connecting the two ends of the pipe. While, for the modeling load conditions the longitudinal compression force was applied along the initial pipe axis.

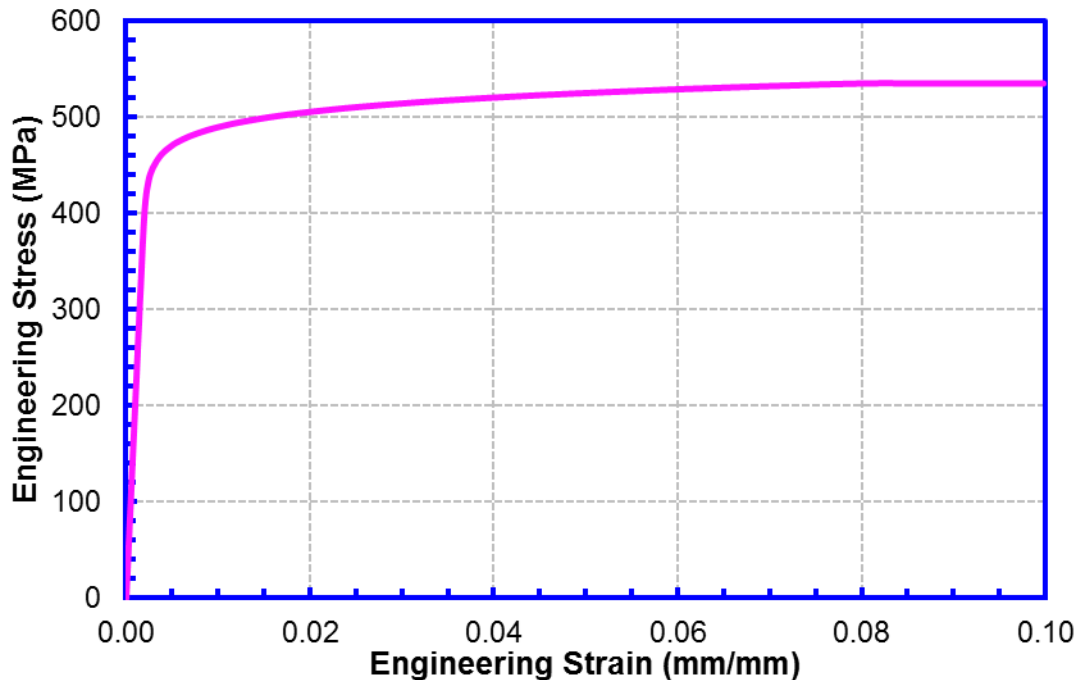


Figure 4-21 Full stress-strain curve used in FEA for X65 pipe

4.3.4.6 Typical Strain Contours

Figure 4-22 shows a typical strain contour when the bending moment at the wrinkle reaches the maximum value for the modeling load conditions. The thick-wall pipe does not deform a lot and the high compressive strain occurs at the bottom of the thin-wall pipe. Small wrinkles are formed close to the transition welds in the thin-wall pipe and strain localization is found near the wrinkle.

Figure 4-23 shows the distribution of the longitudinal strain along the length of the pipe at the bottom of the pipe OD surface. The results also show that the strain in the thick-wall pipe is much smaller than the strain in the thin-wall pipe. The strain in the thin-wall pipe is used in the subsequent numerical parametric studies for developing the CSC assessment models.

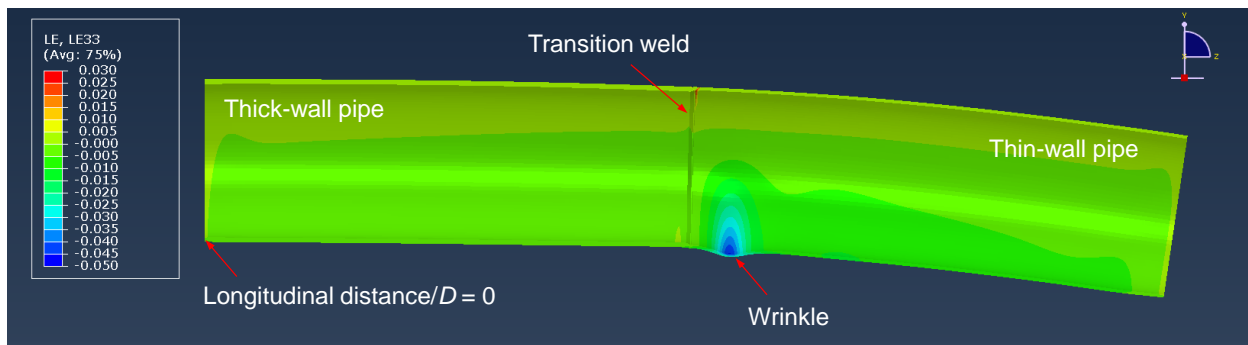


Figure 4-22 Typical longitudinal strain contour on deformed pipe with transition welds under the modeling load conditions

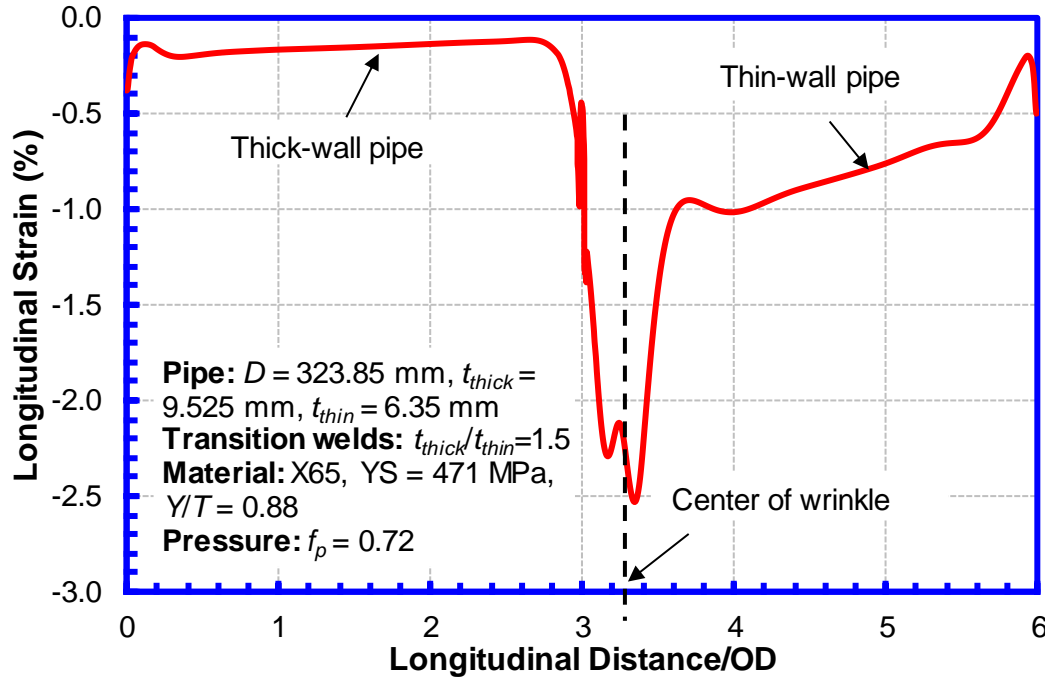


Figure 4-23 Typical longitudinal strain distribution along the length of the pipe with transition welds under the modeling load conditions

4.3.4.7 Calculation of Compressive Strain Capacities

4.3.4.7.1 General Discussions

As discussed in Section 4.3.1, two definitions of the compressive strain capacity (CSC) were used in this project: local CSC and global CSC. Both CSC were determined when the bending moment at the center of the wrinkle reached the maximum value. The detailed procedures for calculating the CSC from the FEA are given in the following sections.

The procedures for the regular girth welds are given in Section 4.3.4.7.2 and the procedures for the transition girth welds are given in Section 4.3.4.7.3. The procedures for the regular girth welds are also used for calculating the CSC for pipes with dents and corrosion anomalies.

4.3.4.7.2 Regular Girth Welds

For the regular girth welds, the local CSC is measured by 2D CSC ($\epsilon_{c,gw}^{crit,2D}$). The 2D CSC ($\epsilon_{c,gw}^{crit,2D}$) is the average compressive strain measured within a $2D$ (D is the pipe outer diameter) gauge length centered at the wrinkle, as shown in Figure 4-24. The 2D CSC ($\epsilon_{c,gw}^{crit,2D}$) should be calculated using the following equation:

$$\epsilon_{c,gw}^{crit,2D} = \epsilon_t - D * (\theta_2 - \theta_1) / l_0 \quad (4-17)$$

where ϵ_t is the tensile strain on the tensile side of the pipe, θ_1 and θ_2 (in the unit of rad) are the rotation angles of the pipe cross sections at the end of the gauge length, l_0 ($= 2D$) is the gauge length, and D is the pipe outer diameter.

Depending on the method to determine the tensile strain (ϵ_t) and rotation angles (θ_1, θ_2), the 2D CSC ($\epsilon_{c,gw}^{crit,2D}$) can be calculated with one of the methods given below. The CSC calculated

from all the methods were found to be similar. For all experimental tests, both the Method 1 (Option 2) and Method 2 were used. In the FEA, all the methods were used. If not mentioned otherwise, the reported CSC from the FEA was calculated with Method 1 (Option 1).

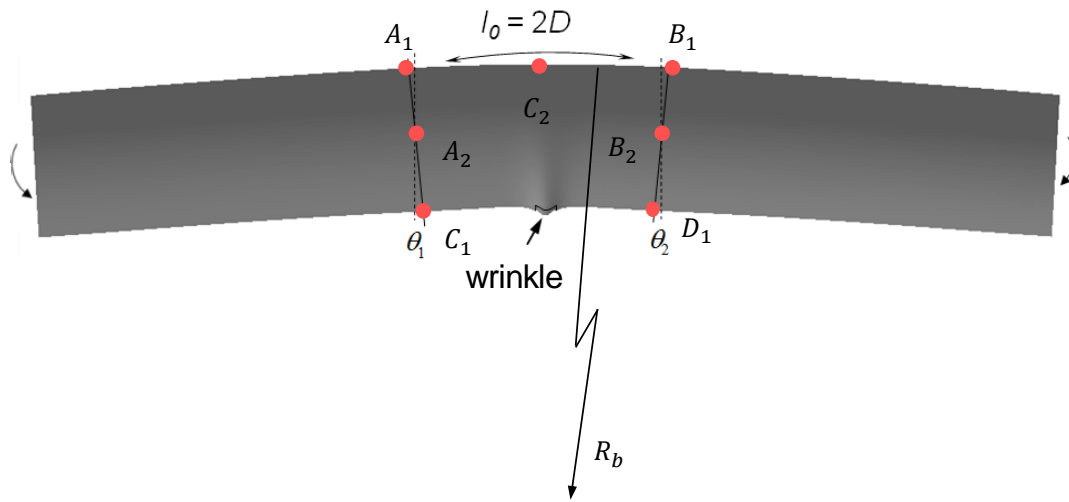


Figure 4-24 Calculation of 2D CSC

- Method 1 (Option 1):

The tensile strain (ε_t) is calculated as the average strain within the gauge length on the tensile side of the pipe by assuming the deformed pipe is a part of a circle with the radius of R_b , as shown in Figure 4-24. The radius (R_b) and rotation angles (θ_1 and θ_2) are determined using the coordinates of the four points (A_1 , B_1 , C_1 and D_1) as shown in Figure 4-24. The tensile strain (ε_t) is calculated by the following equation:

$$\varepsilon_t = R_b * (\theta_2 - \theta_1) / l_0 - 1 \quad (4-18)$$

- Method 1 (Option 2):

The tensile strain (ε_t) is determined as the strain at the center of the gauge (Point C_2) on the tension side of the pipe, as shown in Figure 4-24. The rotation angles (θ_1 and θ_2) are measured at the middle height of the pipe (Points A_2 and B_2), as shown in Figure 4-24.

- Method 2:

The 2D CSC ($\varepsilon_{c,gw}^{crit,2D}$) is directly calculated using the displacement of two points (one is $1D$ to left and the other is $1D$ to the right of the center of the wrinkle) on the bottom side of the pipe (Points C_1 and D_1), as shown in Figure 4-24.

The global CSC is determined from the strain distribution in the area sufficiently away from the wrinkle (remote strain zone) by extrapolating the strain along the outermost compressive fiber of the pipe to the wrinkle location (Figure 4-25). The remote strain zone is one pipe diameter (D) wide and $0.4D$ away from the last strain valley from the center of the wrinkle. In the FEA, due to symmetry conditions, the strain can be measured from the pipe on any side of the girth weld. In the full-scale tests, the strain should be measured from both sides and the averaged strain should be used.

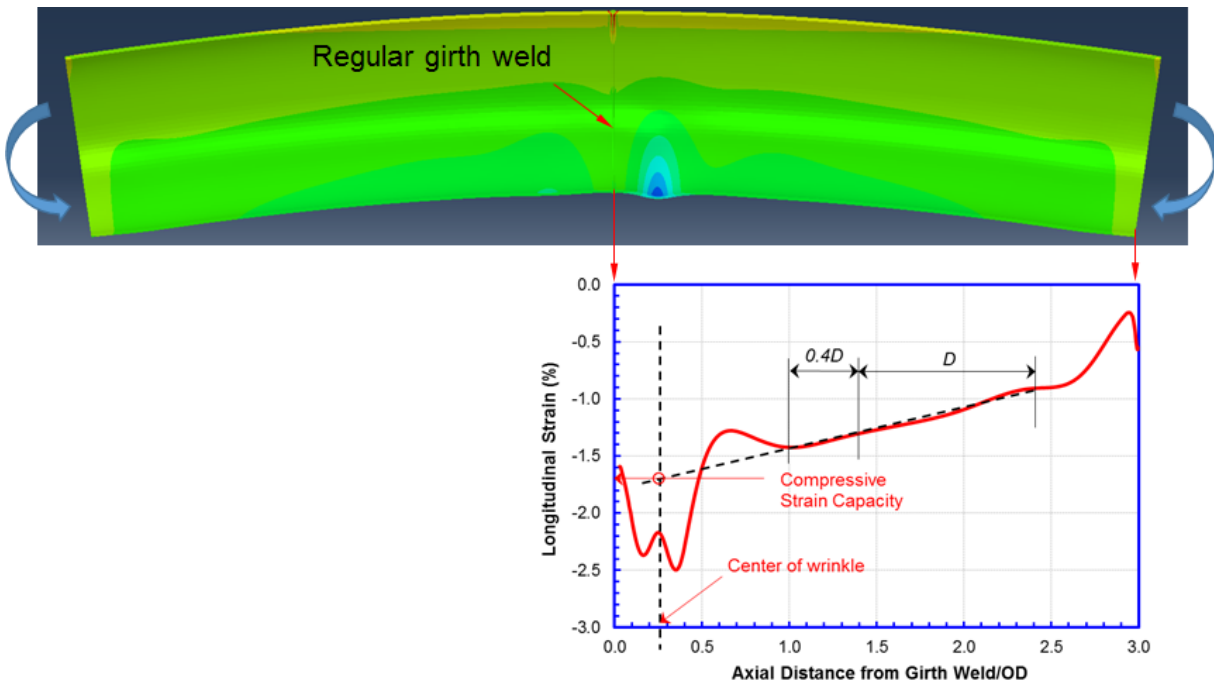


Figure 4-25 Calculation of CSC by extrapolation for regular girth weld

4.3.4.7.3 Transition Welds

For the transition welds, since most strain is found in the thin-wall pipe, the local CSC is defined using the strain in the thin pipe. Equivalent to the 2D CSC ($\varepsilon_{c,gw}^{crit,2D}$) of the regular girth welds, the local CSC of the transition welds is measured as the average compressive strain within a $1D$ gauge length with one end of the gauge at the center of the wrinkle and the other end $1D$ away in the thin-wall pipe, as shown in Figure 4-26. The local CSC of the transition welds is referred to as the 1D single-side CSC, i.e., 1DS CSC ($\varepsilon_{c,tw}^{crit,1DS}$). The 1DS CSC ($\varepsilon_{c,tw}^{crit,1DS}$) should be calculated using the following equation.

$$\varepsilon_{c,tw}^{crit,1DS} = \varepsilon_t - D * (\theta_2 - \theta_1) / l_0 \quad (4-19)$$

where ε_t is the tensile strain on the tensile side of the pipe, θ_1 and θ_2 are the rotation angles of the pipe cross sections at the end of the gauge length, $l_0 (= 1D)$ is the gauge length, and D is the pipe outer diameter.

Depending on the method used to determine the tensile strain (ε_t) and the rotation angles (θ_1 , θ_2), the 1DS CSC ($\varepsilon_{c,tw}^{crit,1DS}$) can be calculated with one of the methods given below. The CSC calculated from all the methods were found to be similar. For all experimental tests, the Method 2 was used. In the FEA, all the methods were used. If not mentioned otherwise, the reported CSC for the FEA was calculated with Method 1 (Option 1).

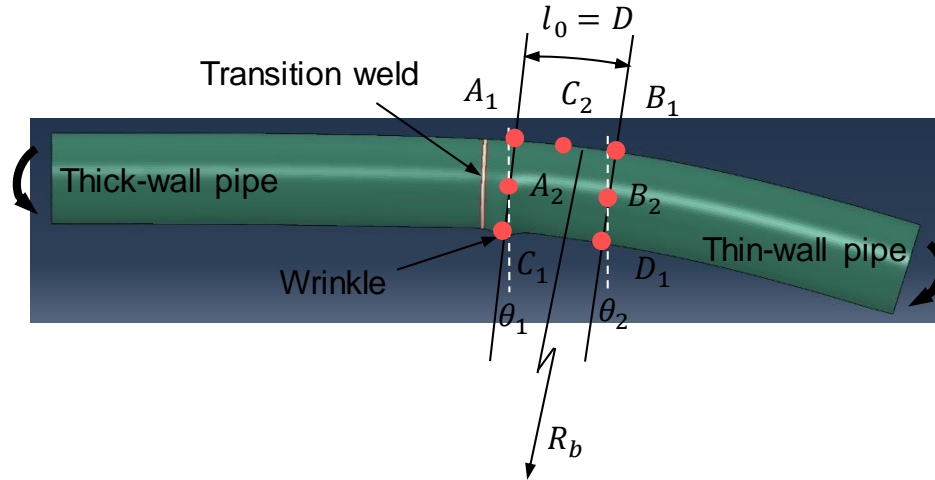


Figure 4-26 Calculation of 1DS CSC for transition welds

- Method 1 (Option 1):

The tensile strain (ε_t) is calculated as the average strain within the gauge length on the tensile side of the pipe by assuming the deformed pipe is a part of a circle with the radius of R_b , as shown in Figure 4-26. The radius (R_b) and rotation angles (θ_1 and θ_2) are determined using the coordinates of the four points (A_1 , B_1 , C_1 and D_1) as shown in Figure 4-26. The tensile strain (ε_t) is calculated by the following equation:

$$\varepsilon_t = R_b * (\theta_2 - \theta_1) / l_0 - 1 \quad (4-20)$$

- Method 1 (Option 2):

The tensile strain (ε_t) is determined as the strain at the center of the gauge (Point C_2) on the tension side of the pipe, as shown in Figure 4-26. The rotation angles (θ_1 and θ_2) are measured at the middle height of the pipe (Points A_2 and B_2), as shown in Figure 4-26.

- Method 2:

The 1DS CSC ($\varepsilon_{c,tw}^{crit,1DS}$) is directly calculated using the displacement of two points (one at the center of the wrinkle and the other is $1D$ away in the thin pipe) on the bottom side of the pipe (Points C_1 and D_1), as shown in Figure 4-26.

The global CSC of the transition welds ($\varepsilon_{c,tw}^{crit,ex}$) is determined from the strain distribution in the remote strain zone in the thin-wall pipe by extrapolating the strain along the outermost compressive fiber of the thin-wall pipe to the wrinkle location (Figure 4-27). The remote strain zone is one pipe diameter (D) wide and $0.4D$ away from the last strain valley from the center of the wrinkle.

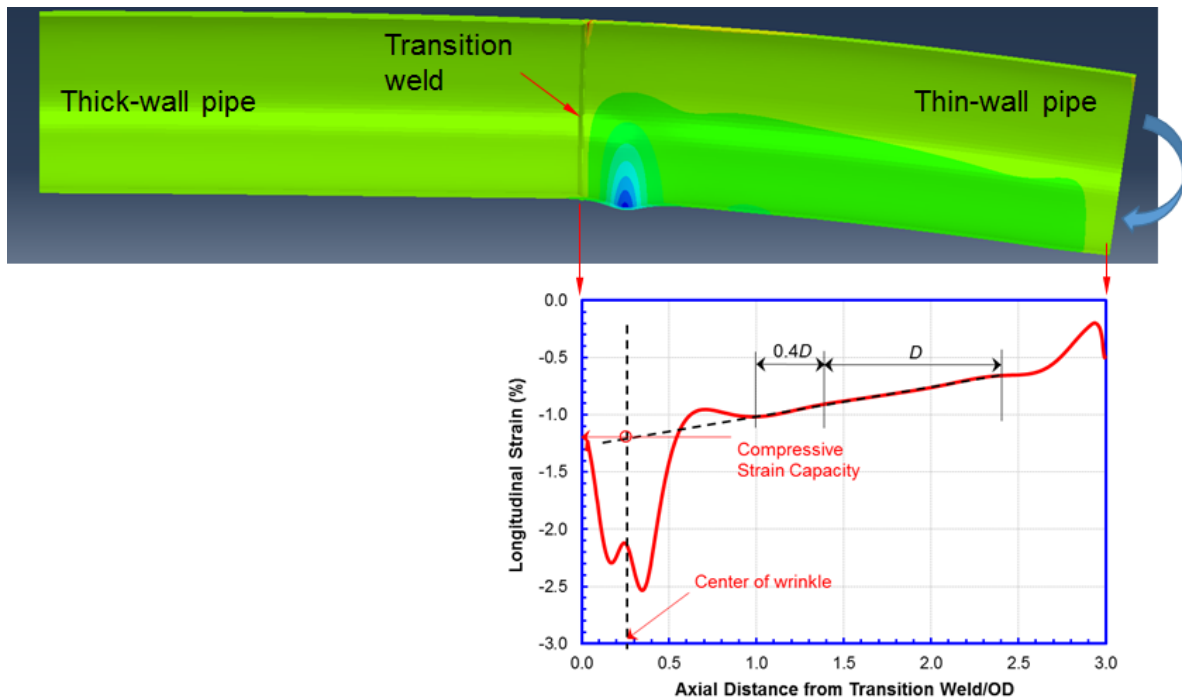


Figure 4-27 Calculation of CSC by extrapolation for transition welds

4.3.4.8 Comparison of CSC between Tests and FEA

Three full-scale tests were done for girth welds: Transition 1 (regular girth weld), Transition 2 (back-beveled weld) and Transition 3 (counterbore-tapered weld). The details of the full-scale tests can be found in Section 3.2. The 2D CSC or 1DS CSC from the full-scale tests were determined using the Method 2 in Sections 4.3.4.7.2 and 4.3.4.7.3 and summarized as “1D Axial One sided VIC Strain” in Table 3-6 in Section 3.2.7.

The CSC by extrapolation from the full-scale tests were determined using the methods shown in Sections 4.3.4.7.2 and 4.3.4.7.3. For example, the determination of the CSC by extrapolation ($\epsilon_{c,tw}^{crit,ex}$) for the full-scale test Transition 2 is shown in Figure 4-28. The remote strain zone used for the strain extrapolation is about $0.8D$ wide and $0.6D$ away from the last strain valley from the center of the wrinkle. The remote strain zone is slightly adjusted to avoid the strain variation caused by the strain gauge, which is about $1.2D$ from to the wrinkle in the axial direction.

The CSC obtained from the full-scale tests are shown in Figure 4-29 (1DS CSC, $\epsilon_{c,tw}^{crit,1DS}$) and Figure 4-30 (CSC by extrapolation, $\epsilon_{c,tw}^{crit,ex}$). The CSC calculated by FEA (for both testing and modeling load conditions) are also shown in Figure 4-29 and Figure 4-30. It should be noted that all the FEA were conducted for the back-beveled welds.

Under the testing load conditions, the FEA results (red triangular marker in Figure 4-29 and Figure 4-30) show no CSC reduction for the transition weld with a wall thickness ratio of 1.5 compared with the CSC of the regular girth weld. The CSC obtained from the full-scale tests (Transitions 1 and 2) showed a consistent trend (i.e., no CSC reduction) with the FEA results.

As discussed in Section 4.3.3, the counterbore-tapered welds are expected to have higher CSC than the back-beveled welds, which is also consistent with the test results (Transitions 2 and 3).

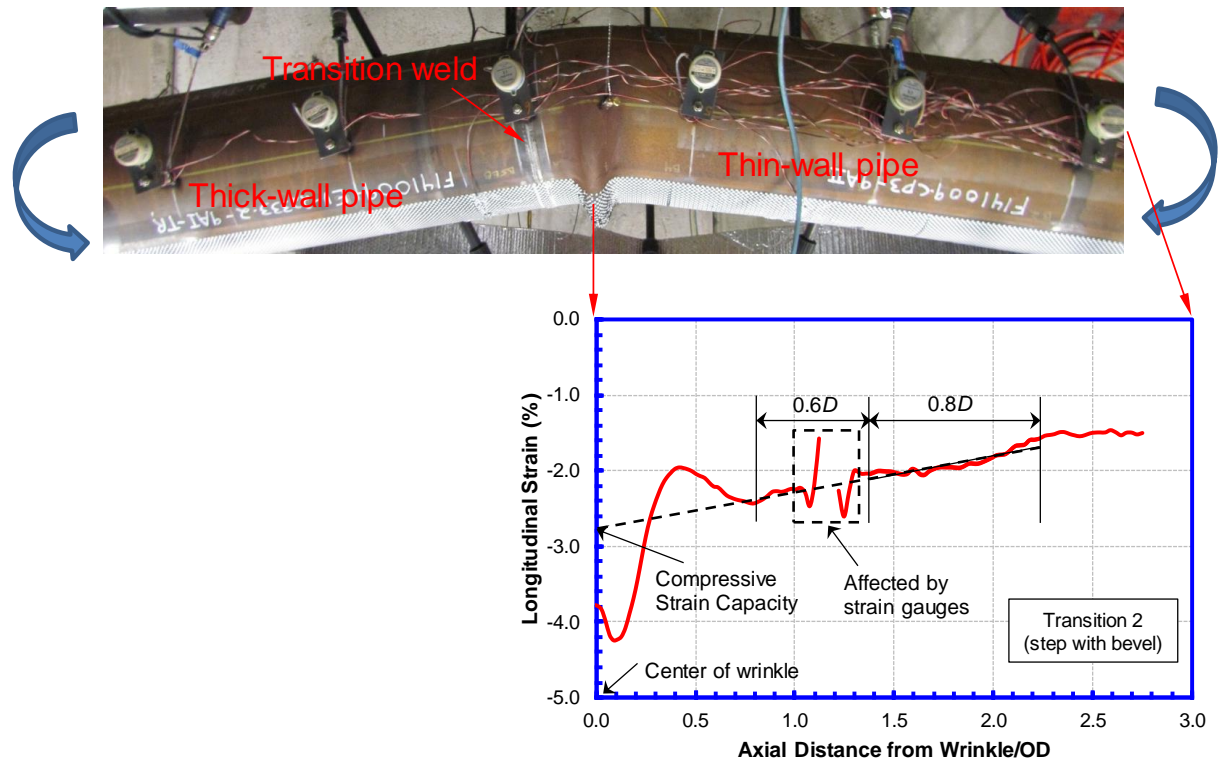


Figure 4-28 Calculation of CSC by extrapolation from full-scale tests

However, under the modeling load conditions, the FEA results (blue square marker in Figure 4-29 and Figure 4-30) show a large CSC reduction for the transition weld with a wall thickness ratio of 1.5 compared with the CSC of the regular girth weld. As discussed in Section 4.3.4.2, the two loading conditions can generate different bending moment distributions along the pipe. Figure 4-31 shows the bending moment distribution along the pipe length under the testing and modeling load conditions. The results show that under the testing load conditions, the maximum bending moment is located at about $1D$ away from the transition weld. Under the modeling load conditions, the maximum bending moment is located right at the transition weld.

The above results show that proper loading conditions are important to capture the true effect of the transition welds on the CSC. The loading conditions used in this project for the full-scale tests of the transition welds are not adequate to show the effect of the transition weld on the CSC and the effect of the transition weld on the CSC was underestimated. Therefore, the modeling load conditions were used in all the FEA aimed at developing the assessment models.

The comparison of the testing and FEA (under the testing load conditions) results shows that the CSC calculated by the FEA is about 20% lower than the test results (Transitions 1 and 2). As shown in later sections, similar difference between the tests and FEA can be found in all bending tests using the same pipe (X65-ERW-1). It is believed that the difference in the measured and calculated CSC was caused by the difference between the material properties used in FEA and the actual material properties.

The pipe used in those tests had some unique features in its stress-strain curves as a function of clock position, which were not captured in the FEA. Figure 4-32 shows the comparison of the stress-strain curves measured from the small-scale tests and used in FEA. The pipe shows much higher strength for the 6 o'clock position than that for the 3 o'clock position. The clock position is measured with respect to the seam weld (i.e., the seam weld is at 12 o'clock position).

In the full-scale tests, the seam weld was positioned near the neutral axis and the materials at the 3 o'clock position were on the outermost compressive fiber (as shown in Figure 4-33). The pipe properties were assumed to be uniform in the FEA and the stress-strain curve used in the FEA was close to the stress-strain curves measured at the 3 o'clock position. Thus, the FEA can capture the pipe behavior on the outermost compressive fiber. However, the FEA didn't capture the high strength materials at the neutral axis (6 o'clock position), which in the actual tests, can prevent pipe ovalization and increase the CSC. As a result, this is, in part, responsible for the observed differences in the measured and calculated CSC.

In addition, the stress-strain curves from the small-scale tests exhibited a finite Lüders strain (~ 2.0%), while the stress-strain curve used in the FEA had a round-house shape. Based on the previous studies [26], the omission of the Lüders strain could also be, in part, responsible for the observed differences in the measured and calculated CSC.

Furthermore, the strain hardening capacity (e.g., pipe Y/T ratio) used in the FEA was similar to that measured from the uni-axial tensile stress-strain curves. The small-scale tests showed that the compressive stress-strain curves had higher strain hardening capacity than the tensile stress-strain curves. Since the CSC is mainly determined by the compressive strain hardening capacity, the FEA may underestimate the CSC due to the underestimation of the strain hardening capacity.

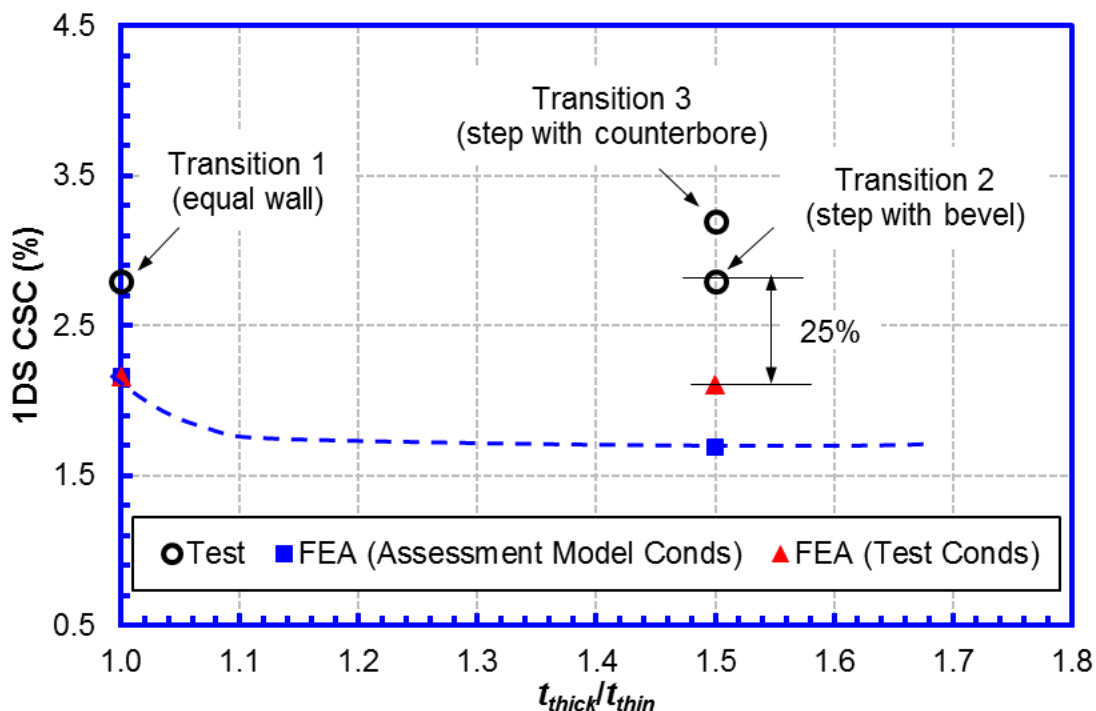


Figure 4-29 1DS CSC of transition welds from test and FEA

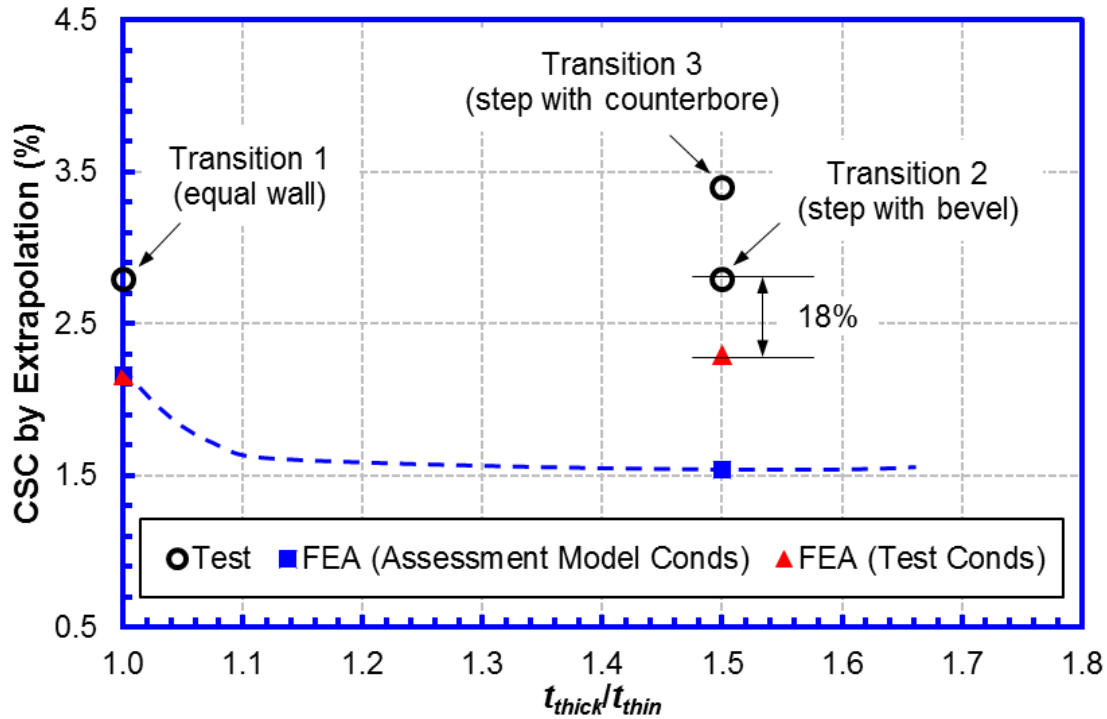


Figure 4-30 CSC by extrapolation of transition welds from test and FEA

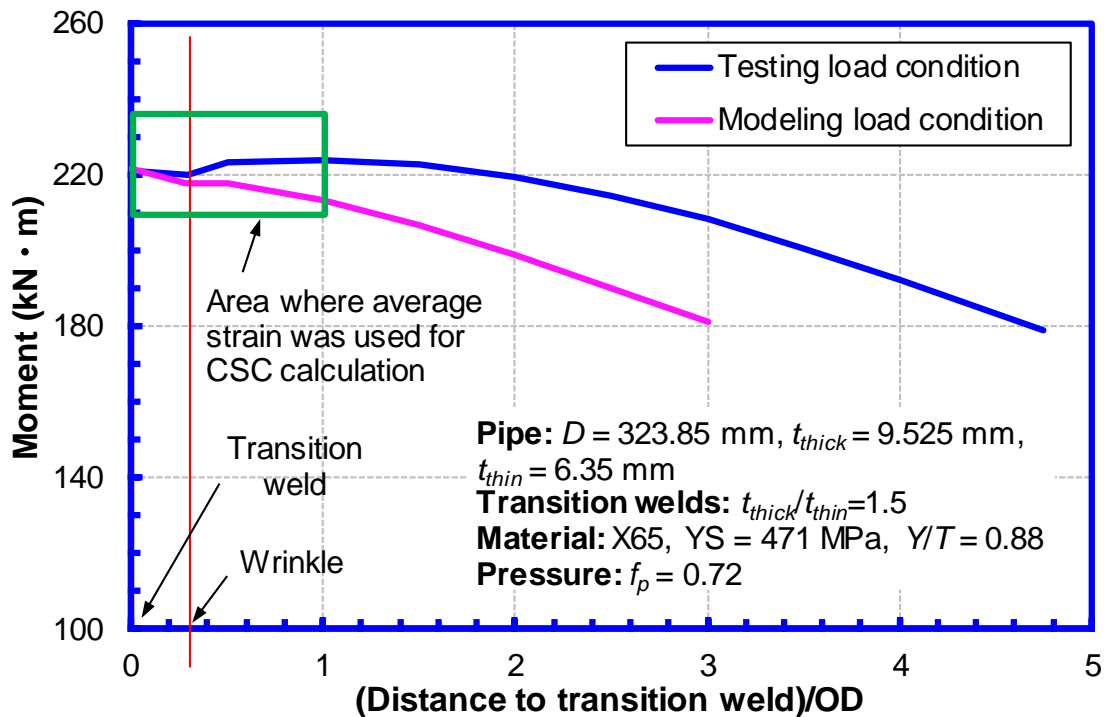


Figure 4-31 Moment distribution along the pipe length from FEA under the testing and modeling load conditions

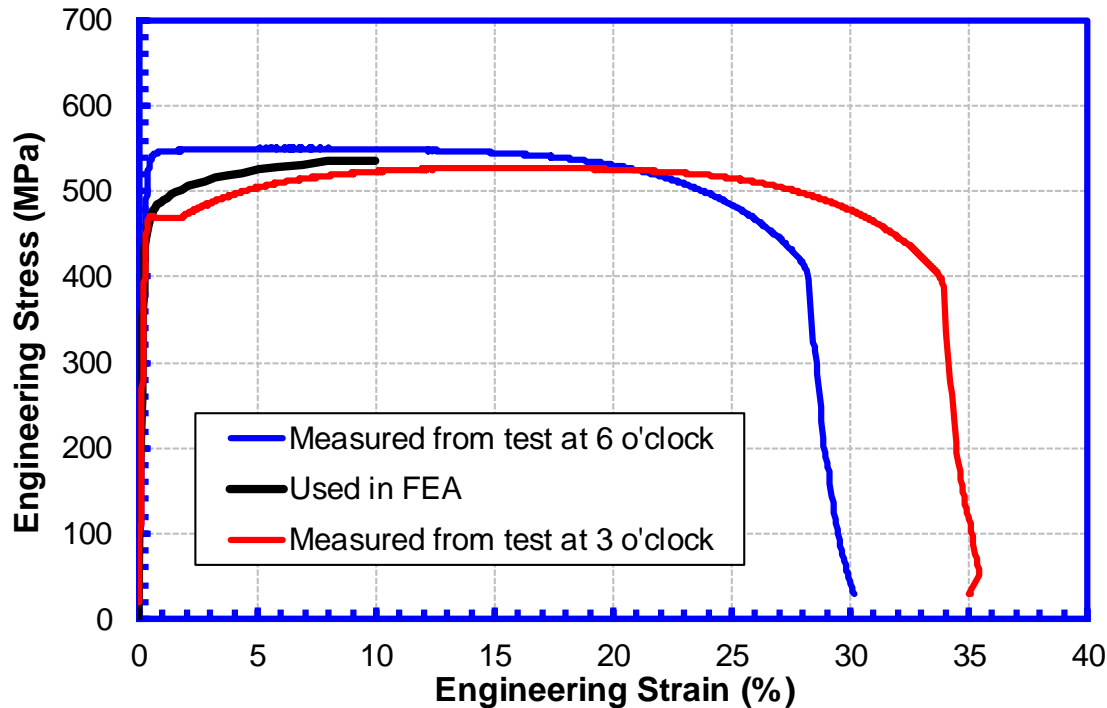


Figure 4-32 Stress-strain curves used in FEA and measured from the small-scale tests

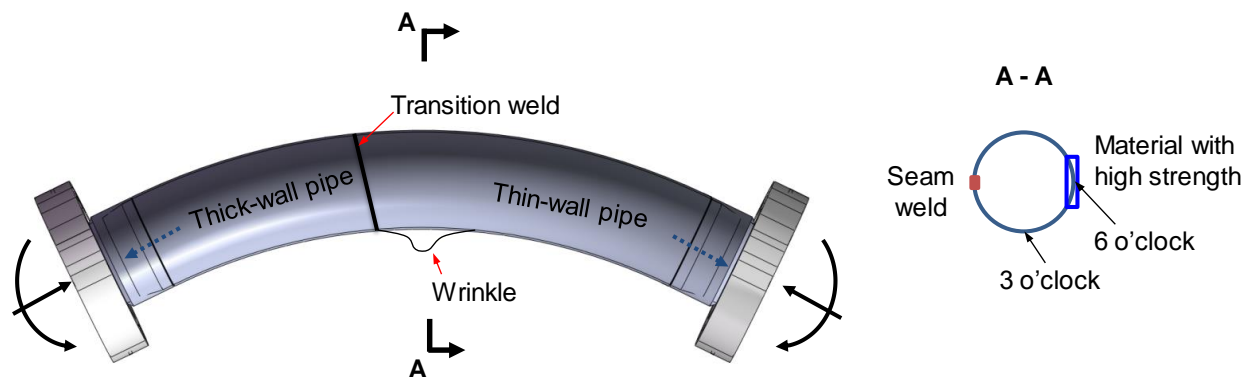


Figure 4-33 Schematics of the full-scale tests of transition welds

4.3.5 Parametric Studies

4.3.5.1 Overview of Parametric Studies

Parametric studies were conducted to investigate the effects of various parameters including the pipe wall thickness ratio (t_{thick}/t_{thin}), weld high-low misalignment (h), internal pressure, pipe geometry imperfection, pipe diameter-wall thickness ratio (D/t_{thin}), and pipe strain hardening capacity (Y/T), on the CSC of the transition welds. The objectives of the parametric studies are to gain better understanding on the key factors, which can affect the CSC of the transition welds and develop equivalent geometry imperfections of the transition welds.

Finite element analyses (FEA) were used for the parametric studies. The FEA models and procedures used in the parametric studies are similar to those introduced in Section 4.3.4.3 to 4.3.4.5. As shown in previous sections, for the transition welds, the strain in the thick-wall pipe

is primarily elastic and the actual stress-strain curve of the thick-wall pipe has minor effect on the calculated CSC. Therefore, in the parametric studies, the stress-strain curve of thick-wall pipe was assumed to be the same with that of the thin-wall pipe.

4.3.5.2 Pipe Wall Thickness Ratio

The purpose of the studies in this section is to understand the effect of the pipe wall thickness ratio on the CSC of the transition welds. The input parameters used in the FEA are shown in Table 4-8. Figure 4-34 shows the FEA results for the 1DS CSC and the CSC by extrapolation with respect to the pipe wall thickness ratio. The input parameters used in FEA are also shown in the figure.

Figure 4-34 reveals that the transition welds lead to a reduction in CSC in comparison to the regular girth welds. The CSC rapidly decreases as the wall thickness ratio increases from 1.0 to 1.1. However, further reduction in the CSC beyond the wall thickness ratio of 1.1 is minimal. Therefore, the following analyses were focused on the cases with the wall thickness ratio of 1.5.

Table 4-8 Input parameters of parametric studies of pipe wall thickness ratio

Key Parameter	t_{thick}/t_{thin}	h	D/t_{thin}	Y/T	f_p	h_g/t_{thin}
		mm				
Value	1, 1.1, 1.2, 1.5, 1.75	0	51	0.88	0.72	0.08

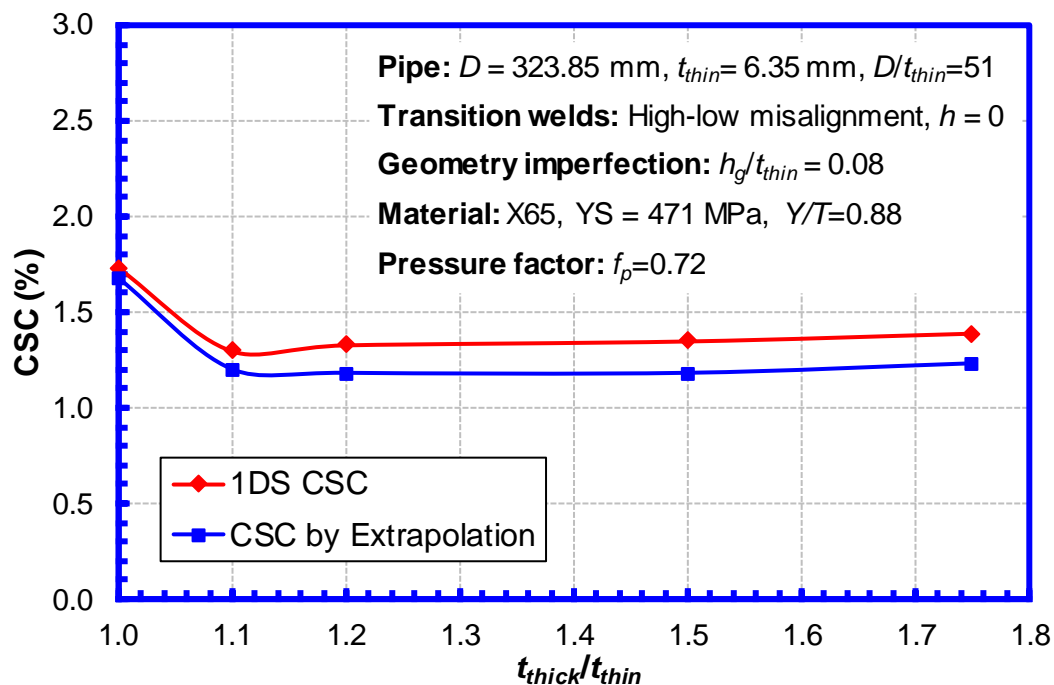


Figure 4-34 CSC of transition welds with different wall thickness ratios

4.3.5.3 Weld High-Low Misalignment

In the previous PHMSA project [26], the weld high-low misalignment showed minor effects on the CSC of the regular girth welds. To study the effect of the weld high-low misalignment on

the CSC of the transition welds, finite element analyses were conducted for the transition welds with 0.0 and 1.6 mm (25% t) high-low misalignment.

Figure 4-35 shows the transition weld profile with the weld high-low misalignment. Table 4-9 shows the input parameters and the calculated 1DS CSC and CSC by extrapolation. Similar to the results for the regular girth welds, the CSC of the transition welds with and without high-low misalignment are very similar. The results confirm that the weld high-low misalignment has limited effects on the CSC of the girth welds. Therefore, the following analyses were conducted without weld high-low misalignment.

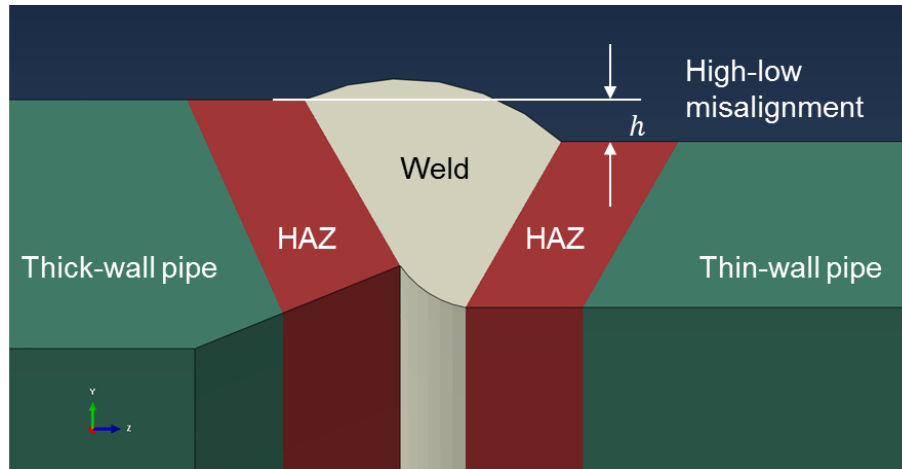


Figure 4-35 Transition weld with high-low misalignment

Table 4-9 CSC of transition welds with different high-low misalignment

h	t_{thick}/t_{thin}	D/t_{thin}	Y/T	f_p	h_g/t_{thin}	1DS CSC	CSC by Extra.
mm						%	%
0	1.5	51	0.88	0.72	0.08	1.36	1.16
1.6						1.32	1.20

4.3.5.4 Internal Pressure

The purpose of the studies in this section is to understand the effect of the internal pressure on the transition-weld induced CSC reduction. Finite element analyses (FEA) were conducted for the regular and transition welds under both pressurized ($f_p = 0.72$) and non-pressurized ($f_p = 0.0$) conditions. The wall thickness ratio (t_{thick}/t_{thin}) of the transition welds was kept at 1.5. Table 4-10 shows the input parameters used in the FEA and the CSC calculated from the FEA. The FEA were not conducted for the regular girth welds under non-pressurized conditions.

The CSC equations for plain pipes (pipes without girth welds or anomalies such as corrosion or dents), i.e., Eq. (4-9), were also used to calculate the CSC of plain pipes. The thin-wall pipe properties were used and the pipe manufacturing geometry imperfection was set at 8% t (same as the FEA). The 2D CSC of the plain pipe under non-pressurized and pressurized conditions were determined to be 0.92% and 1.89%, respectively.

As expected, the results show that the internal pressure increases the CSC. More importantly, under non-pressurized conditions, the 1DS CSC of the transition weld (0.91%) is very close to the 2D CSC of the plain pipe (0.92%). The result indicates that under the non-pressurized conditions, the interaction between the transition weld and the pipe manufacturing geometry imperfection is minimal.

However, under the pressurized conditions ($f_p = 0.72$), the 1DS CSC of the transition weld (1.36%) is much smaller than the 2D CSC of the regular weld (1.73%) and the 2D CSC of the plain pipe (1.89%). The result indicates that the internal pressure can magnify the interaction between the girth welds and the pipe manufacturing geometry imperfection. Therefore, the following analyses were conducted under the pressurized conditions.

Table 4-10 CSC of girth welds under pressurized and non-pressurized conditions

Girth Weld	f_p	h	D/t_{thin}	Y/T	h_g/t_{thin}	CSC by Extra.	2D or 1DS CSC
		mm				%	%
Regular	0	0	51	0.88	0.08	NA	NA
Transition						0.74	0.91
Regular	0.72					1.68	1.73
Transition						1.16	1.36

4.3.5.5 Pipe Manufacturing Geometry Imperfection

4.3.5.5.1 Overview

As discussed in Section 4.3.3, the transition weld may interact with the pipe manufacturing geometry imperfection and the interaction may further reduce the CSC. The purpose of the studies in this section is to understand the interaction between the transition weld and the pipe manufacturing geometry imperfection and to understand how the interaction changes with pipe D/t ratio (Section 4.3.5.5.2) and Y/T ratio (Section 4.3.5.5.3).

4.3.5.5.2 Pipe Diameter-Wall Thickness Ratio

In this section, the effect of the pipe D/t ratio on the interaction between the transition weld and pipe manufacturing geometry imperfection was studied. The pipe D/t ratio was calculated with the thin-wall pipe thickness, i.e., D/t_{thin} . The input parameters are shown in Table 4-11.

Two pipe D/t_{thin} ratios were studied (51 and 72) and for both cases, the pipe wall thickness ratio, t_{thick}/t_{thin} , was kept as 1.5. For $D/t_{thin} = 51$, the pipe OD and thin-pipe wall thickness is 323.85 mm (12.75") and 6.35 mm (0.25"), respectively. For $D/t_{thin} = 72$, the pipe OD and thin-pipe wall thickness is 914.4 mm (36") and 12.7 mm (0.5"), respectively.

Figure 4-36 and Figure 4-37 show the FEA calculated 1D CSC and CSC by extrapolation for the transition welds as a function of the D/t_{thin} ratio, respectively. The input parameters used in the FEA are also given in the figures. As expected, the results show that the CSC decreases with the increase of the geometry imperfection and D/t_{thin} ratio.

More importantly, for the two pipes of different D/t_{thin} ratios, the trends of the relationship between the CSC and pipe manufacturing geometry imperfection are very similar. The results for both D/t_{thin} ratios show that the CSC gradually (linearly) decreases with the increase of the normalized geometry imperfection (h_g/t_{thin}). The results indicate that the interaction between the transition weld and pipe manufacturing geometry imperfection is not greatly affected by the pipe D/t_{thin} ratios.

4.3.5.5.3 Pipe Strain Hardening Capacity

In this section, the effect of the pipe Y/T ratio on the interaction between the transition weld and pipe manufacturing geometry imperfection was studied. The pipe Y/T ratio was measured from the thin-wall pipe. The input parameters are shown in Table 4-12.

Two Y/T ratios were used in the studies (0.88 and 0.77). The stress-strain curve of the pipe with $Y/T = 0.88$ was from the X65 pipe with the yield strength of 471 MPa and ultimate tensile strength of 535 MPa (as shown in Figure 4-21). The stress-strain curve of the pipe with $Y/T = 0.77$ was created based on an X42 pipe with the yield strength of 320 MPa and ultimate tensile strength of 415 MPa.

Figure 4-38 and Figure 4-39 show the FEA calculated 1DS CSC and CSC by extrapolation of the transition welds as a function of the pipe geometry imperfection, respectively. The input parameters used in the FEA are also shown in the figures. As expected, the results show that the CSC of the transition welds decreases with the increase of pipe geometry imperfection and Y/T ratio.

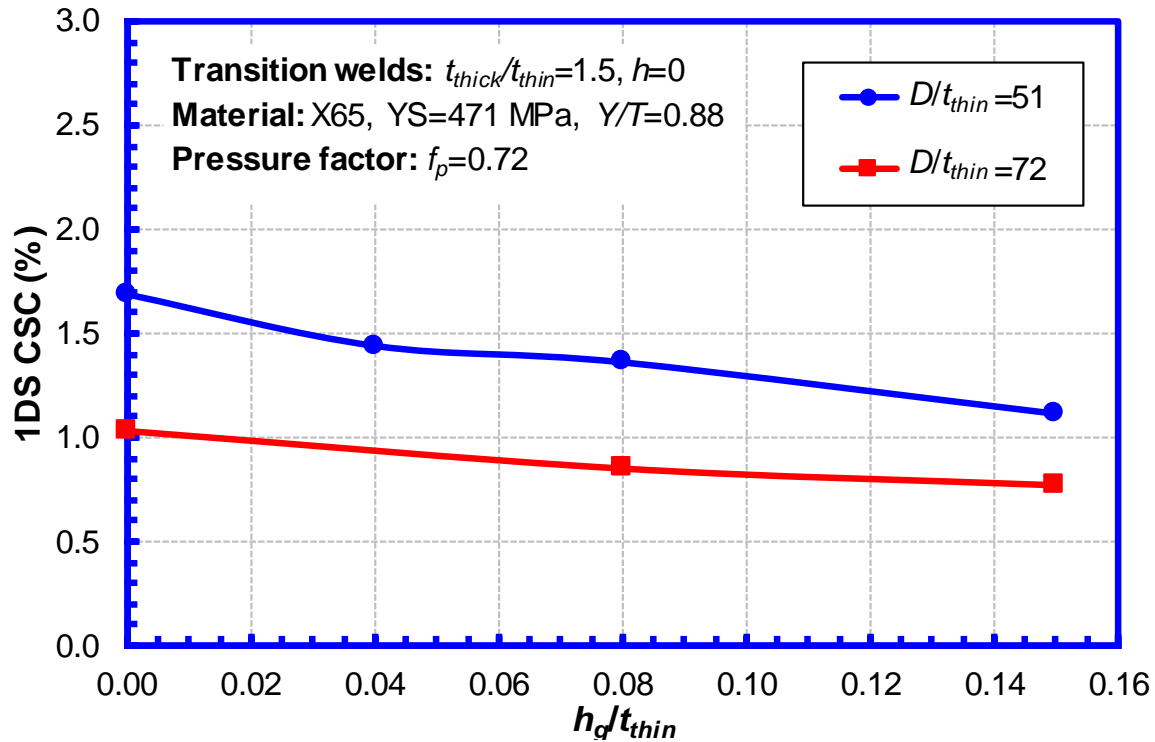
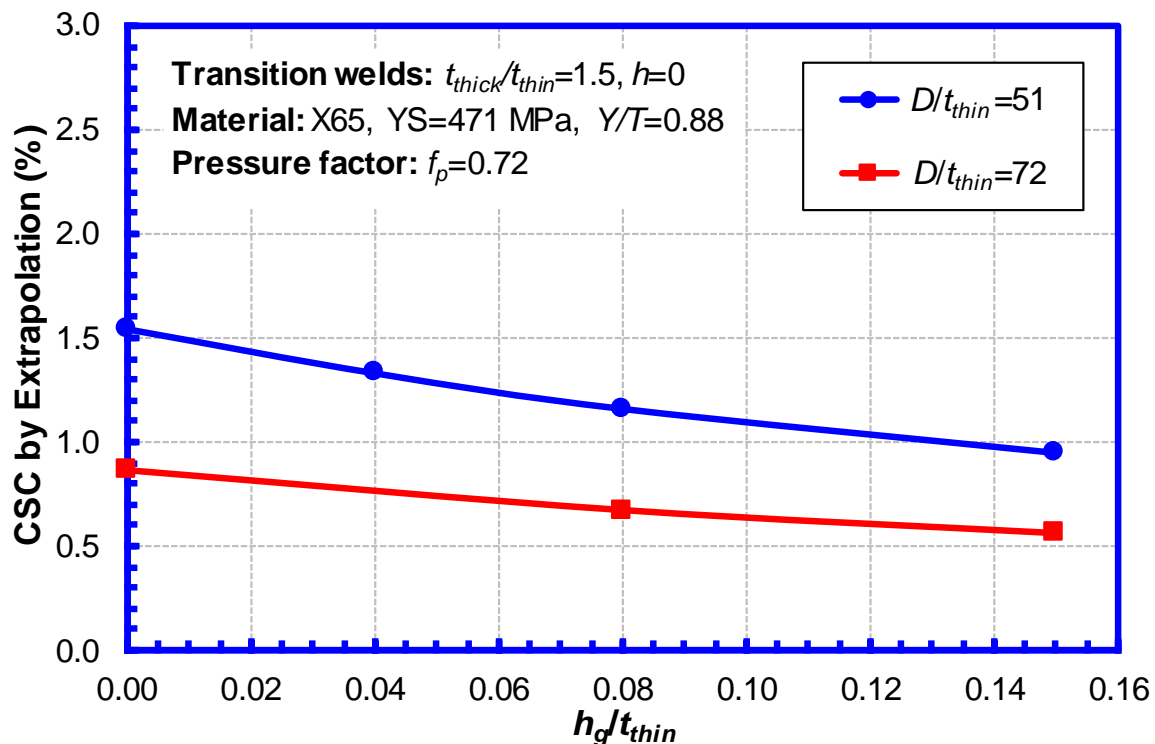
More importantly, for the two pipes with different Y/T ratios, the trends of the relationship between the CSC and pipe manufacturing geometry imperfection are very similar. The results for both pipe Y/T ratios show that the CSC gradually (linearly) decreases with the increase of the normalized geometry imperfection (h_g/t_{thin}). The results indicate that the interaction between the transition weld and pipe manufacturing geometry imperfection is not greatly affected by the pipe Y/T ratios.

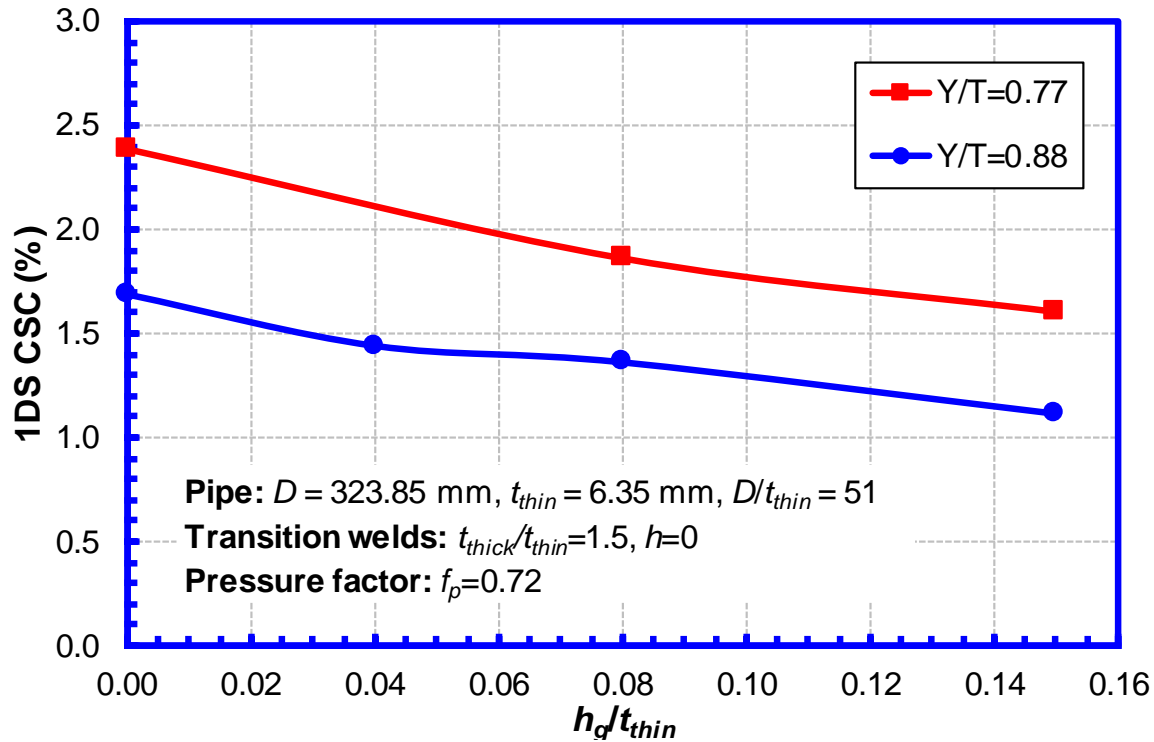
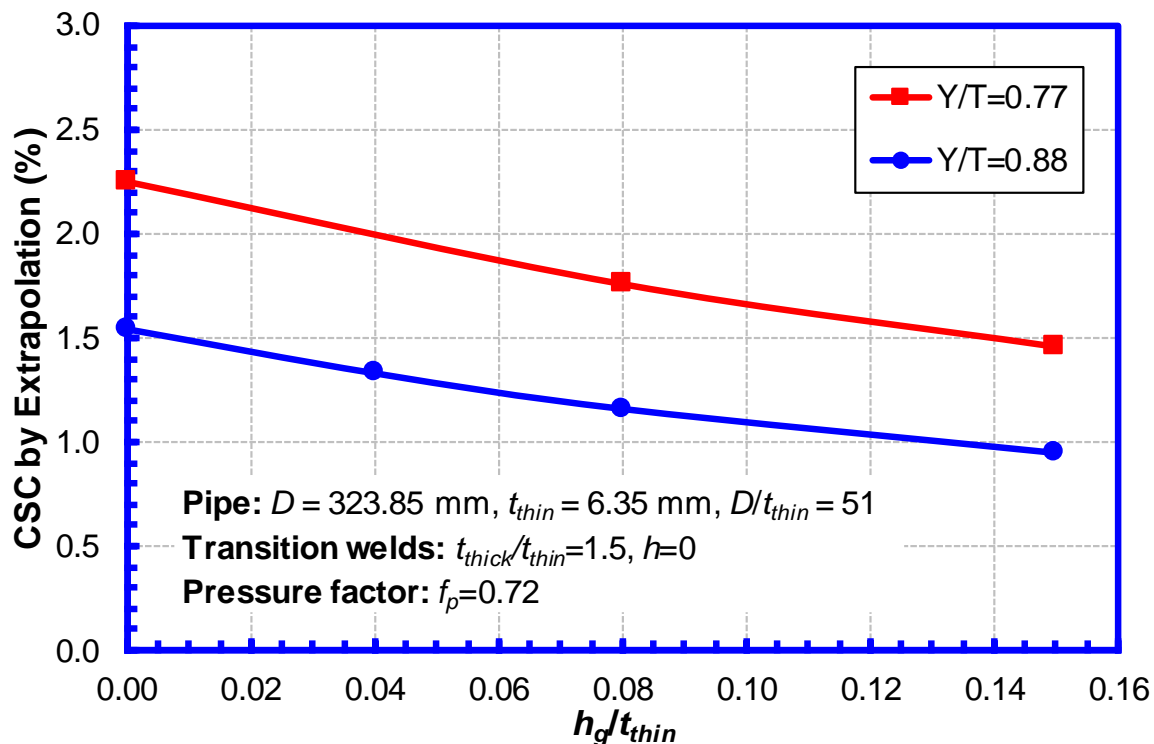
Table 4-11 Input parameters of parametric studies of pipe geometry

Key Parameter	D/t_{thin}	t_{thick}/t_{thin}	h	Y/T	f_p	h_g/t_{thin}
			mm			
Value	51, 72	1.5	0	0.88	0.72	0, 0.08, 0.15

Table 4-12 Input parameters of parametric studies of pipe material properties

Key Parameter	Y/T	D/t_{thin}	t_{thick}/t_{thin}	h	f_p	h_g/t_{thin}
				mm		
Value	0.77, 0.88	51	1.5	0	0.72	0, 0.08, 0.15

Figure 4-36 1DS CSC of transition welds with different D/t_{thin} ratiosFigure 4-37 CSC by extrapolation of transition welds with different D/t_{thin} ratios

Figure 4-38 1DS CSC of transition welds with different Y/T ratiosFigure 4-39 CSC by extrapolation of transition welds with different Y/T ratios

4.3.6 Establishment of Equivalent Geometry Imperfections of Girth Welds

4.3.6.1 Regular Girth Welds

Based on the studies in [26], the CSC equations of regular girth welds were developed in the form of add-on equations to the CSC equations of plain pipes (see Section 4.3.2) by treating the regular girth welds as equivalent geometry imperfections (h_g^e/t). The add-on equations for the equivalent geometry imperfection are shown in the following equations:

$$h_g^e/t = \max(h_g/t, 0.04) \text{ if } h/t < 0.5 \quad (4-21)$$

where h_g/t is the normalized pipe geometry imperfection height and h/t is the ratio between the weld high-low misalignment over the pipe wall thickness. The h_g^e/t , h_g/t , and h/t are all in the unit of mm/mm (in/in).

The interaction between the pipe manufacturing geometry imperfection and the regular girth weld was found to be relative low [26] and therefore was not considered in Eq. (4-21). However, further validations are needed and should be included in future work.

4.3.6.2 Transition Welds

The transition welds were also treated as equivalent geometry imperfections. The 1DS CSC calculated from the parametric studies were plugged into the CSC equation for plain pipes, i.e., Eq. (4-9), to back calculate the equivalent pipe geometry imperfection. The calculated equivalent geometry imperfections are shown in Figure 4-40.

Figure 4-40 shows that the normalized equivalent geometry imperfection (h_g^e/t_{thin}) linearly increases with the increase of the normalized pipe manufacturing geometry imperfection (h_g/t_{thin}). This linear relationship between h_g^e/t_{thin} and h_g/t_{thin} is similar for pipes with different D/t_{thin} and Y/T ratios. The pipes with $D/t_{thin} = 51$ and $Y/T = 0.88$ show the upper bound equivalent geometry imperfection (h_g^e/t_{thin}) for all the cases analyzed. The equivalent geometry imperfection (h_g^e/t_{thin}) slightly decreases as the D/t_{thin} increases and the Y/T decreases.

The relationship between h_g^e/t_{thin} and h_g/t_{thin} for the pipe with $D/t_{thin} = 51$ and $Y/T = 0.88$ was fitted into a linear equation as shown in Figure 4-41. The fitted equation between h_g^e/t_{thin} and h_g/t_{thin} is given below:

$$h_g^e/t_{thin} = 1.70 * (h_g/t_{thin}) + 0.13 \quad (4-22)$$

where the h_g/t_{thin} and h_g^e/t_{thin} are in the unit of mm/mm (in/in).

Since the curve fitting was done with the upper bound h_g^e/t_{thin} and h_g/t_{thin} relationship, the fitted equation can produce conservative estimation of the CSC for the transition welds with $D/t_{thin} \geq 51$ and $Y/T \leq 0.88$.

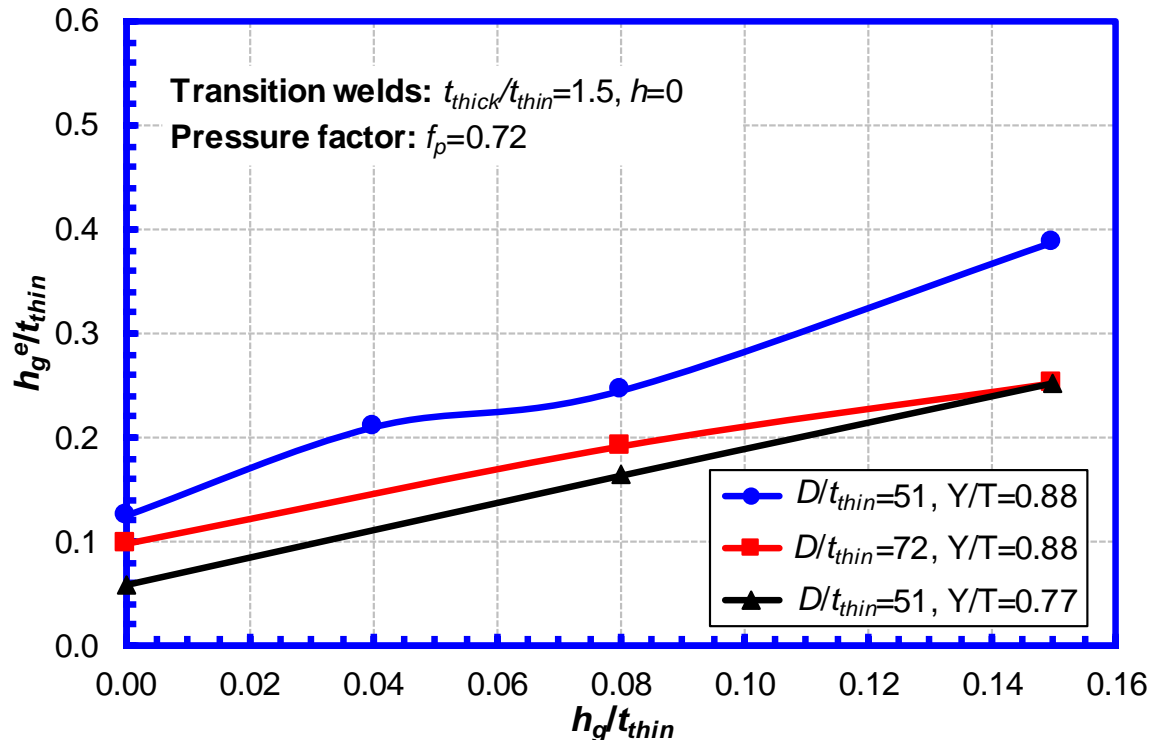
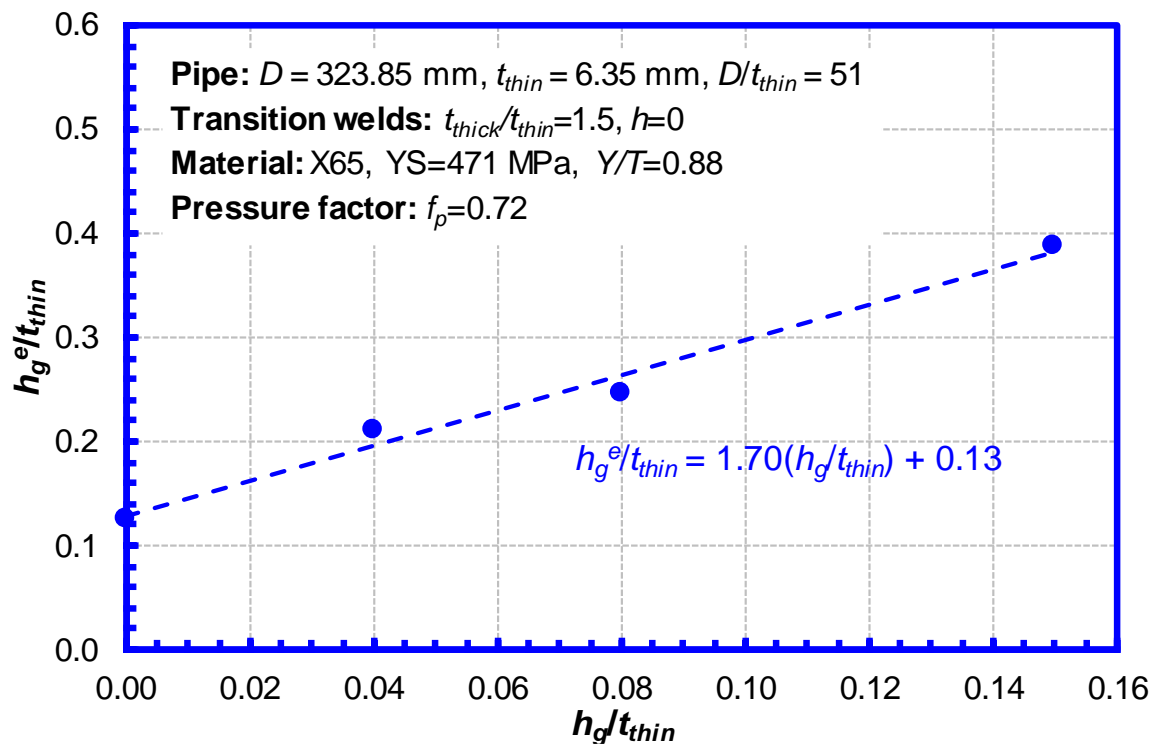
Figure 4-40 Equivalent geometry imperfection of transition welds with different D/t_{thin} and Y/T 

Figure 4-41 Curve fitting of equivalent geometry imperfection of transition welds

4.3.7 Compressive Strain Capacity Equations

4.3.7.1 Equations of 2D CSC

- (1) For plain pipes, the 2D CSC ($\epsilon_{c,plain}^{crit,2D}$) can be calculated using the equations in Section 4.3.2. If the normalized manufacturing geometry imperfection height of the actual pipe (h_g/t) is not available, the following values can be used:

$$h_g/t = \begin{cases} 0.08 & \text{(for pipes manufactured with expansion procedures)} \\ 0.04 & \text{(for pipes manufactured without expansion procedures)} \end{cases} \quad (4-23)$$

The applicable range of the CSC equations for plain pipes is shown in Section 4.3.2.

- (2) For regular girth welds, the 2D CSC ($\epsilon_{c,gw}^{crit,2D}$) can be calculated using the equations in Section 4.3.2 and replacing the h_g/t with the h_g^e/t from Eq. (4-21). The applicable range of the CSC equations for regular girth welds is shown in Section 4.3.2.
- (3) For transition girth welds, the 1DS CSC ($\epsilon_{c,tw}^{crit,1DS}$), which is equivalent to the 2D CSC ($\epsilon_{c,tw}^{crit,2D}$), can be calculated using the equations in Section 4.3.2 by replacing the h_g/t with the h_g^e/t_{thin} calculated by Eq. (4-22). The pipe geometry imperfection height h_g^e or h_g need to be normalized by the thin-wall thickness, t_{thin} .

Due to the limited range of the parameters used in the parametric studies of the transition welds, the applicable range of some parameters shown in Section 4.3.2 is replaced by the following:

- $51 \leq D/t_{thin} \leq 72$;
- $0.0 \leq f_p \leq 0.72$; and
- $0.77 \leq R_{YT} \leq 0.88$.

It should be noted that the CSC equations for the transition welds were derived from the FEA for pressurized conditions ($f_p = 0.72$). The CSC results for non-pressurized conditions (shown in Section 4.3.5.4) indicated that the equivalent geometry imperfection of the transition welds tends to decrease with the decrease of the internal pressure. Therefore, it is believed that the above CSC equations for the transition welds can be used for $f_p < 0.72$ to obtain conservative (lower than actual) estimation of the CSC. However, further validations are needed and should be included in future work.

4.3.7.2 Equations of CSC by Extrapolation

For the transition welds, a linear relationship between the 1DS CSC ($\epsilon_{c,tw}^{crit,1DS}$) and the CSC by extrapolation ($\epsilon_{c,tw}^{crit,ex}$) was established from the FEA results, as shown in Figure 4-42. The relationship between 1DS CSC and CSC by extrapolation is shown in the following equation:

$$\epsilon_{c,tw}^{crit,ex} = 1.03 * \epsilon_{c,tw}^{crit,1DS} - 0.20. \quad (4-24)$$

where the units of $\epsilon_{c,tw}^{crit,ex}$ and $\epsilon_{c,tw}^{crit,1DS}$ are both %. For example, if the strain capacity is 2%, i.e., 0.02 mm/mm (in/in), the $\epsilon_{c,tw}^{crit,ex}$ or $\epsilon_{c,tw}^{crit,1DS}$ is 2.0.

Figure 4-42 and Eq. (4-24) show that for transition welds, the CSC by extrapolation ($\varepsilon_{c,tw}^{crit,ex}$) is smaller than 1DS CSC ($\varepsilon_{c,tw}^{crit,1DS}$). But the difference is relatively small, especially for pipes with high CSC.

More importantly, the FEA in Section 6.6 demonstrated that Eq. (4-24) is also valid for pipes with dents. The results from the dent studies are also included in Figure 4-42. Therefore, it is believed that Eq. (4-24) is also valid for plain pipes and pipes with regular girth welds.

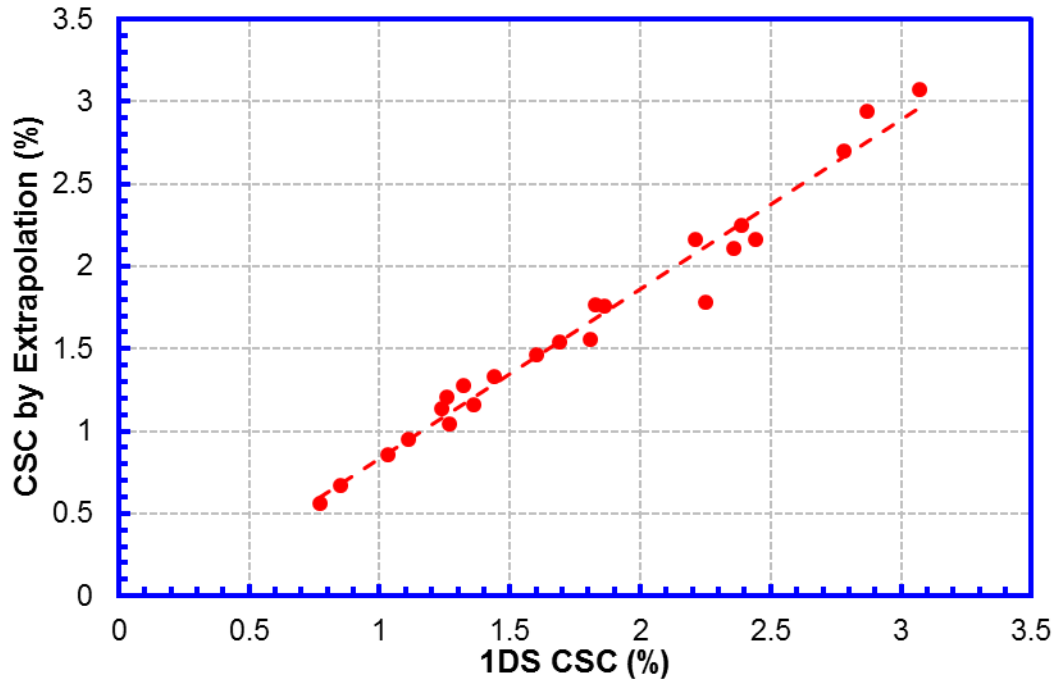


Figure 4-42 Relationship between 1DS CSC and CSC by extrapolation of transition welds

4.3.8 Evaluation of the CSC Equations of Transition Welds

Figure 4-43 and Figure 4-44 show the 1DS CSC and CSC by extrapolation calculated by the FEA and the above CSC equations for the transition welds. All the results shown in Sections 4.3.5.5 and 4.3.6 (for different D/t_{thin} and Y/T ratios) were included in the figures. The results from the CSC equations either match the FEA results very well or slightly smaller than the FEA results (i.e., conservative).

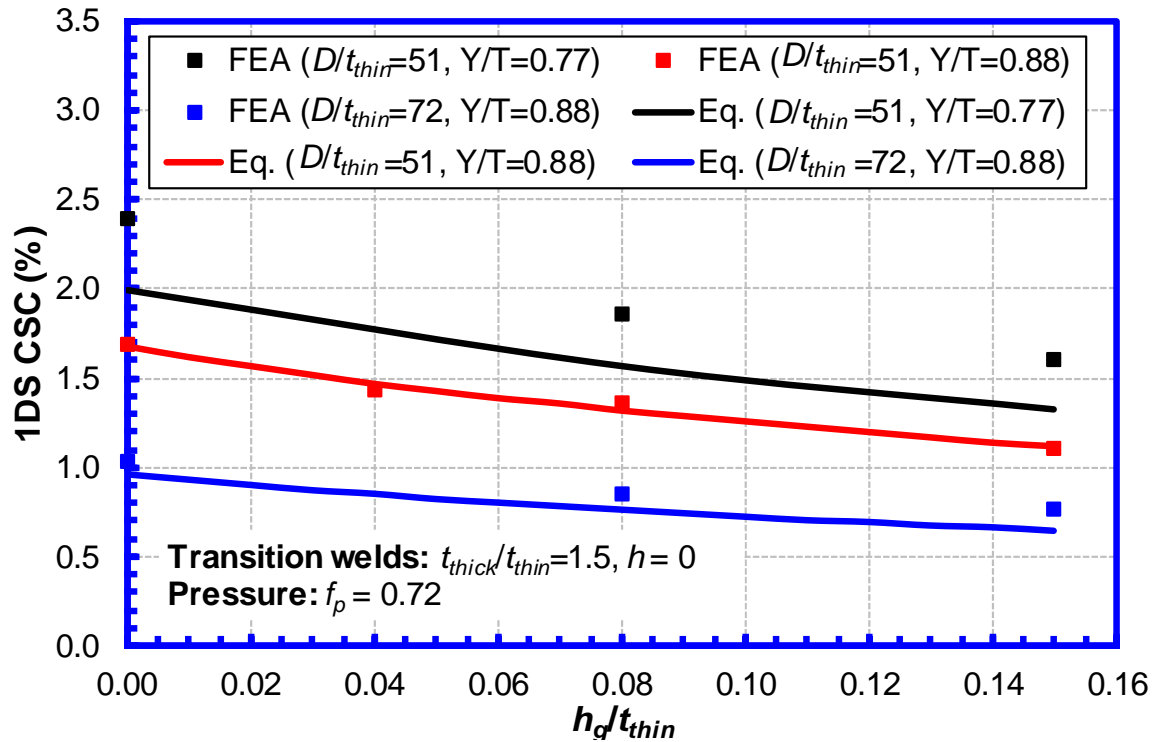


Figure 4-43 Comparison of 1DS CSC between FEA and developed CSC equations

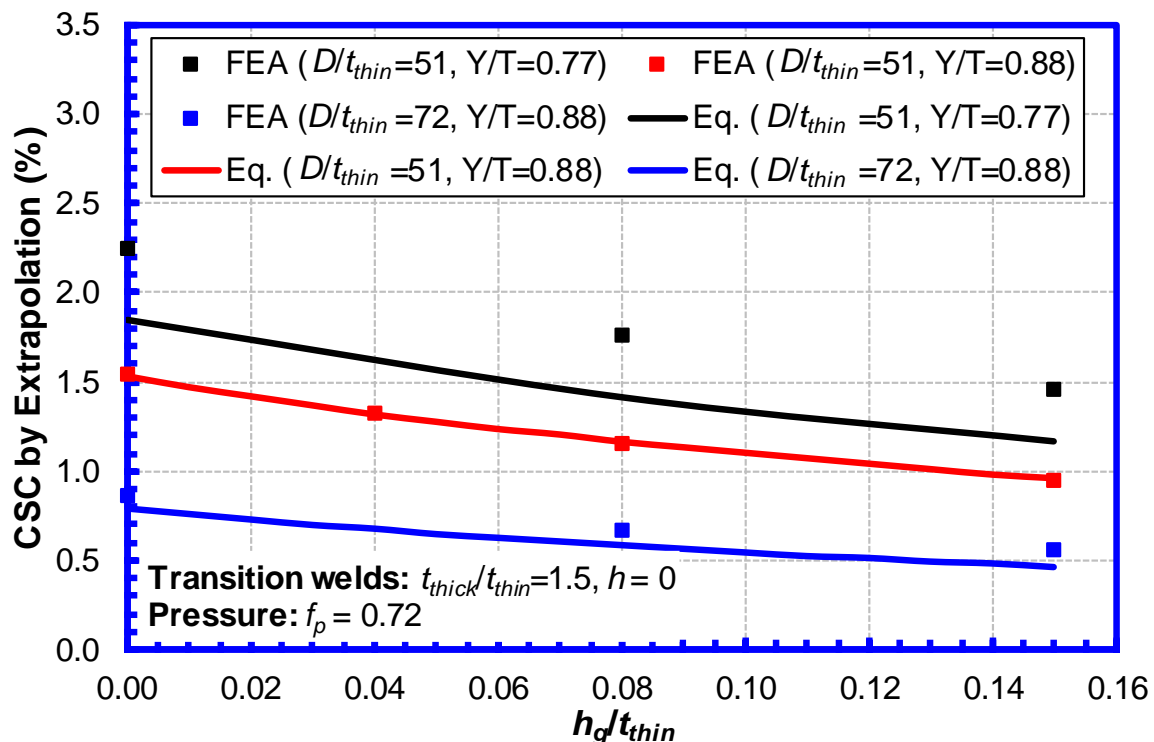


Figure 4-44 Comparison of CSC by extrapolation between FEA and developed CSC equations

5 Pipes with Corrosion Anomalies Subjected to Longitudinal Strain

5.1 Overview of the Studies on Corrosion

5.1.1 Limit States Associated with Corrosion Subjected to Longitudinal Strain

The corrosion anomalies studied within this project are metal loss type anomalies. The shape of an actual corrosion anomaly is typically irregular as shown in Figure 5-1. The anomaly can be one large and continuous feature or a cluster of small ones. The clusters are often combined and treated as one large anomaly.

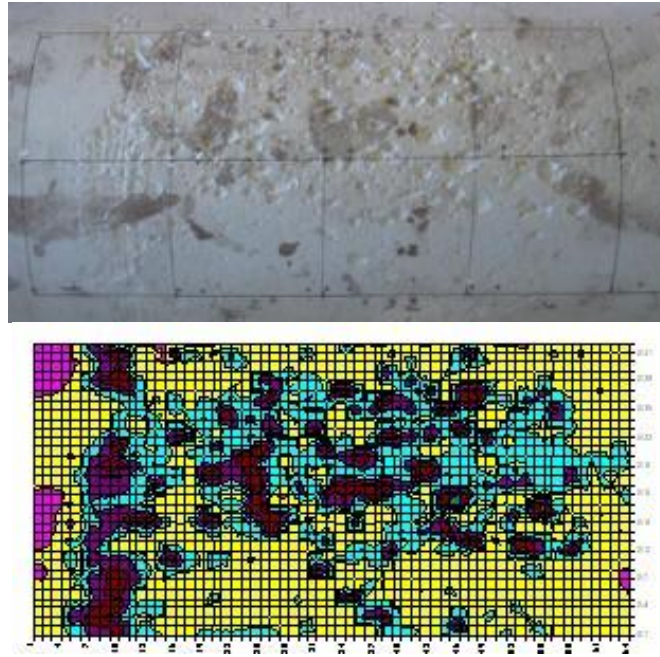


Figure 5-1 A metal loss type corrosion anomaly (www.swri.org)

Depending on the shape and size, the corrosion anomalies can be broadly grouped as general corruptions, grooves (longitudinal and circumferential), pits, etc. [32,71]. The dimensions of the corrosion anomalies include longitudinal length (L_c), circumferential width (W_c) and depth (d_c), as shown in Figure 5-2.

In the existing studies of the metal loss corrosion anomalies, including experimental tests and numerical analyses, the anomalies are typically simplified to be of a regular shape (e.g., rectangle or square) with a flat bottom, as shown in Figure 5-3. In this project, the simplified flat-bottom shape was used for all the corrosion anomalies studied.

For a pipe with metal loss type corrosion anomalies, three limit states (failure modes) need to be considered when the pipe is subjected to longitudinal strain, i.e., tensile rupture, compressive buckling, and burst. The tensile rupture and burst are considered as an ultimate limit state, while the buckling is, in general, considered as a service limit state.

The resistance to the tensile rupture, compressive buckling, and burst is measured by tensile strain capacity (TSC), compressive strain capacity (CSC), and burst pressure, respectively.

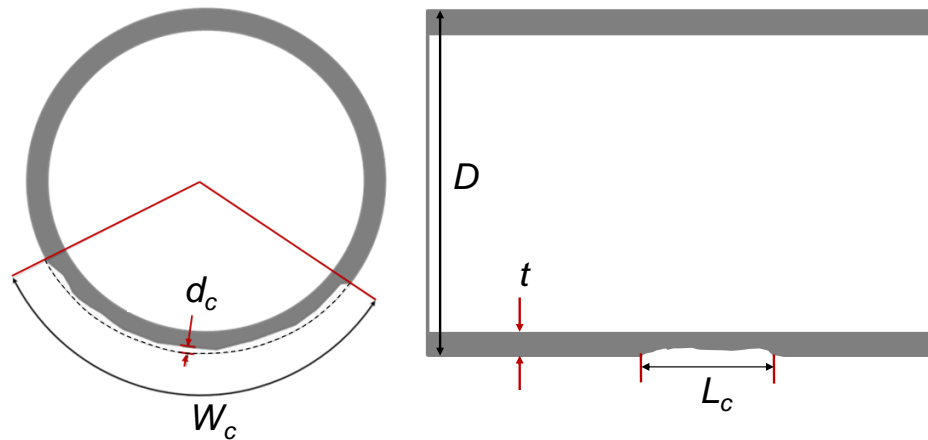


Figure 5-2 Dimensions of pipe segment and corrosion



Figure 5-3 A flat bottom metal loss anomaly

5.1.2 Section Structure and General Approach

In this project, the TSC, CSC, and burst pressure of the pipes containing metal loss corrosion anomalies were all studied. The studies on the TSC, CSC, and burst pressure were presented in Sections 5.2, 5.3, and 5.4, respectively. Interactions between the corrosion anomalies and (girth and/or seam) welds or other anomalies such as dents were not considered in the analyses.

The general approach for studying the TSC of the pipes containing corrosion anomalies and the structure of Section 5.2 are summarized below:

- The application and general definition of the TSC were introduced in Section 5.2.1. The general concept or definition of the TSC was introduced following the discussions of the target application of the TSC, i.e., how the TSC is to be used.
- The studies involved systematic FEA and experimental evaluations. The FEA procedures were introduced and evaluated with the full-scale tests in Section 5.2.2.
- The validated FEA procedures were used to conduct parametric FEA to study the effects of various parameters on the TSC. The parametric FEA were shown 5.2.3.

- Through the parametric FEA, procedures for evaluating the TSC of the pipes containing corrosion anomalies were established and shown in Section 5.2.4.

The general approach for studying the CSC of the pipes containing corrosion anomalies and the structure of Section 5.3 are summarized below:

- The application and general definition of the CSC were introduced in Section 5.3.1. The general concept or definition of the CSC was introduced following the discussions of the target application of the CSC, i.e., how the CSC is to be used.
- The studies involved systematic FEA and experimental evaluations. The FEA procedures were introduced and evaluated with the full-scale tests in Section 5.3.2.
- The validated FEA procedures were used to conduct parametric FEA to study the effects of various parameters on the CSC. The parametric FEA were shown 5.3.3.
- Through the parametric FEA, procedures for evaluating the CSC of the pipes containing corrosion anomalies were established and shown in Section 5.3.4.

The general approach for studying the burst pressure of the pipes with corrosion anomalies and the structure of Section 5.4 are summarized below:

- The background of the burst pressure for the SBDA was introduced in Section 5.4.1. The potential effect of the longitudinal strain on the burst pressure and the gaps in the existing assessment models were introduced.
- The studies for the burst pressure involved sensitivity studies of selected key parameters and experimental evaluations. The FEA procedures and results of the sensitivity studies were discussed in Section 5.4.2.
- The FEA procedures and the sensitivity studies were evaluated with full-scale tests and the evaluation results were shown in Section 5.4.3.
- Based on the sensitivity studies, burst pressure equations for the corroded pipes subjected to longitudinal compressive strain were established and shown in Section 5.4.4.

5.2 Tensile Strain Capacity of Corroded Pipes

5.2.1 Application and Definition of Tensile Strain Capacity

As discussed in Section 4.2.1, the TSC is designated to measure the overall capacity of the pipe to accommodate global/nominal longitudinal strain and deformation. For the pipe with metal loss anomalies, the TSC is defined as the maximum tensile strain the pipe can withstand before any leaking or rupturing. The TSC was measured in the location away from the anomalies to avoid the effect of local strain concentration. As a result, the strain demand should be defined consistently. The details on the calculation of the TSC are given in Section 5.2.2.4.

5.2.2 Analysis of Full-Scale Tests

5.2.2.1 Finite Element Analysis Models

Finite element analyses (FEA) were conducted to simulate the full-scale tensile tests for the pipes with corrosion anomalies. The commercial finite element software ABAQUS® was employed in the FEA. The pipe was modeled with three-dimensional hybrid eight-node solid

elements with reduced integration (C3D8RH). Due to the symmetry conditions in the circumferential and longitudinal directions, as shown in Figure 5-4, only one quarter of the pipe was modeled. Symmetry boundary conditions were applied to the quarter model. The end of the pipe was modeled as a rigid plane to simulate the end plates attached to the pipe in the experimental tests.

The effect of mesh sizes on the analysis results was thoroughly examined. The element was refined adequately to obtain converged (mesh independent) solutions. Along the longitudinal direction, small-sized elements were used at/near the anomaly. The element size was gradually increased towards the end of the pipe for computational efficiency. The smallest element size in the longitudinal direction was 0.5 mm. Along the circumferential and thickness directions, the sizes of the elements were kept uniform. The element sizes in the circumferential and thickness directions were 2.0 mm and 0.6 mm, respectively.

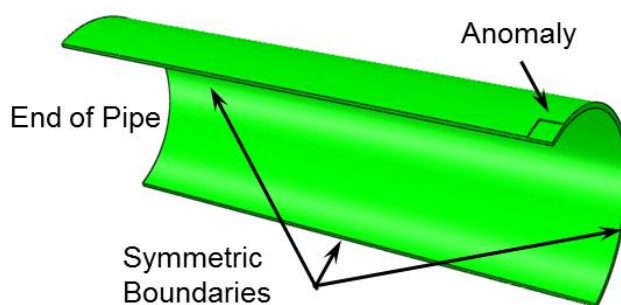


Figure 5-4 The finite element model of a pipe with a corrosion anomaly

5.2.2.2 Loading Conditions

Following the loading procedures in the full-scale tests, the loadings in the FEA were applied in two steps. In the first step, internal pressure was applied to the ID surface of the pipe model to induce hoop stress of 72% SMYS of the pipe (X70). In the second step, uniaxial elongation was applied to the end of the pipe until the maximum load is reached. The internal pressure was kept constant during the second step.

5.2.2.3 Material Properties

The FEA were conducted for two sets of assumed pipe properties, which are shown in Table 5-1. The pipe properties (both circumferential and longitudinal) obtained from the small-scale tensile tests are also shown in Table 5-1. Details about the small-scale test data can be found in Section 2.2.

In the FEA, isotropic material properties were assumed, i.e., the properties of the longitudinal and circumferential directions are the same. However, the small-scale test results show that the pipe has very distinct strain hardening capacities in the circumferential and longitudinal directions. The Y/T ratios (R_{YT}) of the circumferential and longitudinal directions are 0.83 and 0.90, respectively.

The Set 1 properties used in the FEA were determined based on the pipe strengths reported in Mill Certificates before the small-scale tensile test data became available to the project. The Set

1 properties match the circumferential Y/T ratio from the small-scale tests. The Set 2 properties match the pipe longitudinal Y/T ratio from the small-scale tests.

The yield and tensile strengths of both assumed Set 1 and Set 2 properties are lower than the measured pipe strengths. However, it is well known that the TSC of a pipe is mainly determined by the pipe Y/T ratio. Therefore, it is believed that the difference in the assumed and measured pipe strengths will not affect the calculated TSC.

Table 5-1 Materials properties used in the FEA and from the small-scale tests

Material Properties		Used in the FEA		From the Small-Scale Tests	
		Set 1	Set 2	Longitudinal	Circumferential
YS	MPa	547	547	573	556
UTS	MPa	661	607	638	673
Y/T		0.83	0.90	0.90	0.83

The full stress-strain curves (SSC) used in the FEA were constructed with the Set 1 and Set 2 assumed pipe properties shown in Table 5-1 following the procedures developed in [7,28]. Figure 5-5 shows the full SSC of the pipe used in the FEA and obtained from the small-scale tests. It is seen that the Set 1 and Set 2 SSC used in the FEA have similar strain hardening behaviors (shapes) with the circumferential and longitudinal SSC obtained from the small-scale tests, respectively.

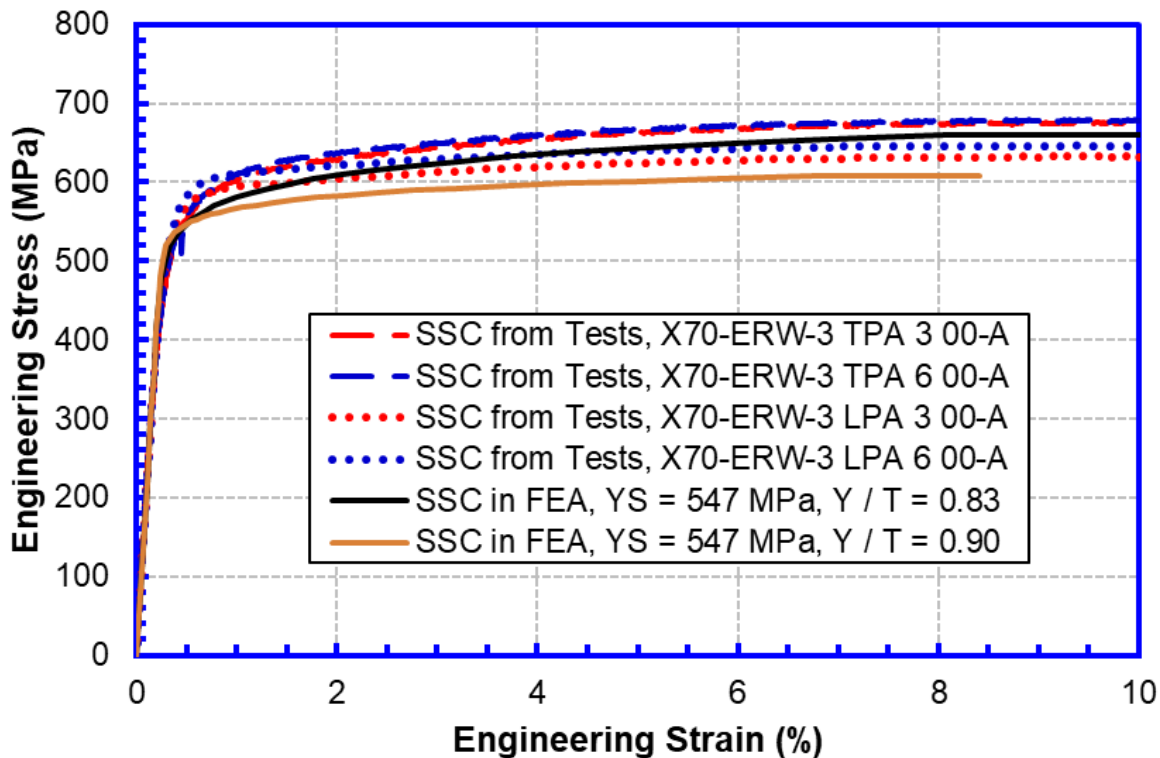


Figure 5-5 Stress-strain curve of the X70 pipe

5.2.2.4 Typical Results and Calculation of Remote Tensile Strain

Figure 5-6 shows a typical longitudinal strain contour at the maximum load plotted on the deformed pipe. The longitudinal strain is found highly concentrated in the corrosion area. In addition, the pipe diameter is found greatly expanded in the corrosion area as evidenced by the bulged-out pipe surface.

Figure 5-7 shows the same longitudinal strain contour shown in Figure 5-6. However, in Figure 5-7, the contour scale is adjusted to show the strain contour outside the corrosion area. The distribution of the longitudinal strain along the length of the pipe at the circumferential locations 0° , 90° , and 180° away from the center of the corrosion is also shown in the inserted line plot, i.e., along the 0° , 90° , and 180° lines.

At all circumferential locations, the longitudinal strain along the length of the pipe varies dramatically close to the end of the pipe due to the end plate effect and close to the corrosion anomaly due to strain concentration at the corrosion. In the region away from the pipe end and the corrosion, the strain along the length of the pipe is relatively constant. The region showing relatively constant strain along the pipe length is referred to as the remote strain zone.

The line plot in Figure 5-7 shows that the longitudinal strain in the remote strain zone varies with the circumferential location. The longitudinal strain on the bottom of the pipe (180° line) is higher than that on the top of the pipe (0° line). The longitudinal strain on the 90° line is similar to the average strain on the 0° and 180° lines. The strain distribution indicates that although uniaxial elongation is applied to the pipe end, global bending is created in the pipe and the bottom of the pipe (180° line) is on the tensile side of the bending.

As shown in the strain contours, the corrosion area deforms much more than the rest of the pipe. The pipe surface near the corrosion area bulges significantly outwards. As a result, around the mid-length of the pipe, the pipe surface on the top (0° line) is greater than the pipe surface on the bottom (180° line). Due to the pipe surface difference, the internal pressure creates a net force pushing the pipe up (from the 180° line to the 0° line), which creates the bending to the pipe.

The average longitudinal strain on the 0° and 180° lines and the longitudinal strain on the 90° line represent the nominal longitudinal membrane/cable tensile strain. In this project, the remote strain is defined either from the longitudinal strain on the 90° line in the remote strain zone or as the average strain on the 0° and 180° lines in the remote strain zone.

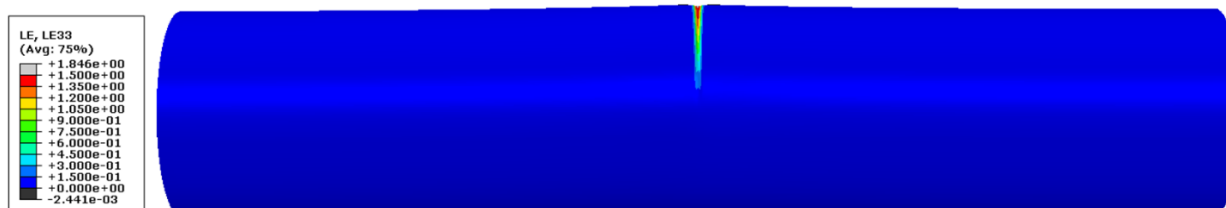


Figure 5-6 Longitudinal strain contour (Specimen 12.c in Table 3-14)

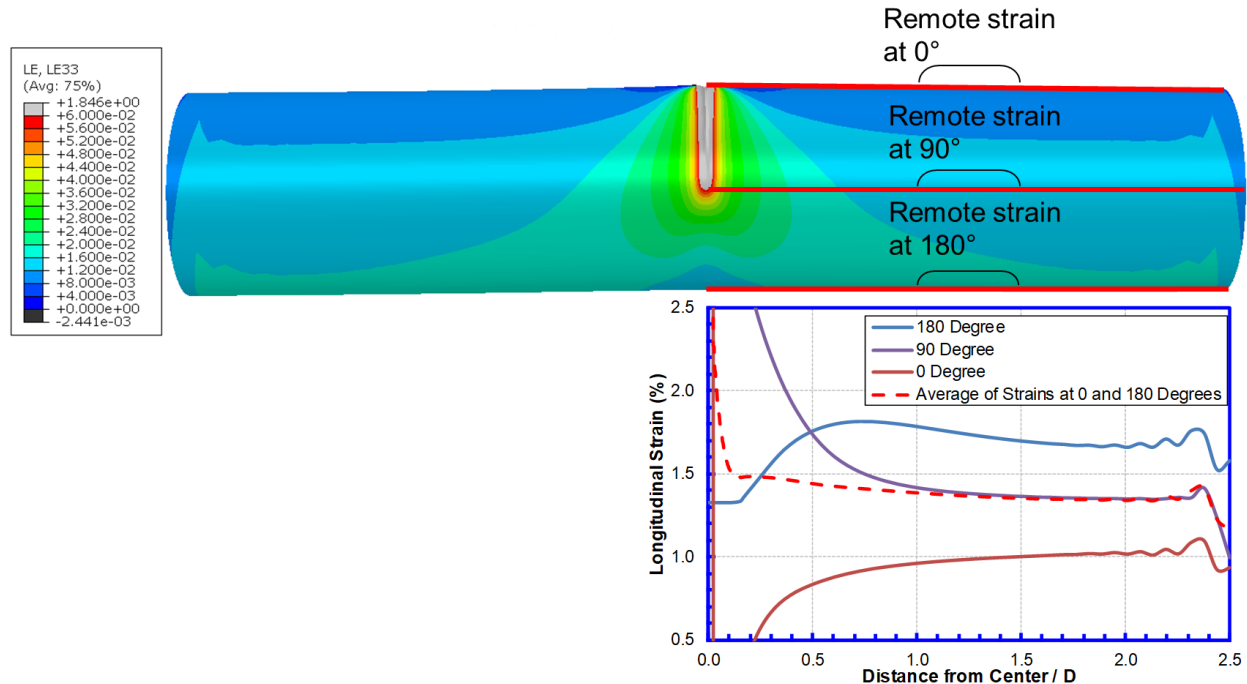


Figure 5-7 Longitudinal strain distribution along the length of pipe (Specimen 12.c in Table 3-14)

5.2.2.5 Failure Criteria

The TSC is defined as the maximum remote strain (Section 5.2.2.4) the pipe can withstand before leaking or rupturing (i.e., failure). To determine the pipe failure in the FEA, five failure criteria, i.e., maximum Mises criterion, DNV criterion [72], API 579 criterion [32], Korea University criterion [73], and maximum load criterion, were examined. All the criteria examined corresponded to ductile failure. Brittle failure of the pipe was not considered.

For the maximum Mises criterion, the pipe failure is defined as the event when the von Mises stress in any element exceeds the UTS of the pipe.

The DNV criterion [72] was used in the development of the burst pressure equation in DNV-RP-F101 [34]. In the DNV criterion, the pipe failure is defined as the event when the von Mises stress inside the whole shear band of the remaining ligament of the corrosion anomaly exceeds the UTS of the pipe.

The API 579 criterion is the local failure criteria specified in ANNEX B of API 579 [32]. In the API 579 criterion, the pipe failure is defined as the event when the equivalent plastic strain in any element exceeds a critical strain. The critical strain depends on the stress triaxiality and pipe stress-strain properties [32].

The Korea University criterion [73] is similar to the API 579 criterion, except that the critical strain is determined from a set of experimental tests of X65 pipes. Similar critical strain was obtained for X80 pipes [74].

In the maximum load criterion, the pipe failure is defined as the event when the maximum applied longitudinal load is reached.

Figure 5-8 shows the typical relationship between the maximum equivalent plastic strain (PEEQ) in the corrosion area and the remote strain. The maximum PEEQ increases with the increase of the remote strain. Although, the remote strain decreases after the maximum remote strain (i.e., load) is reached, the maximum PEEQ always increases.

The pipe failure events determined by the five failure criteria are marked in Figure 5-8. The TSC is the remote strain corresponding to the failure events. With the exception for the TSC predicted by the maximum Mises criterion, the TSC predicted by the other criteria are very close. In this project, the maximum load criterion was employed for determining the TSC due to its simplicity.

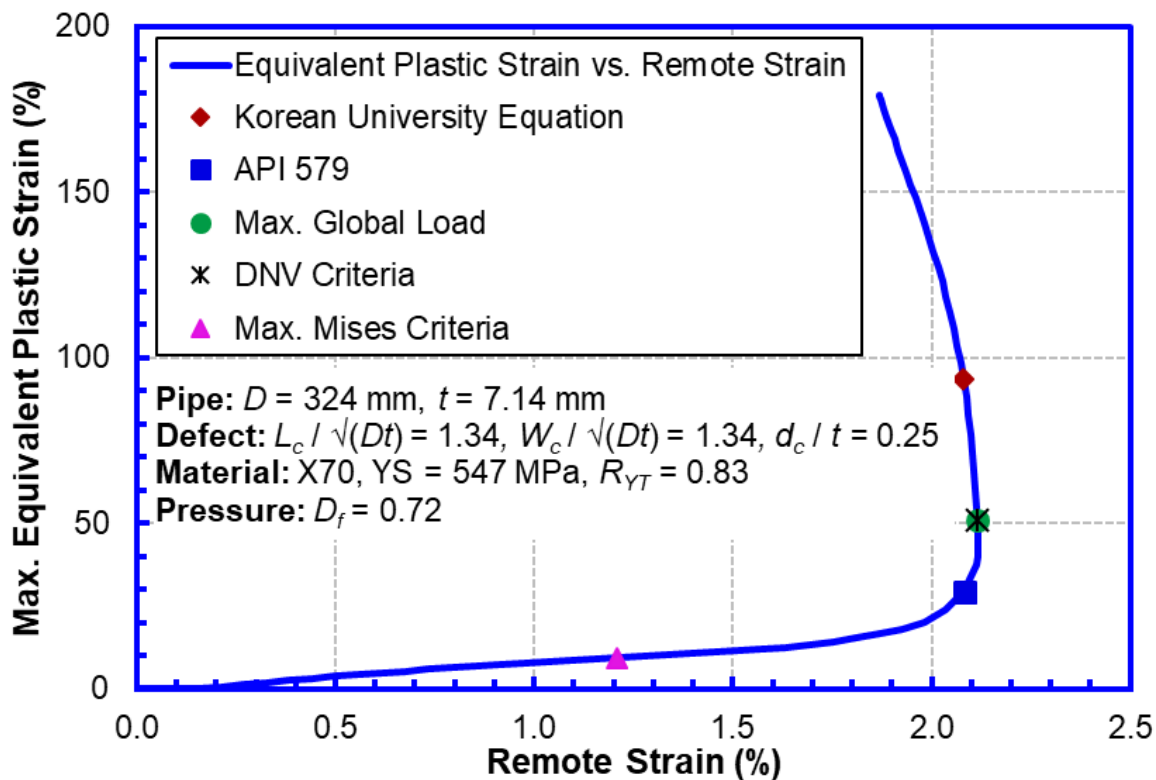


Figure 5-8 Comparison of failure criteria (Specimen 12.a in Table 3-14)

5.2.2.6 Comparison of Experimental and Simulation Results

Three of the four tests (Tests 2 to 4) shown in Table 3-14 were analyzed. The details of the full-scale tests can be found in Section 3.5. The failure location and the TSC predicted by FEA were compared with the test results. As shown in Figure 5-9, the FEA results indicate that high local strain occurs inside the corrosion area near the corrosion edge along the pipe circumference (i.e., perpendicular to the tensile loading). The final failure is predicted at those high strain areas near the edge of the corrosion anomalies, which is consistent with the experimental results.

Table 5-2 shows the TSC obtained from the experimental tests and FEA. As discussed in Section 5.2.2.3, the tested pipes showed significant anisotropic properties, e.g., the pipe Y/T ratios in the longitudinal and circumferential directions are around 0.90 and 0.83, respectively. In the FEA, the pipe was modeled as isotropic materials.

The FEA were conducted with two sets of pipe properties: one with longitudinal properties and the other with circumferential properties. The FEA results show that the calculated TSC are very sensitive to the pipe Y/T ratios. The calculated TSC for $Y/T = 0.90$ is only 50-60% of the TSC for $Y/T = 0.83$.

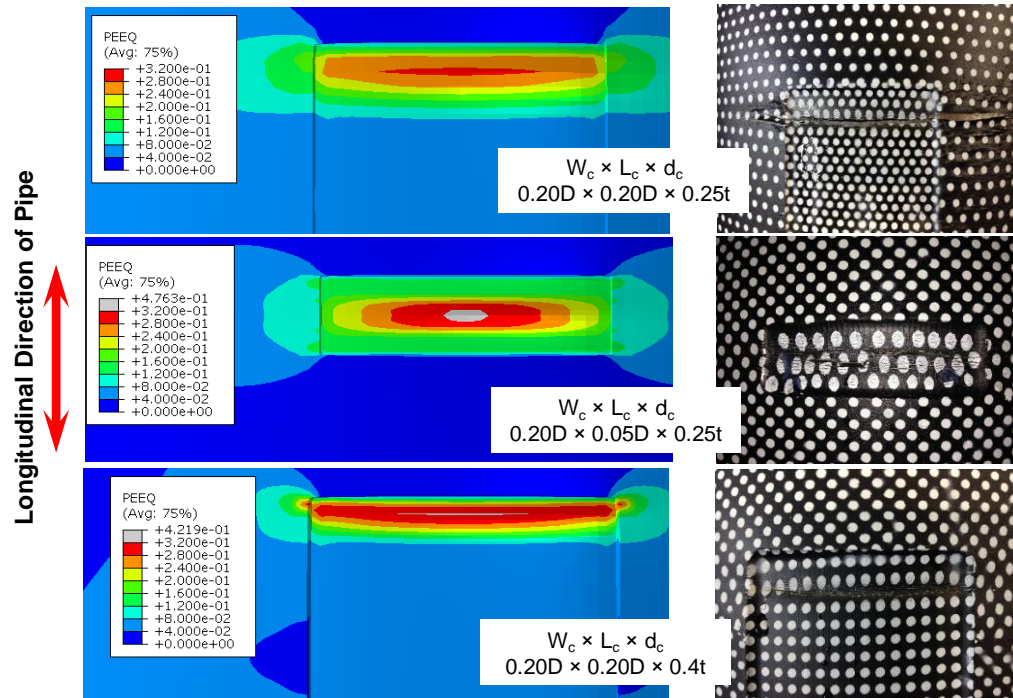


Figure 5-9 Strain concentration and location of ductile failure

Table 5-2 Corrosion feature geometries and TSC from tests and FEA

Size of Pipe		Test Number	Corrosion Feature	Size of Corrosion Anomalies	Tensile Strain Capacity			
D	t				Experiment	FEA, $R_{YT} = 0.83$	FEA, $R_{YT} = 0.90$	FEA, Average
mm	mm			$W_c \times L_c \times d_c$				
324	7.14	1	Baseline (No Feature)	N/A	6.63	N/A	N/A	N/A
		2	General Corrosion	$0.20D \times 0.20D \times 0.25t$	2.66	2.14	1.27	1.70
		3	Circumferential Groove	$0.20D \times 0.05D \times 0.25t$	1.21	1.37	0.68	1.03
		4	Deep General Corrosion	$0.20D \times 0.20D \times 0.40t$	1.04	1.13	0.64	0.89

For Test 2, the FEA using both longitudinal ($Y/T = 0.90$) and circumferential ($Y/T = 0.83$) properties under-predict the TSC measured from the test. For Tests 3 and 4, the FEA using the longitudinal properties ($Y/T = 0.90$) under-predict the measured TSC, while the FEA using the circumferential properties ($Y/T = 0.83$) over-predict the measured TSC. For Tests 3 and 4, the averaged TSC of the longitudinal and circumferential properties show a reasonable match to the measured TSC but is less than the measured TSC.

It is generally believed that the TSC is mainly determined by the pipe longitudinal properties. However, under bi-axial loading conditions (e.g., internal pressure and longitudinal load), the pipe circumferential properties can also play an important role on the TSC. For example, it has been recognized that the pipe circumferential properties can greatly affect the pipe compressive strain capacity [75,76,77,78,79,80]. Results of the present studies show that the TSC of pipes with significant anisotropic properties can be estimated by using the average of the TSC calculated with the longitudinal and circumferential properties. However, additional studies on the significance of material anisotropy on the TSC are needed.

In addition, both the FEA and experimental results show that the pipe with a circumference groove has smaller TSC than the pipe with a general corrosion of the same depth and width (in circumferential direction). Detailed discussions about the corrosion size effects are presented in the following sections.

5.2.3 Parametric Analyses

5.2.3.1 Overview of the Parametric Analysis

Parametric FEA were conducted to study the effect of various parameters on the TSC of the pipes with corrosion anomalies. The finite element models described in Section 5.2.2.1 and the loading conditions shown in Section 5.2.2.2 were used in the parametric analyses.

Appropriate non-dimensional anomaly sizes were determined at first after analyzing different non-dimensional anomaly sizes. Parametric analyses were then conducted to investigate the effects of non-dimensional anomaly sizes, material properties (Y/T ratios), and internal pressure on the TSC. The purposes of the studies include: (1) to gain better understanding on the key parameters which affect the TSC of pipes with corrosion anomalies; (2) to gain better understanding on how the key parameters affect the TSC; and (3) to provide general guidance for assessing the TSC of pipes with corrosion anomalies.

5.2.3.2 Non-Dimensional Anomaly Size

Non-dimensional anomaly sizes were used in the assessment of corrosion anomalies in many practices. For example, in ASME B31G [31], to assess the burst pressure of corroded pipes, the longitudinal length and depth of the corrosion anomalies are normalized by \sqrt{Dt} and t , respectively.

Figure 5-9 indicates that under longitudinal tensile strain, the stress/strain concentration near the edge of the corrosion anomaly initiated and resulted in the tensile rupture. The stress concentration near the edge is mainly caused by the through-wall bending resulting from the wall thickness discontinuity (or transition). More discussions about the bending at the wall thickness transition can be found in [62] for a study of stress concentration at transition welds. The local bending stress at the wall thickness transition has been thoroughly investigated [81,82]. The bending stress was found to follow a harmonic equation (i.e., in the form of a cosine wave) along the length of the pipe. In addition, the bending stress attenuates along the length of the pipe following an exponential equation. The characteristic length of the exponential equation and the wavelength of the harmonic equation are both proportional to \sqrt{Dt} . For example, for materials with Poisson's ratios of 0.3, the wavelength is about $3.4\sqrt{Dt}$ and the magnitude of the bending

stress drops to insignificant values at about $0.85\sqrt{Dt}$. Based on the above observations, it is suggested that the longitudinal length and the circumference width of the corrosion anomaly should be normalized by \sqrt{Dt} . The depth of the corrosion anomaly should be normalized by t .

To validate the non-dimensional corrosion sizes, three groups of FEA were conducted (see Table 5-3). In Group 1, the corrosion length (L_c) and width (W_c) were normalized by the pipe outside diameter (D), which was commonly used in many previous studies. In Group 2, the corrosion length and width were normalized by the pipe wall thickness (t). In Group 3, the corrosion length and width were normalized by \sqrt{Dt} . For all three groups, the corrosion depth was normalized by pipe wall thickness. In each group, multiple FEA were conducted, in which the normalized anomaly size was kept constant, while the pipe diameter, wall thickness, and D/t ratio were varied. In all three groups of analyses, the pressure factor was kept constant at 0.72 and the pipe properties with $Y/T = 0.83$ (see Section 5.2.2.3) were used.

Table 5-3 Parameters for studying non-dimensional anomaly sizes

	D	t	D/t	L_c/D	L_c/t	$L_c/\sqrt{(Dt)}$	W_c/L_c	d_c/t
	mm	mm	mm/mm	mm/mm	mm/mm	mm/mm	mm/mm	mm/mm
Group 1	254	12.7	20	0.10	Variable	Variable	2.0	0.4
	1219	11.7	104					
Group 2	254	12.7	20	Variable	2.0	Variable		
	406	6.35	64					
	1219	11.7	104					
Group 3	254	12.7	20	Variable	Variable	0.45		
	406	6.35	64					
	1219	11.7	104					

Figure 5-10 shows the relationship between the calculated TSC and the pipe dimension (D/t) for all the cases shown in Table 5-3. The results show that when the length and width of the corrosion anomalies are normalized by \sqrt{Dt} and the depth is normalized by t , the TSC is almost independent to the pipe dimensions as long as the non-dimensional corrosion sizes are kept constant. The results confirmed that the longitudinal length and the circumference width of the corrosion anomaly should be normalized by \sqrt{Dt} and the depth of the corrosion anomaly should be normalized by t .

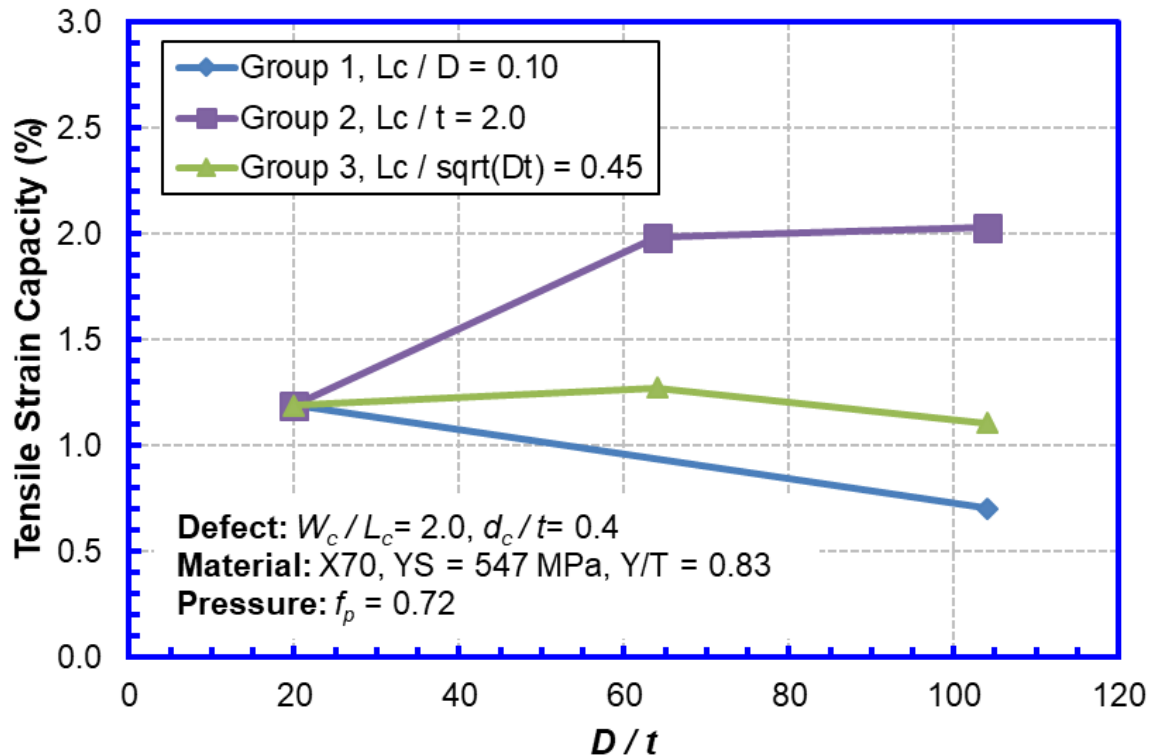


Figure 5-10 TSC vs. pipe D/t ratio for corrosion sizes normalized by different parameters

5.2.3.3 Effect of Anomaly Size

The anomaly sizes investigated are listed in Table 5-4. The analyses were divided into three groups. Groups 1-3 were targeted for the anomaly length, width, and depth, respectively. In all the analyses, the pressure factor (f_p) was kept constant, i.e., $f_p = 0.60$ and the pipe properties with $Y/T = 0.83$ (see Section 5.2.2.3) were used.

Table 5-4 Parameters for studying the effect of corrosion sizes

Group	D	t	f_p	L_c / \sqrt{Dt}	W_c / \sqrt{Dt}	d_c / t
	mm	mm		mm / mm	mm / mm	mm / mm
1	324	7.14	0.60	0.0674, 0.134, 0.337, 0.674, 1.01, 1.34, 3.37	1.34	0.25
2				1.34	0.337, 0.674, 1.34, 3.37	0.25
3				1.34	1.34	0.10, 0.25, 0.30, 0.40

The effects of the length, width, and depth of the corrosion anomaly on the pipe TSC are shown in Figure 5-11 to Figure 5-13, respectively. As shown in Figure 5-11, the TSC is almost independent of the longitudinal length of the corrosion anomaly if the normalized length is beyond a critical value (i.e., $L_c / \sqrt{Dt} \approx 1.7$).

Below the critical length, the TSC decreases rapidly as the length of the corrosion anomalies decreases. As discussed in the previous section, stress concentration can be induced by local through-wall bending stress near the edges of the corrosion anomalies. The local bending stress only affects an area of $0.85\sqrt{Dt}$ from the edge of corrosion. Therefore, the bending stress from the two edges of the corrosion anomaly overlaps when the normalized longitudinal length (L_c/\sqrt{Dt}) is less than 1.7 (i.e., 0.85×2).

The overlap of the bending stress increases the local stress/strain concentration and reduces the TSC. The shorter the corrosion anomalies, the higher the overlapped bending stresses, and the lower the TSC. On the other hand, when $L_c/\sqrt{Dt} > 1.7$, the local bending stresses from the two edges barely interact. As a result, the local stress and the TSC are independent of the longitudinal length of the corrosion anomaly.

On the other hand, the TSC decreases with the increase of the circumferential width (Figure 5-12) and the depth (Figure 5-13) of the corrosion anomaly. The effects of the corrosion sizes on the TSC are consistent with those from the burst pressure studies [39].

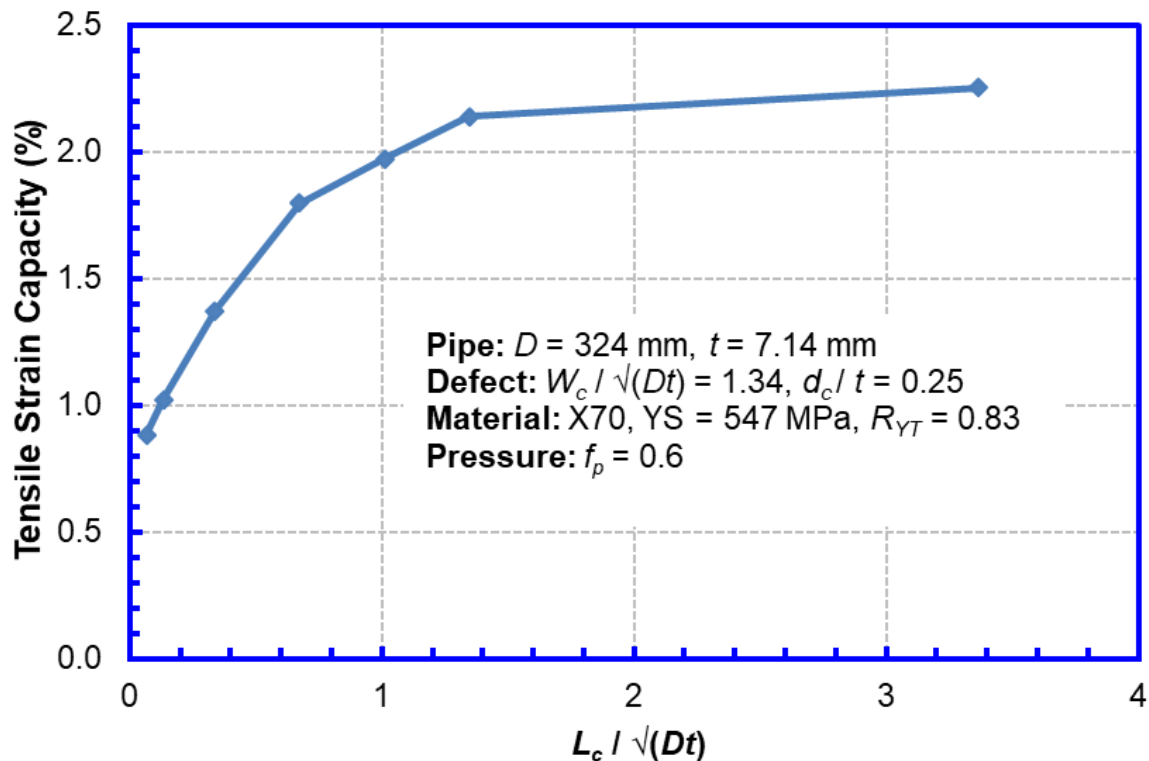


Figure 5-11 TSC vs. normalized longitudinal length of corrosion anomalies

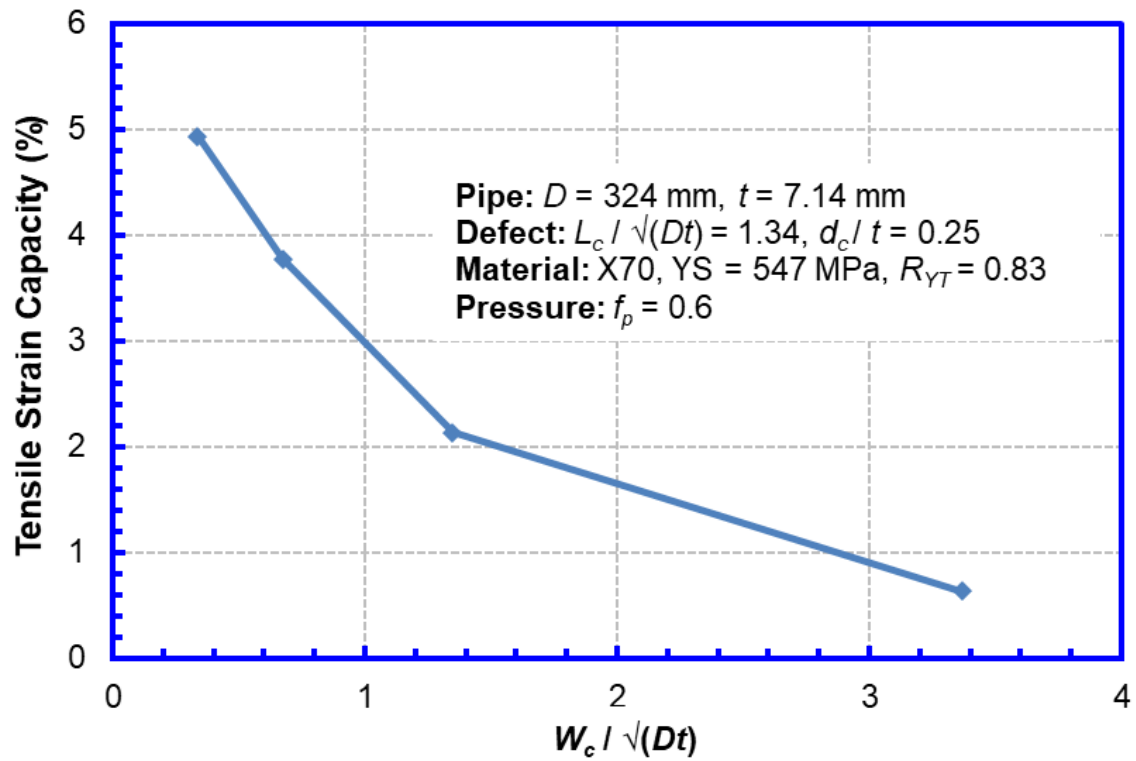


Figure 5-12 TSC vs. normalized circumferential length of corrosion anomalies

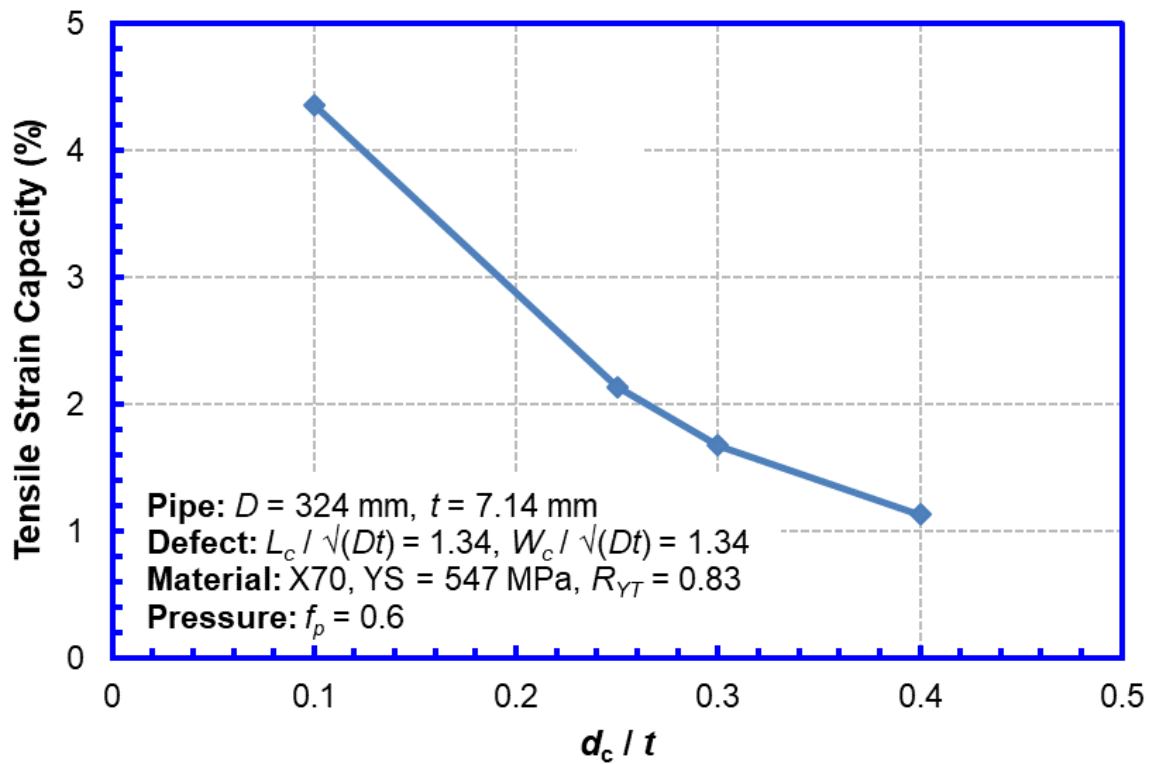


Figure 5-13 TSC vs. normalized depth of corrosion anomalies

5.2.3.4 Effect of Internal Pressure

The parameters used to study the effect of internal pressure are listed in Table 5-5. In all the analyses, the pipe properties with $Y/T = 0.83$ (see Section 5.2.2.3) was used.

The effects of the internal pressure on the TSC of pipes with corrosion anomalies are shown in Figure 5-14. It is shown that the TSC decreases with the increase of internal pressure when the pressure factor (f_p) is less than 0.50. When the pressure factor is beyond 0.50, the TSC is almost independent to internal pressure.

5.2.3.5 Effect of Pipe Y/T Ratio

All the parameters used in studying the effect of pipe Y/T ratios (R_{YT}) are listed in Table 5-6. In the studies, all pipes were kept with the same yield strength, but the ultimate tensile strength was varied to obtain different Y/T ratios. The full stress-strain curves were created using the pipe yield and tensile strengths following the procedures in [7,28].

Two pressure factors ($f_p = 0.60$ and 0.72) were used in the analyses. As discussed in Section 5.2.3.4, the small difference in the pressure factor should not make any difference in the TSC, since both pressure factors are greater than 0.50. Therefore, the results can be treated as being obtained for the same pressure factor.

The effects of the pipe Y/T ratios on the TSC of pipes with corrosion anomalies are shown in Figure 5-15 for different pipe and corrosion sizes. The results show that the TSC decreases with the increase of the Y/T ratio. For pipes with high Y/T ratios, due to the low strain hardening capacity of the materials, high strain concentration at the corrosion edge can be induced, and eventually results in low TSC.

Table 5-5 Parameters for studying the effect of pressure

D	t	f_p	R_{YT}	L_c / \sqrt{Dt}	W_c / \sqrt{Dt}	d_c / t
mm	mm			mm / mm	mm / mm	mm / mm
406	6.35	0.00, 0.15, 0.30, 0.50, 0.60, 0.72	0.83	0.25	0.50	0.40

Table 5-6 Parameters for studying the effect of Y/T ratio

D	t	f_p	R_{YT}	L_c / \sqrt{Dt}	W_c / \sqrt{Dt}	d_c / t
mm	mm			mm / mm	mm / mm	mm / mm
406	6.35	0.72	0.83, 0.88, 0.92	0.25	0.50	0.40
324	7.14	0.60	0.83, 0.90	0.34	1.34	0.25
324	7.14	0.60	0.83, 0.90	1.34	1.34	0.25
324	7.14	0.60	0.83, 0.90	1.34	1.34	0.40

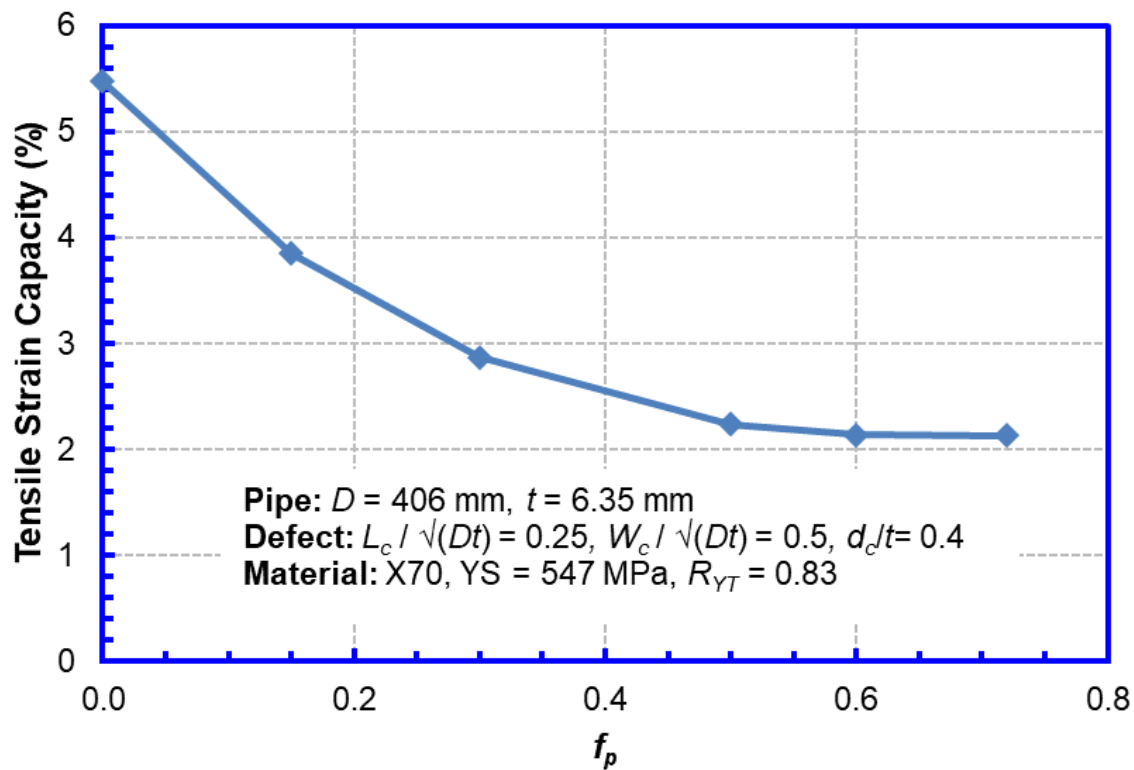


Figure 5-14 TSC vs. pipe internal pressure

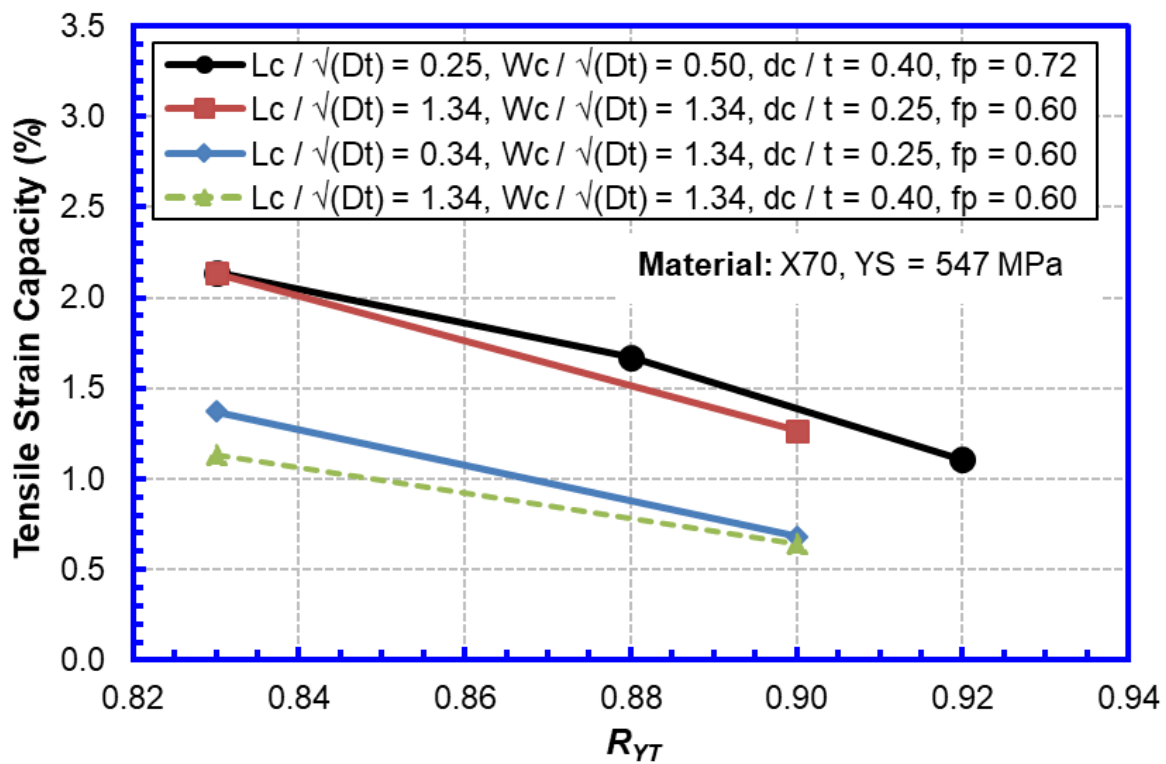


Figure 5-15 TSC vs. Y/T of pipes

5.2.4 Procedures for Assessing Tensile Strain Capacity of Corroded Pipes

The TSC results shown in Figure 5-11 and Figure 5-12 for corrosion anomalies of different L_c/\sqrt{Dt} and W_c/\sqrt{Dt} are plotted in Figure 5-16. Two additional cases ($L_c/\sqrt{Dt} = W_c/\sqrt{Dt} = 0.34$ and $L_c/\sqrt{Dt} = W_c/\sqrt{Dt} = 0.67$) are also shown in Figure 5-16.

The curve for $W_c/\sqrt{Dt} = 1.34$ was analyzed first since it has the most data points. It is found that the relationship between the TSC and L_c/\sqrt{Dt} (when $W_c/\sqrt{Dt} = 1.34$) can be approximated with a bilinear curve. Based on this observation, a set of bilinear TSC curves were developed for all W_c/\sqrt{Dt} values, as shown in Figure 5-16. These bilinear TSC curves are referred to as reference TSC ($\varepsilon_{t,corr}^{ref}$) curves in the following. It should be noted that the reference TSC curves were developed with the TSC values for a single pressure factor (i.e., $f_p = 0.60$), single corrosion depth (i.e., $d_c/t = 0.25$), and single pipe Y/T ratio (i.e., $Y/T = 0.83$).

The reference TSC curves in Figure 5-16 were developed with the TSC values for pipe $Y/T = 0.83$. The TSC was found to decrease as the pipe Y/T ratio increases (as shown in Figure 5-15). The TSC shown in Figure 5-15 were normalized by the reference TSC ($\varepsilon_{t,corr}^{ref}$), i.e., the TSC of the same corrosion size with $Y/T = 0.83$ and the normalized TSC is shown in Figure 5-17. A linear relationship can be found between the normalized TSC and the pipe Y/T ratio. The linear relationship is mainly affected by the corrosion width (W_c) and is insensitive to corrosion depth (d_c) and length (L_c). The lowest curve in Figure 5-17 (i.e., $L_c/\sqrt{Dt} = 1.34$, $W_c/\sqrt{Dt} = 1.34$, $d_c/t = 0.40$, and $f_p = 0.60$) was fitted to a bilinear equation as below:

$$\varepsilon_{t,corr}^{crit}/\varepsilon_{t,corr}^{ref} = \begin{cases} 1.0 & R_{YT} \leq 0.83 \\ -7.14R_{YT} + 6.92 & 0.83 < R_{YT} \leq 0.92 \end{cases}, \quad (5-1)$$

where, $\varepsilon_{t,corr}^{crit}$ is the TSC, $\varepsilon_{t,corr}^{ref}$ is the reference TSC, and R_{YT} is the pipe Y/T ratio.

The reference TSC curves in Figure 5-16 were developed with the TSC values for corrosion depth $d_c/t = 0.25$. As shown in Figure 5-13, the TSC increases as the d_c/t decreases. Thus, the bilinear TSC curves in Figure 5-16 can be conservatively used for $d_c/t \leq 0.25$.

In addition, the reference TSC curves in Figure 5-16 were developed with the TSC values for $f_p = 0.60$. As shown in Figure 5-14, the TSC is almost independent of the internal pressure when $f_p \geq 0.50$. If $f_p < 0.50$, the TSC increases as the pressure decreases. Therefore, the bilinear TSC curves shown in Figure 5-16 are suitable for $f_p \geq 0.50$ and can be conservatively used for $f_p < 0.50$.

Based on the above discussions, the TSC of pipes with corrosion anomalies can be calculated with the assessment procedures given below:

$$\varepsilon_{t,corr}^{crit} = \begin{cases} \varepsilon_{t,corr}^{ref} & R_{YT} \leq 0.83 \\ \varepsilon_{t,corr}^{ref}(-7.14R_{YT} + 6.92) & 0.83 < R_{YT} \leq 0.92 \end{cases}, \quad (5-2)$$

where, $\varepsilon_{t,corr}^{crit}$ is the TSC of pipes with corrosion anomalies, $\varepsilon_{t,corr}^{ref}$ is the reference TSC of pipes with corrosion anomalies, which can be determined using the reference TSC curves in Figure 5-16.

The applicable range of the above procedures depends on the range of the parameters used in the analyses. In addition, all the analyses assume the pipe failure is controlled by plastic collapse (not fracture) and the TSC is independent of fracture toughness. For very narrow circumferential grooves ($L_c \leq t$), fracture may become a concern and the above procedures are not applicable. In summary, the procedures are applicable for the following conditions:

- Corrosion Dimensions: $L_c/\sqrt{Dt} \leq 3.37$, $W_c/\sqrt{Dt} \leq 3.37$, $d_c/t \leq 0.25$, $L_c > t$, $W_c > t$
- Pipe Material Properties: $R_{YT} \leq 0.92$
- Internal Pressure: $f_p \leq 0.8$
- Strain: $\varepsilon_{t,corr}^{ref} \geq 0.2\%$

It should be noted that the assessment procedures were developed based on the analyses with limited ranges of parameters. Further analyses are needed to create the reference TSC curves for additional corrosion depth (d_c/t) and to expand the applicable corrosion length (L_c/\sqrt{Dt}) and width (W_c/\sqrt{Dt}). In addition, further analyses are needed to fully understand the effects of the internal pressure and pipe Y/T ratio on the TSC.

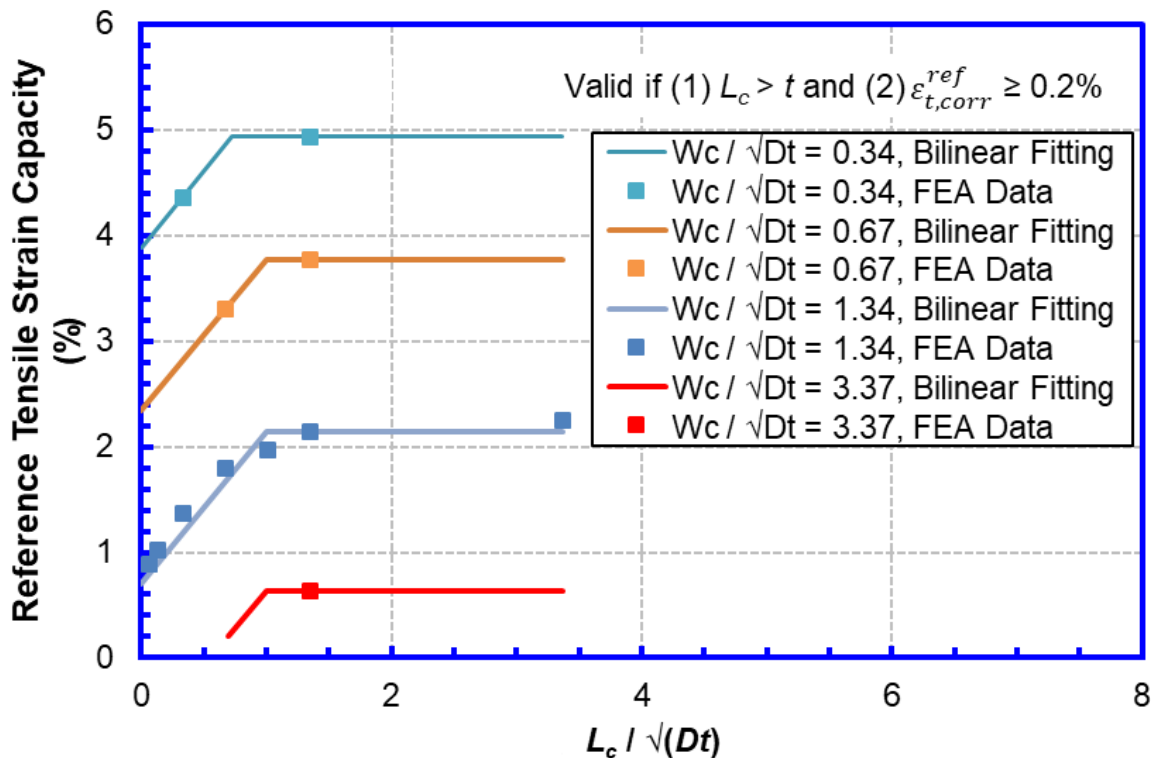
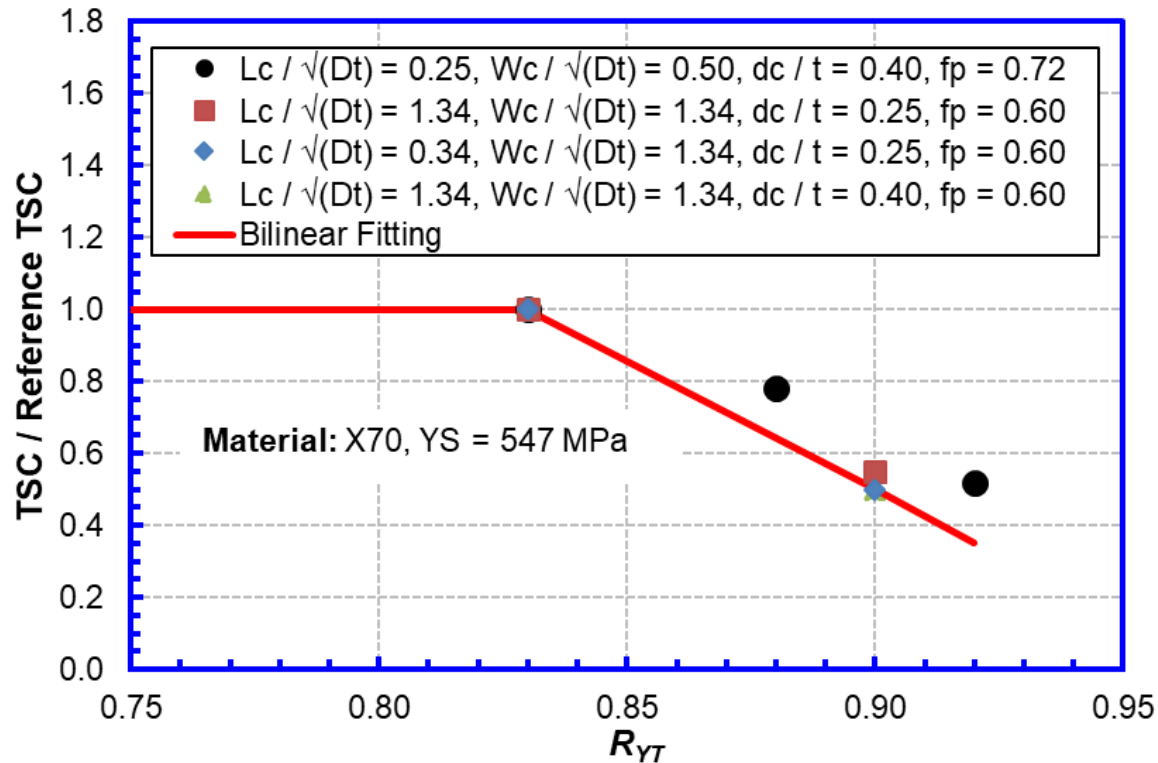


Figure 5-16 TSC data from FEA and the fitting curves for geometric parameters

Figure 5-17 TSC data from FEA and the fitting curves for Y/T ratio

5.3 Compressive Strain Capacity of Corroded Pipes

5.3.1 Application and Definition of Compressive Strain Capacity

As discussed in Section 4.3.1, the compressive strain capacity (CSC) is used to measure the capacity of a pipe to accommodate global/nominal longitudinal deformation. After the maximum bending moment is reached, the compressive strain tends to be highly localized in a small area of the pipe and the pipe capacity to accommodate global longitudinal deformation can become limited. Therefore, the CSC is measured at the maximum bending moment.

Two methods were used to measure the CSC: local CSC (average strain near the wrinkle) and global CSC (strain away from the wrinkle and extrapolated to the wrinkle location). At the maximum bending moment, small wrinkles are often formed, which results in strain localization near the wrinkle. This is especially true for pipes with corrosion anomalies. The local CSC is affected by the strain localization at the wrinkle, but the global CSC is not. The details on the strain calculations can be found in Sections 4.3.4.7.

The pipe integrity is usually determined by comparing strain capacity with strain demand. To properly use the strain capacity determined by this project, the strain demand should be defined consistently with the strain capacity in this project. Otherwise, the assessment results may become either overly conservative or non-conservative.

The local CSC is recommended to be used with the strain demand, which captures the strain localization near a wrinkle, e.g., the strain demand measured from IMU tools using similar gauge length as that used for the CSC. The global CSC is recommended to be used with the strain

demand, which does not capture the strain localization near a wrinkle, e.g., the strain demand determined from finite element analyses using beam-type models for the pipe.

5.3.2 Simulation of Experimental Tests

5.3.2.1 Finite Element Analysis Models

Finite element analyses (FEA) were conducted to simulate the full-scale bending tests for the pipes with corrosion anomalies. The three tests with corrosion anomalies (see Table 3-3) were analyzed. The analyses were conducted with commercial FEA software ABAQUS®. Figure 5-18 shows a typical finite element model used in the analyses. Due to the symmetry conditions in the circumferential and longitudinal directions, only one quarter of the pipe was modeled. Symmetry boundary conditions were applied to the quarter model. The end of the pipe was modeled as a rigid plane to simulate the end plate attached to the pipe in the experiments.

The pipe was modeled using three-dimensional shell elements. The four-node shell elements with reduced interpolation (S4R) were selected. The corrosion anomaly (highlighted in red) was modeled with reduced section thickness.

The effect of the mesh size on the analysis results was thoroughly examined. The element was refined adequately to obtain converged (mesh independent) solutions. In the longitudinal direction, small elements were used in and near the corrosion anomaly and the element sizes were gradually increased towards the end of the pipe for computational efficiency. The smallest element in the longitudinal direction was about 0.8 mm. The element size in the circumferential direction was uniform and about 5.0 mm.

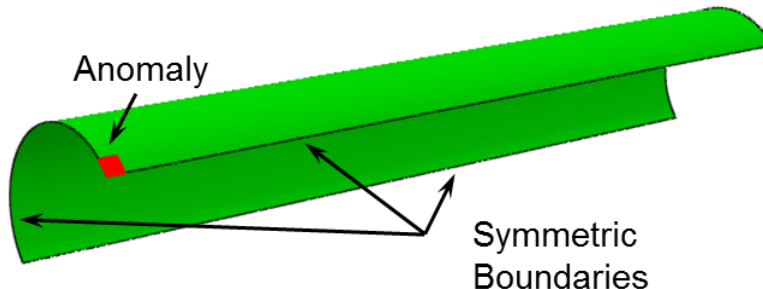


Figure 5-18 Shell pipe model with a corrosion anomaly

5.3.2.2 Loading Conditions and Material Properties

To simulate the loadings applied in the experimental tests, the load in the FEA was applied in two steps. In the first step, an internal pressure was applied to the ID surface of the pipe model to induce a hoop stress of 72% SMYS of the pipe (X65). No internal pressure and external longitudinal load were applied to the pipe end. In the second step, a monotonically increasing rotation was applied to the end of the pipe to induce bending. The corrosion anomaly was kept on the compression side of the bending. The internal pressure was kept constant in the second step.

Since the full-scale bending tests for the pipes with corrosion anomalies used the same pipes with the thin pipes used in the full-scale bending tests of transition welds, the stress-strain curves used in the FEA of the bending tests of transition welds were used in the analyses. The details of the stress-strain curves can be found in Section 4.3.4.4.

5.3.2.3 Typical Results and Calculation of Compressive Strain Capacity

Figure 5-19 shows a typical strain contour at the maximum bending moment from the FEA. The corrosion anomaly (shown at the center of the bottom of the pipe) triggers the formation of an outward wrinkle under the bending load and internal pressure.

The strain is highly concentrated and varies greatly near the wrinkle area. The strain near the pipe end also shows large variation due to the effect of the end plate.

In a finite zone between the wrinkle (i.e., also corrosion) and the pipe end, the strain varies linearly along the pipe length. This finite zone is named remote strain zone. The global CSC is determined using the strain distribution in the remote strain zone. The details on the calculation of the local and global CSC can be found in Section 4.3.4.7.2 (for regular girth welds).

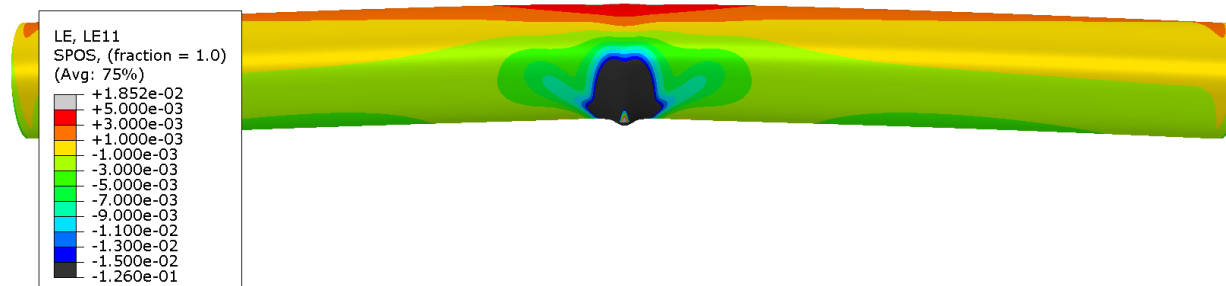


Figure 5-19 Typical strain contour (Test 2 in Table 5-7)

5.3.2.4 Comparison of Full-Scale Testing Data with FEA Results

The CSC predicted by FEA are compared with the testing results in Table 5-7 and plotted in Figure 5-20 and Figure 5-21. Both the local and global CSC values are shown. All CSC were obtained when the moment at the wrinkle location reached the peak value.

For the testing results, Method 2 was used to calculate the local CSC. For the FEA results, both Methods 1 and 2 were used to calculate the local CSC. The local CSC were calculated with the gauge length of 1D and 2D. The FEA results show that the CSC calculated by the two local methods are very similar. In the following FEA, if not mentioned, the local CSC are calculated with Method 1.

Both testing and FEA results show that the local CSC are greater than the global CSC. The local CSC with 1D gauge length are higher than the local CSC with 2D gauge length. The normalized peak moments and the corresponding end rotation angles (i.e., the rotation angles at the peak moments) for all the three tests are shown in Figure 5-22. The moments and rotation angles were normalized by the peak moment and end rotation angle of the baseline case (Specimen 9 (baseline) in Table 3-6), respectively. Among the three tests with corrosion anomalies, the pipe with the circumferential groove shows the highest peak bending moment and end rotation angle. The one with the deepest general corrosion shows the lowest peak bending moment and end rotation angle.

The end rotation angle is directly related to the global deformation and average compressive strain in the pipe. The CSC measured by the local method with 1D gauge in Figure 5-20 don't show a good correlation with the end rotation angle. On the other hand, the CSC by the local

method with 2D gauge and the global method in Figure 5-21 show good correlation with the end rotation angle. Therefore, in the rest of the study, the local CSC are measured by 2D gauge length. However, it should be noted that for very large corrosion anomalies, the local CSC with 2D gauge may not provide a good correlation with the global deformation either [83]. Therefore, the global CSC is recommended to be used.

Overall, the CSC measured from the test and predicted by FEA are reasonably consistent. The CSC predicted by FEA are generally lower than the testing results. The difference between the testing and FEA results is believed mainly due to the difference between the pipe stress-strain curves assumed in the FEA and the actual pipe stress-strain curves (i.e., measured by the small-scale tests). The details of the discussions can be found in Section 4.3.4.8.

Table 5-7 Compressive strain measured by different methods and comparison between FEA and test results

Size of Pipe		Test Number	Corrosion Feature	Size of Corrosion Anomalies $W_c \times L_c \times d_c$	Compressive Strain from Experiments			Compressive Strain from FEA				
D	t				Local Method 2, $l = 1D$	Local Method 2, $l = 2D$	Global Method	Local Method 1, $l = 1D$	Local Method 2, $l = 1D$	Local Method 1, $l = 2D$	Local Method 2, $l = 2D$	Global Method
mm	mm				%	%	%	%	%	%	%	%
324	6.35	1	Baseline (No Feature)	N/A	-3.6	-3.3	-3.7	N/A	N/A	N/A	N/A	N/A
		2	General Corrosion	$0.20D \times 0.20D \times 0.25t$	-2.3	-1.5	-1.0	-2.3	-2.2	-1.5	-1.3	-1.1
		3	Circumferential Groove	$0.20D \times 0.05D \times 0.25t$	-2.8	-2.5	-2.6	-2.2	-2.1	-1.9	-1.8	-1.9
		4	Deep General Corrosion	$0.20D \times 0.20D \times 0.40t$	-2.6	-1.5	-0.7	-2.3	-2.0	-1.3	-1.2	-0.7

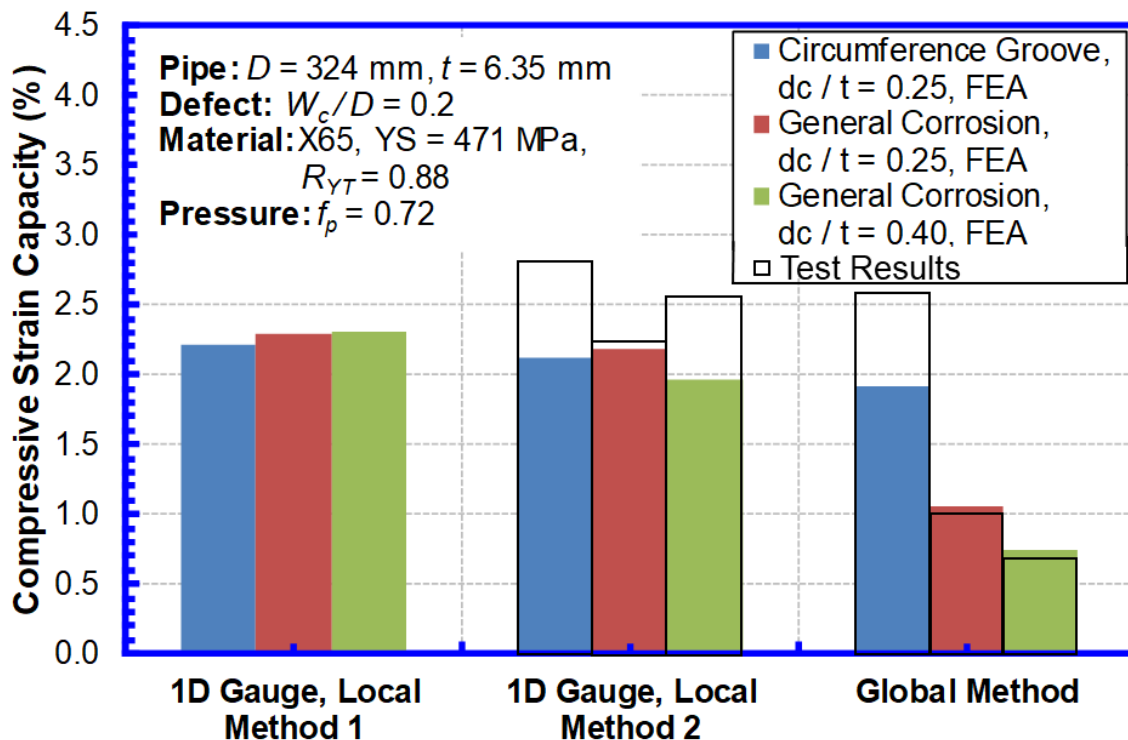


Figure 5-20 Comparison between compressive strains from FEA and tests (1D gauge and global method)

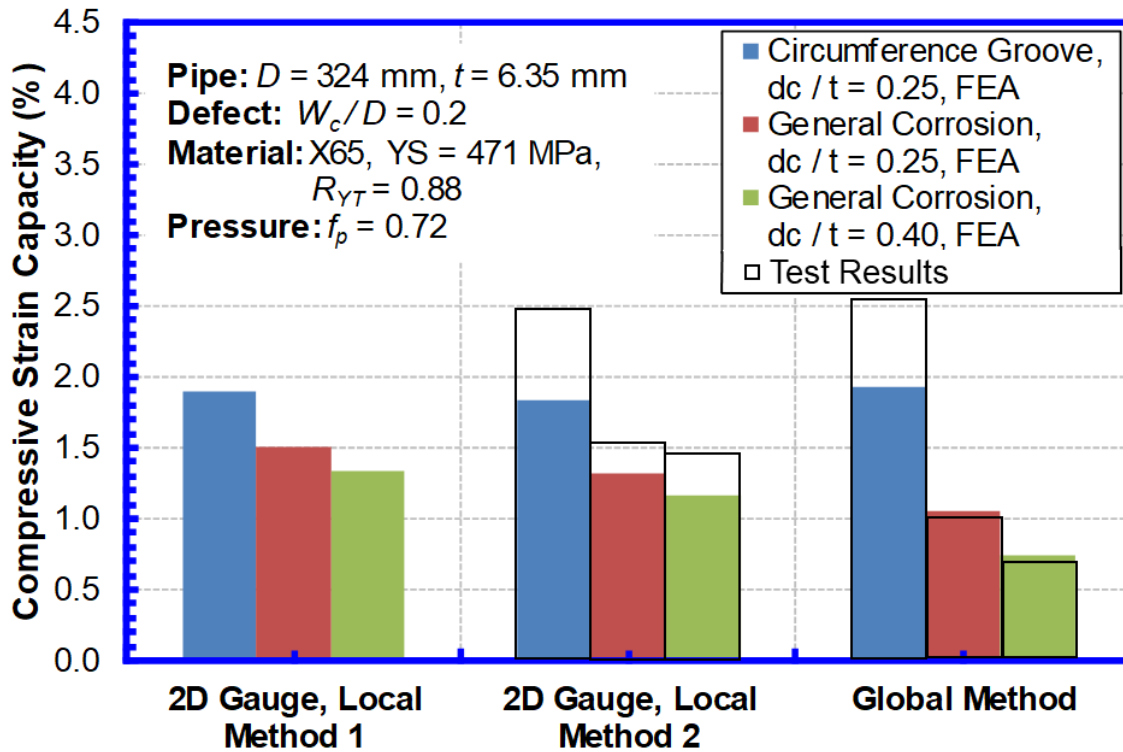


Figure 5-21 Comparison between compressive strains from FEA and tests (2D gauge and global method)

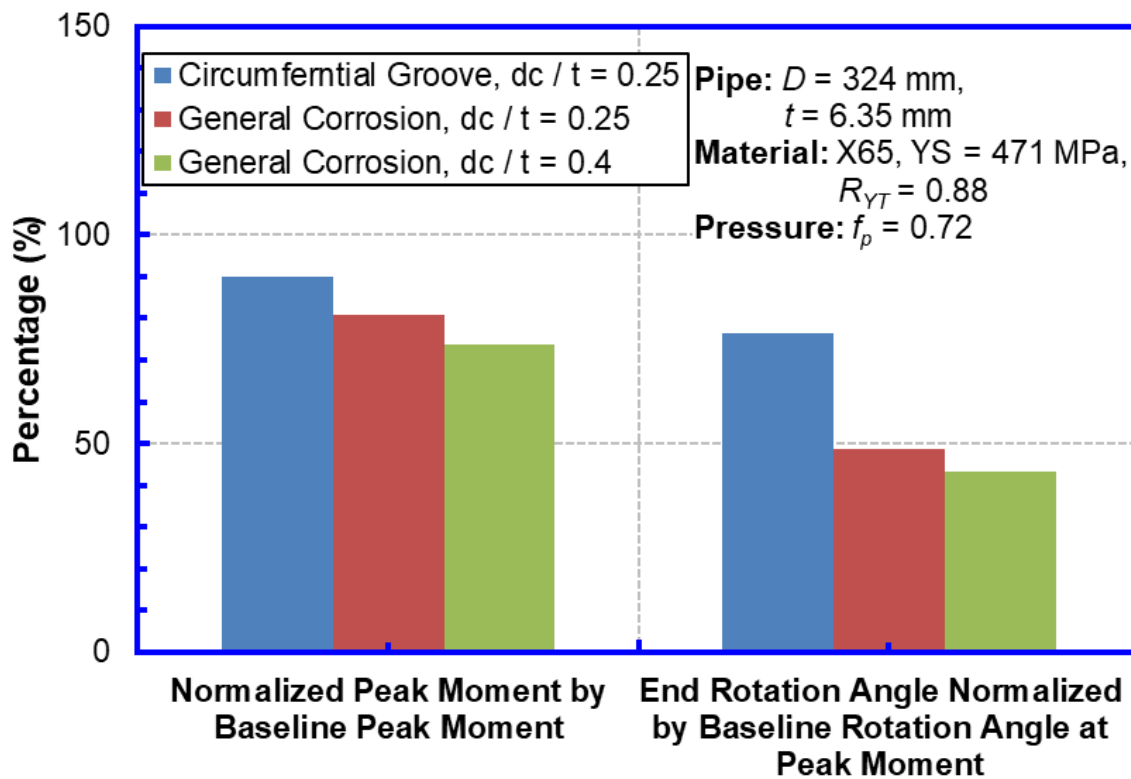


Figure 5-22 Normalized peak moment and rotation angle

5.3.3 Parametric Studies

5.3.3.1 Overview of the Parametric Analyses

Parametric finite element analyses were conducted to study the effects of various parameters, including corrosion sizes, pipe Y/T ratios, internal pressure, and pipe D/t ratios, on the CSC of corroded pipes. The finite element models described in Section 5.3.2.1 were used in the parametric analyses.

5.3.3.2 Effect of Anomaly Sizes

The anomaly sizes investigated are listed in Table 5-8, where the FEA are divided into three groups. Groups 1-3 are targeted for the anomaly length, width, and depth, respectively. In all the analyses, the pipe D/t ratio ($D/t = 51$, $D = 324$ mm and $t = 6.35$ mm) and material properties ($Y/T = 0.88$) are the same as those used in the simulation of the full-scale tests. The pressure factor (f_p) is kept at 0.72.

Table 5-8 Parameters for studying the effect of anomaly sizes

Group	D	t	D/t	f_p	R_{YT}	L_c/\sqrt{Dt}	W_c/\sqrt{Dt}	d_c/t
	mm	mm	mm/mm			mm/mm	mm/mm	mm/mm
1	324	6.35	51	0.72	0.88	0.070, 0.21, 0.35, 0.70, 1.4, 2.1, 3.5	1.4	0.25
2						1.4	0.070, 0.21, 0.35, 0.70, 2.1	0.25
3						1.4	1.4	0.10, 0.40, 0.60

The effects of the corrosion sizes on the CSC of the pipe are shown in Figure 5-23 to Figure 5-25. Both the local CSC measured by Method 1 with 2D gauge (i.e., 2D CSC) and the global CSC (CSC by extrapolation) are shown. The 2D CSC were found to be higher than the CSC by extrapolation since the local method captured the local strain concentration at wrinkle. Figure 5-23 shows that the CSC decreases with the increase of the longitudinal length of corrosion anomalies (L_c/\sqrt{Dt}). The CSC gradually reaches a constant value as L_c/\sqrt{Dt} reaches a critical value (~ 2.0) and the further increase of L_c/\sqrt{Dt} beyond the critical value does not have a major impact on the CSC.

As discussed in Section 5.2.3.2, the wavelength of the through-wall bending stress in a pipe is about $3.4\sqrt{Dt}$. Since wrinkles are the results of excessive through-wall bending stress, the wrinkles should have similar wavelength. For small L_c/\sqrt{Dt} , the wrinkle cannot be contained by the corrosion and must extend outside the corrosion. As a result, the CSC can be increased by the region with the regular wall thickness. The larger the L_c/\sqrt{Dt} , the smaller the regular wall thickness region in the wrinkle and therefore the smaller the CSC. When L_c/\sqrt{Dt} reaches about 2.0, the bulged-out part of the wrinkle can be fully contained inside the corrosion and the effect of the regular wall thickness region on the CSC is greatly reduced. Therefore, further increase of L_c/\sqrt{Dt} shows minimum effect on the CSC. The CSC also decreases with the increase of circumferential width (W_c/\sqrt{Dt}) and the depth (d_c/t) of the corrosion anomalies, as shown in Figure 5-24 and Figure 5-25, respectively.

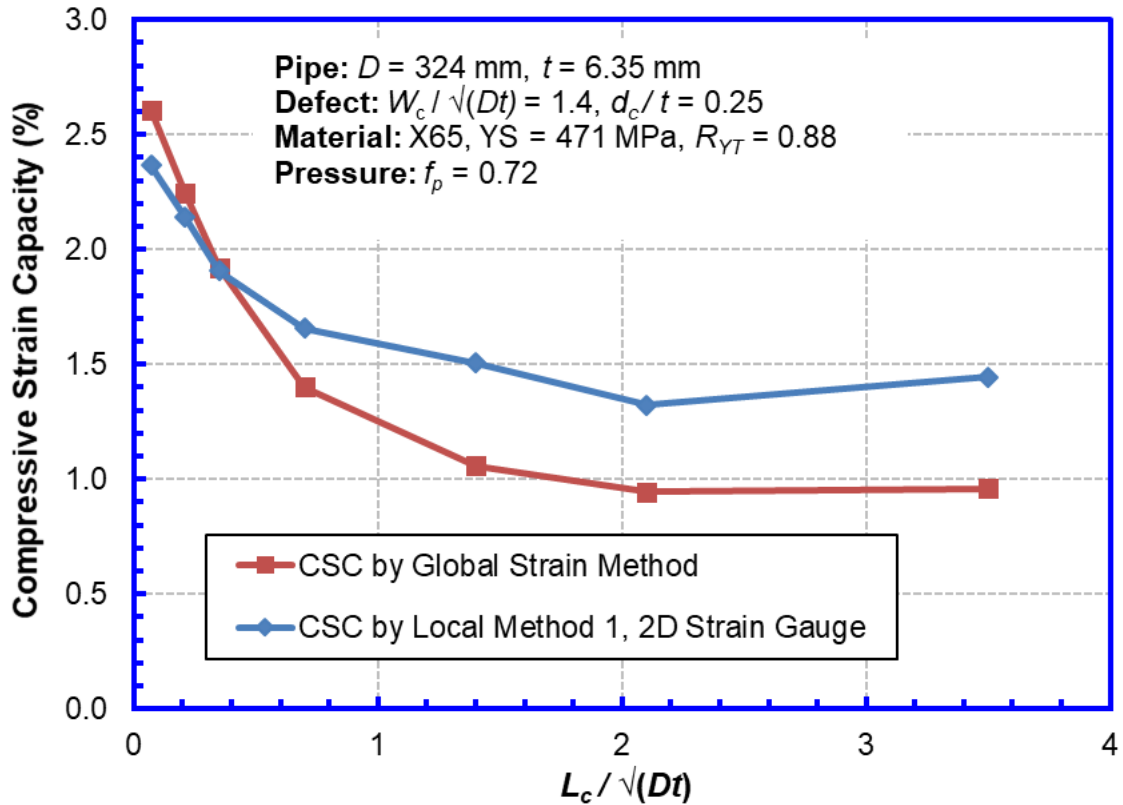


Figure 5-23 CSC vs. normalized longitudinal length of corrosion anomalies

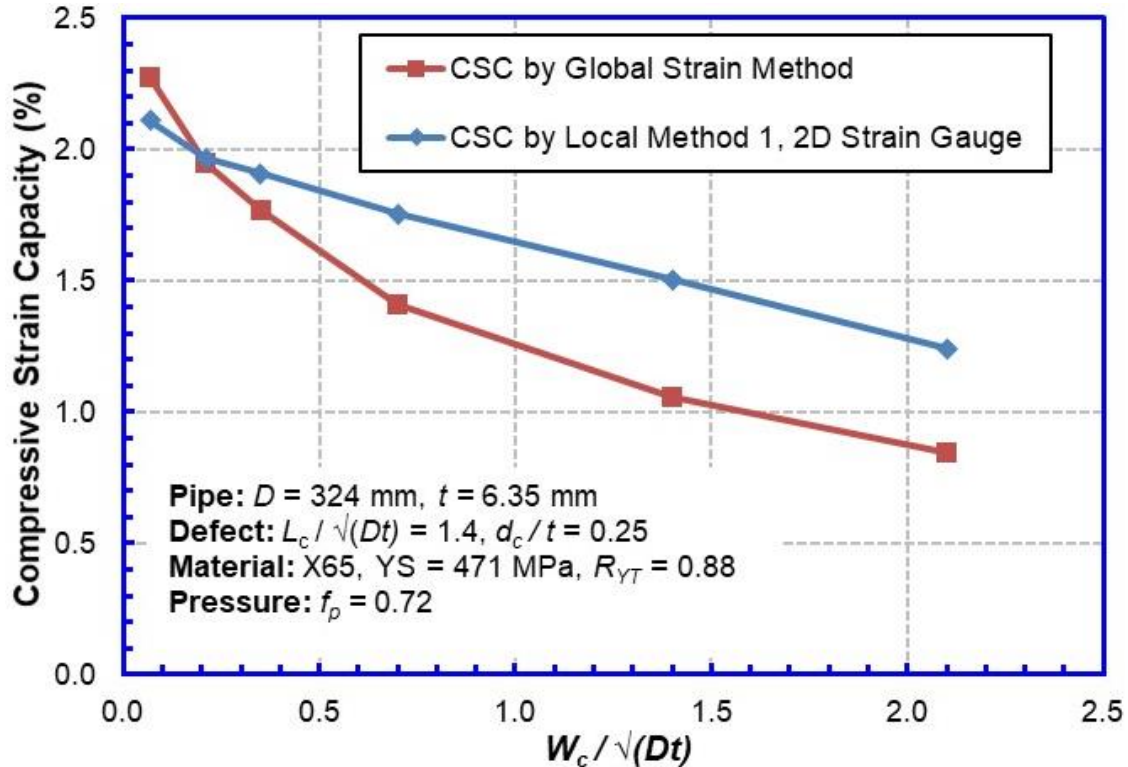


Figure 5-24 CSC vs. normalized circumferential width of corrosion anomalies

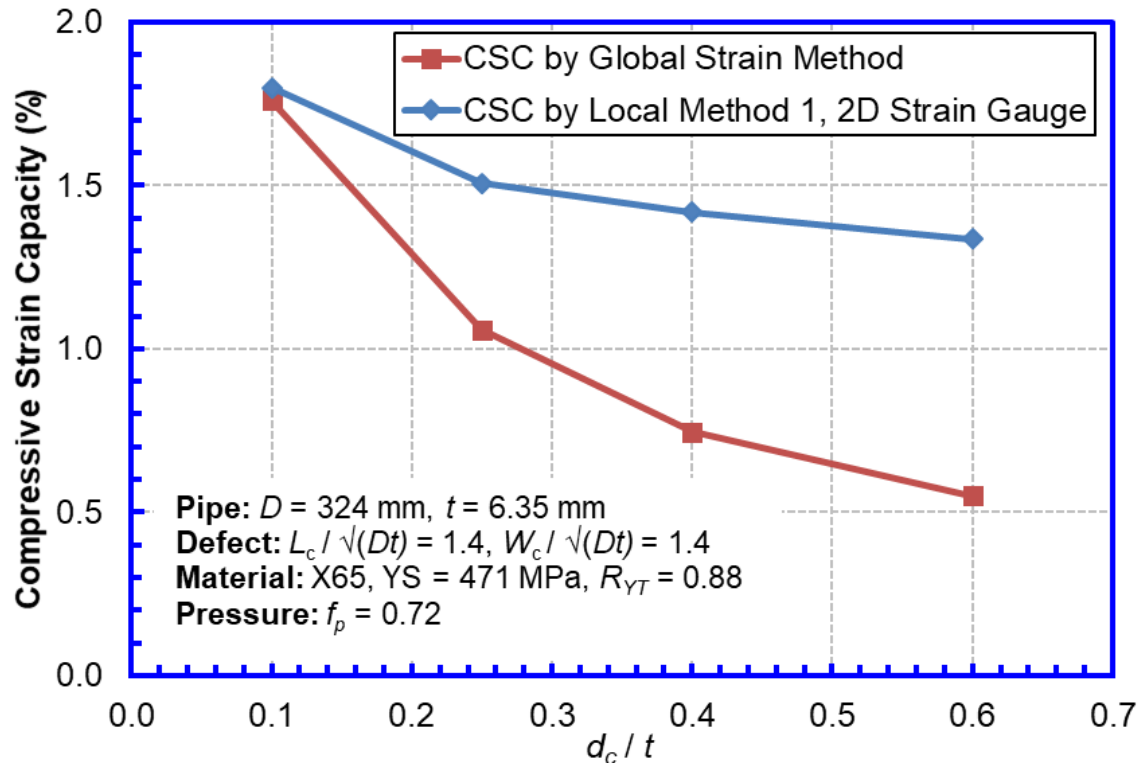


Figure 5-25 CSC vs. normalized depth of corrosion

5.3.3.3 Effect of Internal Pressure

The parameters used to study the effect of internal pressure are shown in Table 5-9. Three pressure factors (f_p) were used in the FEA. In all the analyses, the pipe D/t ratio ($D/t = 51$, $D = 324$ mm and $t = 6.25$ mm) and material properties ($Y/T = 0.88$) were the same as those used in the simulation of the full-scale tests. Figure 5-26 shows that the CSC increases with the internal pressure. The pressure effect is more obvious at relatively high internal pressure ($f_p > 0.50$). The results are consistent with the trend in the prior work [26] on the CSC of plain pipes.

5.3.3.4 Effect of Pipe Y/T Ratio

The parameters used to study the effect of pipe Y/T ratios (R_{YT}) are shown in Table 5-10. Three pipe Y/T ratios were used in the FEA. In all the analyses, the pipe yield strength was kept the same as that used in the simulation of the full-scale tests (471 MPa) and the ultimate tensile strength was varied to obtain the target pipe Y/T ratios. The pipe D/t ratio was the same as that used in the simulation of the full-scale tests ($D/t = 51$, $D = 324$ mm, $t = 6.35$ mm). The pressure factor (f_p) was kept at 0.72. Figure 5-27 shows that the CSC decreases with the increase of the Y/T ratio. The results are consistent with those in the prior work [26] on the CSC of plain pipes.

5.3.3.5 Effect of Pipe D/t Ratio

The parameters used to study the effect of pipe D/t ratio are listed in Table 5-10. Three pipe D/t ratios were used in the FEA and the corresponding pipe dimensions (D and t) were also shown. In all the analyses, the material properties were the same as those used in the simulation of the full-scale tests ($Y/T = 0.88$). The pressure factor (f_p) was kept at 0.72. Figure 5-28 shows that the CSC decreases with the increase of the D/t ratio. The effect of the D/t ratio on the CSC

is especially large for small D/t ratios, e.g., D/t ratios from 20 to 51. The results are consistent with those in the prior work [26] on the CSC of plain pipes.

Table 5-9 Parameters for studying the effect of pressure

D	t	D/t	f_p	R_{YT}	L_c/\sqrt{Dt}	W_c/\sqrt{Dt}	d_c/t
mm	mm	mm/mm			mm/mm	mm/mm	mm/mm
324	6.35	51	0.00, 0.50, 0.72	0.88	1.4	1.4	0.25

Table 5-10 Parameters for studying the effect of pipe Y/T ratio

D	t	D/t	f_p	R_{YT}	L_c/\sqrt{Dt}	W_c/\sqrt{Dt}	d_c/t
mm	mm	mm/mm			mm/mm	mm/mm	mm/mm
324	6.35	51	0.72	0.84, 0.88, 0.92	1.4	1.4	0.25

Table 5-11 Parameters for studying the effect of pipe D/t ratio

D	t	D/t	f_p	R_{YT}	L_c/\sqrt{Dt}	W_c/\sqrt{Dt}	d_c/t
mm	mm	mm/mm			mm/mm	mm/mm	mm/mm
324	6.35	51.0	0.72	0.88	1.4	1.4	0.25
254	12.7	20.0					
1219	11.7	104					

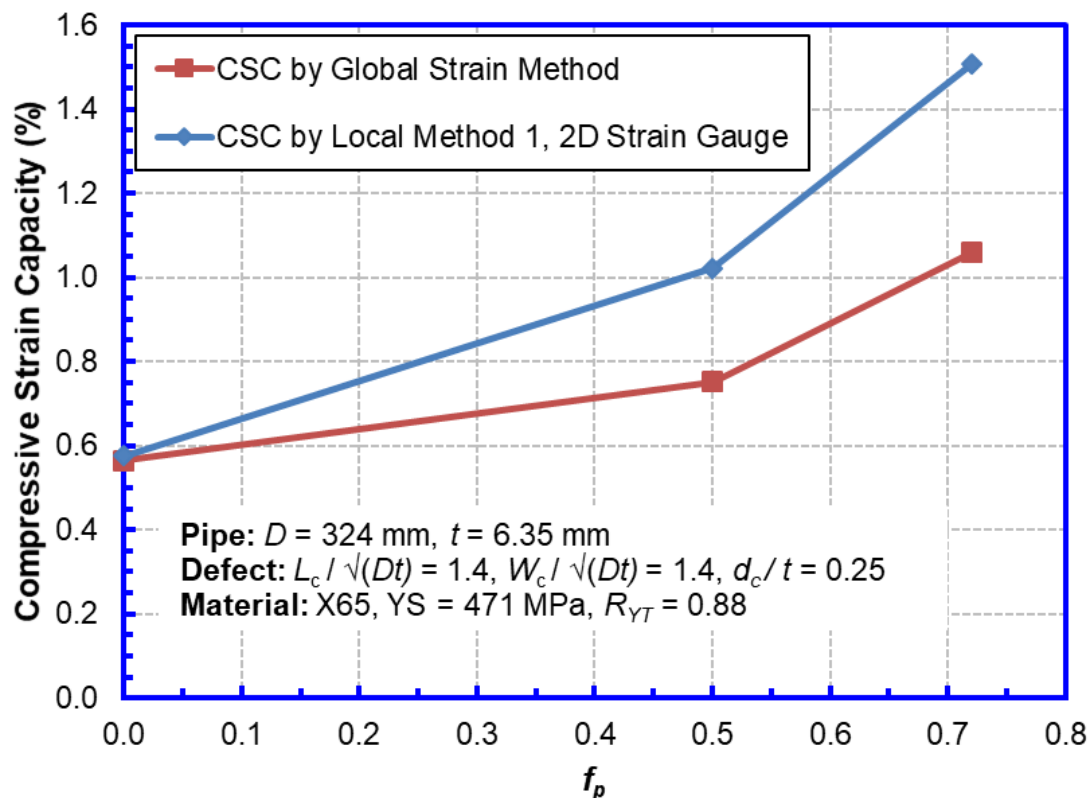
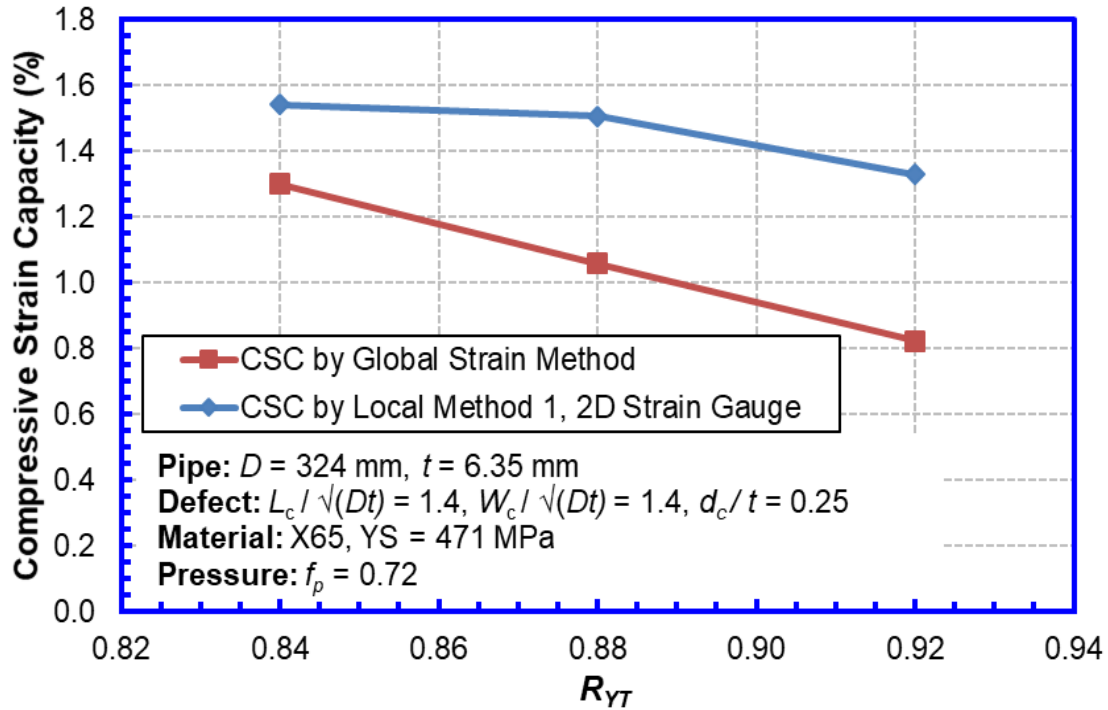
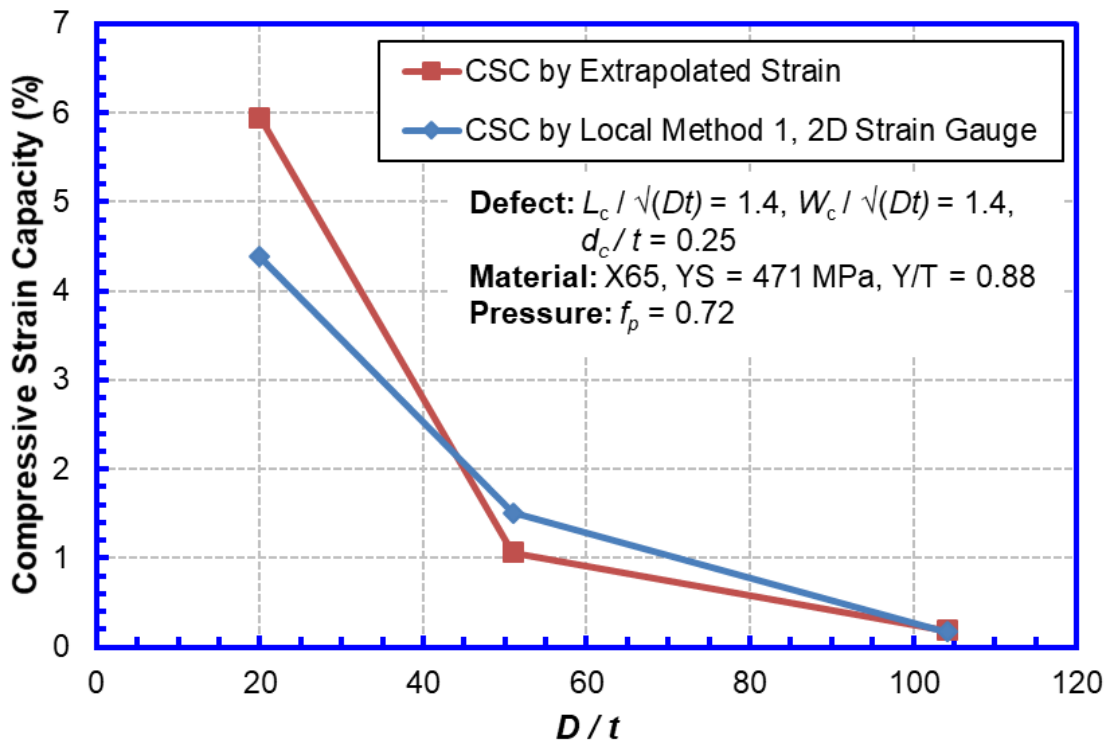


Figure 5-26 CSC vs. pipe internal pressure

Figure 5-27 CSC vs. Y/T ratio of pipeFigure 5-28 CSC vs. D/t ratio of pipe

5.3.4 Procedures for Assessing Compressive Strain Capacity of Corroded Pipes

As discussed in Section 5.3.2.4, for corroded pipes, the local CSC (especially the local CSC measured with 1D gauge length) may not correlate with the pipes' capacity to withstand the longitudinal deformation. Therefore, the procedures for assessing the CSC of corroded pipes were developed for the global CSC (i.e., CSC by extrapolation) only.

The global CSC (CSC by extrapolation) shown in Figure 5-23 and Figure 5-24 for corrosion anomalies of different L_c/\sqrt{Dt} and W_c/\sqrt{Dt} are plotted in Figure 5-29. The CSC from three additional FEA cases ($L_c/\sqrt{Dt} = W_c/\sqrt{Dt} = 0.35, 0.70$, and 2.1) are also included.

The data for $W_c/\sqrt{Dt} = 1.4$ were analyzed first since they have the most data points. The CSC - L_c/\sqrt{Dt} relationship for $W_c/\sqrt{Dt} = 1.4$ was found to follow an exponential curve. Similar exponential curves were developed for other W_c/\sqrt{Dt} , as shown in Figure 5-29. Those exponential curves are referred to as reference CSC ($\epsilon_{c,corr}^{ref}$) curves in the following. The reference CSC curves were developed with the CSC values for a single pipe D/t ratio (i.e., $D/t = 51$), single pressure factor (i.e., $f_p = 0.72$), single corrosion depth (i.e., $d_c/t = 0.25$), and single pipe Y/T ratio (i.e., $Y/T = 0.88$).

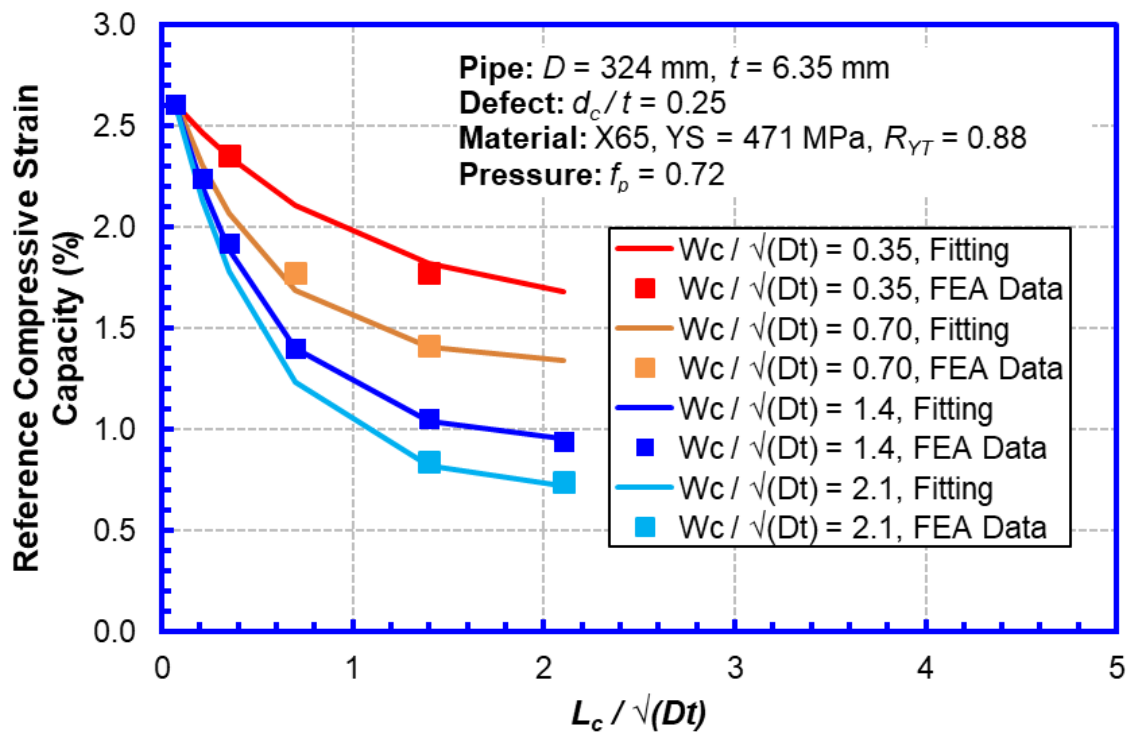


Figure 5-29 Reference CSC curves

The effects of the internal pressure, pipe D/t ratio, and pipe Y/T ratio on the CSC of plain pipes were studied in a prior PHMSA supported project [26]. Simplified equations were created to quantify those effects, see Eq. (4-9). Based on Eq. (4-9), the CSC of the pipes with corrosion anomalies can be calculated as indicated below:

$$\varepsilon_{c,corr}^{crit} = \varepsilon_{c,corr}^{ref} (2.87 - 2.13R_{YT}) (452.6f_p + 213.5) \left(\frac{D}{t}\right)^{-1.6}, \text{ if } f_p \geq f_{pc}, \quad (5-3)$$

where,

$$f_{pc} = 1.8 \times 10^{-4} \left(\frac{D}{t}\right)^{-1.6}. \quad (5-4)$$

In the above equations, $\varepsilon_{c,corr}^{crit}$ is the CSC of pipes with corrosion anomalies and $\varepsilon_{c,corr}^{ref}$ is the reference CSC determined using Figure 5-29.

For the cases analyzed in the parametric studies, i.e., Section 5.3.3.3 (pressure effect), 5.3.3.4 (Y/T effect), and 5.3.3.5 (D/t effect), the CSC ($\varepsilon_{c,corr}^{crit}$) were calculated with Eq. (5-3). The CSC calculated by the equation were compared with the FEA results in Figure 5-30 to Figure 5-32. As shown in Figure 5-30, Eq. (5-3) tends to provide conservative (lower than actual) CSC for pipe $D/t \leq 51$, but non-conservative CSC for pipe $D/t > 51$. Therefore, the Equation (5-3) can be used for pipes with $D/t \leq 51$ conservatively.

As shown in Figure 5-31, Eq. (5-3) tends to provide conservative (lower than actual) CSC for pipe $Y/T \leq 0.88$, but non-conservative CSC for pipe $Y/T > 0.88$. Therefore, the Eq. (5-3) can be conservatively (i.e., predict lower than actual CSC) used for $Y/T \leq 0.88$.

Figure 5-32 shows that Eq. (5-3) tends to provide non-conservative (higher than actual) CSC for pipe $f_p < 0.72$. Therefore, Eq. (5-3) is not recommended to be used for $f_p < 0.72$. For pipe with $f_p \geq 0.72$, it is recommended to use Eq. (5-3) by setting $f_p = 0.72$.

The reference CSC curves in Figure 5-29 are for $d_c/t = 0.25$. As shown in Figure 5-25, the CSC increases as the d_c/t decreases. As a result, the reference CSC curves in Figure 5-29 can be conservatively used for $d_c/t \leq 0.25$.

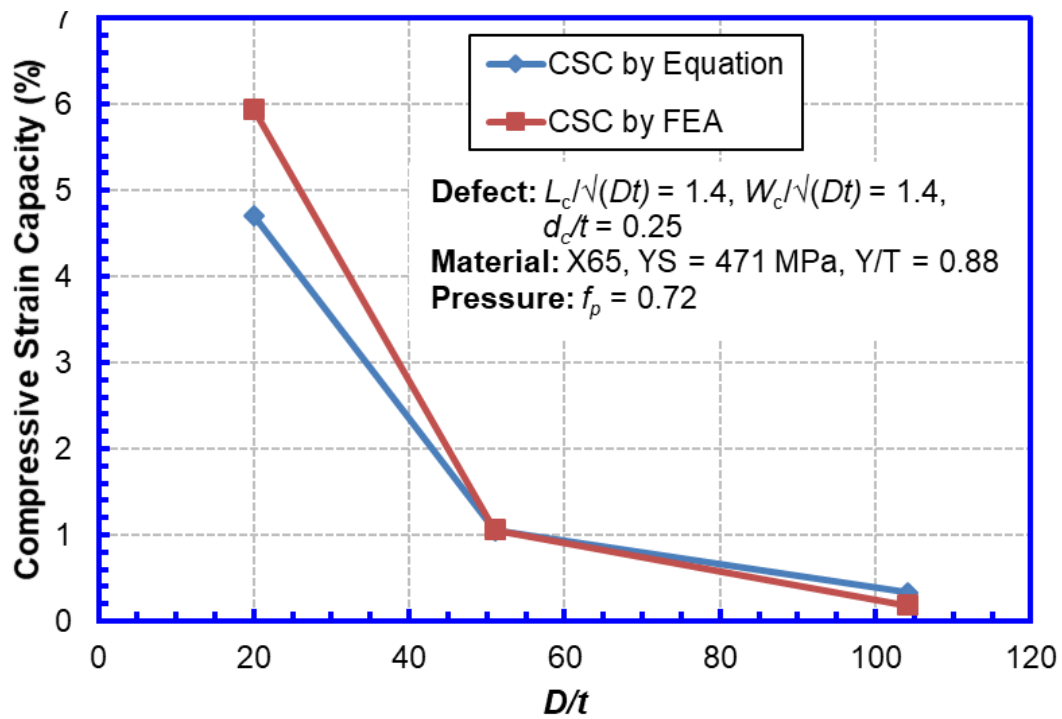
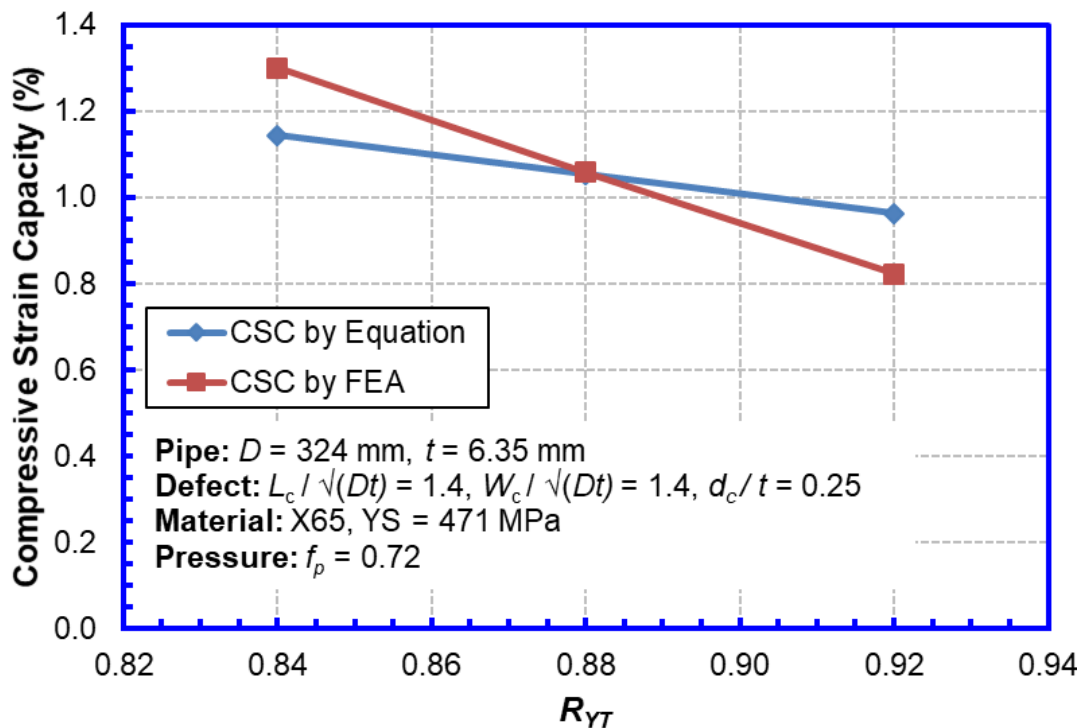
Based on the above discussions, the CSC of the pipes with corrosion anomalies can be calculated following the assessment procedures given below:

$$\varepsilon_{c,corr}^{crit} = 539.3\varepsilon_{c,corr}^{ref} (2.87 - 2.13R_{YT}) \left(\frac{D}{t}\right)^{-1.6}. \quad (5-5)$$

The assessment procedures are applicable for the following conditions:

- Pipe Dimensions: $20 \leq D/t \leq 51$
- Corrosion Dimensions: $L_c/\sqrt{Dt} \leq 2.1$, $W_c/\sqrt{Dt} \leq 2.1$, $d_c/t \leq 0.25$, $L_c > t$, $W_c > t$
- Pipe Material Properties: $0.84 \leq R_{YT} \leq 0.88$.
- Pressure Factor: $f_p \geq 0.72$

It should be noted that the assessment procedures were developed based on the analyses with limited ranges of parameters. Further analyses are needed to create the reference CSC curves for additional corrosion depths (d_c/t) and expand the applicable corrosion length (L_c/\sqrt{Dt}) and width (W_c/\sqrt{Dt}). In addition, further analyses are needed to fully understand the effects of the internal pressure, pipe D/t ratio and pipe Y/T ratio on the CSC.

Figure 5-30 CSC calculated using FEA and the CSC equation for different D/t ratiosFigure 5-31 CSC calculated using FEA and the CSC equation for different Y/T ratios

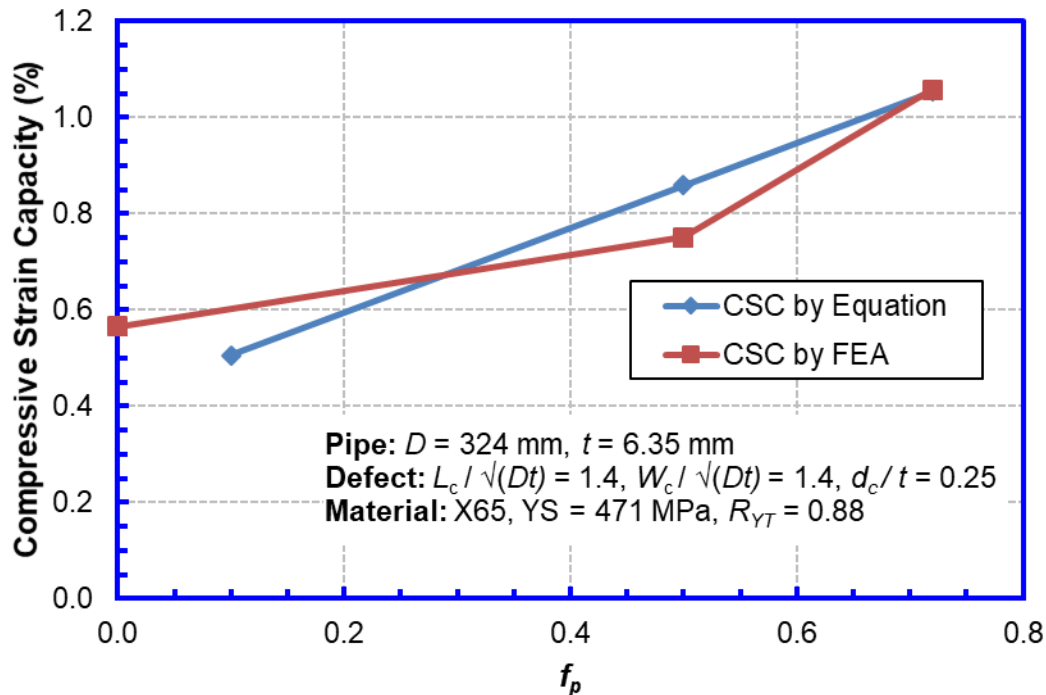


Figure 5-32 CSC calculated using FEA and the CSC equation for different internal pressures

5.4 Burst Pressure of Corroded Pipes Subjected to Longitudinal Strain

5.4.1 Background and Application of Burst Pressure

The burst pressure is the maximum internal pressure a pipe can withstand without bursting (or leaking). The burst pressure of pipes with corrosion anomalies has been extensively studied and multiple burst pressure equations are available in codes and standards [31,32,33,34].

For a pipe with a corrosion anomaly, the calculated burst pressure can be used to verify the safety margin of the maximum allowable operating pressure (MAOP). If the minimum safety margin cannot be met, the anomaly needs to be repaired.

In most existing burst pressure equations, the primary load considered is the pipe hoop stress induced by the internal pressure. The effect of the longitudinal stress on the burst pressure is not considered. However, it is known that the longitudinal tensile stress can increase the burst pressure, whereas the longitudinal compressive stress can reduce the burst pressure. The burst pressure equation in DNV-RP-F101 [34] considers the reduction of the burst pressure due to a constant compressive stress. The increase of the burst pressure due to the longitudinal tensile stress is usually not considered.

Like the longitudinal stress, the longitudinal tensile strain tends to increase the burst pressure and the longitudinal compressive strain may reduce the burst pressure. The DNV equation is not applicable for pipes subjected to longitudinal compressive strain, since the longitudinal stress is not constant as the internal pressure increases. Under a constant longitudinal compressive strain, the longitudinal stress decreases as the internal pressure increases.

5.4.2 Analysis of Burst Pressure of Corroded Pipes under Longitudinal Strain

5.4.2.1 Overview of the Analysis

The focus of the analyses in this section was on the effect of the longitudinal compressive strain on the burst pressure of pipes with corrosion anomalies. The burst pressures under various longitudinal compressive strains were calculated with finite element analyses (FEA) to determine how the longitudinal strain affects the burst pressure. Both the size and shape of the corrosion anomalies were varied in the FEA to examine if the effect of the longitudinal compressive strain on burst pressure varies with the corrosion size and shape.

Since the existing burst pressure equations can be conservative (i.e., predicted burst pressure is lower than actual burst pressure) for pipes subjected to longitudinal tensile strain, the effect of the longitudinal tensile strain on the burst pressure was not studied.

5.4.2.2 Finite Element Analysis Models

Finite element analyses (FEA) were conducted to simulate the burst of corroded pipes under constant longitudinal compressive strain. The finite element models used in the analyses were similar to those used to simulate the full-scale tensile tests of corroded pipes shown in Section 5.2.2.1. But, the element size of the finite element model was adjusted to accommodate the change of the main/dominate load (or failure driver).

For the burst, the failure driver is the hoop stress. Therefore, the mesh in the circumferential direction was refined to obtain converged solutions. Uniform elements of 0.5 mm were used in the circumferential direction. In the longitudinal direction, the elements were small at the anomaly and were gradually increased towards the end of the pipe for computational efficiency. The smallest element size in the longitudinal direction was 1.0 mm. In the thickness direction, the element was also uniform. The element size was 0.7 mm.

5.4.2.3 Loading Conditions and Material Properties

The loading conditions were similar to those used in the full-scale tests. The load in the FEA was applied in three steps. In the first step, an internal pressure was applied to the ID surface of the pipe model to induce a hoop stress of 72% SMYS of the pipe (X70). The end of the pipe was load free in the longitudinal direction. In the second step, a monotonically increasing rotation was applied to the end of the pipe to induce the target 2D compressive strain (by Local Method 1) at the corrosion area. The corrosion anomaly was kept on the compression side. The internal pressure was kept constant during the second step. In the third step, the internal pressure was increased until the maximum pressure was reached (i.e., burst event), while the displacement and rotation at the end of the pipe were fixed. Additional discussions about the determination of the burst event in FEA can be found in Section 5.4.2.5.

Since the burst pressure is mainly determined by the circumferential properties, the same pipe properties ($Y/T = 0.83$) used to simulate the full-scale tensile tests were used in the FEA. The details of the pipe properties can be found in Section 5.2.2.3. The properties used in FEA had lower strength than (but similar Y/T ratio with) the actual pipe circumferential properties.

5.4.2.4 Parameters in the FEA

The parameters used in the analyses are listed in Table 5-12. Both general corruptions (i.e., square patch) and grooves (longitudinal and circumferential) were analyzed. Two depths were studied, i.e., 25% and 40% of wall thickness.

The maximum compressive strain analyzed was 2.3%. The compressive strain was defined as the average compressive strain within a 2D gauge length centered at the wrinkle location, i.e., 2D compressive strain. The 2D compressive strain was calculated with the Local Method 1 as defined in Section 5.3.2.3. For most cases in Table 5-12, the applied 2.3% 2D compressive strain is beyond the compressive strain capacity of the pipe and an obvious wrinkle can be found right at the corrosion location. Therefore, the results presented in this section are suitable for wrinkle-corrosion interactions.

Table 5-12 Value of corrosion feature geometries and compressive strain

D	t	Corrosion ID	Corrosion Feature	L_c / \sqrt{Dt}	W_c / \sqrt{Dt}	d_c / t	2D Compressive Strain
mm	mm			mm / mm	mm / mm	mm / mm	%
324	7.14	1	General Corrosion	1.34	1.34	0.25	0.0, -0.2, -0.8, -1.5, -2.3
		2	General Corrosion	1.34	1.34	0.40	0.0, -1.5, -2.3
		3	Long. Groove	1.34	0.34	0.25	0.0, -1.5, -2.3
		4	Long. Groove	1.34	0.34	0.40	0.0, -1.5, -2.3
		5	Circum. Groove	0.34	1.34	0.25	0.0, -1.5, -2.3

5.4.2.5 Typical Results and Failure Criteria

Figure 5-33 and Figure 5-34 show the strain contours of a corroded pipe under 2.3% 2D compressive strain. It is found that an outward wrinkle is formed at the corrosion and grows under bending load and internal pressure (see Figure 5-33). The compressive strain is highly concentrated at the corrosion edges along the pipe circumference (see Figure 5-34).

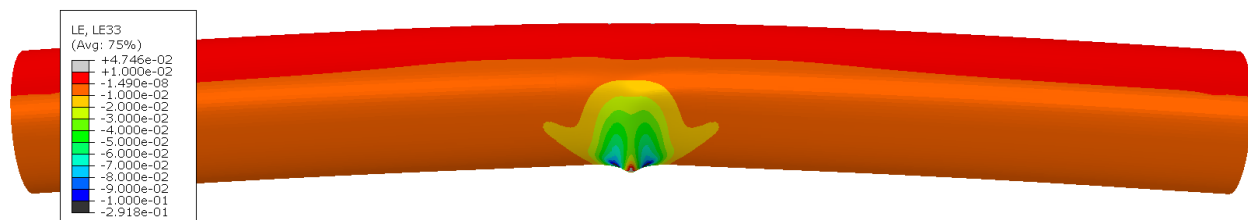


Figure 5-33 Longitudinal strain contour of the corroded pipe under 2.3% 2D compressive strain – side view (Specimen 10.c in Table 3-10)

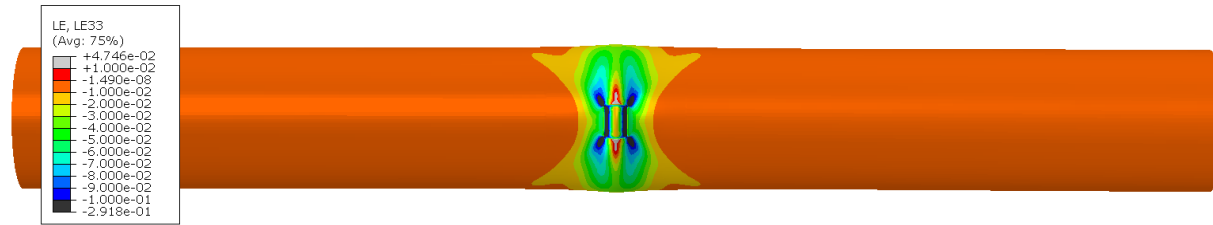


Figure 5-34 Longitudinal strain contour of the corroded pipe under 2.3% 2D compressive strain – bottom (compression side) view (Specimen 10.c in Table 3-10)

To properly determine the burst event using the FEA, the failure criteria discussed in Section 5.2.2.5 for determining the tensile strain failure were applied. The predicted burst pressures were compared with the test data. The comparison showed that all the local failure criteria, i.e., the maximum Mises, DNV[72], API 579 [32], and Korea University criteria [73], can significantly under-predict the burst pressure under high longitudinal compressive strains. The maximum load criterion was therefore selected. In the FEA, the burst was defined as the event when the maximum pressure is reached. The Riks analysis method [84] was used to determine the maximum pressure.

5.4.2.6 Effect of Longitudinal Strain on Burst Pressure

To quantify the effect of the longitudinal compressive strain on the burst pressure, a burst pressure ratio is defined. The burst pressure ratio is defined as the ratio between the burst pressure of the pipe under a given longitudinal compressive strain and the burst pressure of the pipe under no longitudinal compressive strain.

Figure 5-35 shows the relationship between the burst pressure ratio and the longitudinal compressive strain. The results show that the burst pressure decreases with the increase of the longitudinal compressive strain. However, the reduction of the burst pressure due to the longitudinal compressive strain is very small. In addition, the reduction of the burst pressure is obvious only for the deep longitudinal groove. For example, for the longitudinal groove of $d_c/t = 0.40$, at 2.3% 2D compressive strain, the maximum reduction in the burst pressure is about 13%. While for the others (i.e., longitudinal groove of $d_c/t = 0.25$, general corrosion, and circumferential groove), the maximum reduction is less than 5%, when the pipe is under 2.3% longitudinal compressive strain.

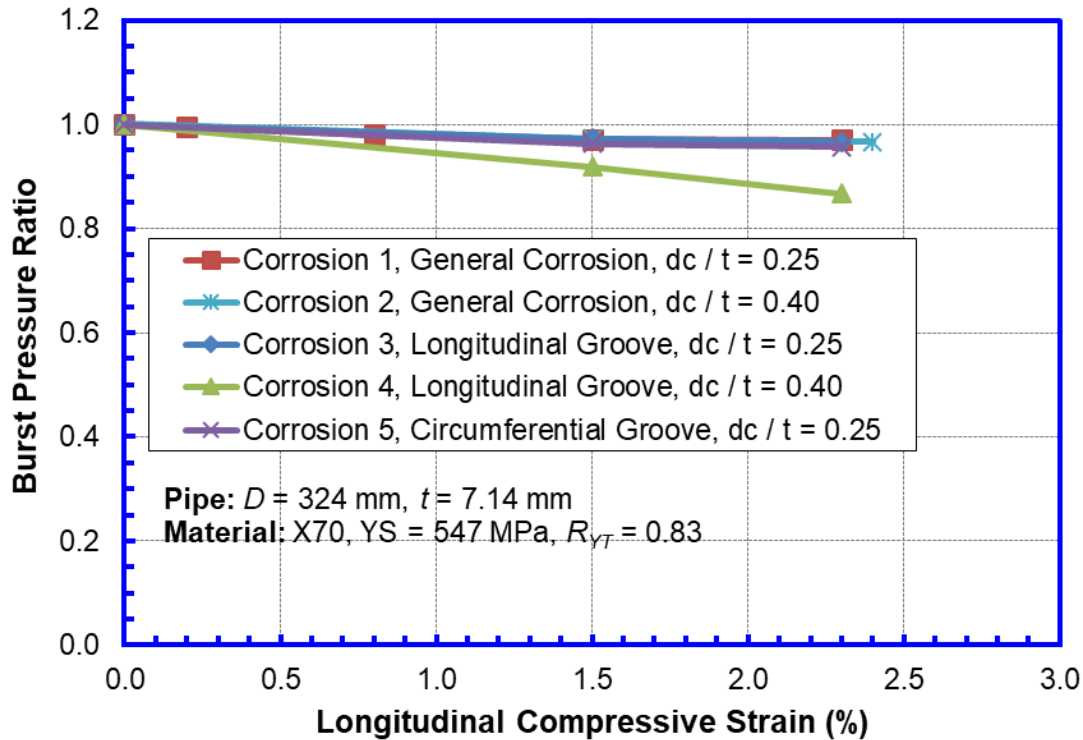


Figure 5-35 Effect of pre-bend strain on burst pressure of corroded pipe

5.4.3 Comparison of the FEA and Experimental Results

Table 5-13 shows the burst pressure ratios obtained from tests and FEA. Two burst pressure ratios from the tests are shown in Table 5-13. One is calculated from the burst pressures directly measured from the tests (i.e., Directly Measured). The other is calculated from the adjusted burst pressures (i.e., Adjusted), which are adjusted to account for the strength variation of the testing pipes. The details of the tests can be found in Section 3.3.

Table 5-13 Corrosion feature geometries and burst pressure estimated by tests and FEA

D	t	Test Number	Specimen ID	Corrosion Feature	L_c/D	W_c/D	d_c/t	2D Comp. Strain (Local Method 1)	Test Burst Pressure Ratio		FEA Burst Pressure Ratio
					mm/mm	mm/mm	mm/mm		Directly Measured	Adjusted	
324	7.14	2	10.a	Base line 2 (Longitudinal Groove)	0.2	0.05	0.4	No	1.0	1.0	1.0
		3	10.b	Longitudinal Groove	0.2	0.05	0.4	-2.3	0.95	0.85	0.87
		4	10.c	General Corrosion	0.2	0.2	0.4	-2.3	1.01	0.88	0.97

It is well known that the pipe strength can vary even in the same pipe and therefore the actual strength of the pipe specimens used in the different tests may vary. Since the burst pressure is directly related to the pipe strength and the change of the burst pressure due to the longitudinal compressive strain is relatively low, the strength variation among the pipe specimens may override or offset the burst pressure change due to the compressive strain.

To estimate the strength variation among the different pipe specimens, the history of the pressure vs. circumferential strain was obtained from the tests and FEA. The circumferential

strain was obtained at two locations (End A and End B) on the pipe OD surface which are $1.5D$ away from the center of the corrosion (both sides) in the longitudinal direction and 90° away from the center of the corrosion in the circumferential direction. The pressure-strain history is related to the circumferential stress-strain curve of the pipe specimen.

Since the corrosion anomalies changed the maximum bending moment and the longitudinal stress in the pipe, the different specimens were under different biaxial loadings. Therefore, the pressure-strain history of different tests cannot be directly compared to determine the strength difference among the different specimens. However, the difference between the experimental and FEA pressure-strain histories of the same test can show the difference between the actual strength and the strength used in the FEA.

The pressure-strain histories of the three tests shown in Table 5-13 are shown in Figure 5-36 to Figure 5-38. For Test 2 (the reference test), the actual pipe strength is slightly lower than that assumed in the FEA. However, for Tests 3 and 4, the actual pipe strength is higher than that assumed in the FEA. Thus, for Tests 3 or 4, the directly measured burst pressure ratios could be higher than that from the FEA.

The burst pressure ratios were adjusted based on the strength difference shown in Figure 5-36 to Figure 5-38. The adjusted burst pressure ratios are listed in Table 5-13. The adjusted burst pressure ratios from the tests show a similar trend as that predicted by FEA and match the FEA results reasonably well.

Both the test and FEA results indicate that the longitudinal grooves are more susceptible to the burst pressure reduction under the longitudinal compressive strain than the other types of corrosion anomalies.

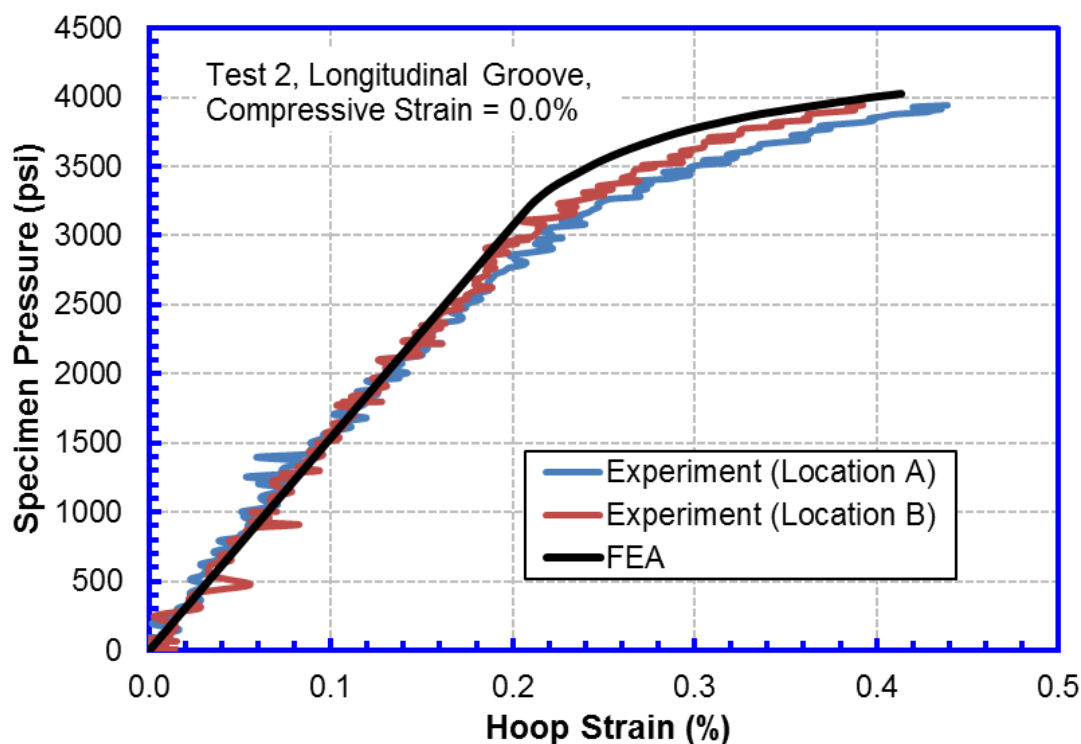


Figure 5-36 Specimen pressure vs. hoop strain for Test 2 (Specimen 10.a in Table 3-10)

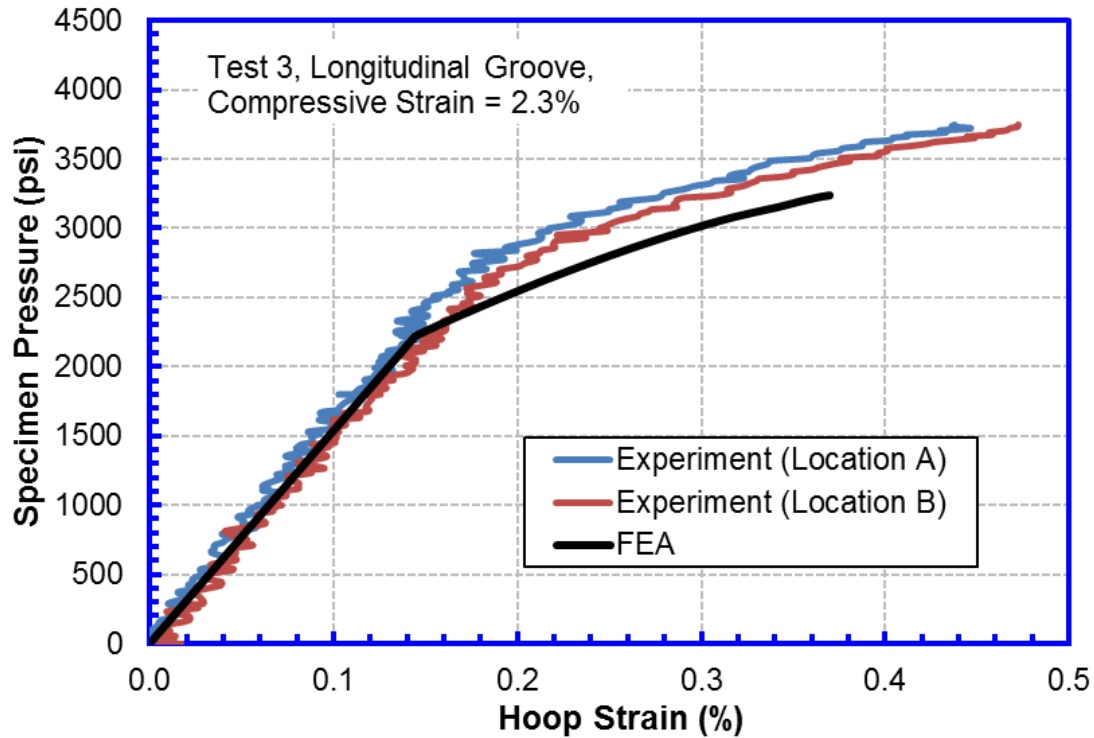


Figure 5-37 Specimen pressure vs. hoop strain for Test 3 (Specimen 10.b in Table 3-10)

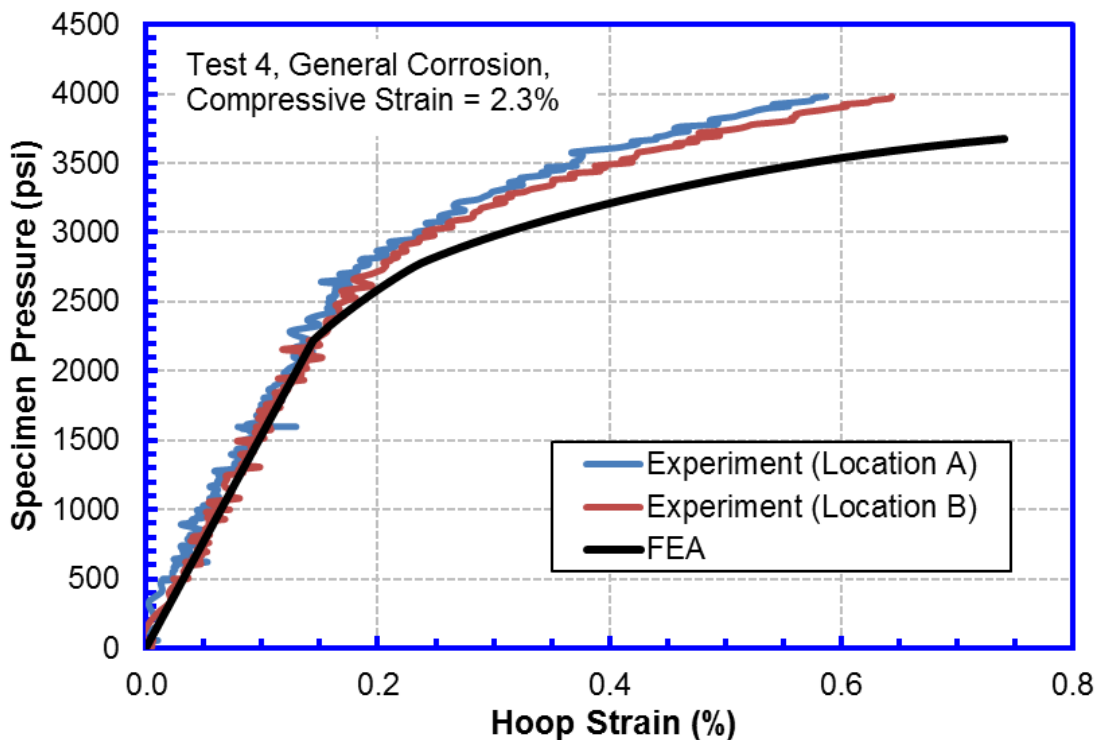


Figure 5-38 Specimen pressure vs. hoop strain for Test 4 (Specimen 10.c in Table 3-10)

5.4.4 Burst Pressure Equation for Corroded Pipes Subjected to Longitudinal Strain

Using the lower bound burst pressure ratios shown in Figure 5-35, an assessment equation was developed to calculate the burst pressure of corroded pipes experiencing the longitudinal compressive strain:

$$P_b^{\varepsilon_c} = P_b \cdot [1.00 - 5.76|\varepsilon_c^{dem}|], \quad (5-6)$$

where, $|\varepsilon_c^{dem}|$ is the magnitude of the longitudinal compressive strain demand, i.e., the strain to be applied to the pipe. In Eq. (5-6), the unit of ε_c^{dem} is mm/mm. For example, if the longitudinal compressive strain demand is -2%, $|\varepsilon_c^{dem}|$ should be set at 0.02. P_b is the burst pressure of the corroded pipe under no longitudinal compressive strain, which may be determined from existing codes and standards, e.g., ASME B31G [31], DNV-RP-F101 [34], etc.

Equation (5-6) is applicable to the following conditions:

- Corrosion Dimensions: $L_c/\sqrt{Dt} \leq 1.3$, $W_c/\sqrt{Dt} \leq 1.3$, $d_c/t \leq 0.40$, $L_c > t$, $W_c > t$
- Longitudinal compressive strain demand: $0 < |\varepsilon_c^{dem}| \leq 0.02$

6 Pipes with Dents Subjected to Longitudinal Strain

6.1 Overview of the Studies on Dents

6.1.1 Limit States Associated with Dents Subjected to Longitudinal Strain

Dents in a pipe are permanent plastic deformation, which produces a gross disturbance of the pipe circular cross section (Figure 6-1). Dents can be broadly categorized as plain dents and complex dents [85]. The plain dents have smooth profiles and contain no injurious defects such as gouges and corrosion anomalies. In addition, the plain dents do not interact with girth welds, seam welds, and major structural discontinuities (such as stiffening rings and tees). The complex dents are those dents interacting with gouges, grooves, scratches, seam or girth welds, and/or other stress risers. The focus of this project is on plain dents.



Figure 6-1 Dent in a pipe

Dent depth is one critical parameter of the dents. The dent depth is defined as the maximum reduction in the pipe diameter between the deformed and original pipes as shown in Figure 6-2. The dent depth includes both the local surface indentation and the deviation from the nominal pipe circular cross section (i.e., ovality). The dent depth may be affected by many factors such as indentation force, pipe diameter, wall thickness, internal pressure, pipe material properties, and restraint conditions.

Depending on the restraint conditions, the dents can be broadly grouped into unrestrained and restrained dents. For the unrestrained dents, the objects that generated the dents are removed after the indentation. For the restrained dents, the objects that generated the dents stay in place after the indentation. In addition, the dents can be formed either in construction (no internal pressure) or in service (with internal pressure).

For pipes subjected to longitudinal strain, the plain dents are known to have minor effects on the burst pressure and tensile strain capacity of the pipe. However, the dents can greatly affect the compressive strain capacity (CSC) of the pipe.

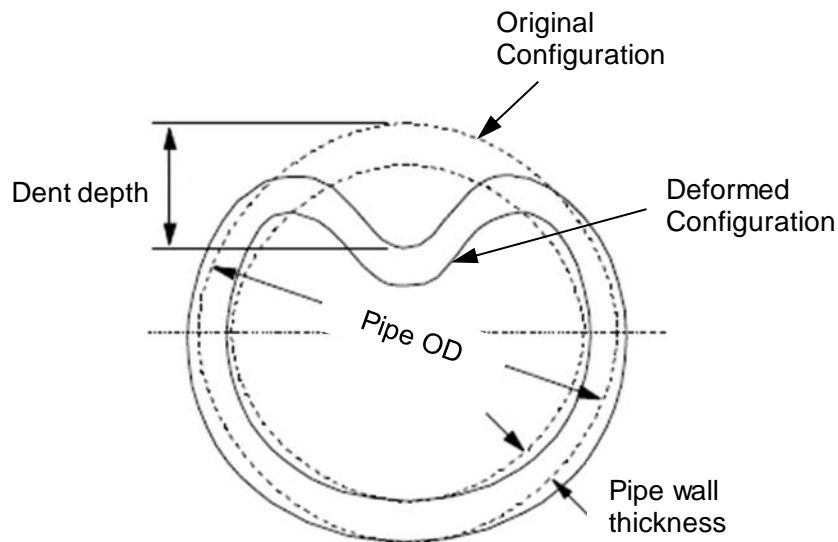


Figure 6-2 Definition of dent depth

6.1.2 Section Structure and General Approach

In this project, the effect of the plain dents on the pipe CSC was studied through systematic finite element analyses and full-scale tests. The definition of the CSC can be found in Section 4.3.1. The general approach for the studies and the structure of this section are listed below:

- The effects of dent forming (in construction vs. in service) and restraint (restrained vs. unrestrained) conditions on the pipe CSC were studied through systematic FEA (see Section 6.2). The conditions led to the lowest CSC were determined from those studies. Those conditions were used in the full-scale tests and parametric FEA.
- The FEA procedures were evaluated with the full-scale test results. The evaluation was shown in Section 6.3.
- The validated FEA procedures were used to conduct parametric FEA to study the effects of various parameters on the CSC. The parametric FEA were shown in Section 6.4.
- Similar to the girth welds, the dents were treated as equivalent geometry imperfections. The equivalent geometry imperfections for dents were determined from the parametric FEA (see Section 6.5).
- The CSC equations for pipes containing dents were developed and presented in Section 6.6.

6.2 Effects of Dent Forming and Restraint Conditions on Compressive Strain Capacity

6.2.1 Rationale of Analysis

A dent can be formed during construction (no internal pressure) or in-service (with internal pressure). At the same time, the dent can be under different restraint conditions: i.e., restrained or unrestrained. The severity of the dent is typically measured by its depth. However, different forming and restraint conditions can result in different stress and strain conditions in the dent area even for the dents of the same depth. As a result, those dents may behave differently under bending and show different CSC.

To examine the effects of the dent forming and restraint conditions on the CSC of the pipe, finite element analyses (FEA) were conducted to simulate different dent forming processes and restraint conditions and determine the CSC of the pipe under bending. The analysis results were used to determine the conditions for the full-scale experimental tests and the numerical studies for developing CSC assessment models.

The dent types (characterized by forming and restraint conditions) analyzed in this section are shown in Table 6-1.

Table 6-1 Summary of types of dents analyzed in FEA

Dent Types		Related Field Conditions	
Formed in Construction	Unrestrained	<ul style="list-style-type: none"> The dent was formed during construction (without internal pressure); The dented pipe experienced hydrostatic testing; The dented pipe experienced operating pressure fluctuations; and 	The object caused the dent was removed after the indentation.
	Restrained	<ul style="list-style-type: none"> The dented pipe experienced large longitudinal compressive strain due to ground movement. 	The object caused the dent stayed in place after the indentation.
Formed in Operation	Unrestrained	<ul style="list-style-type: none"> The dent was formed in operation (with internal pressure); The dented pipe experienced operating pressure fluctuations; and 	The object caused the dent was removed after the indentation.
	Restrained	<ul style="list-style-type: none"> The dented pipe experienced large longitudinal compressive strain due to ground movement. 	The object caused the dent stayed in place after the indentation.

6.2.2 Finite Element Analysis Models

Commercial FEA software ABAQUS® was used for the analysis. A typical FEA model is shown in Figure 6-3. Due to the symmetry conditions in pipe circumferential and longitudinal directions, only one quarter of the pipe was modeled. The pipe was modeled using 4-node quadrilateral shell elements with reduced integration (S4R) and large-strain formulation. The object that causes the dent (referred to as indenter) was of spherical shape and simulated with an analytical rigid surface (ARSR). The interaction between the indenter and pipe was simulated through surface to surface contact.

The pipe dimensions were kept the same as those used for the full-scale experimental tests. The pipe outer diameter (D) and wall thickness (t) were 323.85 mm (12.75 in) and 6.35 mm (0.25 in), respectively. The diameter of the spherical indenter was 114.3 mm (4.5 in, $\sim 0.35D$). The pipe end was modeled as a rigid plane to simulate the end plates attached to the pipe in the full-scale tests. The length of the pipe in the FEA model (half pipe) was $5D$. The pipe length was kept long enough to avoid the effect of the rigid pipe end on the stress/strain near the dents.

The effect of mesh sizes on the analysis results was thoroughly examined. The element was refined adequately to obtain converged (mesh independent) solutions. The element size in the pipe longitudinal and circumferential direction was determined as about 2.16 mm ($D/150$) and 8.15 mm, respectively.

The CSC of plains pipes were found to be greatly affected by the pipe geometry imperfection created during pipe manufacturing [26]. The dent forming process can create much higher geometry imperfections than those created in manufacturing. Therefore, the manufacturing pipe geometry imperfection was not modeled in the CSC analyses of the pipes with dents.

6.2.3 Material Properties

The pipes used in the full-scale tests are the same as those used in the full-scale bending tests of transition welds (Section 3.2). The small-scale test data were not available when the FEA was conducted. The same material properties as those used in the FEA of the bending tests of transition welds were used, see Section 4.3.4.4.

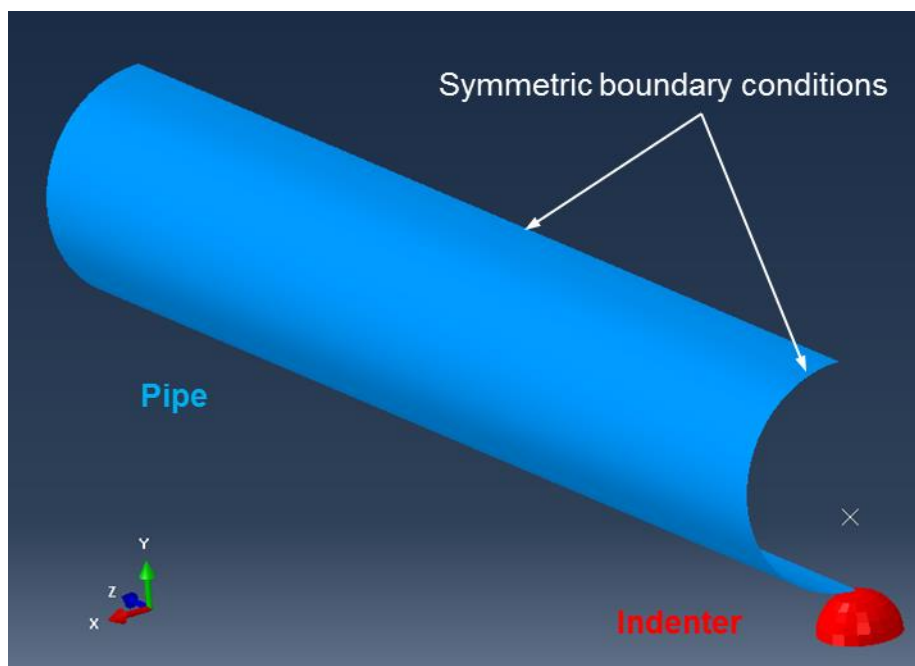


Figure 6-3 Example FEA model for dented pipe

6.2.4 Analysis Process

Multiple loading steps were used to simulate the dent formation, pressure cycles, and pipe deformation under bending. Table 6-2 shows the loading steps for the dents (unrestrained and restrained) formed in construction. Step 1 is to simulate the dent forming (in construction) by applying indentation to the pipe without internal pressure. In Step 2, the indenter is removed to allow dent elastic re-rounding (unrestrained dents) or is kept in place to prevent dent elastic re-rounding (restrained dents). Step 3 is to simulate the pressure cycle from hydrostatic testing. Step 4 is to simulate the pressure cycles from the pressure fluctuations during operation. Five pressure cycles are used since the analysis results show that the dent size does not change after five pressure cycles. In Step 5, the lateral bending moment is applied to simulate the bending load due to ground movement when the pipe is pressurized.

Table 6-3 shows the loading steps for the dents (unrestrained and restrained) formed in service. In Step 1, internal pressure is applied to the pipe ID surface to generate a hoop stress of 72% SMYS (X65). In Step 2, an indentation is applied to the pipe with internal pressure to

simulate the dent formation in service. Step 3 is the same as Step 2 for dents formed in construction except that the pipe is pressurized. Step 4 and Step 5 are the same as Step 4 and Step 5 for dents formed in construction, respectively.

Table 6-2 Analysis process for dents formed in construction

Step #	Step Description		Construction_ Unrestrained	Construction_ Restrained
	Simulation in FEA	Related Field Conditions		
1	Apply indentation to the pipe without internal pressure	The dent was formed in construction.	✓	✓
2	Remove indenter to allow elastic re-rounding	The object caused the dent is removed.	✓	
	Keep indenter in place and do not allow elastic re-rounding	The object caused the dent keeps in contact with the pipe.		✓
3	Apply first pressure cycle, Hoop stress/SMYS: 0% → 90% → 0%	Hydrostatic test	✓	✓
4	Apply additional five pressure cycles: 0% ≤ Hoop stress/SMYS ≤ 72%	Pressure fluctuations during operation	✓	✓
5	Apply bending with internal pressure: Hoop stress/SMYS = 72%	Ground movement	✓	✓

Table 6-3 Analysis process for dents formed in service

Step #	Step Description		In- operation_Un restrained	In- operation_ Restrained
	Simulation in FEA	Related Field Conditions		
1	Pressurize the pipe to Hoop stress/SMYS = 72%	The pipe is operated in service.	✓	✓
2	Apply indentation to the pipe with internal pressure	The dent was formed in operation.	✓	✓
3	Remove indenter to allow elastic re-rounding	The object caused the dent is removed.	✓	
	Keep indenter in place and do not allow elastic re-rounding	The object caused the dent keeps in contact with the pipe.		✓
4	Apply additional five pressure cycles: 0% ≤ Hoop stress/SMYS ≤ 72%	Pressure fluctuations during operation	✓	✓
5	Apply bending with internal pressure: Hoop stress/SMYS = 72%	Ground movement	✓	✓

6.2.5 Typical Analysis Results and Calculation of Compressive Strain Capacity

6.2.5.1 Typical Analysis Results

Figure 6-4 shows the typical dent profile and the longitudinal strain contour on the pipe ID surface after all pressure cycles and before the bending moment is applied. It is seen that the dent has a smooth profile (smooth change in curvature) and strain concentration occurs in and near the dent.

The time history of the dent depth at different loading steps is shown in Figure 6-5. The dent depth at the end of initial indentation (before the indenter is removed) is about 32.7 mm (10% D). After the indenter is removed, the dent depth decreases to 23.8 mm (7.4% D), which is usually referred to as elastic re-rounding. The hydrostatic pressure cycle causes a significant reduction in the dent depth, which is usually referred to as plastic re-rounding. The operating pressure cycles do not show further reduction to the dent depth. After all pressure cycles, the residual dent depth with the internal pressure ($f_p = 0.72$) decreases to 11.8 mm (3.6% D) i.e., less than 40% of the initial indentation depth. During the operation pressure cycles, it is seen that the dent depth decreases with the increase of the internal pressure. But, the change of the dent depth with the internal pressure is relatively small. The dent depth at high pressure ($f_p = 0.72$) is about 90% of the dent depth at zero pressure. At the end of the history plot, the dent depth increases rapidly when the bending moment is applied.

Under the bending moment, wrinkles are created near the shoulder of the dent. Figure 6-6 shows the typical longitudinal strain contour as the bending moment at the wrinkle location reaches its peak value. The small wrinkles formed at the shoulder of the dent can be seen. The strain localization is found near the wrinkle.

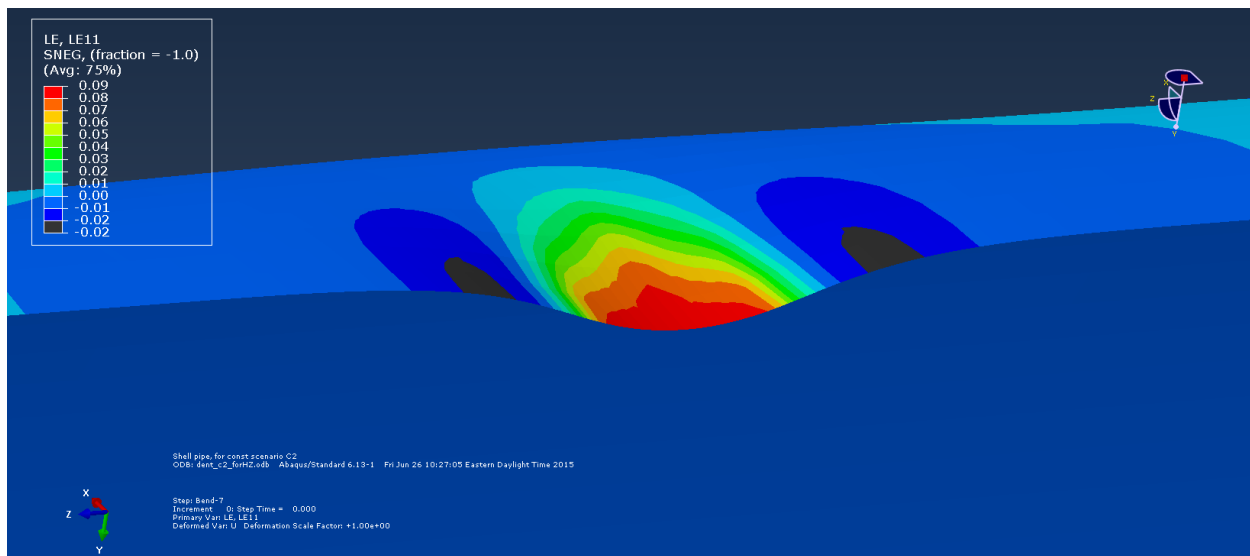


Figure 6-4 Dent profile and longitudinal strain contour on pipe ID surface after pressure cycles and before bending moment is applied (unrestrained dents formed in construction)

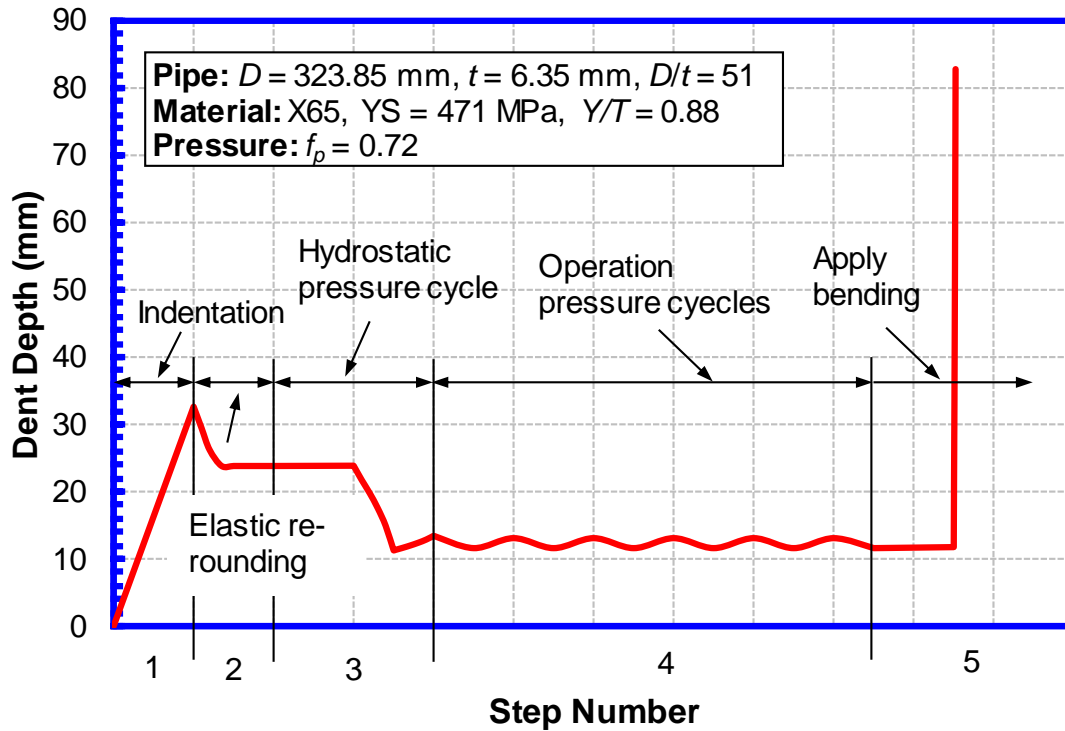


Figure 6-5 Time history of dent depth

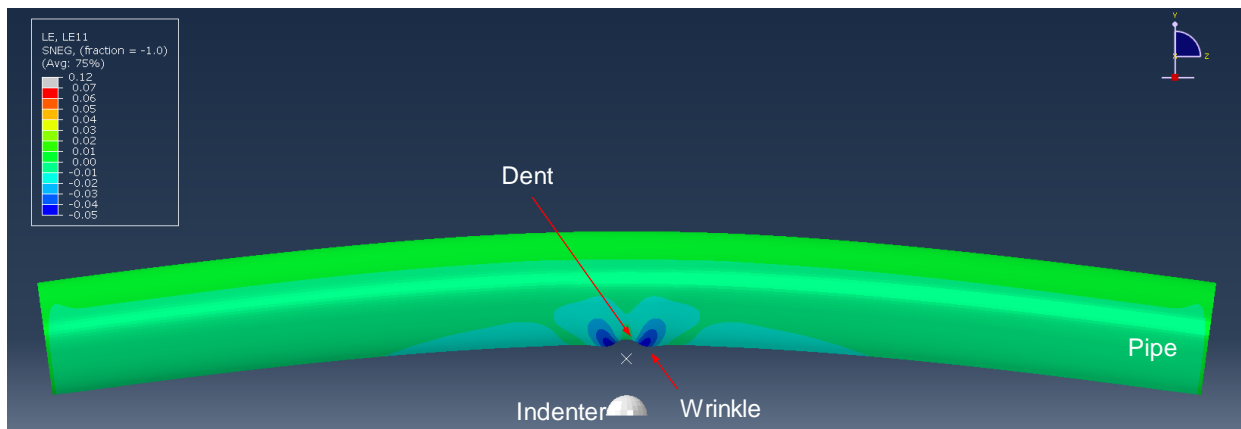


Figure 6-6 Typical longitudinal strain contour on deformed pipe with dent

6.2.5.2 Calculation of Compressive Strain Capacities

Two types of compressive strain capacities were calculated from the FEA results, i.e., the local CSC and global CSC. Both CSCs were calculated when the bending moment at the center of the wrinkle reaches the peak value. The local CSC is referred to as 2D CSC ($\epsilon_{c,dent}^{crit,2D}$) and the global CSC is referred to as CSC by extrapolation ($\epsilon_{c,dent}^{crit,ex}$). The details about the calculation of the CSC can be found in Section 4.3.4.7.2 (i.e., for regular girth welds).

6.2.6 CSC Calculated at Different Dent Forming and Restraint Conditions

A series of finite element analyses (FEA) were conducted to obtain the CSC of pipes with dents of different depths under different forming (in-construction vs. in-service) and restraint (unrestrained vs. restrained) conditions. The FEA results are shown in Figure 6-7 and Figure 6-8 for 2D CSC and CSC by extrapolation, respectively. In those figures, the dent depth (d_{dp}) is the residual dent depth after all pressure cycles and under high internal pressure ($f_p = 0.72$).

Figure 6-7 and Figure 6-8 show that the CSC decreases with the increase of the dent depth. For the dents of the same depth, the unrestrained dents show lower CSC than the restrained dents and the dents formed in construction (i.e., without internal pressure) show lower CSC than the dents formed in service (i.e., with internal pressure). Therefore, among the four conditions, the unrestrained dents formed in construction show the lowest CSC.

Based on the above studies, it was decided to conduct the full-scale tests using unrestrained dents formed with zero internal pressure (in construction). In addition, the following FEA were focused on the same conditions.

6.2.7 Effect of Indenter Sizes on CSC

The hard objects (i.e., indenters), which created the dents, can have various shapes (e.g., size and sharpness of the edge/corner). Therefore, the dents of the same depth may have different shapes. Two spherical indenters were analyzed in this section, one has a 63.5-mm diameter (~20% pipe OD) and the other has a 114.3-mm diameter (~35% pipe OD).

Figure 6-9 and Figure 6-10 show the comparison of the dent profiles generated by the two indenters (after all pressure cycles and with internal pressure) along the pipe longitudinal and hoop direction, respectively. It is seen that under the same initial indentation depth (d_{di}), the dents generated by the small indenter show larger residual dent depth, smaller radius (i.e., larger curvature and higher local strain) than the dents generated by the large indenter.

The CSCs of the dents generated by the two indenters are shown in Figure 6-11 (2D CSC) and Figure 6-12 (CSC by extrapolation), respectively. The CSCs are shown as a function of residual dent depth (d_{dp}) measured under internal pressure. The normalized indentation depth (d_{di}/D) is also shown in the figures.

The results show that as long as the residual dent depth is the same, the effect of the indenter size on the CSC is marginal. For a dent found in the field, since the indenter shape and size are often not known, the reproduction of the exact dent shape in the FEA simulations can be a significant challenge. Since the CSC is mainly affected by the dent depth, it is expected that the difference between the actual and simulated dent shapes should not affect the determination of the CSC.

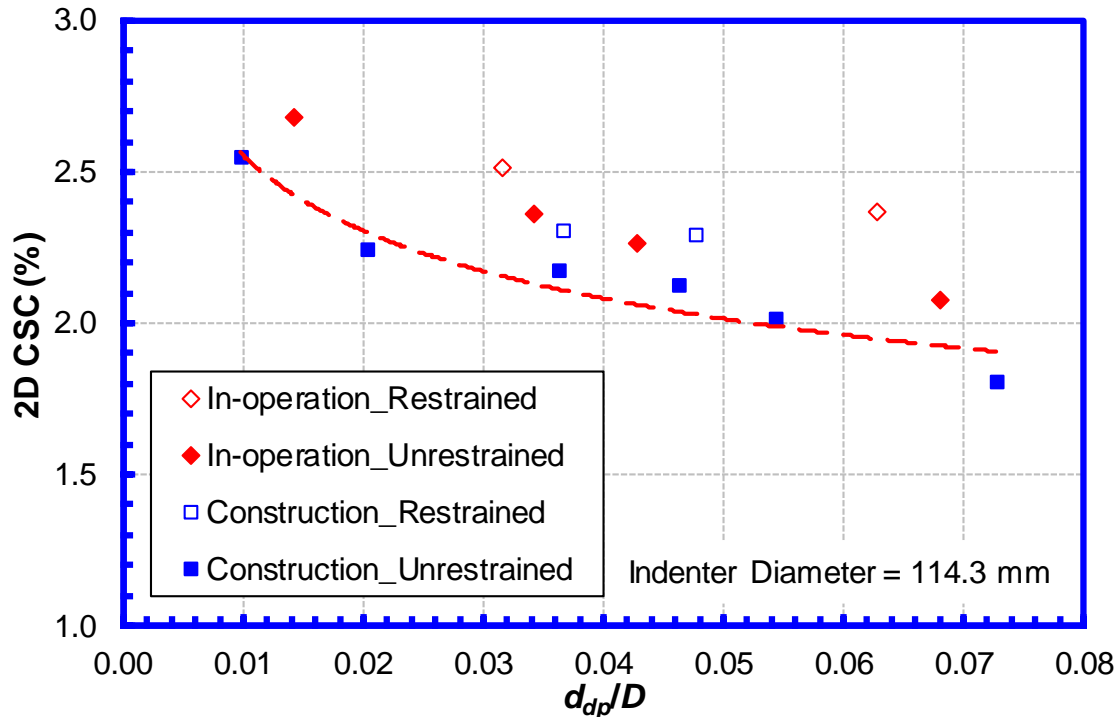


Figure 6-7 2D CSC vs. dent depth for different forming and restraint conditions

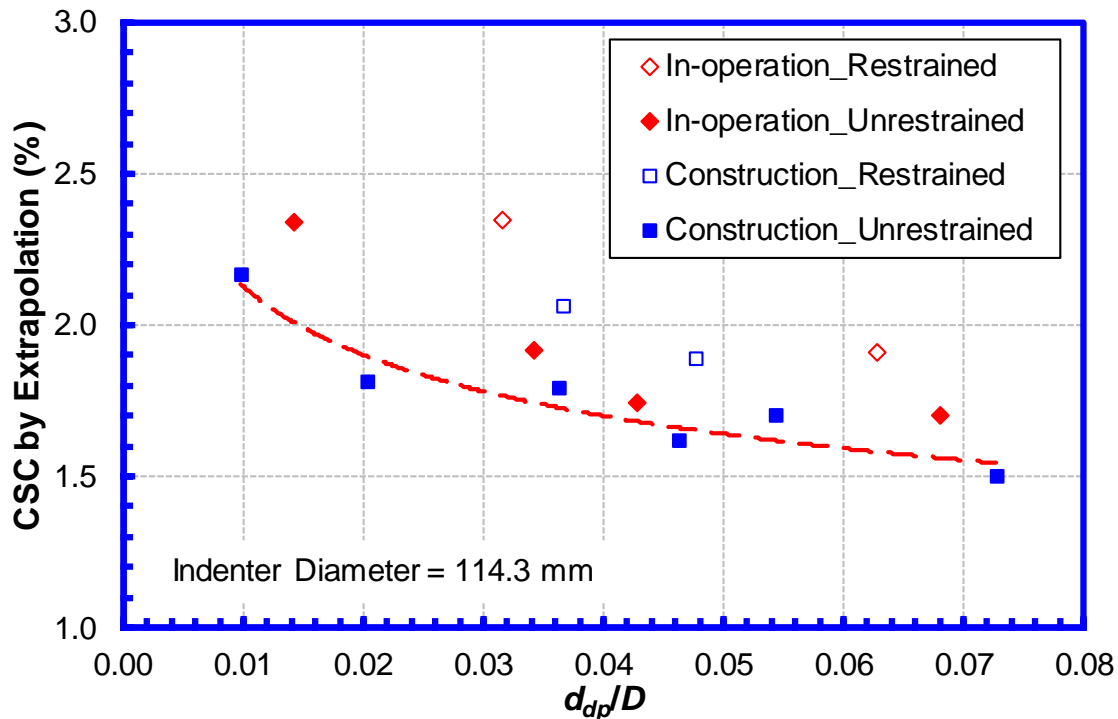


Figure 6-8 CSC by extrapolation vs. dent depth for different forming and restraint conditions

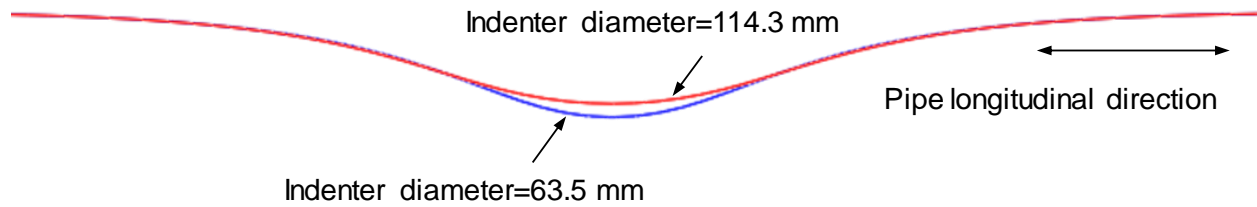


Figure 6-9 Comparison of the dent profile along pipe longitudinal direction generated by the indenters with different diameters under the same indentation depth of $d_{di}/D = 0.08$

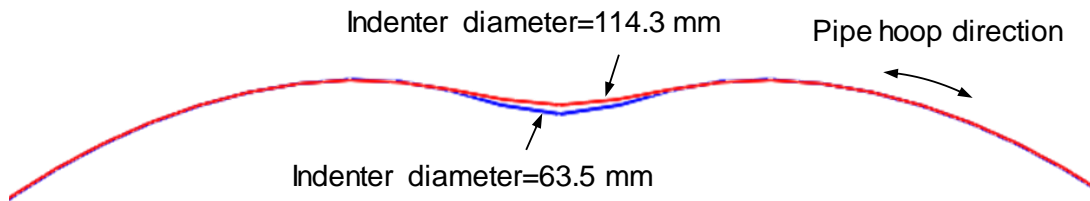


Figure 6-10 Comparison of the dent profile along pipe hoop direction generated by the indenters with different diameters under the same indentation depth of $d_{di}/D = 0.08$

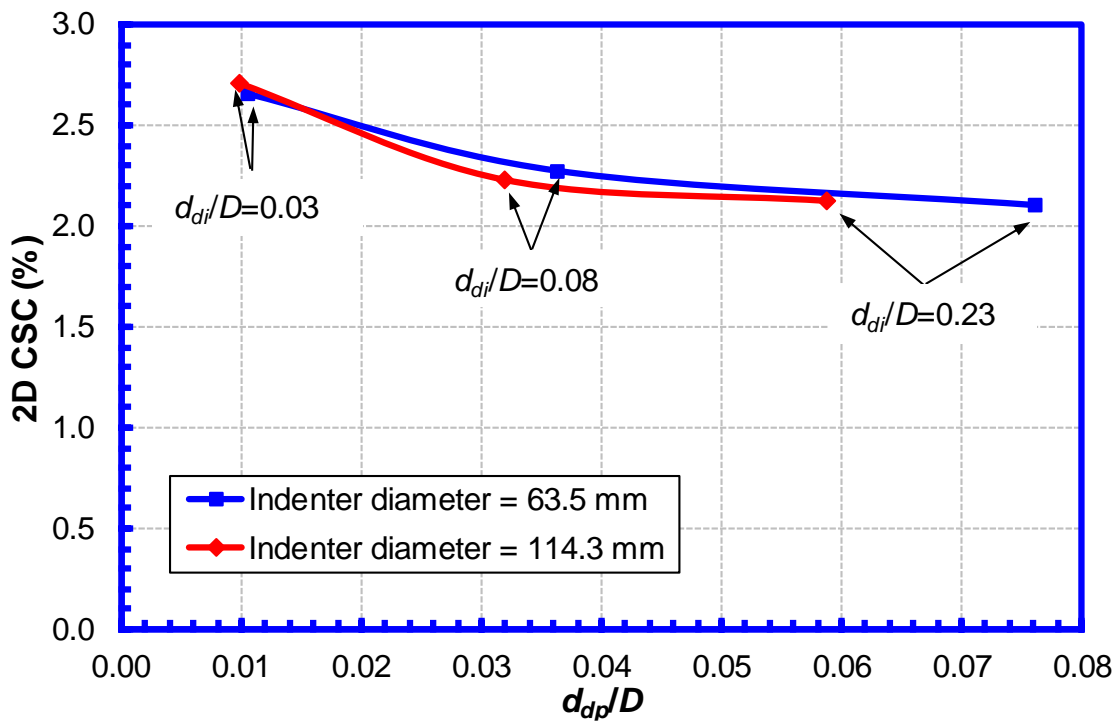


Figure 6-11 2D CSC of dented pipes under different indenter sizes

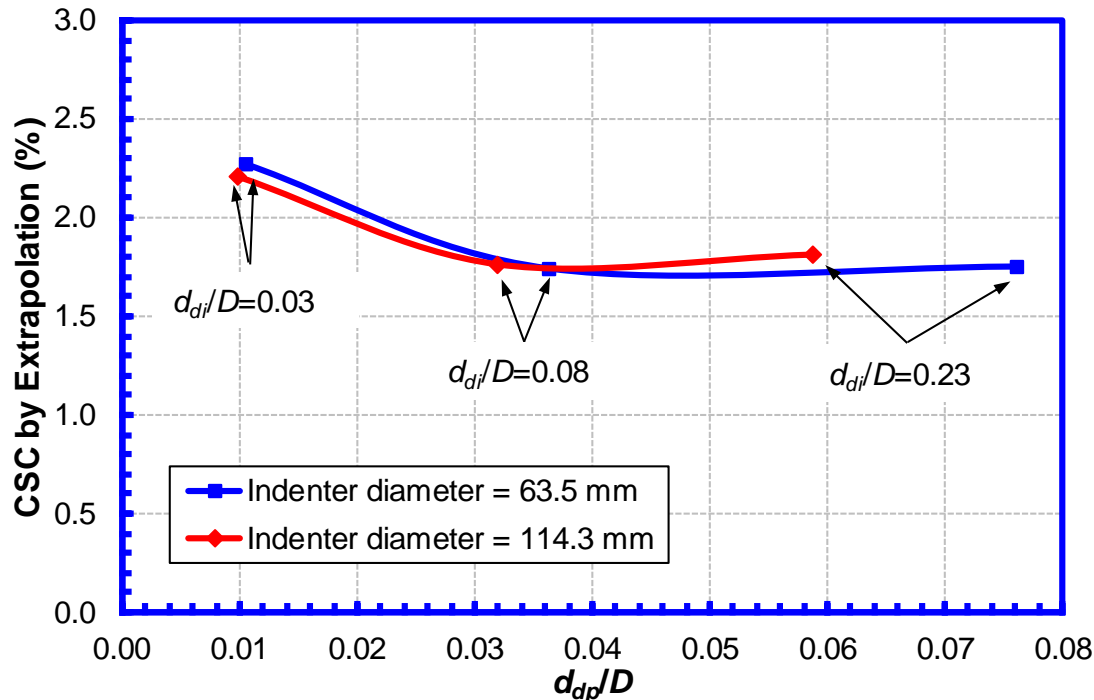


Figure 6-12 CSC by extrapolation of dented pipes under different indenter sizes

6.3 Comparison of Full-Scale Testing with FEA Results

6.3.1 Predicted vs. Measured Dent Depths

Figure 6-13 shows the relationship between the dent depth (d_{de}) after elastic re-rounding and the residual dent depth (d_{d0}). Both the depths predicted by FEA and measured from experiments are shown. d_{de} is the dent depth after the elastic re-rounding and before any pressure cycles. d_{d0} is the dent depth after plastic re-rounding due to all pressure cycles and before the bending moment is applied. Both dent depths were measured with zero internal pressure. Figure 6-13 shows that there is a reasonably good agreement for the trend of increasing d_{d0} with the increase of d_{de} between the FEA and test results. For the same d_{de} , the d_{d0} calculated from the FEA is slightly larger than the one measured from the test.

6.3.2 Predicted vs. Measured CSC of Dented Pipes

Figure 6-14 and Figure 6-15 show the comparison of the CSC measured from the full-scale tests and calculated by the FEA. In both figures, the CSCs are shown as a function of the residual dent depth (d_{d0}) with zero internal pressure. Figure 6-14 shows the 2D CSC and Figure 6-15 shows the CSC by extrapolation. For calculating the CSC by extrapolation from the full-scale tests, the similar method as the one for transition welds is used, see Section 4.3.4.8. The only difference is the strain should be measured from both sides of the wrinkle and the averaged strain should be used as the CSC by extrapolation. The general trends between the CSC and the dent depth predicted by the FEA and measured from the tests show a very good agreement. However, the FEA predicted CSC is consistently lower than the test results (about 20%). The difference between the predicted and measured CSC is believed to be caused by the difference between the pipe stress-strain curve assumed in the FEA and the actual stress-strain curve measured in small-scale tests (additional discussions can be found in Section 4.3.4.8).

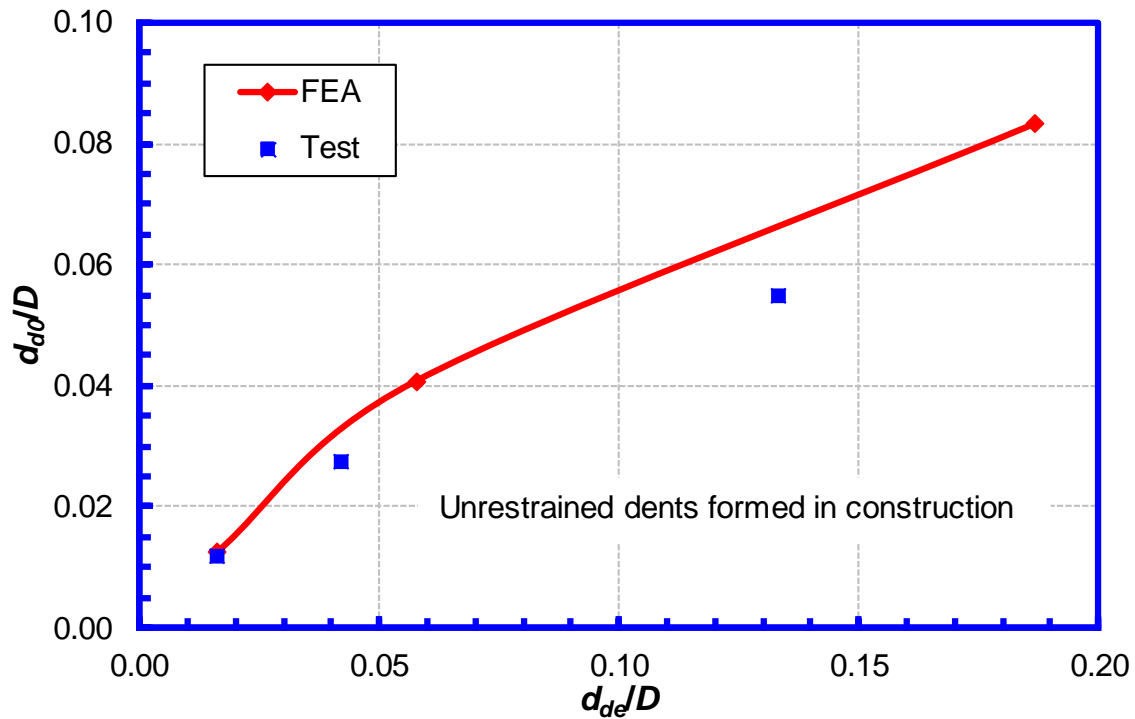


Figure 6-13 Comparison of dent depths obtained from FEA and tests

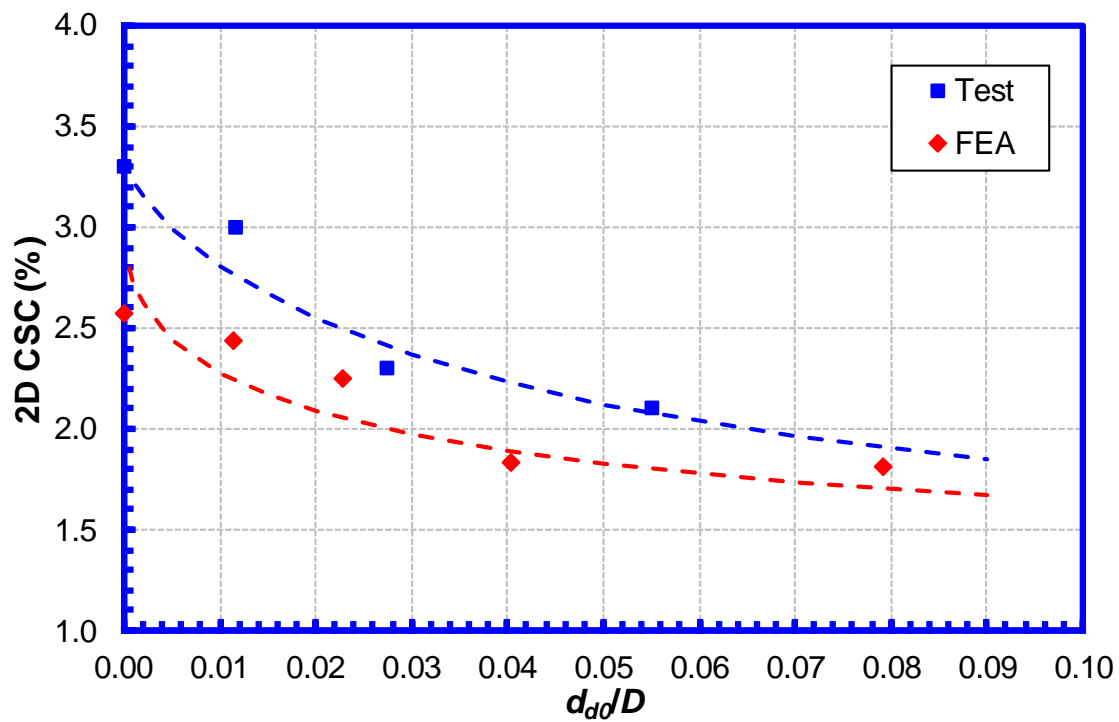


Figure 6-14 2D CSC vs. dent depth from FEA and test

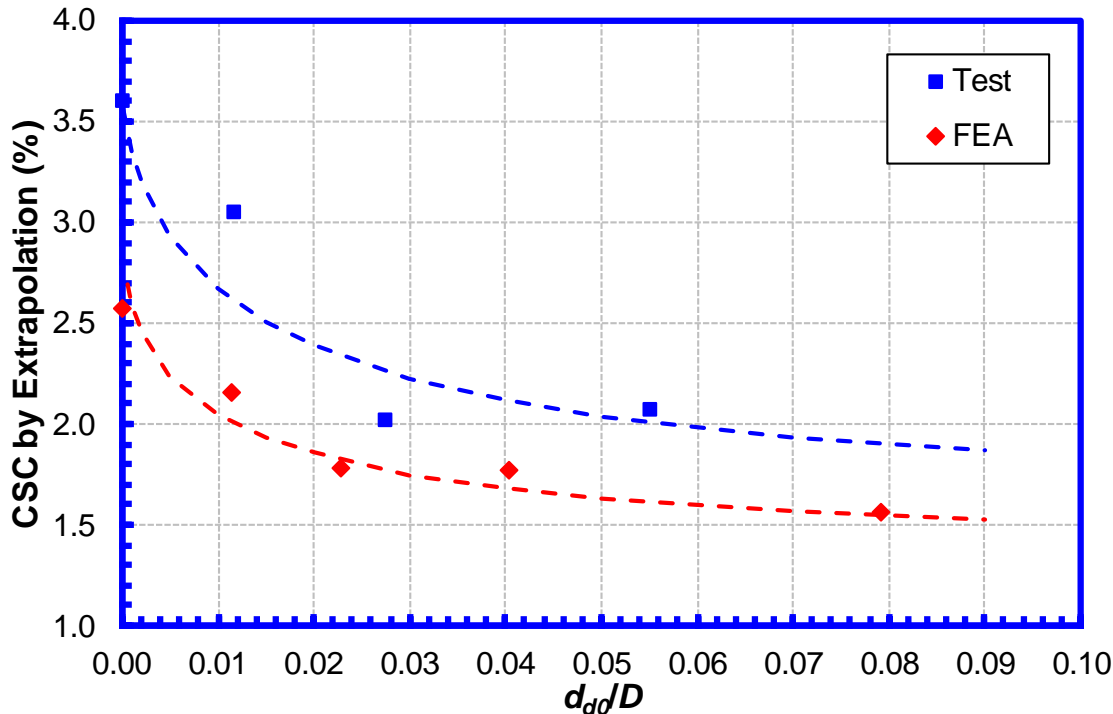


Figure 6-15 CSC by extrapolation vs. dent depth from FEA and test

6.4 Parametric Studies of CSC of Dented Pipes

6.4.1 Overview of the Parametric Studies

Parametric studies were conducted to study the effects of the pipe material property (Y/T), pipe geometry (D/t), and internal pressure on the CSC of pipes of different dent depths. The objectives of the studies are: (1) to gain better understanding on the key factors that affect the CSC; (2) to gain better understanding on how the key factors affect the CSC; and (3) to develop CSC equations for the assessment of dented pipes subjected to longitudinal strain. The focus of the parametric studies was on how the different parameters affect the relationship between the CSC and the dent depth. In the studies, if not otherwise mentioned, the dent depth was measured as the residual dent depth with internal pressure ($f_p = 0.72$).

As mentioned in Section 6.2.6, the unrestrained dents formed in construction were analyzed in the parametric studies. The dent forming and re-rounding processes shown in Table 6-2 were followed. The FEA models were shown in Section 6.2.2. If not mentioned otherwise, the material properties shown in Section 6.2.3 were used in the parametric analyses.

6.4.2 Effect of Pipe D/t Ratio on CSC

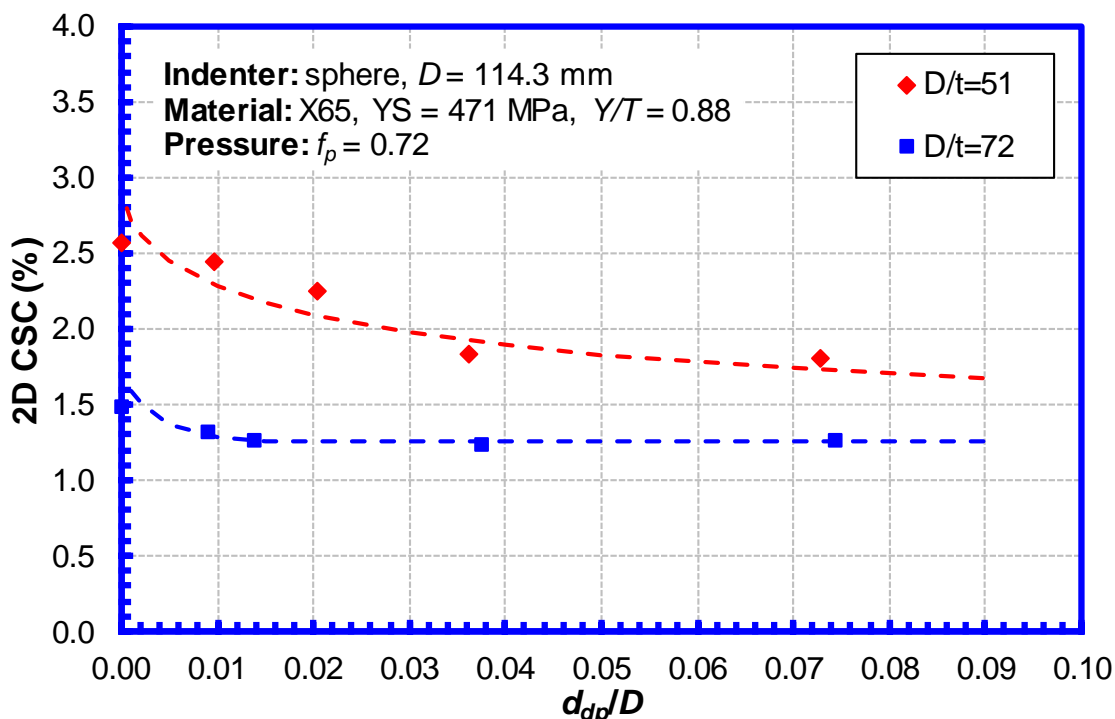
Table 6-4 shows the input parameters used in the analyses, in which two pipe D/t ratios (51 and 72) are selected. For $D/t = 51$, the pipe OD and wall thickness is 323.85 mm (12.75") and 6.35 mm (0.25"), respectively. For $D/t = 72$, the pipe OD and wall thickness is 914.4 mm (36") and 12.7 mm (0.5"), respectively. Four "Target Dent Depths" are analyzed. The "Target Dent Depth" are the target residual dent depths for the analyses. Since the re-rounding of the dent cannot be precisely controlled, the actual residual dent depths obtained in the simulations are slightly different from the target values.

Table 6-4 Input parameters of parametric studies of pipe geometry

Key Parameter	Indenter Diameter		D/t	Y/T	f_p	Target Residual Dent Depth
	mm	in				% OD
Value	114.3	4.5	51, 72	0.88	0.72	1%, 3%, 6%, 8%

Figure 6-16 shows the relationship between the 2D CSC and the normalized residual dent depth and Figure 6-17 shows the relationship between the CSC by extrapolation and the normalized residual dent depth. The results for two D/t ratios (51 and 72) with internal pressure ($f_p = 0.72$) are shown in both figures. The input parameters used in the FEA are also given in the figures. The CSC for $d_{dp} = 0$ was obtained using the CSC equations in Section 4.3.2 for plain pipes with geometry imperfection $h_g/t = 0.01$ and internal pressure $f_p = 0.72$. The high CSC measured from the full-scale test of the plain pipe indicates that the geometry imperfection of the pipe should be small and 1% is assumed here to calculate the CSC for $d_{dp} = 0$.

As expected, the results show that the CSC for $D/t = 51$ is higher than that for $D/t = 72$. In addition, the results show that the CSC decreases with the increase of the dent depth. However, the rate of the change of the CSC with respect to the dent depth is different for different pipe D/t ratios. For $D/t = 51$, the CSC decreases gradually with the increase of the dent depth within the normalized dent depth (d_{dp}/D) range 0 to 0.07. For $D/t = 72$, the CSC decreases rapidly with the increase of the dent depth for d_{dp}/D from 0 to 0.01. Once d_{dp}/D reaches 0.01, the CSC is almost independent of the further increase of the dent depth.

Figure 6-16 Relationship between 2D CSC and dent depth for different D/t ratios

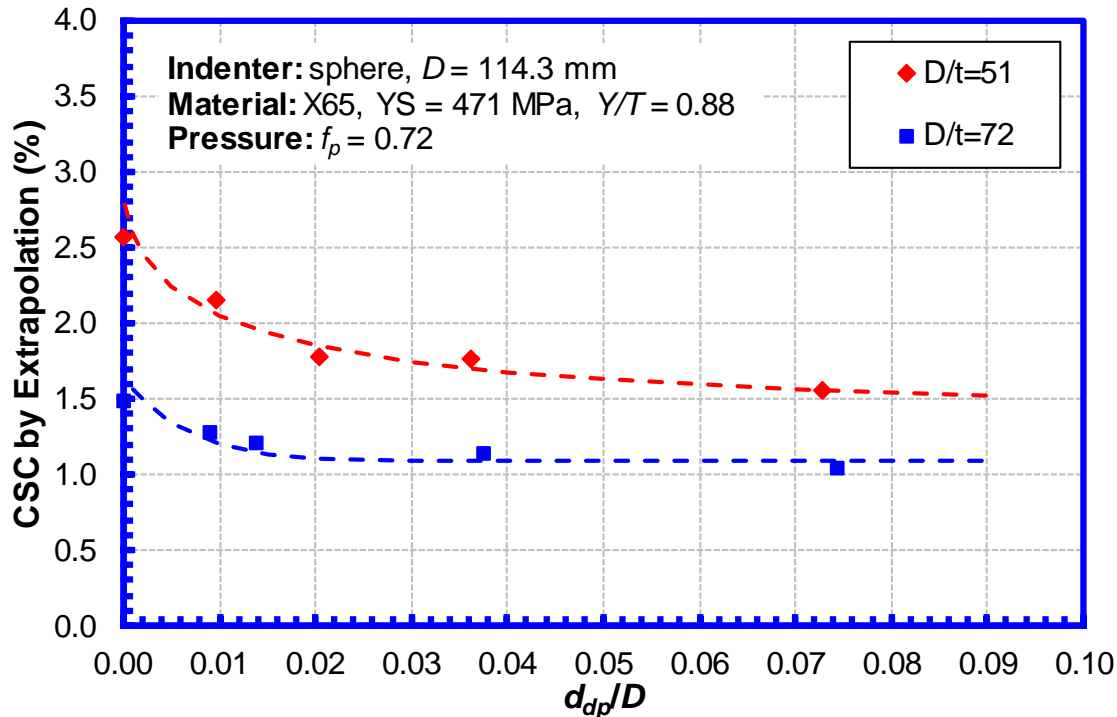


Figure 6-17 Relationship between CSC by extrapolation and dent depth for different D/t ratios

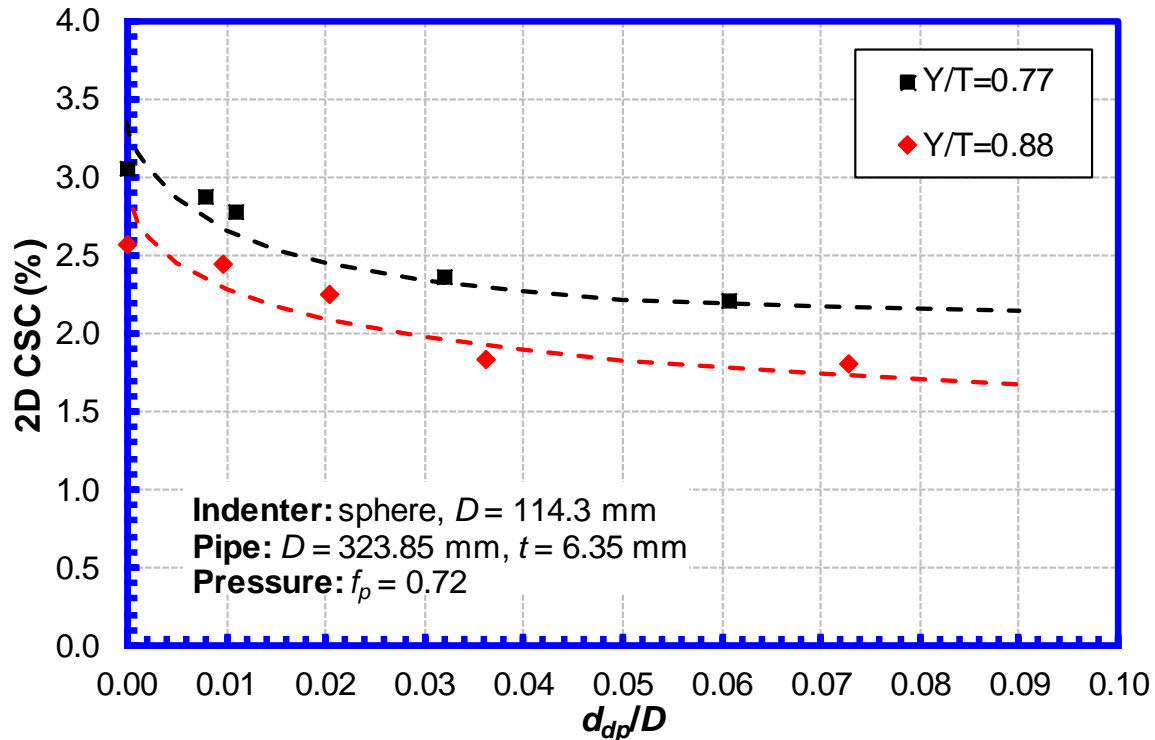
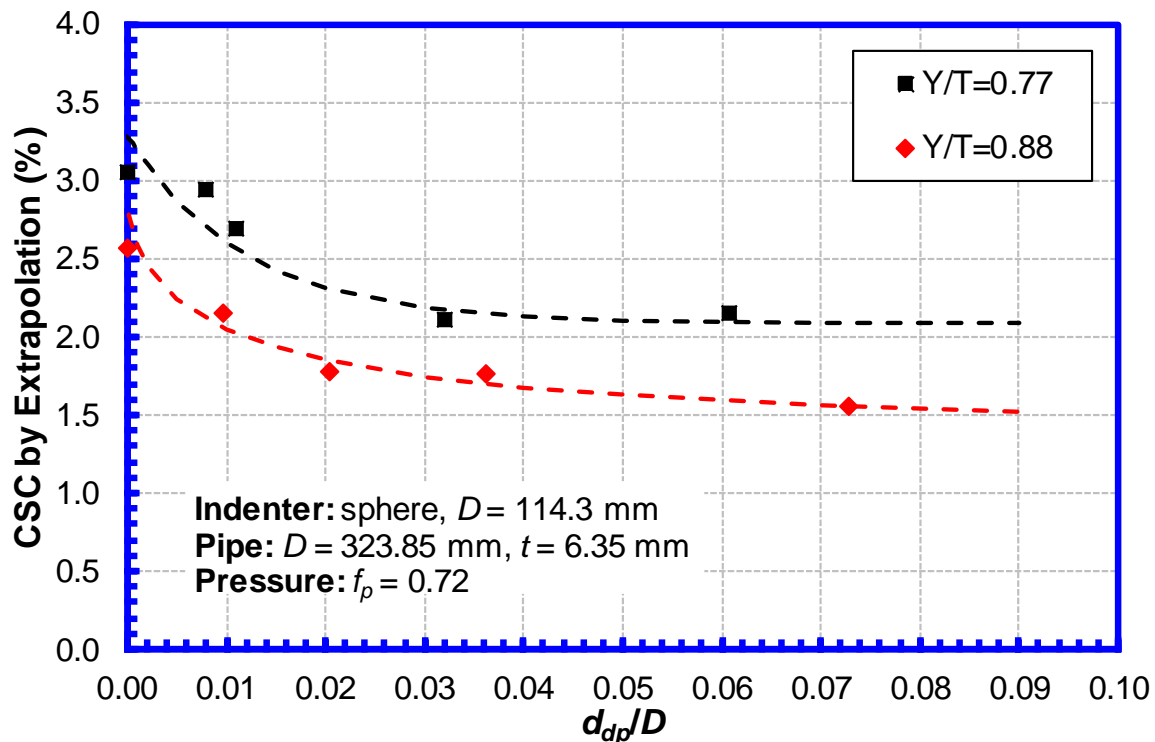
6.4.3 Effect of Pipe Y/T Ratio on CSC

Table 6-5 shows the input parameters used in the analyses, in which two Y/T (0.77 and 0.88) and four target dent depths were selected. The pipe stress-strain curve for $Y/T = 0.88$ was the same as that of the X65 pipe (yield strength of 471 MPa and ultimate tensile strength of 535 MPa) shown in Section 6.2.3. The full stress-strain curve for $Y/T = 0.77$ was created following the procedures given in [7,28] using assumed pipe yield strength (320 MPa) and ultimate tensile strength (415 MPa). The yield strength and ultimate tensile strength were obtained from an actual X42 pipe.

Table 6-5 Input parameters of parametric studies of pipe material property

Key Parameter	Indenter Diameter		D/t	Y/T	f_p	Target Residual Dent Depth
	mm	in				% OD
Value	114.3	4.5	51	0.77, 0.88	0.72	1%, 3%, 6%, 8%

Figure 6-18 shows the relationship between the 2D CSC and the normalized residual dent depth with internal pressure ($f_p = 0.72$) for the two Y/T ratios. Figure 6-19 shows the relationship between the CSC by extrapolation and the normalized residual dent depth with internal pressure ($f_p = 0.72$) for the two Y/T ratios. The input parameters used in the analyses are also shown in the figures. Similar to Section 6.4.2, the CSC for $d_{dp} = 0$ was obtained using the CSC equations in Section 4.3.2 for plain pipes with geometry imperfection $h_g/t = 0.01$ and internal pressure $f_p = 0.72$.

Figure 6-18 Relationship between 2D CSC and dent depth for different Y/T ratiosFigure 6-19 Relationship between CSC by extrapolation and dent depth for different Y/T ratios

As expected, the results show that the CSC decreases with the increase of the Y/T ratio and the dent depth. Furthermore, the rate of the change of the CSC with respect to the dent depth is very similar for the different pipe Y/T ratios. The CSC gradually decrease with the increase of the dent depth within the normalized dent depth (d_{dp}/D) range 0 to 0.07.

For pipes with high Y/T ratios, due to the low strain hardening capacity, high level of strain localization can be generated at the wrinkle and eventually results in low CSC. When the pipe specific Y/T ratio is not available, a realistic upper-bound Y/T ratio should be used for the assessment of the pipe CSC.

6.4.4 Effect of Internal Pressure on CSC

The CSC-dent depth relationships obtained in the previous sections were for bending the dented pipe with high internal pressure ($f_p = 0.72$) conditions. In this section, the effect of the internal pressure on the CSC-dent depth relationship for bending the dented pipe with and without internal pressure was analyzed. Table 6-6 shows the parameters used in the analyses, in which two pressure levels ($f_p = 0$ and 0.72) and four target dent depths were studied.

Figure 6-20 shows the relationship between the 2D CSC and the normalized residual dent depth for the two pressure levels. Figure 6-21 shows the relationship between the CSC by extrapolation and the normalized residual dent depth for the two pressure levels. The input parameters used in the analyses are also shown in the figures. In both figures, the residual dent depths (d_{dp}) were measured with internal pressure ($f_p = 0.72$). The CSC for $d_{dp} = 0$ was obtained using the CSC equations in Section 4.3.2 for plain pipes with geometry imperfection $h_g/t = 0.01$ and internal pressure $f_p = 0$ or 0.72 .

As expected, the results show that the CSC decreases with the increase of the dent depth and the decrease of the internal pressure. However, the rate of the change of the CSC with respect to the dent depth is very different between pressurized and non-pressurized conditions. For pressurized conditions, the CSC decreases gradually with the increase of the dent depth within the d_{dp}/D range 0 to 0.07. For non-pressurized conditions, the CSC decreases rapidly with the increase of the dent depth for the d_{dp}/D range 0 to 0.01. Once d_{dp}/D reaches 0.01, the CSC is almost independent to the further increase of the dent depth.

In addition, the results demonstrate that the reduction of the CSC due to the dents is higher under non-pressurized conditions than that under pressurized conditions. For example, as shown in Figure 6-20, under zero pressure ($f_p = 0$), the 2D CSC of $d_{dp}/D = 0$ is about 3 times the 2D CSC of $d_{dp}/D = 0.07$. However, under high pressure ($f_p = 0.72$), the 2D CSC of $d_{dp}/D = 0$ is about 1.4 times the 2D CSC of $d_{dp}/D = 0.07$.

Table 6-6 Input parameters of parametric studies of pipe internal pressure

Key Parameter	Indenter Diameter		D/t	Y/T	f_p	Target Residual Dent Depth
	mm	in				% OD
Value	114.3	4.5	51	0.88	0, 0.72	1%, 3%, 6%, 8%

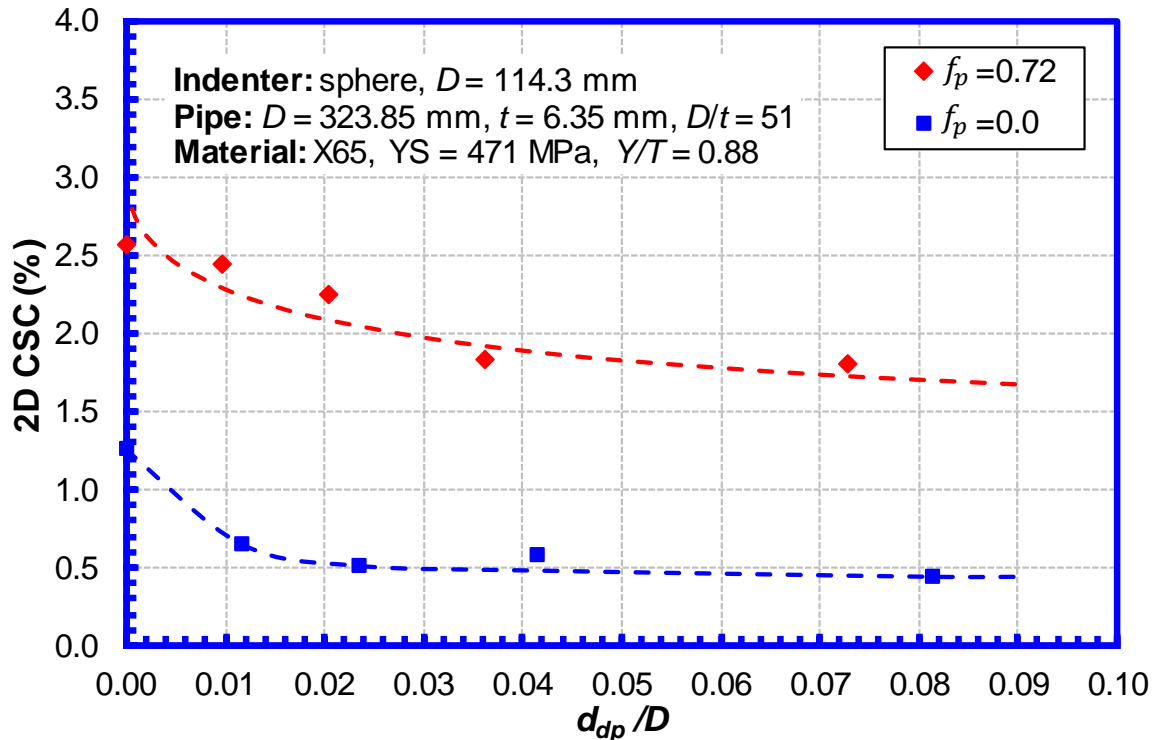


Figure 6-20 2D CSC of dented pipes with different pressure factors

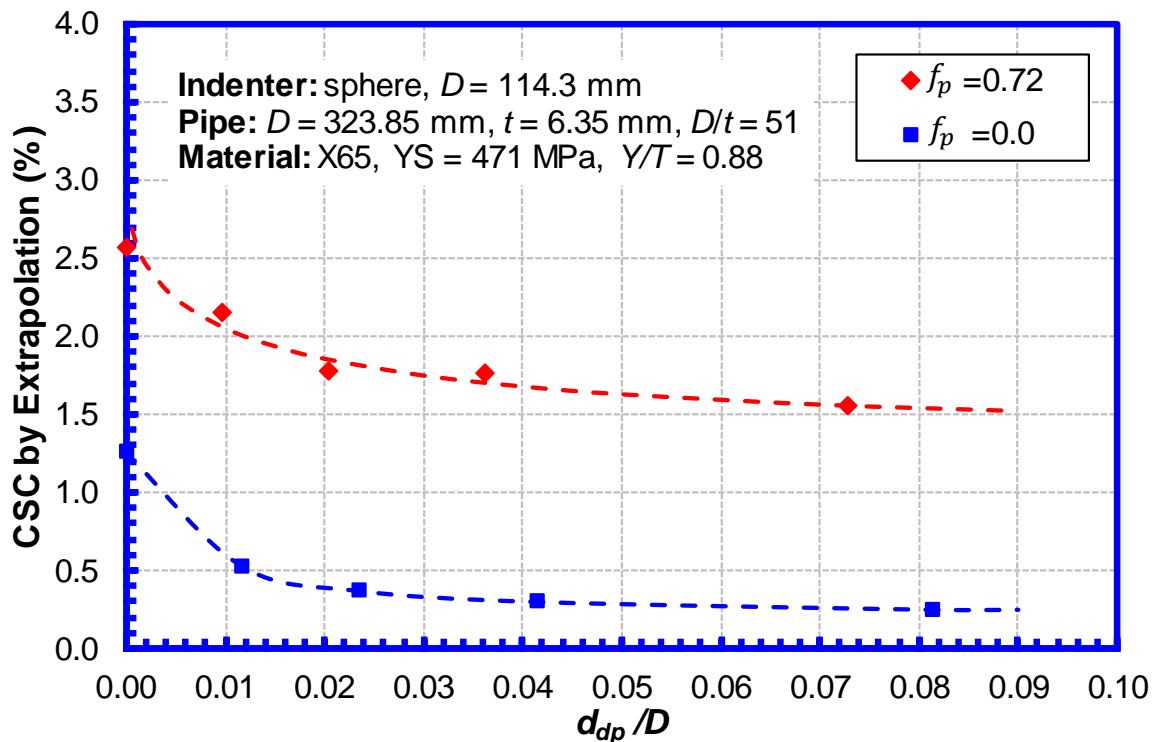


Figure 6-21 CSC by extrapolation of dented pipes with different pressure factors

6.5 Establishment of Equivalent Geometry Imperfections of Dented Pipes

The CSC equation for plain pipes, i.e., Eqs. (4-9) to (4-16) in Section 4.3.2, is given as a function of pipe geometry imperfections generated by pipe manufacturing. Additional discussions about the pipe geometry imperfections can be found in Section 4.3.3. The dents are in fact one type of geometry imperfections. Therefore, the CSC equation of plain pipes, i.e., Eqs. (4-9) to (4-16), can be extended to cover the pipes with dents if equivalent geometry imperfections for dents can be established.

In this section, the equivalent geometry imperfection heights for dents are established. For each 2D CSC calculated in the parametric studies (in Figure 6-16 and Figure 6-18), Eqs. (4-9) to (4-16) were used to back calculate the equivalent geometry imperfection height that can lead to the 2D CSC. The 2D CSC was used in the calculation because the CSC in Eqs. (4-9) to (4-16) is given as 2D CSC.

The equivalent geometry imperfection heights (h_g^e/t) calculated for different dent depths are shown in Figure 6-22 and Figure 6-23. Figure 6-22 and Figure 6-23 are created from the parametric studies in Section 6.4.2 (at different pipe D/t ratios) and Section 6.4.3 (at different pipe Y/T ratios), respectively. It should be noted that the h_g^e/t given in Figure 6-22 and Figure 6-23 are for pressurized conditions ($f_p = 0.72$). The h_g^e/t for unpressurized conditions ($f_p = 0$) in the parametric studies in Section 6.4.4 is greater than the upper bound geometry imperfection height applicable for Eqs. (4-9) to (4-16) (i.e., $h_g^e/t > 0.30$). Therefore, the results for unpressurized conditions are not shown.

Figure 6-22 and Figure 6-23 show that the h_g^e/t of a given dent is greatly affected by the pipe D/t ratio. But, the pipe Y/T ratio shows minor effect on the h_g^e/t . Based on the results shown above, the h_g^e/t of dents (shown in Figure 6-22 and Figure 6-23) were fitted into a function of normalized dent depth (d_{dp}/D) and pipe D/t ratio as shown in the following:

$$h_g^e/t = 0.01 * [0.019 * (D/t) + 1.4] (100 * d_{dp}/D)^{[-0.023*(D/t)+1.9]} \quad (6-1)$$

where the d_{dp}/D , D/t , and h_g^e/t ratio are in the unit of mm/mm.

If the calculated h_g^e/t is smaller than the pipe manufacturing geometry imperfection h_g/t , the h_g/t should be used to calculate the pipe CSC. For this condition, the pipe manufacturing geometry imperfection limits the CSC and the wrinkle can be formed out of the dent area.

It should be noted that Eq. (6-1) is only applicable for high pressure conditions ($f_p = 0.72$). The comparison of the h_g^e/t calculated with Eq. (6-1) and the original data shown in Figure 6-22 and Figure 6-23 is shown in Figure 6-24. The fitted and original results show a good agreement.

6.6 Compressive Strain Capacity Equations of Dented Pipes

6.6.1 Equations for 2D CSC

The 2D CSC equations for plain pipes, i.e., Eqs. (4-9) to (4-16) in Section 4.3.2, can be used to calculate the 2D CSC for the pipes with dents by replacing the pipe geometry imperfection height (h_g/t) with the equivalent geometry imperfection height (h_g^e/t) calculated from Eq. (6-1).

Due to the limited range of the parameters used in the parametric studies of dented pipes, the applicable range of some parameters shown in Section 4.3.2 should be replaced by the following:

- (1) $51 \leq D/t \leq 72$;
- (2) $0.72 \leq f_p \leq 0.80$;
- (3) $0.77 \leq R_{YT} \leq 0.88$; and
- (4) $0 \leq d_{dp}/D \leq 0.08$.

6.6.2 Equations for CSC by Extrapolation

The CSC by extrapolation ($\epsilon_{c,dent}^{crit,ex}$) for dents can be calculated from the 2D CSC ($\epsilon_{c,dent}^{crit,2D}$). It is found that the relationship between 2D CSC and CSC by extrapolation for girth welds is also applicable for dents. The equation is given below and the details of the equation can be found in Section 4.3.7.2.

$$\epsilon_{c,dent}^{crit,ex}(\%) = 1.03 * \epsilon_{c,dent}^{crit,2D}(\%) - 0.20 \quad (6-2)$$

6.6.3 Evaluation of the CSC Equations of Dented Pipes

Figure 6-25 and Figure 6-26 show the 2D CSC and CSC by extrapolation calculated by FEA and the developed CSC equations. The results from the CSC equations match the FEA results very well. It should be noted that the same set of FEA results (in Figure 6-22 and Figure 6-23) were used to develop the CSC equations. Therefore, this comparison confirms the accuracy of the development process.

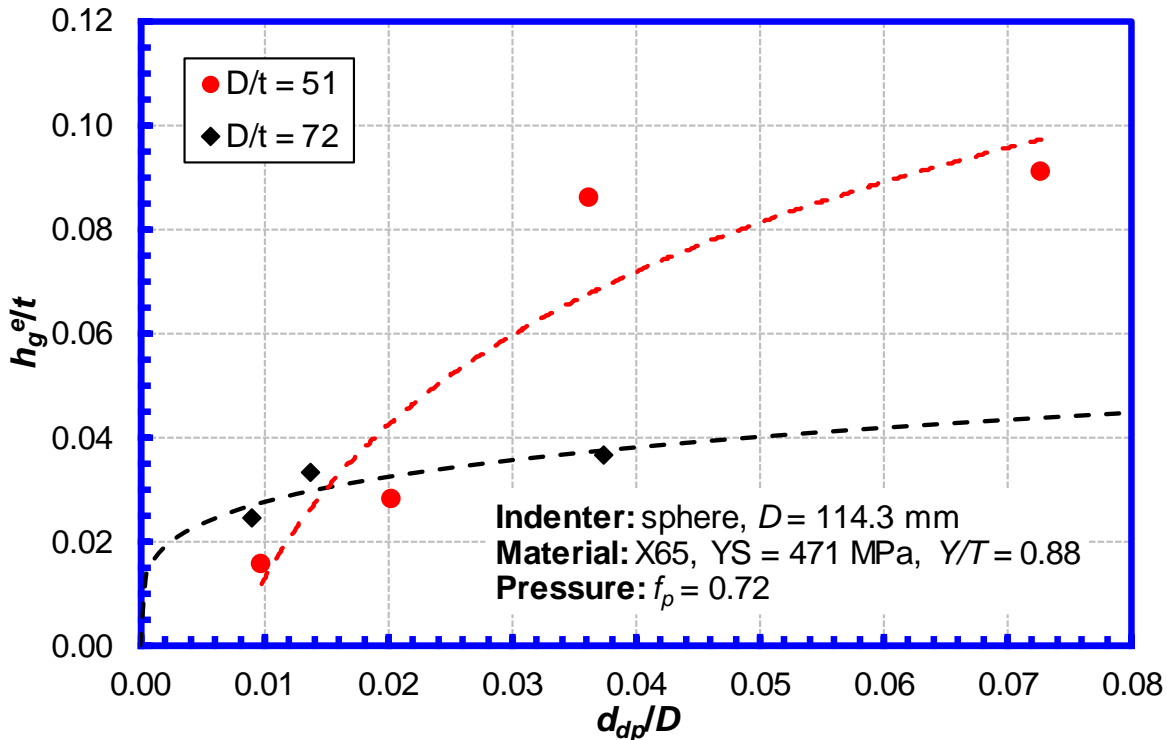


Figure 6-22 Equivalent geometry imperfection vs. dent depth for different D/t ratios

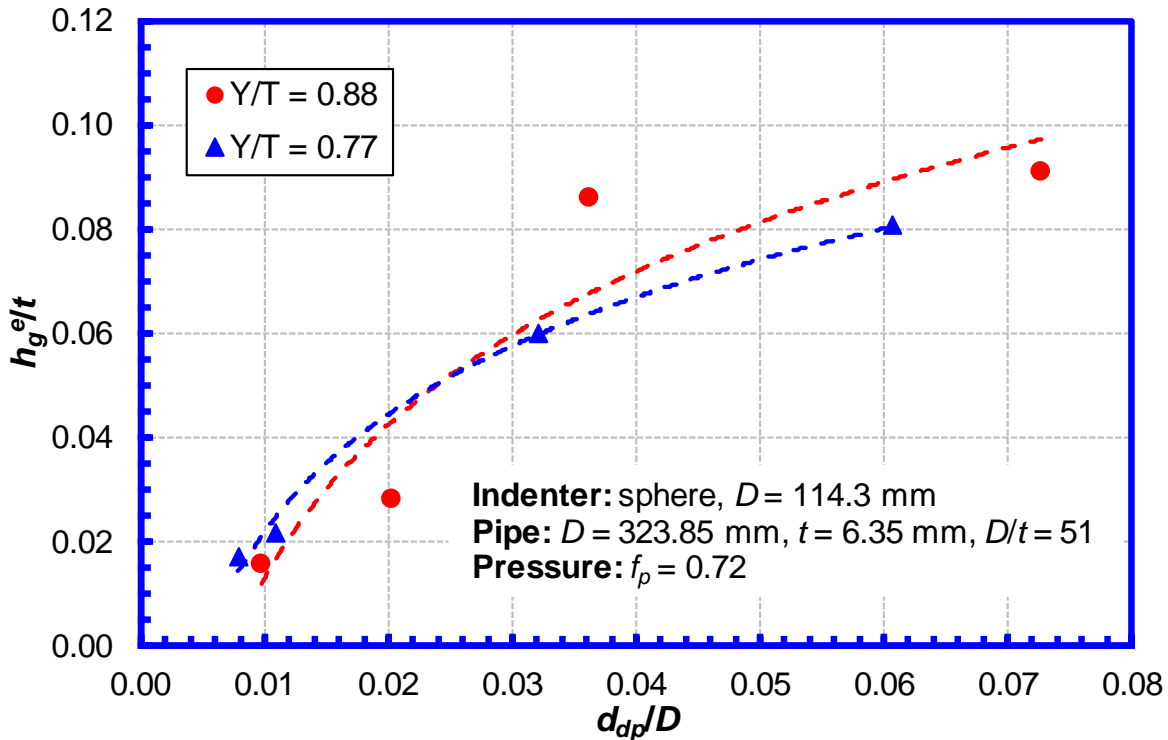
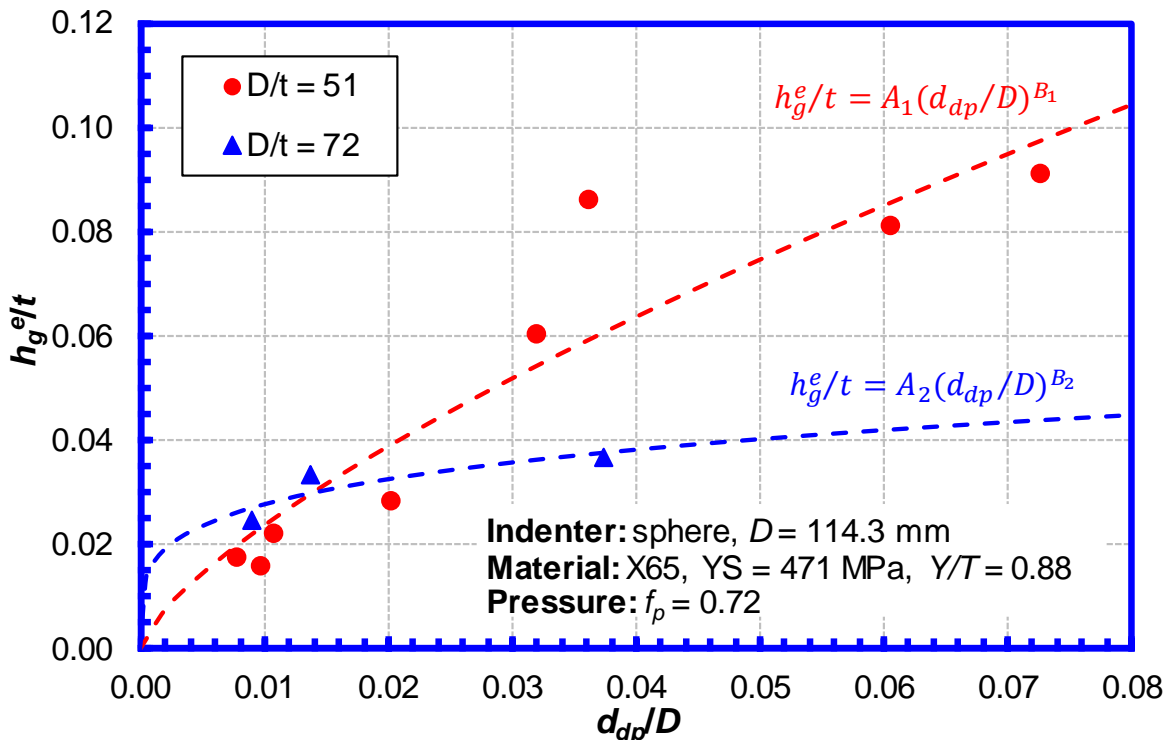
Figure 6-23 Equivalent geometry imperfection vs. dent depth for different Y/T ratios

Figure 6-24 Fitted equation of equivalent geometry imperfection

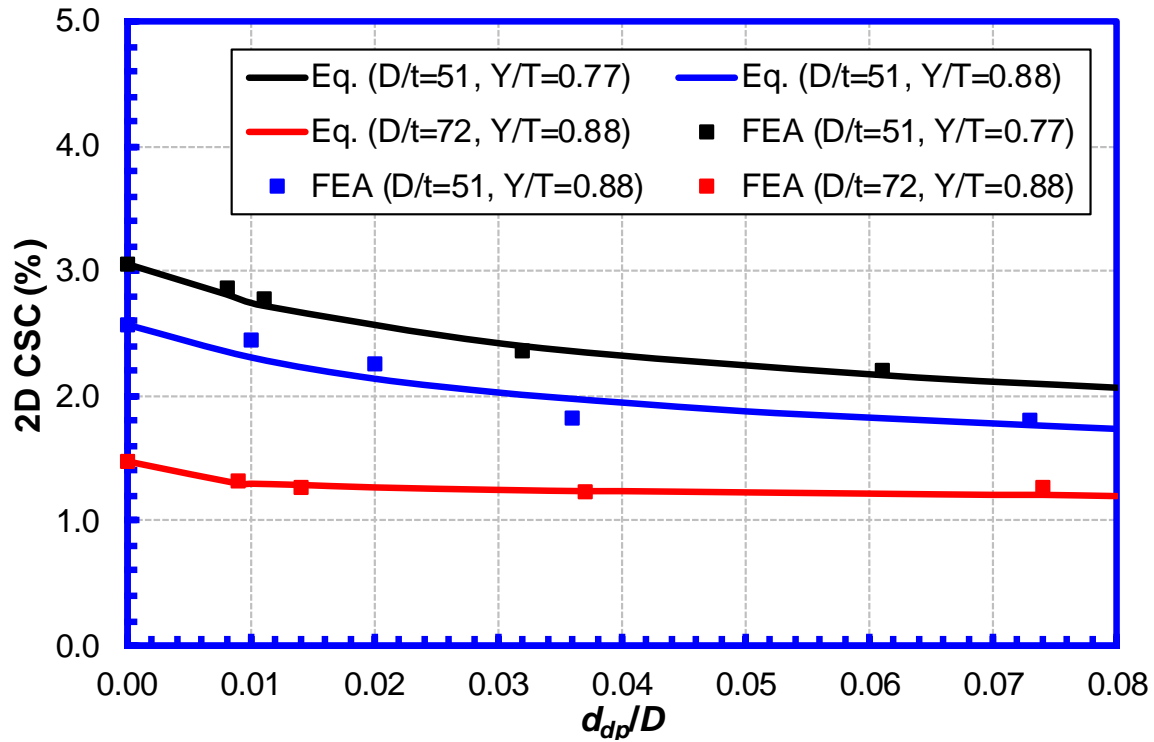


Figure 6-25 Comparison of 2D CSC from developed equations and FEA

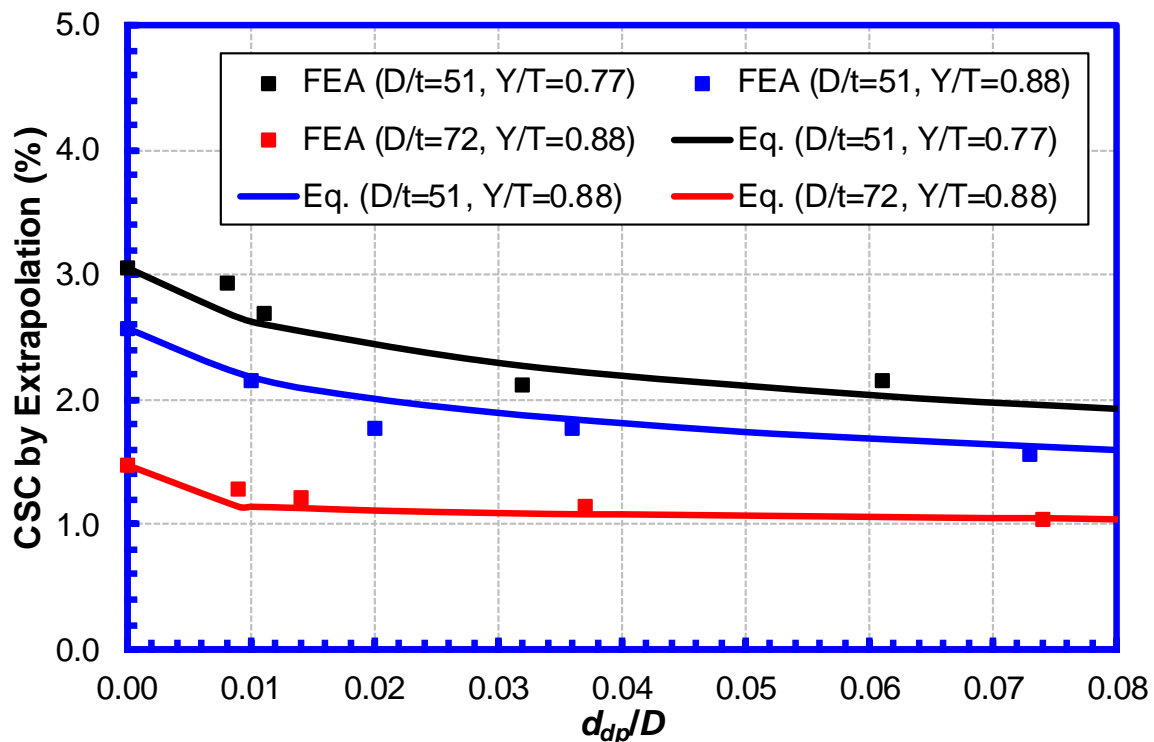


Figure 6-26 Comparison of CSC by extrapolation from developed equations and FEA

7 Pipes with Wrinkles Subjected to Longitudinal Strain

7.1 Overview of the Studies on Wrinkles

7.1.1 Limit States Associated with Wrinkles Subjected to Longitudinal Strain

Wrinkles are local pipe wall distortion formed by excessive compressive loading, as shown in Figure 7-1. Outward wrinkles are often formed under internal pressure and inward wrinkles are often formed under no or very low internal pressure.



(a) wrinkle formed at no internal pressure (b) wrinkle formed at high internal pressure

Figure 7-1 Wrinkles in pipes [86]

For buried pipelines, wrinkles are often caused by the bending and/or axial compression load generated by ground movement hazards. When a wrinkle is detected in the field, the maximum longitudinal load (i.e., force or bending moment) that the pipe can carry has often been reached. In another word, the longitudinal compressive strain capacity has been exceeded (since the strain capacity is often defined as the strain at the maximum load).

The form of a wrinkle is usually considered as a service limit state and does not result in immediate leaking or rupturing. So, even if a wrinkle is formed, the pipeline can still be safely operated if no additional ground movement (i.e., longitudinal load) is expected. However, it is concerned that the wrinkle may compromise the pressure containment capacity of the pipe due to the large longitudinal compressive strain and hoop tensile strain observed at the wrinkle location. The focus of the analyses in this project is to examine the effects of the wrinkles and longitudinal and hoop strains on the burst pressure of the pipe. The assessment of the other limit states of the wrinkles (e.g., fatigue, ductile fracture initiation strain, etc.) can be found in [87].

7.1.2 Section Structure and General Approach

In this project, the effects of the wrinkle and longitudinal compressive strain on the pipe burst pressure were studied through finite element analyses and full-scale tests. The general approach for the studies and the structure of this section are listed below:

- Finite element analyses (FEA) were conducted to simulate the formation of the wrinkles and the burst behaviors of the wrinkled pipes subjected to longitudinal compressive strain. The FEA methods and procedures are introduced in Section 7.2.

- The FEA results were compared with the full-scale test data. Based on the FEA and test results, the mechanisms responsible for the wrinkles' effects were discussed. The results were shown in Section 7.3.
- The methods for assessing the burst pressure of wrinkled pipes were discussed in Section 7.4.

7.2 Finite Element Analyses

7.2.1 Finite Element Analysis Models

Finite element analyses (FEA) were conducted to simulate the formation of wrinkles and the burst of wrinkled pipes. The pipe size and testing setup used in the full-scale tests (see Section 3.4) were used in the FEA. The commercial finite element software ABAQUS® was used for the analyses.

A typical FEA model is shown in Figure 7-2, in which the pipe has a girth weld at the center of the pipe. Due to symmetric conditions in the circumferential direction, only a half of the pipe (half circumference) was modeled. Symmetry boundary conditions were applied to the relevant boundaries as shown in Figure 7-2. The end of the pipe was modeled as a rigid plane to simulate the end plate attached to the pipe in the experiment. For the pipe sections reinforced with collars (highlighted in red in Figure 7-2), the radial displacement of the pipe was constrained.

The pipe was modeled with three-dimensional hybrid eight-node solid elements with reduced integration (C3D8RH). The effect of mesh sizes on the results was thoroughly examined. The element was refined adequately to obtain converged (mesh independent) solutions. Since the wrinkle and burst can occur at any locations, the element was kept uniform throughout the pipe. The element sizes in the longitudinal, circumferential, and thickness directions are 3.0 mm, 4.0 mm, and 2.1 mm, respectively.

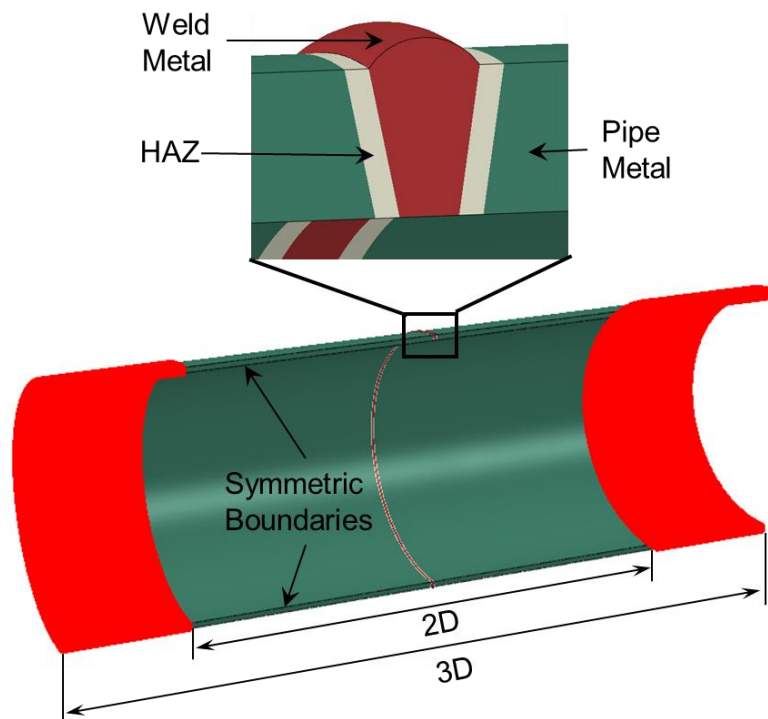


Figure 7-2 The finite element model of a pipe joint

7.2.2 Loading Conditions and Material Properties

Similar to the loading conditions used in the full-scale tests (Section 3.4), the loadings in the FEA were applied in three steps. In the first step, internal pressure was applied to the ID surface of the FEA model to induce a hoop stress of 72% SMYS (X80), while the end of the pipe was fixed in the longitudinal direction. In the second step, longitudinal compression was applied to the pipe until the target compressive strain at the wrinkle was reached. The internal pressure was kept constant in the second step. In the third step, the internal pressure was increased until the maximum pressure was reached, while the ends of the pipe were fixed to maintain the target longitudinal compressive strain.

The stress-strain curves of the pipe and girth weld used in the FEA were obtained from the small-scale tests conducted in the prior PHMSA project [26], which are shown in Figure 7-3. The stress-strain curves of the HAZ materials was assumed to be 5% lower than the pipe stress-strain curve (i.e., 5% softening).

The same pipe materials were tested in this project too (as shown in Section 2.2). The pipe stress-strain curves obtained from the two projects showed similar strength levels and very low uniform strains. However, the values of the uniform strain were somewhat different. Since the burst pressure is mainly controlled by the strength of the material, the difference in the uniform strain should not greatly affect the analysis results.

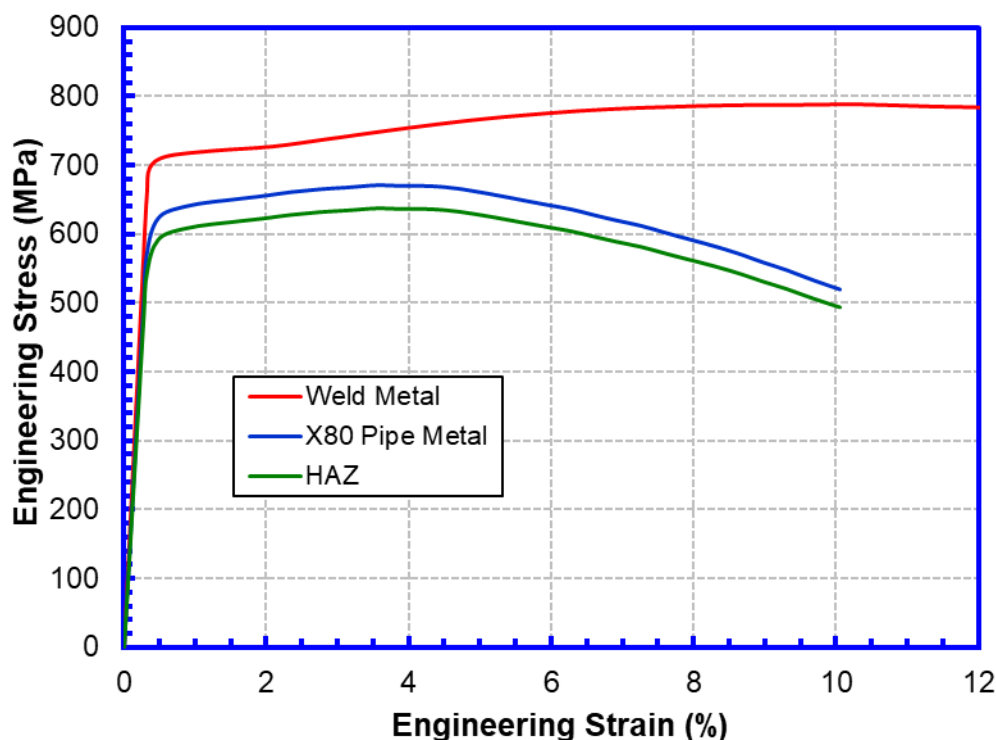


Figure 7-3 Stress-strain curves of the X80 pipe and girth weld

7.2.3 Typical Results and Failure Criteria

The circumferential strain contour of a pipe with a severe wrinkle is shown in Figure 7-4. The contour is shown when the maximum pressure is reached. Very high circumferential strain can be found at the wrinkle area. The burst is defined as the event when the maximum pressure is reached. Additional discussions about the selection of the failure event can be found in Section 5.4.2.5.

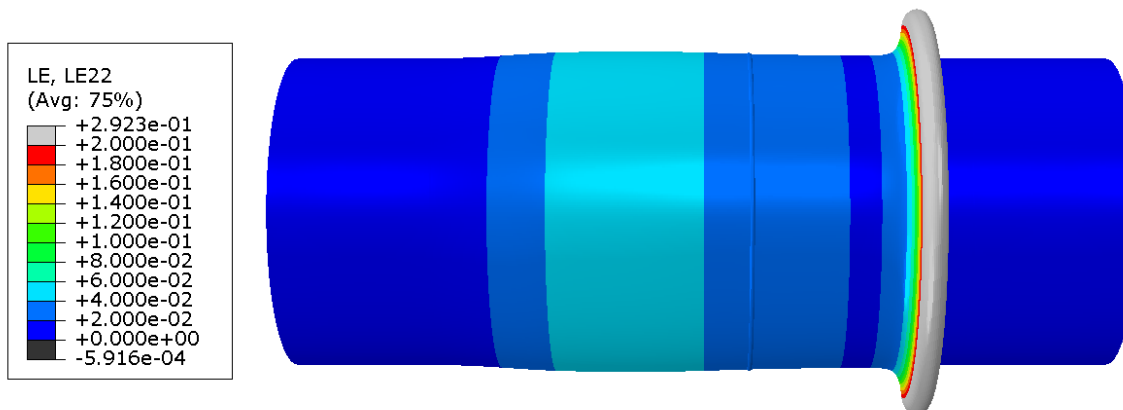


Figure 7-4 Circumference strain contour of specimen 11.c in Table 3-13

7.3 Comparison of Full-Scale Testing Data with Finite Element Analyses

The burst pressures of two pipes with different wrinkle heights and compressive strains were calculated with FEA. The FEA results are shown in Table 7-1 (see Tests 2 and 3). The wrinkle height was calculated as the distance between the peak and valley of the wrinkle (see Figure 7-5)

and the 2D strain was calculated as the average compressive strain in a 2D gauge length centered at the wrinkle. The negative strain value indicates that the 2D strain is compressive strain.

Table 7-1 also shows the burst pressure of a wrinkle-free pipe (Test 1). The burst pressure of the wrinkle-free pipe was estimated with an analytical equation given below:

$$\sigma_{mises} = \sqrt{(\sigma_h^2 - \sigma_h \sigma_a + \sigma_a^2)}$$

where σ_{mises} , σ_h , and σ_a are the von Mises, hoop, and longitudinal (axial) stress, respectively. The hoop stress was calculated as $\sigma_h = \frac{PD}{2t}$, where P is the internal pressure, D is the pipe outer diameter, and t is the wall thickness. The longitudinal stress was calculated as $\sigma_a = \nu \sigma_h$, where $\nu = 0.3$ is the Poisson's ratio (i.e., assuming zero longitudinal strain). The burst pressure was obtained by setting the von Mises stress to the pipe ultimate tensile strength (672 MPa).

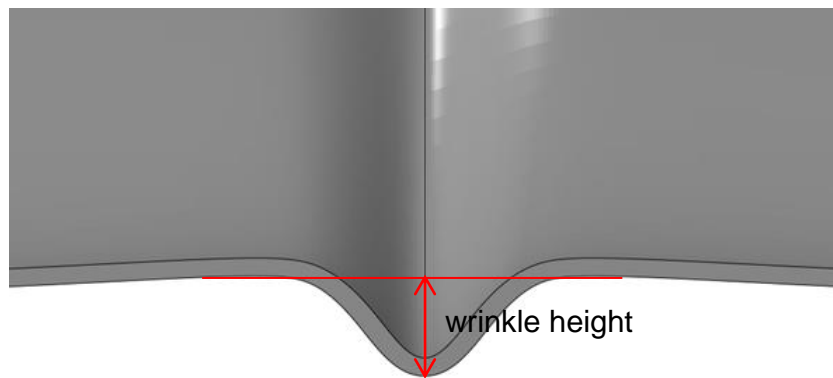


Figure 7-5 Definition of wrinkle height for inward and outward wrinkles [87]

The burst pressure in Table 7-1 was normalized by the burst pressure of the wrinkle-free pipe (i.e., Test 1). Figure 7-6 and Figure 7-7 show the normalized burst pressure as a function of the 2D compressive strain and wrinkle height, respectively. The experimental results are also shown in the Figure 7-6.

The effects of the compressive strain and wrinkle on the burst pressure are found to be very limited. For the pipe with a very severe wrinkle, which is folded onto itself (2D compressive strain is -17% and wrinkle height is 16%D), the reduction of the burst pressure is only about 10 - 15%. No change is found in the burst pressure when the compressive strain is below 2% and the wrinkle height is less than 4%D. In addition, the burst location is away from the wrinkle, which indicates that the high strain around the wrinkle does not negatively affect the burst pressure.

Instead, the decrease of the burst pressure by the extremely large wrinkle is likely caused by the change of biaxial loading conditions. Due to the Poisson's effect, the high internal pressure near the burst can generate high longitudinal tensile stress in the pipe even if the pipe is under a high compressive strain before the pressure is increased to burst the pipe. This high longitudinal tensile stress tends to increase the burst pressure. For the pipe with an extremely large wrinkle, the wrinkle increases the pipe compliance and therefore the longitudinal tensile stress caused by the internal pressure can be reduced (See Table 7-1 and Table 7-2).

The nominal longitudinal stress at burst calculated by the FEA and measured from the tests are shown in Table 7-1 and Table 7-2, respectively. The nominal longitudinal stress at burst was calculated with the longitudinal net section force and the pipe cross section area. For the wrinkle of $4\%D$ height and $1\sim 2\%$ 2D compressive strain, a tensile longitudinal stress is shown at the time of burst. On the other hand, for the extremely large wrinkle ($16\%D$ height and $17\sim 18\%$ 2D compressive strain), the longitudinal stress remains as compressive stress at the time of burst. It is believed that the severe wrinkle increases the compliance of the pipe and therefore reduces the longitudinal stress induced by the Poisson's effect and internal pressure.

Table 7-1 Burst pressure calculated by FEA and analytical method

D	t	Test Number	Wrinkle Height	2D Strain	Burst Pressure	Longitudinal Stress at Burst
mm	mm		%D	%	MPa	MPa
610	12.7	1	0.00	0.00	31.6	N/A
		2	4.08	-2.03	31.5	129.9
		3	15.83	-17.72	27.0	-45.3

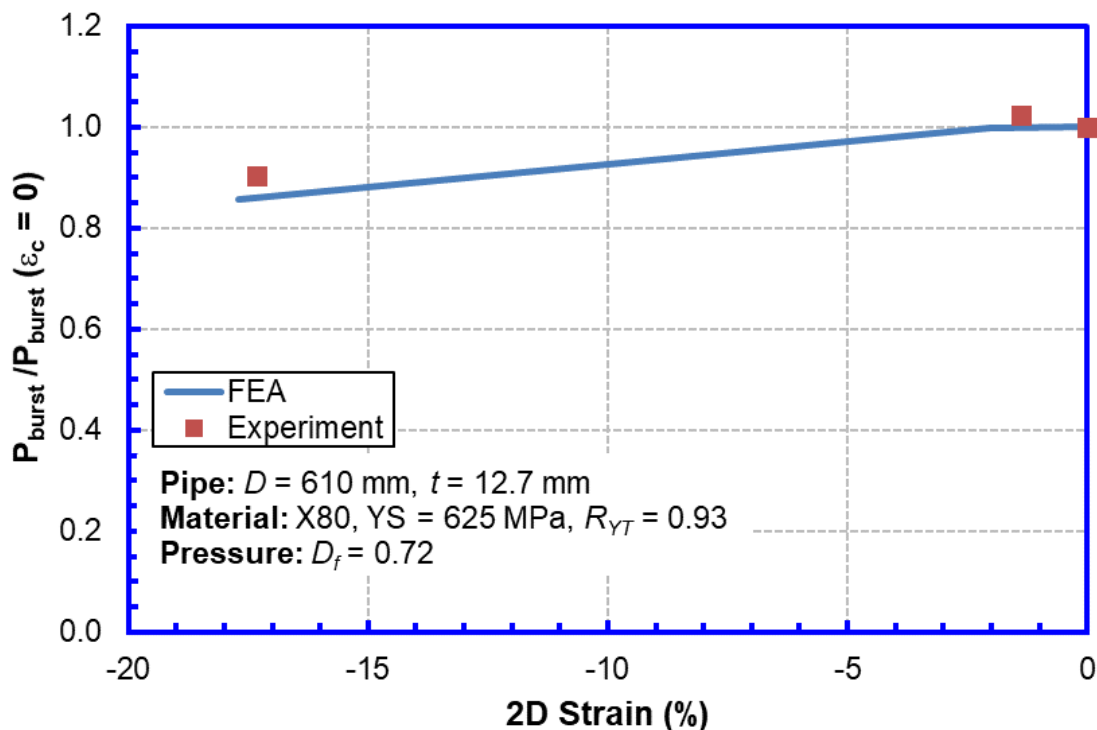


Figure 7-6 Change of burst pressure with longitudinal compressive strain at the wrinkle

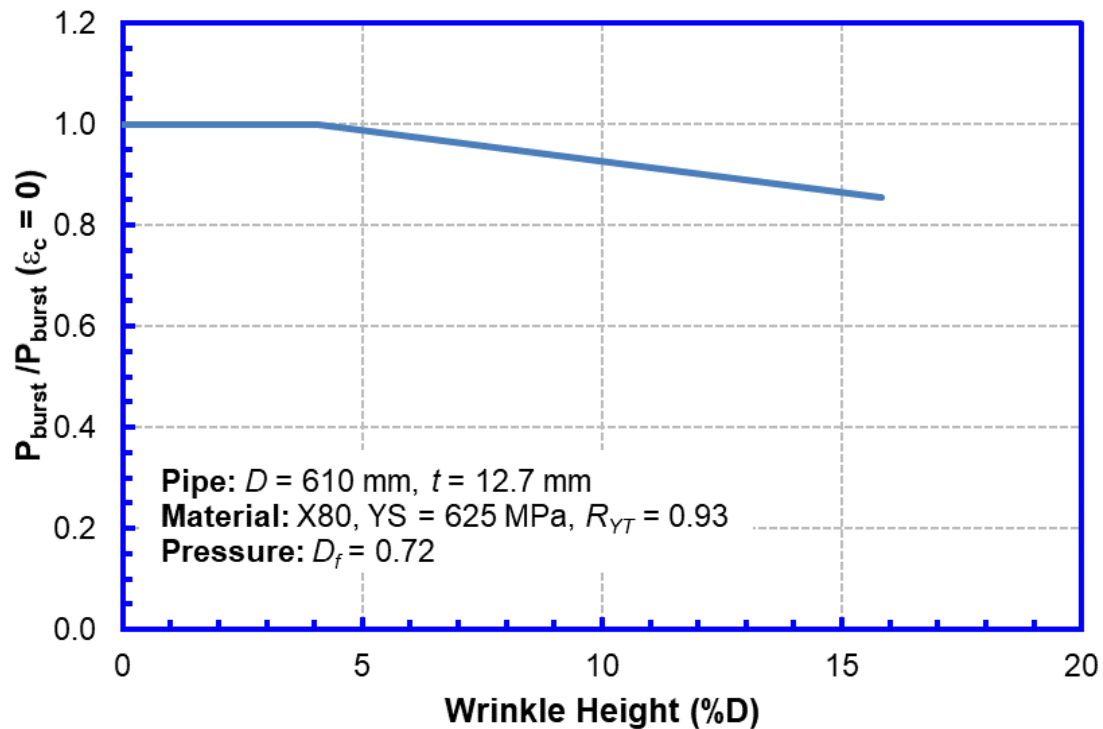


Figure 7-7 Change of burst pressure with wrinkle height

Table 7-2 Results measured from tests

D	t	Test Number	2D Strain	Burst Pressure	Longitudinal Stress at Burst
mm	mm		%	MPa	MPa
610	12.7	1	0.00	31.2	N/A
		2	-1.38	31.9	94.5
		3	-17.34	28.2	-42.9

7.4 Burst Pressure of Wrinkled Pipes under Compressive Strain

In summary, no reduction in the burst pressure can be observed for wrinkles of reasonable sizes (e.g., $4\%D$) and at reasonable compressive strain levels (e.g., -2%). For extremely large wrinkles, the maximum reduction in the burst pressure is about 10% - 15%, which is mainly caused by the reduction of the tensile force at the time of burst (due to the increase of the pipe longitudinal compliance caused by the large wrinkle).

Based on the observations, it is concluded that the wrinkles under longitudinal compressive strain have minor effects on the burst pressure of the pipe. The burst pressure of a pipe is not affected by the wrinkles of reasonable sizes and at reasonable compressive strain levels.

8 Concluding Remarks

8.1 General

The key objective of this project was to develop practical guidelines and tools for the SBDA of pipeline segments containing transition welds and anomalies. In this regard, the SBDA methods were expanded to pipes with transition girth welds, corrosion anomalies, dents, and wrinkles. Two types of transition welds, i.e., back-beveled and counterbore-tapered welds, were studied. For corrosion anomalies, the metal-loss type corrosion anomalies were studied. For dents and wrinkles, the studies were limited to plain dents and wrinkles (i.e., no gouges or cracks). No interactions between the anomalies and/or welds were considered.

The resistance to the most critical or relevant limit states associated with the transition welds and the anomalies were investigated. For the transition welds, the TSC and CSC were studied. For corrosion anomalies, the TSC, CSC, and burst pressure were studied. For dents, the CSC was studied. For wrinkles, the burst pressure was studied.

The technical work conducted in this project included finite element analyses (FEA), small-scale material tests, and large-scale tests. The FEA results were used to assist the specimen and instrumentation design for the large-scale tests and to develop the SBDA guidelines. The large-scale tests generated resistance data for the studied limit states, which were used to evaluate the SBDA guidelines. The small-scale tests provided necessary inputs to assist the large-scale test design/confirmation and evaluate the SBDA guidelines. The highlights of the output are given below.

- Large-scale tests and associated limit state
 - Curved wide plate (CWP) tests for girth welds including transition welds – TSC
 - Full-scale pressurized bending tests for girth welds including transition welds – CSC
 - Full-scale pressurized tensile tests for metal loss corrosion anomalies - TSC
 - Full-scale pressurized bending tests for metal loss corrosion anomalies - CSC
 - Full-scale pressurized bending and burst tests for metal loss corrosion anomalies – burst pressure under longitudinal compressive strain
 - Full-scale pressurized bending tests for plain dents - CSC
 - Full-scale pressurized compression and burst tests for wrinkles – burst pressure under longitudinal compressive strain
- Assessment guidelines or equations
 - TSC and CSC of pipes with girth welds including transition welds
 - TSC and CSC of pipes containing metal loss corrosion anomalies
 - Burst pressure of pipes containing metal loss corrosion anomalies under longitudinal compressive strain
 - CSC of pipes containing plain dents
 - Burst pressure of pipes containing wrinkles under longitudinal compressive strain

The key technical findings are summarized in the following sections.

8.2 Girth Welds

8.2.1 Tensile Strain Capacity

The tensile strain capacity (TSC) of a transition girth weld was found to be greatly affected by the strength difference between the thick-wall and thin-wall pipes of the girth weld (see details in Sections 4.2.3.1 and 4.2.4.3). The existing pipe strength and thickness specifications for the transition weld, which focus on pressure containment (e.g., ASME B31.8) are not adequate for the pipes subjected to high longitudinal strain (i.e., for the SBDA).

In this project, enhanced pipe strength and wall thickness specifications for the back-beveled and counterbore-tapered transition welds were developed. The enhanced specifications address both pressure containment and longitudinal strain. The goal of the enhanced specifications is to prevent strain localization in the pipe wall thickness transition area and achieve reasonable TSC in the pipe.

The enhanced pipe strength and thickness specifications for the counterbore-tapered welds are given below (see details in Section 4.2.3.1):

- The longitudinal yield and ultimate tensile strengths of the thick-wall pipe should not be less than those of the thin-wall pipe.
- The SMYS of the thick-wall pipe should not be less than the SMYS of the thin-wall pipe.
- If the wall thickness ratio is greater than 1.50, the wall thickness ratio should be treated as 1.50 for design and assessment.

The enhanced pipe strength and thickness specifications for the back-beveled welds are given below (see details in Section 4.2.4.3):

- The longitudinal ultimate tensile strength of the thick-wall pipe should not be less than the longitudinal flow strength of the thin-wall pipe, where the flow strength of the thin-wall pipe is the average of the yield strength and ultimate tensile strength of the thin-wall pipe.
- $R_t \geq \max(R_G, R_y, R_u)$, where R_t is the ratio between the thickness of thick-wall pipe and that of the thin-wall pipe; R_G is the ratio between the SMYS of thin-wall pipe and that of the thick-wall pipe; R_y is the ratio between the longitudinal yield strength of thin-wall pipe and that of the thick-wall pipe; R_u is the ratio between the longitudinal ultimate tensile strength of the thin-wall pipe and that of the thick-wall pipe.
- If the wall thickness ratio (R_t) is greater than 1.50, the wall thickness ratio should be treated as 1.50 for design and assessment.

Assessment equations were developed to calculate the TSC of the transition girth welds. For the counterbore-tapered transition welds, the PRCI-CRES TSC equations [28] for the regular girth welds can be directly used if the enhanced pipe strength and thickness specifications are met (see details in Section 4.2.3.2.1). An easy-to-use procedure was developed to calculate the TSC when the enhanced pipe strength and thickness specifications are not satisfied (see details in

Section 4.2.3.2.2). The procedure uses the PRCI-CRES TSC equations and the full longitudinal stress-strain curves of the thin and thick pipes.

For the back-beveled transition welds, assessment equations were developed to calculate the TSC when the enhanced pipe strength and thickness specifications are satisfied (see details in Section 4.2.4.5). The assessment equations include the PRCI-CRES TSC equations for the regular girth welds and a transition weld TSC reduction factor. The TSC reduction factor depends on the longitudinal yield strength ratio between the thin and thick pipes and the TSC of the corresponding regular girth weld.

A total of eight curved-wide plate (CWP) tensile tests were conducted to assess the TSC of a regular girth weld (4 tests) and a counterbore-tapered transition weld (4 tests) (see details in Section 3.6). Both HAZ and WCL flaws were tested. Comprehensive small-scale material tests were conducted to obtain the weld and pipe strength and/or toughness properties. Both girth welds exhibited a high degree of strength overmatching ($> 20\%$ based on pipe and weld UTS) and reasonable apparent toughness (> 0.4 mm, i.e., 0.016 in). The measured TSC appeared independent of the weld type (regular vs. counterbore-tapered) and flaw location (HAZ vs. WCL). All the tests failed in the pipe material and achieved very high TSC. The measured TSC showed very large scatters. The pipe materials used for the CWP tests satisfied the enhanced pipe strength and thickness specifications. Therefore, the TSC were calculated with the PRCI-CRES TSC equations directly. The calculated TSC showed consistent results with those measured from the CWP tests (see details in Section 4.2.3.3).

8.2.2 Compressive Strain Capacity

In the current practice, an external axial compressive force is often applied to the pipe in the bending tests measuring the compressive strain capacity (CSC). The axial compressive force is used to cancel the end-cap tensile force generated by the internal pressure and to produce lower-bound CSC. However, due to this external axial compressive force, the applied bending moment along the length of the pipe is not uniform (see details in Sections 4.3.4.1 and 4.3.4.2).

The analyses in this project demonstrated that due to the non-uniform bending moment, proper loading conditions must be used in full-scale bending tests in order to capture the effect of the girth welds on the CSC (see details in Section 4.3.4.8). The loading should be applied in such a way that the highest moment (at least on the thin pipe) is reached at the transition weld. Under proper loading conditions, the finite element analyses (FEA) in this project showed that the CSC can be greatly reduced by the transition weld (e.g., the CSC of a transition girth weld is about 20%-30% lower than the CSC of a regular girth weld for a 324-mm (12.75") OD and 6.35-mm (0.25") wall X65 pipe). The back-beveled weld showed a higher reduction to the CSC than the counterbore-tapered weld. The reduction of the CSC was largely independent of the wall thickness ratio of the two pipes joined by the welds as long as the wall thickness ratio is greater than 1.10.

Assessment equations were developed to calculate the CSC of the regular and transition girth welds (see details in Section 4.3.7). The same equations were used for the back-beveled and counterbore-tapered welds. The equations were based on the CRES CSC equations for plain

pipes developed in a prior PHMSA-supported project, in which the pipe manufacturing geometry imperfection was recognized as a key input parameter.

In the girth weld CSC equations, the girth welds (regular and transition welds) are simplified as equivalent geometry imperfections. The equivalent geometry imperfections of regular girth welds are $4\%t$ (t is pipe wall thickness). An equation for calculating the equivalent geometry imperfections of transition welds was developed, in which the equivalent geometry imperfections increase with the increase of the pipe manufacturing geometry imperfections. For the pipes with negligible manufacturing geometry imperfections, the equivalent geometry imperfections of the transition girth welds are $13\%t$.

Four full-scale bending tests (with pressure) were conducted in this project to investigate the effect of the transition welds on the CSC (see details in Section 3.2): one for a plain pipe (reference test), one for a regular girth weld, one for a back-beveled weld, and one for a counterbore-tapered weld. The tests demonstrated the effect of the regular girth weld on the CSC. However, the loading conditions used for the bending tests of the transition welds did not meet the recommended loading conditions. As a result, the test data showed that the CSC of the regular and transition welds are similar. The test data are consistent with the FEA results and confirm the effect of the loading conditions on the CSC (see details in Section 4.3.4.8).

8.3 Pipes with Corrosion Anomalies

8.3.1 Tensile Strain Capacity

The analyses in this project showed that the TSC of a pipe could be greatly reduced by corrosion anomalies. For example, for a 324-mm (12.75") OD and 7.14-mm (0.281") wall X70 pipe, the general corrosion of $0.20D$ (D is OD) long/wide and $0.40t$ (t is wall thickness) deep, can reduce the TSC of the pipe from 6-7% to about 1% (see details in Section 5.2.2, e.g., Table 5-2). The reduction in the TSC was greatly affected by the size and shape of the anomaly (see details in Section 5.2.3). Increasing the circumferential width or depth of the anomaly decreases the TSC. The TSC is largely independent of the longitudinal length of the anomaly, if the longitudinal length is greater than a critical value ($\sim\sqrt{Dt}$). However, if the longitudinal length is less than the critical value, the TSC decreases with the decrease of the longitudinal length. Therefore, the circumferential groove often leads to a higher reduction in the TSC than the general corrosion or the longitudinal groove of similar dimensions.

The guidelines developed for determining the TSC of pipes with corrosion anomalies include two key components (see details in Section 5.2.4): a TSC diagram for determining a reference TSC for a given corrosion size and an equation to convert the reference TSC to the final TSC by considering the effect of pipe properties and internal pressure.

Four full-scale tensile tests (with pressure) were conducted in this project to investigate the effect of corrosion anomalies on the TSC (see details in Section 3.5): one for a plain pipe (reference test) and three with various anomaly sizes. The tests showed consistent results with the FEA and confirmed the effect of the anomaly size on the CSC discussed above (see details in Section 5.2.2.6).

8.3.2 Compressive Strain Capacity

The analyses in this project showed that the CSC of a pipe could be greatly reduced by corrosion anomalies. For example, for a 324-mm (12.75") OD and 6.35-mm (0.25") wall X65 pipe, the general corrosion of $0.20D$ (D is OD) long/wide and $0.40t$ (t is wall thickness) deep, can reduce the CSC of the pipe from more than 3% to less than 1% (see details in Section 5.3.2, e.g., Table 5-7). The reduction in the CSC was greatly affected by the size and shape of the anomaly (see details in Section 5.3.3). Increasing the depth, circumferential width, and/or longitudinal length of the anomaly decreases the CSC. However, if the longitudinal length of the anomaly is greater than a critical value ($\sim 2\sqrt{Dt}$), the CSC is largely independent of the longitudinal length. Therefore, the general corrosion often leads to a larger reduction in the CSC than the circumferential or longitudinal grooves of similar dimensions.

The guidelines developed for determining the CSC of pipes with corrosion anomalies include two key components (see details in Section 5.3.4): a CSC diagram for determining a reference CSC for a given corrosion size and an equation to convert the reference CSC to the final CSC by considering the effect of pipe properties, pipe D/t ratios, and internal pressure.

Four full-scale tensile tests (with pressure) were conducted in this project to investigate the effect of the corrosion anomalies on the CSC (see details in Section 3.2): one for a plain pipe (reference test) and three for pipes with various anomaly sizes. The test results were consistent with the FEA results, which confirmed the effect of the anomaly size on the CSC discussed above (see details in Section 5.3.2.4).

8.3.3 Burst Pressure

The analyses in this project showed that the burst pressure of a corroded pipe could be further reduced by the longitudinal compressive strain (see details in Section 5.4.2). Increasing the longitudinal compressive strain decreases the burst pressure. The higher the corrosion depth, the greater the further reduction in the burst pressure due to the same longitudinal compressive strain. However, the magnitude of the further reduction in the burst pressure due to the longitudinal compressive strain is relatively small. For a corrosion anomaly, with depth up to of 40% of pipe wall thickness, the longitudinal compressive strain up to 2% can reduce the burst pressure by about 12% compared with the burst pressure without the longitudinal compressive strain.

A burst pressure reduction equation was developed to calculate the burst pressure of corroded pipes subjected to longitudinal compressive strain (see details in Section 5.4.4). The pressure reduction equation is a function of the longitudinal compressive strain and can be applied to the existing burst pressure equations for corroded pipes.

Four full-scale burst tests were conducted in this project to investigate the effect of the longitudinal compressive strain on the burst pressure of corroded pipes (see details in Section 3.3): one for a plain pipe (reference test), one for a corroded pipe without longitudinal compressive strain, and two for corroded pipes at 2.3% compressive strain with different anomaly shapes (longitudinal groove and general). The tests showed a maximum of ~15% reduction in the burst pressure induced by the longitudinal compressive strain, which is consistent with FEA results discussed above (see details in Section 5.4.3).

8.4 Pipes with Dents

Depending on their restraint conditions, the dents can be broadly divided into two categories, namely, restrained and unrestrained. Both the restrained and unrestrained dents could be formed in construction or in service (formed under different pressure levels). The analyses in this project showed that the CSC could be reduced by all types of dents (see details in Section 6.2). For the dents of the same depth, the unrestrained dents formed in construction show the highest reduction to the CSC. The CSC reduction under zero internal pressure is much larger than that under high internal pressure (see details in Section 6.4). In addition, the CSC decreases as the dent depth increases.

Assessment equations were developed for calculating the CSC of the pipes containing dents under high internal pressure (see details in Section 6.6). The equations are based on the CRES CSC equations for plain pipes developed in a prior PHMSA-supported project, in which the pipe manufacturing geometry imperfection is recognized as a key input parameter.

In the dent CSC equations, the dents are simplified as equivalent geometry imperfections (see details in Section 6.5). The equivalent geometry imperfection for a given dent can be determined by the equation developed in this project, in which the equivalent geometry imperfections vary with the dent depth and pipe D/t ratio.

Four full-scale bending tests (with pressure) were conducted in this project to investigate the effect of the dents on the CSC (see details in Section 3.2): one for a plain pipe (reference test) and three for pipes with various dent depths. The tests demonstrated that the dents can reduce the CSC. The test results are consistent with the FEA results (see details in Section 6.3).

8.5 Pipes with Wrinkles

Wrinkles can be formed by excessive axial/longitudinal compressive load. When a wrinkle is found in the field, the load experienced by the pipe would often have exceeded the maximum load capacity of the pipe. As a result, the pipe cannot resist any further increase of the longitudinal load. In this project, it was assumed that the longitudinal strain applied to the pipe was fixed. The analyses were focused on the burst pressure of the wrinkles experiencing high longitudinal compressive strain.

The analyses in this project showed that the wrinkles of reasonable sizes and longitudinal strain (e.g., height of $4\%D$ or average compressive strain of 2%), had negligible effects on the burst pressure of the pipe (see details in Section 7.2). Even the severe wrinkles of extreme sizes (e.g., a wrinkle folded onto itself) showed very limited effects on the burst pressure (i.e., $< 15\%$ reduction) as long as the wrinkles did not form any cracks in the pipe wall. In addition, the reduction of the burst pressure was mainly caused by the increase of the pipe longitudinal compliance due to the severe wrinkles, not the strain/stress concentration at the wrinkles. Therefore, it was concluded that wrinkles experiencing longitudinal compressive strain may not negatively affect the pipe burst pressure in the absence of cycle loads in the form of lateral bending or pressure fluctuation (see details in Section 7.4). Cycle loads can initiate or cause growth of flaws, which in turn may change the stiffness of the pipeline segment, potentially leading to high-cycle or low-cycle fatigue failures. The effects of fatigue loads were not part of the project scope and were not examined in this project.

Three full-scale burst tests were conducted in this project to study the effect of the wrinkles on the burst pressure (see details in Section 3.4): one was a reference test without any wrinkle and two tests were conducted with wrinkles formed before burst testing. The test results are consistent with the FEA results discussed above (see details in Section 7.3).

8.6 Gaps and Future Work

Some new issues and topics for further investigation regarding the SBDA have been identified during the project. The critical issues are summarized below.

Expansion of Assessment Guidelines and Equations

The work conducted in this project covered a wide scope of work, which included different limit states (e.g., tensile rupture, compressive buckling, and burst) for different features (e.g., girth welds, corrosion anomalies, dents, and wrinkles). The critical issues (e.g., controlling parameters and mechanisms) of those features were examined. Through parametric finite element analyses (FEA), assessment guidelines or equations for those features were established and evaluated with large-scale tests. However, due to time and budget limits, the parametric FEA (i.e., corrosion TSC/CSC, dent CSC, and to some extent, transition weld TSC/CSC) were conducted within a limited range. As a result, the corresponding assessment guidelines and equations are applicable for a limited range. Future work is needed to conduct additional parametric FEA and expand the applicable range of the assessment guidelines and equations.

Pipe specifications for strain-based design

The pipe strength may vary from joint to joint. A “tight” variation of the pipe strength within one pipe order could be in the range of 10 - 15 ksi. The API 5L PSL2 pipes are currently allowed to have variations larger than 15 ksi. Most of the work on the TSC of girth welds has been focused on the girth weld joining pipes of the same strength. When a high strain event occurs in the field, the strain tends to concentrate in the pipe with low strength. To prevent highly localized strain or strain concentration, the strength difference between the pipes on either side of a girth weld should be limited to a reasonable range. Proper pipe specifications are needed for the strain-based-design pipelines.

Assessment of corrosion anomalies with complicated shapes

The TSC of a pipe is found to be greatly affected by the size of the corrosion anomalies. Narrow circumferential grooves were found to have lower TSC than the general corrosions of the same width and depth, i.e., the shorter the anomaly longitudinal length, the lower the TSC. It should be noted that this observation was found from the corrosion anomalies having flat bottoms.

The actual corrosion anomalies found in field often have complicated shapes. As discussed in the above, combining all the corroded area into one long anomaly in longitudinal could over-predict the TSC using the assessment models developed in this project. For instance, linking multiple circumferentially-oriented groove corrosion patches in the longitudinal direction, thus making them more like a general corrosion, can potentially underestimate the negative impact of groove corrosion. Therefore, it may become a challenge to determine the proper length of an

anomaly with complicated shapes. Future work is needed to understand of the impact of the anomaly shape on the TSC of the corroded pipes. The work is critical for developing ILI tool screening criteria and assessment procedures.

SBDA for cyclic loadings

All the limit states investigated in this project were for static loadings. For the SBDA, the limit state for cyclic loadings (e.g., fatigue) is also an important issue. It is especially true for dents. An optional task was proposed to study the fatigue resistance of dents for the SBDA conditions (i.e., subjected to high longitudinal strain and cyclic pressure and temperature loadings). The task was not selected due to the budget limit. Future work is needed to study the fatigue for the SBDA conditions.

Additional large-scale tests of pipes with anomalies

The testing program in this project consisted of a small number of tests to facilitate checks/evaluations of the assessment models developed. Due to the limited tests, some key parameters could not be adequately addressed. For example, for the corrosion anomalies, three tests were conducted to examine the effects of the depth and length of the anomaly. The effects of the anomaly width and shape were not addressed. Therefore, additional full-scale tests are needed.

Curved-wide plate tests of transition welds

The counterbore-tapered transition welds that were tested in this project were only made using the FCAW process. Due to budget and time limits, the back-beveled transition welds and the transition welds made with SMAW processes were not prepared and evaluated. The back-beveled transition welds and the SMAW process are commonly used. Therefore, it is important to understand the TSC of the back-beveled transition welds and the transition welds made with SMAW. Additional curved-wide-plate tests of the back-beveled transition welds and the transition welds made with SMAW are needed. In addition, the influence of the weld strength mismatch may also need to be investigated given the potential for a wide range of weld mismatch that can be obtained with FCAW/SMAW processes.

9 Reference

- 1 Zhang, F., Liu, M., Wang, Y.-Y., Yu, Z., and Tong, L., 2012, "Strain Demand in the Areas of Mine Subsidence," *Proceedings of the 9th International Pipeline Conference*, Calgary, Alberta, Canada September 24-28.
- 2 Zhang, F., Liu, M., Wang, Y.-Y., Yu, Z., and Tong, L., 2012, "Integrity of Pipeline in Area of Mine Subsidence," *Proceedings of the 9th International Pipeline Conference*, Calgary, Alberta, Canada, September 24-28.
- 3 Liu, M., Wang, Y.-Y., and Yu, Z., 2008, "Response of Pipelines under Fault Crossing," *Proceedings of the 18th International Offshore and Polar Engineering Conference*, Vancouver, Canada, July 6-11.
- 4 Wang, Y.-Y., Ma, J., and Kulkarni, S., 2013, "Assessment of Vintage Girth Welds and Challenges to ILI Tools," *Journal of Pipeline Engineering*, vol. 12 Issue 2, p117-126, June.
- 5 "Management of Ground Movement Hazards for Pipelines," final report, CRES Project No. CRES-2012-M03-01, 2017.
- 6 Wang, Y.-Y., Liu, M., Zhang, F., Horsley, D., and Nanney, S., 2012, "Multi-tier tensile strain design models for strain-based design Part I - fundamental basis," *Proceedings of the 9th International Pipeline Conference*, Calgary, Alberta, Canada, September 24-28.
- 7 Liu, M., Wang, Y.-Y., Song, Y., Horsley, D., and Nanney, S., 2012, "Multi-tier Tensile Strain Models for Strain-Based Design Part II - Development and Formulation of Tensile Strain Capacity Models," *Proceedings of the 9th International Pipeline Conference*, Calgary, Alberta, Canada, September 24-28.
- 8 Liu, M., Wang, Y.-Y., Horsley, D., and Nanney, S., 2012, "Multi-tier tensile strain design models for strain-based design Part III - model evaluation against experimental data," *Proceedings of the 2012 9th International Pipeline Conference*, Calgary, Alberta, Canada, September 24-28
- 9 Wang, Y.-Y. and Liu, M., 2013, "Status and Applications of Tensile Strain Capacity Models," *Proceedings of the 6th Pipeline Technology Conference*, Ostend, Belgium, October 7-9.
- 10 Kibey, S., Issa, J.A., Wang, X., and Minnaar, K., 2009, "A simplified, parametric equation for prediction of tensile strain capacity of welded pipelines," *Proceedings of the 4th Pipeline Technology Conference*, Ostend, Belgium, October 12-14.
- 11 Fairchild, D., Kibey, S., Tang, H., Krishnan, V., Macia, M., Cheng, W., and Wang, X., 2012, "Continued advancements regarding capacity prediction of strain-based pipelines," *Proceedings of the 9th International Pipeline Conference*, Calgary, Alberta, Canada, September 24-28.
- 12 Tang, H., Panico, M., Fairchild, D., Crapps, J., Cheng, W., 2014, "Strain Capacity Prediction of Strain-Based Design Pipelines," *Proceedings of the 10th International Pipeline Conference*, Calgary, Alberta, Canada, September 29 - October 3.

- 13 Østby, E, 2005, "New strain-based fracture mechanics equations including the effects of biaxial loading, mismatch and misalignment," *Proceeding of the 24th International Conference on Offshore Mechanics and Arctic Engineering*, Halkidiki, Greece, June 12-17.
- 14 Sandvik, A., Østby, E, Naess A., Sigurdsson G., and Thaulow, C., 2005, "Fracture control – offshore pipelines: probabilistic fracture assessment of surface cracked ductile pipelines using analytical equations," *Proceeding of the 24th International Conference on Offshore Mechanics and Arctic Engineering*, Halkidiki, Greece, June 12-17.
- 15 Østby, E., Torselletti, E., and Levold, E., 2006, "A strain-based approach to fracture assessment of pipelines," *Proceedings of FITNET 2006*, International Conference on Fitness-for-service, Amsterdam, Netherlands, May 17-19.
- 16 Østby, E., 2007, "Proposal for a strain-based fracture assessment procedure for offshore pipelines" *Proceedings of the 17th International Offshore and Polar Engineering Conference*, Lisbon, Portugal, July 1-6.
- 17 Otsuka, A., et al., 1980, "Effect of Stress Triaxiality on Ductile Fracture Initiation of Low Strength Steel," *J. of the Society of Material Science*, Japan, Vol. 29, No. 322, pp. 717-723.
- 18 Toyoda, M., et al., 2001, "Criterion for Ductile Cracking for the Evaluation of Steel Structure under Large Scale Cyclic Loading," *Proc. Of 20th International Conference on Offshore Mechanics and Arctic Engineering*, OMAE 2001-MAT-3103.
- 19 Igi, S. and Suzuki, N., 2007, "Tensile Strain Limits of X80 High-Strain Pipelines," *Proceedings of the 17th International Offshore and Polar Engineering Conference*, Lisbon, Portugal, July 1-6.
- 20 Det Norske Veritas (DNV), 2010, "Submarine Pipeline Systems," DNV Offshore Standard, DNV-OS-F101.
- 21 Canadian Standard Association (CSA), 2011, "Oil and Gas Pipeline Systems," CSA Standard, CSA Z662-11.
- 22 American Petroleum Institute (API), 1999, "Design, Construction, Operation, and Maintenance of Offshore Hydrocarbon Pipelines (Limit State Design)," API Recommended Practice, API RP 1111.
- 23 Dorey, A.B, Murray, D.W., and Cheng, J.J.R., 2002, "Material Property Effects on Critical Buckling Strains in Energy Pipelines," *Proceedings of the 4th International Pipeline Conference*, Calgary, Alberta, Canada, Sep. 29 - Oct. 3.
- 24 Dorey, A.B, Murray, D.W., and Cheng, J.J.R., 2006, "Initial Imperfection Models for Segments of Line Pipe," *Transactions of the ASME*, v128, p322 -329.
- 25 Dorey, A.B., Murray, D.W., and Cheng, J.J.R., 2006, "Critical Buckling Strain Equations for Energy Pipelines - A Parametric Study," *Journal of Offshore Mechanics and Arctic Engineering*, v128, p248-255.
- 26 Liu, M., Wang, Y.-Y., Zhang, F., and Kotian, K., 2014, "Realistic Strain Capacity Models for Pipeline Construction and Maintenance," final report to US DOT PHMSA, US DOT

- Contract No. DTPH56-10-T-000016, October 15, 2014.
<http://primis.phmsa.dot.gov/matrix/PrjHome.rdm?prj=361&btn=Modern+Search>.
- 27 Liu, M., Wang, Y.-Y., Zhang, F., Wu, X., and Nanney, S., 2013, "Refined Compressive Strain Capacity Models," *Proceedings of the 6th Pipeline Technology Conference*, Ostend, Belgium, October 7-9.
 - 28 Wang, Y.-Y., Liu, M., and Song, Y., 2011, "Second Generation Models for Strain-Based Design," final report to US DOT PHMSA, US DOT Contract No. DTPH56-06-T000014, <http://primis.phmsa.dot.gov/matrix/PrjHome.rdm?prj=201>
 - 29 "Strain-Based Design – Possible Conditions," US DOT PHMSA, February 2015.
 - 30 Canadian Standard Association (CSA), 2007, "Oil and Gas Pipeline Systems," CSA Standard, CSA Z662-07.
 - 31 American Society of Mechanical Engineering (ASME), 2009, "Manual for Determining the Remaining Strength of Corroded Pipelines," ASME Standard, ASME B31G.
 - 32 American Society of Mechanical Engineering (ASME) and American Petroleum Institute (API), 2007, "Fitness-For-Service," API 579/ASME FFS-1.
 - 33 Leis, B. and Stephens, D., 1997, "An Alternative Approach to Assess the Integrity of Corroded Line Pipe-Part II: Alternative Criterion", Volume 4, 7th International Offshore and Polar Engineering Conference, Honolulu, HI, May.
 - 34 Det Norske Veritas (DNV), 2010, "Corroded Pipelines," Recommended Practice DNV-RP-F101.
 - 35 Cosham A., and Hopkins P., 2004, "The Assessment of Corrosion in Pipelines - Guidance in the Pipeline Defect Assessment Manual (PDAM)," *Pipeline Pigging and Integrity Management Conference*, Amsterdam, the Netherlands, May 17 – 18.
 - 36 Chauhan, V. and Brister, J., 2009, "A review of methods for assessing the remaining strength of corroded pipelines," final report to US DOT PHMSA, US DOT Contract No. DTPH56-05-T0003, November.
 - 37 Liu, J., Mortimer, L., and Wood, A., 2009, "Corrosion assessment guidance for high strength steels," final report to US DOT PHMSA, US DOT Contract No. DTPH56-05-T0003, November.
 - 38 Swankie, T., Robinson, M., Liu, J., Crossley, J., and Morgan, G., 2010, "The assessment of corrosion damage in pipelines subjected to cyclic pressure loading," final report to US DOT PHMSA, US DOT Contract No. DTPH56-05-T0003, February.
 - 39 Leis, B.N., and Zhu, X.K., 2005, "Corrosion assessment criteria: rationalizing their use for vintage vs. modern pipelines," final report to US DOT PHMSA, US DOT Contract No. DTRS56-03-T0014, September.
 - 40 Chauhan, V., and Swankie, T., 2010, "Guidance for assessing the remaining strength of corroded pipelines," final report to US DOT PHMSA, US DOT Contract No. DTPH56-05-T0003, April.

-
- 41 Liu, J., Chauhan, V., Ng, P., Wheat, S., and Hughes, C., 2009, "Remaining strength of corroded pipe under secondary (biaxial) loading," final report to US DOT PHMSA, US DOT Contract No. DTPH56-05-T0003, August.
 - 42 American Society of Mechanical Engineering (ASME), 2016, "Gas Transmission and Distribution Piping Systems," ASME Standard, ASME B31.8.
 - 43 Eiber R.J. and Bubenik T.A., 1993, "Fracture Control Plan Methodology," The 8th Symposium of Line Pipe Research, Houston, TX, Arlington, VA, September 26-29.
 - 44 Hopkins P., Jones D.G., and Clyne A., 1983, "Recent Studies of the Significance of mechanical Damage in Pipelines," AGA/EPRG Seminar V, San Francisco, CA, September.
 - 45 Cosham A., and Hopkins P., 2002, "The Pipeline Defect Assessment Manual," *Proceedings of the 4th International Pipeline Conference*, Calgary, AB, Canada, September 29 – October 3.
 - 46 Semiga, V., 2012, "Dent fatigue life assessment," final report to US DOT PHMSA, US DOT Contract No. DTPH56-10-T000013, January.
 - 47 Chell, G., and Crouch, A., 2007, "Nonlinear harmonic-based mechanical damage severity criteria for delayed failures in pipelines," final report to US DOT PHMSA, US DOT Contract No. DTRS56-04-T001, April.
 - 48 Keating, P.B., and Hoffmann, R.L., 1997, "Fatigue behavior of dented petroleum pipelines," final report to US DOT PHMSA, US DOT Contract No. DTRS56-95-C0003, May.
 - 49 Zarea, M., Batisse, R., Leis, B., Cardin, P., and Vignal, G., 2012, "Full scale experimental database of dent and gouge defects to improve burst and fatigue strength models of pipelines," *Proceedings of the 9th International Pipeline Conference*, Calgary, Alberta, Canada, September 24-28.
 - 50 Tiku, S., Semiga, V., Dinovitzer, A., and Vignal, G., 2012, "Full scale cyclic fatigue testing of dented pipelines and development of a validated dented pipe finite element model," *Proceedings of the 9th International Pipeline Conference*, Calgary, Alberta, Canada, September 24-28.
 - 51 Zhu, X. K., Leis, B. N. and Clark, E. B., 2007, "Integrity Management for Wrinkle bends and Buckles," Report for US DOT PHMSA.
 - 52 Wang, Y.-Y., Liu, M., Long, X., Stephens, M., Petersen, R., and Gordon, R., 2011, "Validation and Documentation of Tensile Strain Limit Design Models for Pipelines," final report to US DOT PHMSA, US DOT Contract No. DTPH56-06-T000014, August 2, <http://primis.phmsa.dot.gov/matrix/PrjHome.rdm?prj=200>.
 - 53 Wang, Y.-Y., Zhou, H., Tyson, W.R., Gianetto, J.A., Quintana, M.A. and Weeks, T.S., 2011, "Curved Wide Plate Test Results and Transferability of Test Specimens," final report 277-T-11, PHMSA Agreement # DTPH56-07-T-000005, September.
 - 54 Wang, Y.-Y., Zhou, H., Liu, M., Tyson, W.R., Gianetto, Weeks, T., Richards, M., McColskey, J.D., Quintana, M.A. and Rajan, V.B., 2011, "Weld Design, Testing, and

- Assessment Procedures for High Strength Pipelines,” final summary report 277-S-01, PHMSA Agreement # DTPH56-07-T-000005, September.
- 55 Wang, Y.-Y., Liu, M., and Song, Y., 2012, “Tensile Strain Models for Strain-Based Design of Pipelines,” *Proceedings of the ASME 2012 31st International Conference on Ocean, Offshore and Arctic Engineering*, OMAE 2012-84241, Rio de Janeiro, Brazil, July 1-6.
 - 56 Wang, Y.-Y., Zhang, F., Liu, M., Cho, W., and Seo, D., 2012, “Tensile Strain Capacity of X80 and X100 Welds,” *Proceedings of the ASME 2012 31st International Conference on Ocean, Offshore and Arctic Engineering*, OMAE 2012-84240, Rio de Janeiro, Brazil, July 1-6.
 - 57 Liu, M., Zhou, H., Wang, B., and Wang, Y.-Y., 2017, “Guideline for Strain-Based Design and Assessment (SBDA) of Pipeline Segments,” US DOT Contract No. DTPH56-14-H-00003.
 - 58 American Society for Testing and Materials (ASTM) International, 2015, “Standard Test Methods for Tension Testing of Metallic Materials,” ASTM International Standard, ASTM E8/E8M-15.
 - 59 American Society for Testing and Materials (ASTM) International, 2016, “Standard Test Methods and Definitions for Mechanical Testing of Steel Products,” ASTM International Standard, ASTM A370-16.
 - 60 The International Organization for Standardization, 2016, “Metallic Materials – Method of Test for the Determination of Quasistatic Fracture Toughness of Welds,” International Standard, ISO 15653.
 - 61 CanmetMATERIALS, 2010, “Recommended Practice: Fracture Toughness Testing Using SE(T) Samples with Fixed-Grip Loading,” Report No. 2010-31(TR).
 - 62 Dekhane, A., Liu, M., and Martens, M., 2016, “Minimum Counterbore Length and Taper Angle Criteria for Transition Welds,” *Proceedings of the 11th International Pipeline Conference*, Calgary, Alberta, Canada, September 26–30.
 - 63 American Society of Mechanical Engineering (ASME), 2016, “Pipeline Transportation Systems for Liquids and Slurries,” ASME Standard, ASME B31.4.
 - 64 Liu, M., Zhang, F., Kotian, K., and Nanney, S., 2014, “Refined modeling processes and compressive strain capacity models,” *Proceedings of the 10th International Pipeline Conference*, Calgary, Alberta, Canada, September 29 - October 3.
 - 65 Suzuki, N., Kondo, J., Endo, S., Ishikawa, N, Okastu, M., and Shimamura, J., 2006, “Effect of Geometry Imperfection on Bending Capacity of X80 Linepipe,” *Proceedings of 6th International Pipeline Conference*, Calgary, Alberta, Canada, September 25-29.
 - 66 Suzuki, N., Kondo, J., Ishikawa, N, Okastu, M., and Shimamura, J., 2007, “Strain Capacity of X80 High Strain Line Pipes,” *Proceedings of the 26th International Conference on Offshore Mechanics and Arctic Engineering*, San Diego, California, June 10 - 15.

-
- 67 Sato T., Mikami, Y., Mochizuki, M., Suzuki, N., and Toyota, M., 2008, "Parametric Study on The Effect of Geometric Imperfections on the Bending Capacity of High Strength Linepipes," *Proceedings of the 7th International Pipeline Conference*, Calgary, Alberta, Canada, September 29 - October 3.
- 68 Suzuki, N., Zhou, J., and Toyoda, M., 2008, "Compressive Strain Limits of High-Strength Linepipes", *Proceedings of 7th International Pipeline Conference*, Calgary, Alberta, Canada, September 29 - October 3.
- 69 Suzuki, N., and Toyoda, M., 2002, "Critical Compressive Strain of Linepipes Related to Work Hardening Parameters," *Proceedings of 21st International Conference on Offshore Mechanics and Arctic Engineering*, Oslo, Norway, June 23 - 28.
- 70 Suzuki, N. and Igi, S., 2007, "Compressive Strain Limits of X80 High-Strain Line Pipes," *Proceedings of 17th International Offshore and Polar Engineering Conference*, p3246, Lisbon, Portugal, July 1 - 6.
- 71 European Pipeline Operators Forum, 1998, "Specifications and Requirements for Intelligent Pig Inspection of Pipelines," Shell International Exploration and Production, Version 2.1, November.
- 72 Fu, B., and Kirkwood, M.G., 1995, "Predicting Failure Pressure of Internally Corroded Linepipe Using the Finite Element Method," *Proc. of the 14th Int. Conf. on Offshore Mech. & Arctic Eng.*, Copenhagen, Denmark, Vol. V, pp. 175 – 184.
- 73 Oh, C.-S., et al., 2011, "A Finite Element Ductile Failure Simulation Method Using Stress-Modified Fracture Strain Model," *Engineering Fracture Mechanics*, 78, pp. 124 – 137.
- 74 Sadasue, T., et al., 2004, "Ductile Cracking Evaluation of X80/X100 High Strength Linepipes," *Proceedings of the 5th International Pipeline Conference*, Calgary, Alberta, Canada.
- 75 Fathi, A., Cheng, J.J.R., Adeeb, S., and Zhou, J., 2010, "Critical Buckling Strain in High Strength Steel Pipes Using Isotropic-Kinematic Hardening," *Proceedings of the 8th International Pipeline Conference*, Calgary, Alberta, Canada, September 27 - October 1.
- 76 Liu, M. and Wang, Y.-Y., 2007, "Modeling of Anisotropy of TMCP and UOE Linepipes," *International Journal of Offshore and Polar Engineering Conference*, vol. 17, No. 4, pp. 288-293, December.
- 77 Hilgert, O., Zimmermann, S., and Kalwa, C., 2012, "Anisotropy – Benefits for UOE Line Pipe," *Proceedings of the 9th International Pipeline Conference*, Calgary, Alberta, Canada, September 24 – 28.
- 78 Fathi, A., Cheng, J.J.R., 2012, "A Parametric Study on Buckling Response of High Strength Steel Pipes with Anisotropic Material Properties," *Proceedings of the 9th International Pipeline Conference*, Calgary, Alberta, Canada, September 24 – 28.
- 79 Adeeb, S., Zhou, J., and Horsley, D., 2006, "Investigating The Effect of UOE Forming Process on The Buckling of Line Pipes Using Finite Element Modeling," *Proceedings of the 6th International Pipeline Conference*, Calgary, Alberta, Canada, September 25 – 29.

-
- 80 Tsuru, E., Agata, J., and Nagata, Y., 2010, "Analytical Approach for Buckling Resistance of UOE Linepipe with Orthogonal Anisotropy under Combined Loading," *Proceedings of the 8th International Pipeline Conference*, Calgary, Alberta, Canada, September 27 – October 1.
- 81 Lotsberg, I., 1998, "Stress Concentration Factors at Circumferential Welds in Tubulars," *Marine Structures*, 11, pp. 207-230.
- 82 Det Norske Veritas (DNV), 2011, "Fatigue Design of Offshore Steel Structures," DNV Offshore Standard, RP C-203.
- 83 Chen, Q., et al., 2010, "Remaining Local Buckling Resistance of Corroded Pipelines," *Proceedings of the 8th International Pipeline Conference*, Calgary, Alberta, Canada, September 27 – October 1.
- 84 ABAQUS/Standard User's Manual (ver 6.13), 2013, Dassault Systèmes Simulia Corp., Providence, RI, USA
- 85 Baker, M., 2009, "Mechanical Damage," final report to US DOT PHMSA, US DOT Contract No. DTRS56-02-D-70036, April.
- 86 Zimmerman, T., Timms, C., Xie, J., and Asante, J., 2004, "Buckling resistance of large diameter spiral welded linepipe," *Proceedings of the 5th International Pipeline Conference*, Calgary, Alberta, Canada, October 4 – 8.
- 87 Liu, M., Wang, Y.-Y., Sen, M., and Song, P., 2016, "Integrity Assessment of Post-Peak-Moment Wrinkles," *Proceedings of the 11th International Pipeline Conference*, Calgary, Alberta, Canada, September 26 – 30.



Natural Resources
Canada

Ressources naturelles
Canada